A Biomechanical-Biochemical Hypothesis for the Role of Collagen in Injury

by

Jeffery Matthew Barrett

A thesis
presented to the University of Waterloo
in fulfillment of the
thesis requirement for the degree of
Doctor of Philosophy
in
Kinesiology

Waterloo, Ontario, Canada, 2022

Examining Committee Membership

The following served on the Examining Committee for this thesis. The decision of the Examining Committee is by majority vote.

External Examiner: **Salvatore Federico**, Ph.D.
Professor, Dept. of Mechanical and Manufacturing Engineering,
Schulich School of Engineering, University of Calgary

Supervisor: **Jack P. Callaghan**, Ph.D.
Professor, Dept. of Kinesiology and Health Sciences,
Faculty of Health, University of Waterloo

Internal-External Member: **Duane S. Cronin**, Ph.D.
Professor, Dept. of Mechanical and Mechatronics Engineering,
Faculty of Engineering, University of Waterloo

Internal Member: **Clark R. Dickerson**, Ph.D.
Professor, Dept. of Kinesiology and Health Sciences,
Faculty of Health, University of Waterloo

Internal Member: **Joe Quadrilatero**, Ph.D.
Professor, Dept. of Kinesiology and Health Sciences,
Faculty of Health, University of Waterloo

Author's Declaration

I hereby declare that I am the sole author of this thesis. This is a true copy of the thesis, including any required final revisions, as accepted by my examiners.

I understand that my thesis may be made electronically available to the public.

Abstract

Low back pain affects 80% of the population at some point in their lives and is the most common musculoskeletal complaint for workplace injuries. Further, it presents as episodic, with sufferers typically experiencing recurrent flares of symptoms. However, the mechanisms that underpin chronic, recurrent low back pain are still disputed, and many cases are paradoxically related to sedentary occupations. Therefore, this thesis explores whether the pathomechanics of low back pain may be partially explained in terms of extracellular matrix homeostasis with a particular focus on collagen. The balance of collagen synthesis, degradation, and mechanical disruption, mediated through an inflammatory response, is foundational for chronic degenerative diseases like tendonitis, osteoarthritis, and degenerative disc disease. Still, it is unclear whether the same pathways may be involved in recurrent low back pain. For this reason, this thesis formulates a mathematical model of this response, supported by three experimental studies that aim to describe the degradation and mechanical disruption properties of collagenous tissues.

Some experiments have suggested that the rate of collagen disruption in collagenous tissues may be related to the strain rates they experience. However, there has yet to be an experiment to quantify this effect. Thus, the first experimental study in this thesis aimed to quantify whether the rate of damage accumulation is directly proportional to the strain rate. Fifty rat-tail tendon specimens were strained to failure, on one axis of a biaxial biological tissue testing apparatus (Cellscale, Waterloo, Ontario), at one of five strain rates: 0.01, 0.05, 0.10, 0.15 or 0.20 s^{-1}. Force and displacement, later normalized to nominal stress and strain, were least-squares fit to a computational model of collagen fibril recruitment employing a Tobolsky-Eyring rate law to describe the rate of bond-breaking among the fibrils. Overall, the direct proportion constant increased linearly with the magnitude of the applied strain rate, yet the exponential parameter did not. Ultimately, this result suggested that the rate of collagen disruption in collagenous tissues may indeed be linearly related to the magnitude of strain rate.

In response to potential damage to the extracellular matrix, the resident fibroblasts of soft tissues secrete inflammatory cytokines and matrix-degrading enzymes. Previous studies have suggested that mechanical strain to collagen may inhibit these enzymes, suggesting a potential remodelling mechanism that spares frequently used fibrils. Further, the stress-strain curve of biological tissues exhibits a prominent toe-region as a higher proportion of collagen fibrils become engaged. However, this mechanism implies that the activity of collagenases would be proportionately inhibited throughout the toe region. Thus, this study explored whether this graded inhibition of collagenases would occur for tissues held at loads corresponding to specific proportions of collagen fibrils being uncrimped. Ninety-two

rat tail tendon samples were mounted along one axis of a biaxial biological tissue testing apparatus (Cellscale, Waterloo, Ontario), immersed in a Ringer's solution bath heated to 37°C with or without the presence of collagenase from *C. histolyticum*. Their force-elongation curves were measured, and its derivative evaluated to determine instantaneous stiffness-elongation. Tendons were held at levels of force corresponding to 0, 25, 50, 75 and 100% of the linear region's stiffness, corresponding to approximately that proportion of collagen being uncrimped, for two-hours. Following this exposure, tendons were strained to failure at 0.2 s^{-1}, and the change in linear region modulus was evaluated. Linear regressions between applied strain and the change in tissue stiffness suggested that mechanical strain proportionately inhibited the activity of collagenases inside the toe region. These results supported the proposed fibril selection hypothesis and were consistent with the fibril recruitment model.

Several experimental studies have documented inflammatory responses downstream of repetitive lifting and cyclic loading in rat-tail intervertebral discs. These inflammatory responses precede the synthesis of matrix-degrading enzymes, which may contribute to a substantive feedforward inflammatory loop. However, none of these experiments have aimed to detect an inflammatory response downstream of a static flexion-induced creep on the intervertebral disc. Therefore, the purpose of this experiment was to document an inflammatory response in the rat-tail intervertebral disc downstream of a statically applied moment. Sixty rats were assigned to one of four time points (0, 8, 24, and 72 hours), two loading conditions (15 or 75 Nmm), or control for nine total groups. A robotic arm (Yaskawa Inc., Japan) applied a static moment to the caudal motion segment between vertebrae 8 and 9 of the experimental groups, at the specified loading magnitude, for one hour. Before and immediately after this creep protocol, the robotic arm determined the passive moment-angle curve of the motion segment. After waiting the prescribed time for each timepoint group, their passive moment-angle curves were measured again, the animals sacrificed, and the annulus fibrosis harvested between Ca8-9. Western Blot analyses were conducted to measure IL-1β, MMP-1, MMP-8, and TIMP-1. Overall, despite a substantial initial lengthening of the neutral zone (12.0 to 25.9°), the creep exposure had no long-term mechanical consequences. This response was similarly reflected in the physiological outcome measures, where there was no sign of an inflammatory or remodelling response downstream of the applied mechanical creep. Ultimately, these results suggested that cyclic loading, compression, or a higher magnitude exposure may be required to induce an inflammatory response downstream of mechanical loading.

The final contribution of this thesis was the development of a mathematical model of collagen engagement, damage, synthesis, and enzymatic degradation. This model was divided into a mechanical model, which dealt with the sequential fibril engagement in the

toe region and failure according to the earlier Tobolsky-Eyring rate law. The physiological model focused on modelling the response of the fibroblast to damage-sensing. The mechanical model reproduced many salient features of viscoelastic materials, like creep, stress-relaxation, hysteresis and rate-dependence. Further, with the Tobolsky-Eyring rate law, the model could reproduce many features of fatigue, like the S-N curve or the results of creep-rupture experiments. The physiological model predicted a tri-phasic response, with an initial pro-inflammatory wave, followed by an anti-inflammatory wave and a remodelling phase, which was consistent with the description of the acute inflammatory response but could not be calibrated to experimental data. This combined model predicted an inflammatory response downstream of a mechanical exposure in a threshold-constant relationship.

This thesis explored collagen homeostasis as a potential contributor to chronic low back pain pathomechanics. It successfully measured the strain-rate proportionality of collagen rupture and the strain inhibition of collagenases, both of which are related to the rates of degradation and mechanical disruption of extant fibrils. It also showed that mechanical creep in isolation might not be a sufficient inflammatory stimulus in the annulus fibrosis of the intervertebral disc. A pain-generating pathway stemming from a one-time creep exposure may not elicit a painful inflammatory response. The mathematical model developed based on this work predicted a threshold-constant adaptive response to mechanical loading, and the exposure to living rats may have been below this threshold. However, more experimental work is required to establish this effect rigorously. Ultimately, this thesis further elucidated the potential interplay between mechanical exposures and physiological responses.

Acknowledgements

There is no shortage of people who made this thesis possible. I am eternally grateful for the mentorship and supervision of Dr. Jack Callaghan, who, in addition to being an exemplar academic, has always encouraged and challenged me to rise to new heights. In some cases, literally: I would never have learned to ski without his emboldening, nor would I have flown to the numerous distant conferences during this degree. Jack, it truly has been a blast working for you all these years!

I would also like to thank the members of my committee: Drs Joe Quadrilatero, Clark Dickerson, and Duane Cronin. I understand this is a long document that stretches across many different fields, and I appreciate your insights, thoroughness, and discussion.

The lockdowns and pandemic have really highlighted for me what truly makes graduate school rewarding: the people with whom you share lab space and solidarity. These fellow students, past and present, include David C. Kingston (honourary), Jonathan Park, Donna Fok, Betty Nenadov, Michał Glinka, Jessa Buchman-Pearle, Graham Mayberry, Mamiko Noguchi, Brendan Pinto, and Lia Tennant. A special acknowledgement for Jackie Zehr, for the invaluable help and long hours with the robotic arm. I would also like to single-out Daniel Viggiani, whose comradery (*e.g.* Body Improvement Club, Project Crustulum, Trivia Hosting), dungeon-mastering, and musical insights (*e.g.* Champloo II) will be sorely missed. I would also like to acknowledge the PhD thesis of Daniel Viggiani for acknowledging that Jonathan Park's master's thesis acknowledges the master's thesis of Daniel Martel for acknowledging that my master's thesis acknowledgments acknowledge Dan Viggiani's master's thesis acknowledgements section.

It would be remiss of me to forget to thank the other Kinesiology students who, while not being members of my lab, also shaped my unique graduate school experience. These include Taylor Winberg, Daniel Martel, Annemarie Laudanski, Natasha Ivanochko, Daniel Armstrong, Egor Avrutin, and Steven Pretty. Without your friendship and support, the grad school slog would have been a dull affair.

I am incredibly thankful to the people who taught me the important skills for completing this thesis: Jeff Rice for teaching me how to solder, and for his assistance in designing and building many of the apparatuses used throughout this thesis. Fasih Rahman for teaching me how to Western Blot, and getting all my esoteric Ronnie Coleman and SpongeBob SquarePants references. Finally, Jean Flanagan for teaching me basic animal handling and ethics in research.

Outside of Kinesiology, I would especially like to thank my friends and Arkham Horror squad: Sasha Graham, Sascha Lecours, and Pierson Browne. I have yet to spend more than an hour with each of you without learning something new about game design, personal finance, World War II, statistics, and computer programming. To this day, I do not understand how none of y'all are billionaires.

I would like to formally acknowledge the funding sources over these many years: the Natural Sciences and Engineering Council of Canada (NSERC), the Ontario government for their support, and the Ross and Doris Dixon Charitable Foundation for the Doctoral Thesis Completion Award. Finally, I would like to thank Dr. Russ Tupling for the opportunity to instruct KIN 713, an honour rarely bestowed upon graduate students, and a favour not lost on me.

Of course, I would like to thank my parents, Rosemary and Michael Barrett. I am forever grateful for your love, support, and patience as I pursued my interests. My siblings, Nicholas, Rebecca, Jacob, Darin, and Lorabeth: coming home to your warm embraces and catch-ups helped make living away from home tolerable. I would also like to thank Rebecca's guinea pigs for their morale support.

This acknowledgements section would never be complete without mentioning the dogs, the miniature schnauzers, Odin and Misty, whose high spirits always put me in a good mood. And, naturally, Willow, for being a big, supportive floof and (unlicensed) emotional support dog.

Finally, with candour, this thesis would never have been possible without the support of my partner, Kayla Fewster. I could not have made it through the lockdowns without you and Willow as a source of entertainment, let alone the dark days analyzing and writing up a doctoral thesis. I wouldn't trade anything for our long days in the lab, terrifying cross-country moves in the bitter cold, or miserable alpine hikes in the summer heat; they're as important as the delicious triumphant food, warm relaxing movie-watching, and breathtaking worldly vistas. Nothing makes me happier than when we smile at each-other and know that we got through it together. You're simply the best, I adore you, and I cannot wait for our next adventure!

Dedication

In loving memory of Misty.

Table of Contents

List of Tables

List of Figures

List of Acronyms

AF Annulus Fibrosus 9–12, 15, 16, 28, 30, 40, 42, 90, 91, 98, 99, 111, 112

BCA Bicinchoninic acid 43, 100, 111

DAMP Damage Associated Molecular Pattern 93, 143–146, 149–152, 155–165, 170, 172, 176, 178, 181–183

ECM Extracellular Matrix 6, 7, 10, 12, 15, 28, 30–33, 36–40, 70, 89, 113, 115, 142, 144, 148, 158, 161, 166, 176

EP Endplate 9, 11, 12

FSU Functional Spinal Unit 9, 18, 158, 180

HMC Hamiltonian Monte Carlo 63, 80, 102

IL-1 Interleukin-1 33, 34, 36–40, 90–94, 100, 101, 110, 111, 144, 145, 147, 148, 155, 157, 158, 165, 166, 182

IVD Intervertebral Disc 3, 7, 9, 11, 12, 18, 19, 28, 36, 39, 41, 42, 89–91, 94, 99, 101, 109–111, 143, 157, 158, 187

LBP Low Back Pain 1, 3, 184, 187

MAPK Mitogen Activated Protein Kinase 33–37, 52, 92, 144

MMP Matrix Metalloproteinase 27, 30–34, 36–40, 44, 45, 47, 70, 85–87, 89–91, 93–95, 100, 101, 110, 117, 142, 148–152, 155–159, 161, 162, 164, 165, 169, 181–183, 187

NP Nucleus Pulposus 9–12, 18, 28, 30, 39–41, 99

ODE Ordinary Differential Equation 36, 47, 51, 52, 59, 94, 119, 121, 122

PDE Partial Differential Equation 24, 116, 118–122, 129, 140

TGF-β Transforming Growth Factor-β 145–147, 155, 157, 164–166

TIMP Tissue Inhibitors of Metalloproteinases 32, 44, 90, 91, 93, 95, 101, 108, 109, 148, 151, 152, 155, 157, 162

TNF-α Tumor Necrosis Factor-α 32, 36, 37, 39, 40, 90, 92, 110, 144, 155, 157, 158

List of Symbols

$\hat{A}$ Normalized concentration of the anti-inflammatory stimulus. 142, 147, 156, 165

$\hat{C}$ Normalized concentration of collagen. 142, 148, 168, 170

$\hat{D}$ Normalized concentration of damage associated molecular patterns (*e.g.* decorin). 141, 142, 144, 145, 149, 157, 169

$\hat{I}$ Normalized concentration of collagenase inhibitors. 142, 148, 169

K_i Inhibition constant. 48

K_m Michaelis constant. 47, 72, 117

$\hat{P}$ Normalized concentration of the pro-inflammatory stimulus. 142, 144, 147, 156, 158, 161, 165

Q_λ The λ^{th} raw moment of the collagen strain distribution, where $\lambda = 0, 1, 2, \ldots$. 119

$\hat{S}$ Normalized concentration of pro-collagen. 142, 156, 169

$V_{\mathbf{max}}$ Maximum rate of reaction catalyzed by an enzyme. 47, 72

$\hat{Y}$ Normalized concentration of collagenases. 142, 148, 169

α Breaking function collision parameter. 56, 117

β Breaking function shape parameter. 56, 117

$\kappa(x)$ Active-site counting function. 72, 117, 149, 169

$\dot{D}$ Rate of damage accumulation to collagen fibrils. 24

$\dot{C}$ Rate of degradation of collagen by matrix-degrading enzymes. 24

η Standard deviation of the initial slack strain in a population of collagen fibrils. 25

k_B The Boltzmann Constant, approximately 1.380×10^{-23} J·K^{-1}. 55

$k_{\mathbf{cat}}$ Enzyme catabolic constant. 47, 117

μ Average initial slack strain in a population of collagen fibrils. 25

$\rho(x,t)$ Distribution of strain among a population of collagen fibrils. 22–24, 71, 72, 116, 118–121, 129, 168, 173, 179

v Strain rate. 23, 55, 61, 116, 117, 173

$\dot{S}$ Rate of synthesis of new collagen fibrils. 24

Chapter 1

General Introduction

1.1 Scope of the Problem

Approximately 80% of the population experiences Low Back Pain (LBP) at some point in their lives (Walker, 2000). Of these cases, 65% become chronic and never experience a remission from their symptoms (Cassidy, Carroll, & Côté, 1998). Much to this point, the best predictor of low back pain is previous low back pain (Taylor, Goode, George, & Cook, 2014). Troubling still, more than half (60%) of lower back pain cases do not show radiographic evidence of damage and are subsequently diagnosed with so-called 'idiopathic low back pain' (Iizuka et al., 2017).

Some epidemiological studies have associated chronic LBP with specific occupations, many of which are considered sedentary (Riihimäki, Tola, Videman, & Hänninen, 1989; Burdorf, Naaktgeboren, et al., 1993; Seifert, Messing, & Dumais, 1997). These results do not fit the classical theory of injury because the load magnitudes do not seem substantial enough to degrade the tissue's tolerance, much less exceed it. However, these paradoxical findings seem to suggest that there may be a mechanism for pain or tissue disruption that the classical theory has overlooked. Therefore, the purpose of this thesis is to modify this theory to account for some of the potentially physiological underpinnings of soft tissue pain, injury and dysfunction.

1.2 Thesis Overview

The rate of change of collagen in the extracellular matrix is composed of three terms: (1) the rate of collagen fibril degradation through mechanical means, (2) the rate of fibril catabolism, and (3) the rate of collagen fibril synthesis. This thesis is divided into four studies; the first three tackle one of these rate factors, and the last one attempts to synthesize their results into a holistic model (Figure 1.1). The first study considers the rate of mechanical damage to collagen fibres as a function of tissue strain rate. The second study focuses on type I collagen fibre turnover by matrix metalloproteinases in an *in vitro* environment. The third experimental study aims to study the rate of type I collagen fibre synthesis and degradation in a rat model following a creep protocol. The fourth study aims to synthesize the results of these three arms in an *in silico* differential equation model of collagenous tissue. The aim is that the holistic model, incorporating mechanical damage in conjunction with fibroblast physiology, will provide a more biofidelic way of modelling the tissue's response to seemingly innocuous exposures and provide insight into potential pathways for injury or pain generation.

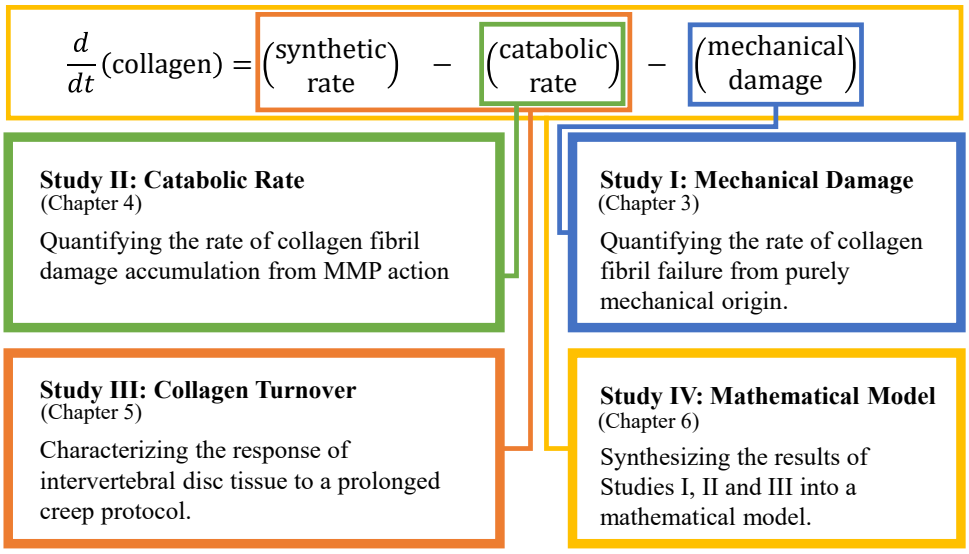

Figure 1.1: The connections, and specific objectives of the four studies contained in this proposal. Each study aims to tackle a specific term in this equation: from mechanical damage (**Study I**), to biochemical breakdown (**Study II**), to measuring term contributions *in vivo* (**Study III**), and, finally, synthesizing the results into a holistic model (**Study IV**).

1.3 Global Thesis Objective

The primary goals of this thesis are twofold. The first is to derive a holistic mathematical model for collagen homeostasis in the extracellular matrix of soft tissue, which incorporates the mechanical damage to collagen fibrils and the physiology of fibril synthesis and catabolism. The aim is that this mathematical model will provide the means to simulate and explain chronic injuries arising from seemingly innocuous exposures. Accomplishing this task means quantifying three terms in the proposed holistic soft tissue model: synthesis, catabolism, and mechanical damage, evaluated in the experimental studies of this thesis.

The second primary goal of this thesis is to test the Mountain of a Mole Hill Hypothesis: the hypothesis that a minor injury to the collagen fibrils leads to an exaggerated response from the immune system and resident fibroblasts of the Intervertebral Disc (IVD). In response to injury, fibroblasts discharge inflammatory cytokines. In many other soft tissues—like tendons, cartilage, and nucleus pulposus—inflammatory cytokines have an autocrine effect, increasing the synthesis of matrix-degrading enzymes. This mechanism could provide tissues with the means for a feed-forward inflammatory loop, wherein slight damage, coupled with periods of under-use, can predispose tissue to recurrent disruption. If such a mechanism exists, it may form the basis for LBP reporting associated with sedentary tasks.

1.4 Specific Thesis Objectives

In addressing the two major thesis objectives, several specific objectives will be explored.

1. To develop a quantitative model for the rate of collagen fibril failure, as a function of both strain and strain rate (**Study I**). This relates to the first global objective, as one of the terms of the collagen homeostasis equation is mechanical damage.

2. To develop a mathematical model for the rate of collagen fibre destruction by matrix degrading enzymes and to explore how strain interacts with the rate of catabolism

of fibrils (**Study II**). This, once again, relates to the first global thesis objective, as molecular catabolism is yet another term in the equation.

3. To explore the role of inflammation in the synthesis of new collagen and matrix degrading enzymes following a mechanical creep exposure (**Study III**). Inflammation is intimately tied to genetic expression of both collagen and matrix-degrading enzymes, which feed in to the holistic model in both the synthesis and catabolic terms.

4. To synthesize mechanical and physiologic responses to injury and creep in a holistic mathematical model (**Study IV**).

1.5 Significance

Despite the preponderance of evidence correlating sedentary exposures and lower back pain, there remains a scarcity of mechanistic experimental work that can link chronic low-magnitude exposure to a pain-causing mechanism (Walker, 2000; Seifert et al., 1997; Riihimäki et al., 1989; Burdorf et al., 1993; Nelson-Wong, Flynn, & Callaghan, 2009). Over the last several decades in biomechanical research, there have been considerable advances in understanding the phenomena that may contribute to low back pain. Similarly, the last few decades have seen significant strides in the understanding of cellular mechanisms which may lead to painful tissue degeneration (Freemont, 2008; Risbud & Shapiro, 2014). The overall goal of this thesis is to bridge the gap between mechanical and physiological literature using a combination of *in vivo*, *in vitro*, and *in silico* techniques.

The design goal of the *in vivo* work aims to demonstrate that painful, degenerative changes may occur downstream from a prolonged innocuous mechanical exposure. Most cellular and genetic studies attempting to explain non-specific low back pain are often divorced from mechanical exposure. The *in vivo* study in this thesis aimed to alleviate some of this disparity.

Conversely, insights gleaned from the *in vitro* arm of this thesis are focused on producing evidence that slight mechanical exposures have the potential to induce a feed-forward

inflammatory response. These studies may highlight the role of both mechanical and biochemical events, which may culminate in low back pain.

Finally, the *in silico* arm of this research proposal aims to mathematically model, through a systems biology approach, both the biochemical and biomechanical attributes of the fibroblast and its extracellular matrix. This model's sensitivity analyses may provide insights into the pathways that would provide the biggest benefit by being targeted by drugs, therapies, or prevention efforts.

Chapter 2

Review of Literature

2.1 Overview

Injuries are typically dichotomized as acute or chronic, but both follow from the same theoretic framework used throughout this thesis (Figure 2.1). The foundational premise is that an injury occurs when the applied load exceeds a tissue's tolerance (Kumar, 2001; Gabbett, 2016; McGill, 1997). The applied load is exclusively a matter of mechanics; however, the tissue's tolerance is a function of both physics and physiology (Ker, Wang, & Pike, 2000). With too little mechanical stimuli, tissues can atrophy, and their tolerance becomes compromised. Similarly, with too much mechanical loading, the rate of mechanical damage exceeds the tissue's capacity to synthesize repairs. However, with adequate rest periods, the tissue can recover following a mechanical exposure, and—in some cases—even increase its tolerance, making it less prone to future injury. Therefore, in light of this theory, an acute injury arises from a single event that exceeds the tissue tolerance, whereas a chronic injury results from the gradual loss of tissue tolerance from multiple non-injurious loading events. This thesis aims to capture this behaviour in a mathematical model. A weak assumption is that the tissue's tolerance is related to the total amount of constituents in the Extracellular Matrix (ECM) of the tissue.

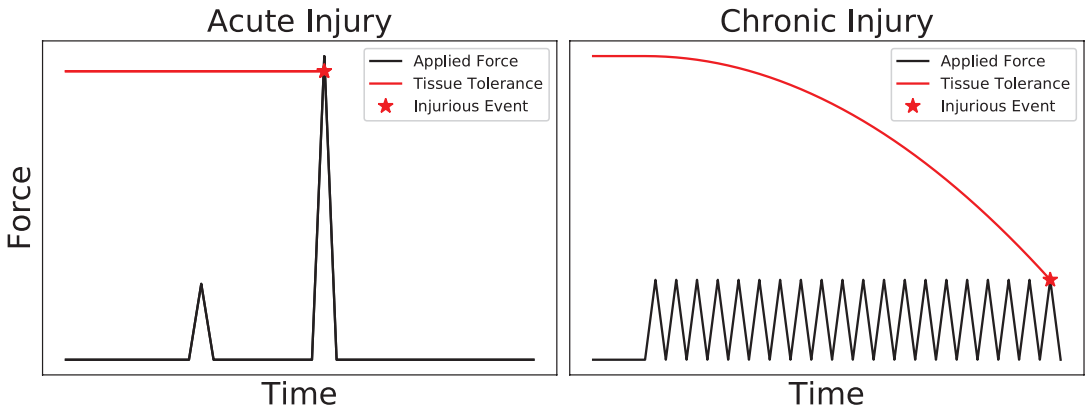

Figure 2.1: Conceptual model of acute and chronic injuries. (Left) An acute injury, which arises from a single loading event which exceeds the tissue's tolerance. (Right) A chronic injury scenario where the applied load does not change, but the tissue's tolerance eventually reduces to the point where a previously non-injurious level of force induces and injury. Image adapted from McGill (1997).

The bulk of this thesis concerns itself with exploring how soft tissues—the Intervertebral Disc (IVD), in particular—regulate the homeostasis of their ECM. That is to say how the resident fibroblasts of soft tissues balance the synthesis of new collagen fibrils with the catabolism and damage external loads impart onto older fibrils. This tremendous balancing act places these resident fibroblasts as the centrepiece in maintaining the tissue's tolerance and integrity. Fundamentally, the rate of change of collagen fibrils must be equal to the synthetic rate, less the catabolic rate, less the rate at which damage is accruing to these fibrils (Equation 2.1).

$$\frac{d}{dt}\,(\text{collagen}) = (\text{synthetic rate}) - (\text{catabolic rate}) - (\text{damage rate}) \tag{2.1}$$

As this is a thesis exploring the pathology and mechanics of low back pain, the first part of this literature review focuses on the anatomy and histology of the lumbar spine, with an emphasis on the IVD. Following this each term in Equation 2.1 is explored independently. Starting with how mechanical loads disrupt the collagen fibrils; and progressing into the biochemical homeostasis: how collagen fibrils are synthesized and catabolized by resident fibroblasts. The review finishes by highlighting the role of inflammation in the biochemical homeostasis of the ECM.

2.2 Lumbar Anatomy

The lumbar spine is comprised of five vertebrae, labelled L1 through L5, with intervertebral discs between each, labelled by the joints they span (*e.g.* L4-L5 is the disc spanning the L4 and L5 vertebrae). The vertebrae are all of similar morphology, affording the traversal of the spinal cord through the lumbar spine into the lower extremities and abdominal cavity (White & Panjabi, 1990; Standring, 2008). Despite the critical role of protecting the spinal cord and transmitting load from the torso to the lower extremities, the lumbar spine possesses considerable flexibility: capable of 50 to 60 degrees of flexion, 20 degrees of extension, 25 to 30 degrees of lateral bending and 15 to 32 degrees of axial twist (Ng, Kippers, Richardson, & Parnianpour, 2001; Van Herp, Rowe, Salter, & Paul, 2000). The lumbar spine is equipped with a vast set of ligaments and joints which interact harmoniously to limit these ranges of motion (Figure 2.2).

2.2.1 The Vertebrae & Ligaments

Each vertebra has a cylindrical vertebral body composed of trabecular bone with a thin layer of cortical bone at its periphery. Emerging on either side of the posterior-lateral aspects of the vertebral body are the pedicles, which fuse, once again, at the midline to form the neural arch. The spinous process extends from the midline of the neural arch posteriorly; whereas the transverse processes jet out on the lateral aspects of the pedicles (White & Panjabi, 1990; Standring, 2008). On both the superior and inferior surfaces of the pedicles are the facet articular surfaces, which, in the lumbar spine, articulate in an upright fashion. A vertebra's pedicles, articular pillars, transverse and spinous processes together form that vertebra's posterior element.

Two vertebrae with their IVD form the Functional Spinal Unit (FSU)—the fundamental articular unit in the spine (White & Panjabi, 1990). The superior facet surface of the inferior vertebra articulates with the inferior facet surface of the superior vertebra, forming the zygapophyseal (or facet) joint (Standring, 2008). The role of the facet joint is to restrict the translational degree of freedom of the superior vertebra over the inferior one. Similarly,

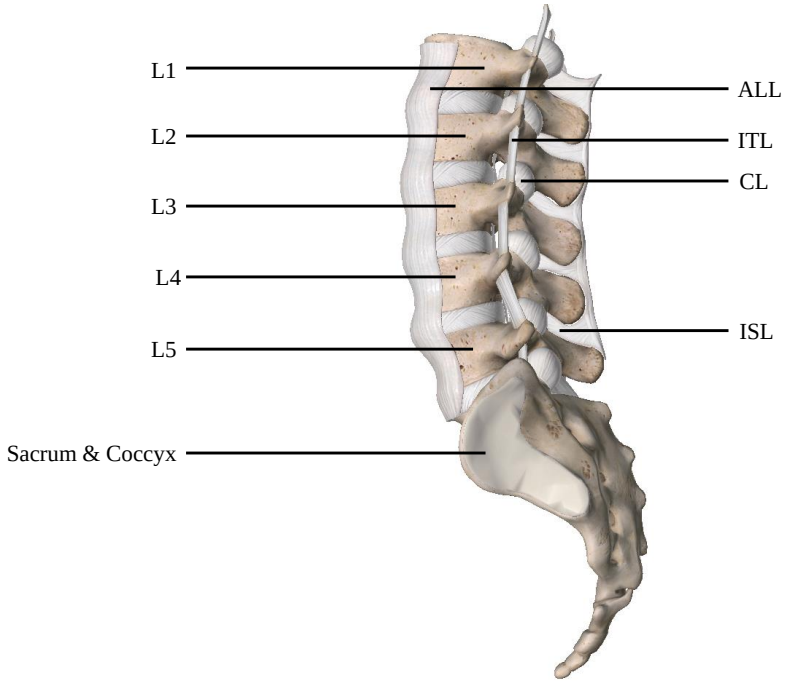

Figure 2.2: Basic lumbar spine anatomy. The vertebrae are numbered L1 through L5; between each is the Intervertebral Disc. Inferior to the lumbar spine is the sacrum and coccyx. Ligamentous members labelled on the diagram are the anterior longitudinal ligament (ALL), the interspinous ligament (ISL), the inter-transverse ligament (ITL) and the facet capsular ligament (CL).

distracting the facets is limited by the facet capsular ligament, which becomes engaged during posterior shearing and flexion of the FSU (Prasad, King, & Ewing, 1974).

The Anterior Longitudinal Ligament spans the anterior portion of the FSU along the entire length of the spine. On the posterior aspect of the vertebral bodies, in a similar fashion to the ALL, resides the posterior longitudinal ligament (PLL), which also traverses the entire length of the spine. The spinous ligament spans the space between the spinous processes of adjacent vertebrae; and the intertransverse ligament does the same between transverse processes. Finally, the ligamentum flavum, a ligament best known for its high elastin content (Evans & Nachemson, 1968; Buckwalter, Cooper, & Maynard, 1976), spans the remaining portions of the neural arch.

2.2.2 The Intervertebral Disc

The Intervertebral Disc (IVD) is composed of three anatomically distinct regions: the Nucleus Pulposus (NP), Annulus Fibrosus (AF), and the Endplate (EP) (Humzah & Soames, 1988; White & Panjabi, 1990; Urban & Roberts, 2003). The NP, as its name suggests, resides in the centre of the disc (Figure 2.3). It is a jelly-like substance, comprised of a rich network of type II collagen, which is integrated with a population of the glycosaminoglycans (GAGs) and the proteoglycan aggrican (Smith, Nerurkar, Choi, Harfe, & Elliott, 2011). The negative charge from these constituents makes the NP strongly hydrophilic, with water making up 90% of its wet weight at birth, steadily decreasing to 70% by age 60 (Oda, Tanaka, & Tsuzuki, 1988; Sivan et al., 2014; Antoniou et al., 1996). The resident cells of the NP are of notochord origin and are often described as chondrocyte-like cells (Sive et al., 2002). They gradually decrease in size and number as their host ages. These cells synthesize matrix constituents like the type II collagen that is most abundant in the NP, but also types IV, IX, and XI (Bruehlmann, B. Rattner, R. Matyas, & A. Duncan, 2002; Hayes, Benjamin, & Ralphs, 2001; Kandel et al., 2007).

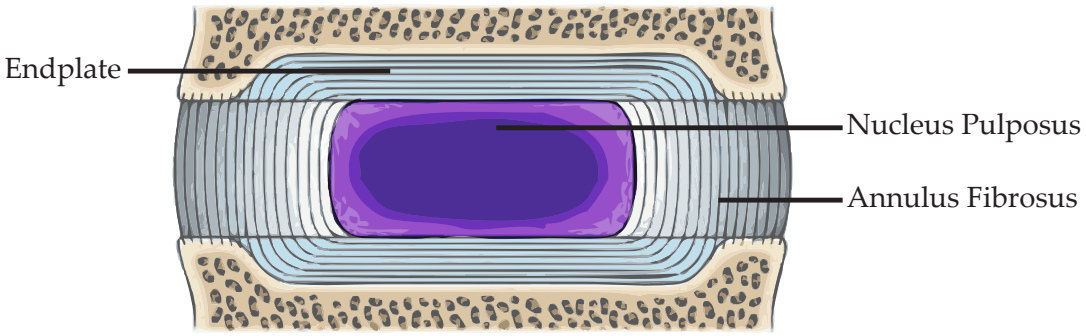

Figure 2.3: Longitudinal section of the intervertebral disc anatomy, clearly delineating the three anatomically distinct regions. The Nucleus Pulposus (NP) resides at the disc's centre, radially encased by the Annulus Fibrosus (AF). This composite structure is then sandwiched between two cartilagenous endplates (EP). Adapted from Standring (2008).

The NP is wrapped circumferentially by the AF, which possesses a highly organized

concentric layered structure. Between two adjacent layers, collagen fibrils oriented between 45° and 60° form the preceding layer (Figure 2.4) (Cassidy, Hiltner, & Baer, 1989; Marchand & Ahmed, 1990; Mengoni et al., 2015; Tampier, Drake, Callaghan, & McGill, 2007). The ECM of the AF is primarily water, which constitutes 70% of its wet weight (Urban & Roberts, 2003). Of its dry weight, the outer AF is predominantly type I collagen, which transitions to a more type II collagen dominated phenotype in the inner AF (Sivan et al., 2014); in either case supplemented by a small amount of elastin (Hayes et al., 2001; Yu, Fairbank, Roberts, & Urban, 2005). Despite the increased type II collagen in the innermost layers of the AF, it is not continuous with the NP; and a well-pronounced boundary between the two structures is a hallmark of a healthy disc. Indeed, as the NP degenerates, the boundary between the NP and AF becomes indistinguishable (Smith et al., 2011). Unlike the NP, the resident fibroblasts of the AF are not of notochord origin, but from the sclerotome (Smith et al., 2011). Additionally, the outermost layers of the AF house a population of fusiform fibroblasts, each stretched in the direction of the collagen fibres they are contained in. Conversely, the inner layers of the AF are more rounded in shape.

The final constituent of the IVD is the endplate, which sandwiches the NP and AF on their superior and inferior boundary. The EP is composed of hyalin cartilage, housing a population of chondrocytes which manage the synthesis and turnover of its type II collagen network. Like the AF and NP, the endplate is primarily water, collagen, and proteoglycans (Roberts, Menage, & Urban, 1989). Some collagen or elastin fibres, known as Sharpey's Fibres, originate in the end plate and terminate in the AF, and facilitate the mechanical linkage between the two structures (Johnson, Chetty, Moore, Stewart, & Jones, 1982).

The IVD is almost entirely avascular, relying on diffusion of nutrients and oxygen from distal capillary beds in the vertebral bodies to the NP and AF (Holm, Maroudas, Urban, Selstam, & Nachemson, 1981). As such, the cells throughout the disc are adapted to survive in an environment that is oxygen and nutrient-poor. Additionally, only the outer third of the AF and EP have efferent nerve supplies, which is thought to preclude the NP and inner AF from being a significant source of nociception (Bogduk, 1983).

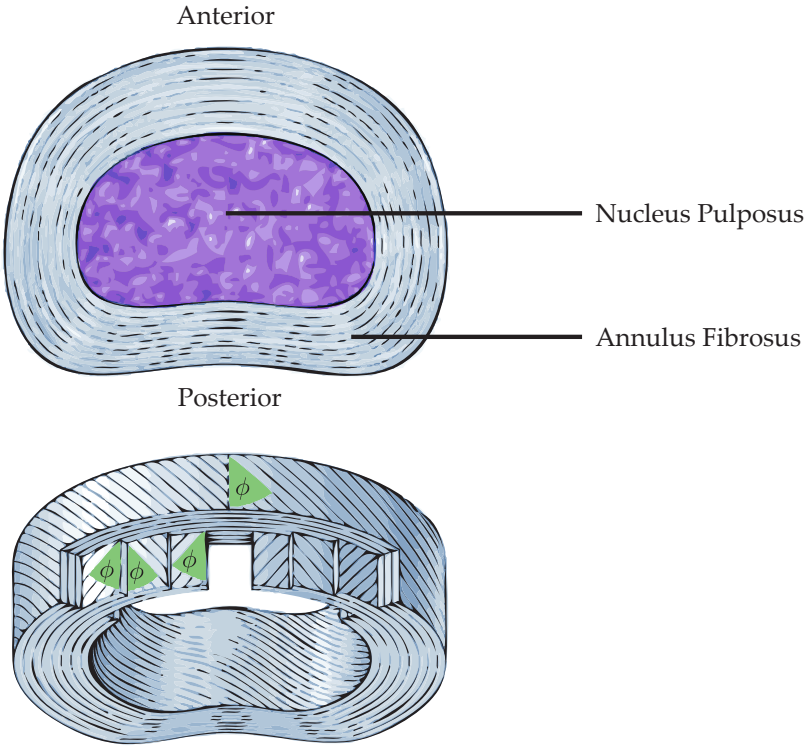

Figure 2.4: Transverse section of the Intervertebral disc. The delineation of NP and AF can be seen in the top image; and the angle between adjacent layers of AF being between 45 and 60 degrees portrayed in the bottom image. Adapted from Standring (2008).

2.3 Soft Tissue Mechanics

This section provides an overview of soft tissue mechanics, beginning with definitions of stress and strain and developping into more advanced topics like viscoelasticity, damage, fatigue and failure. These topics are highly developed, and continue to undergo rapid advancements as technology is better able to enable more advanced experimentation. Therefore, the content on these topics contained here is primarily topical in nature; although it may help motivate the modelling decisions made in later chapters.

Tissue mechanics, as a discipline, is concerned with the deep connection between the magnitude of force or stress acting on a tissue and that tissue's deformation or strain (Kenedi, Gibson, Evans, & Barbenel, 1975; Epstein, 2012). A tissue, throughout this document,

refers to biological tissues: the host cells and their surrounding ECM. Biological tissues exhibit a characteristic elastic response to strain, but also a dependence on strain rate—a property known as viscoelasticity. As this thesis primarily focuses on the AF and tendons, special attention is given to tissues abundant in type I collagen.

2.3.1 Strain, Stress, and Constitutive Equations

Strain is a tensor quantity, which has many definitions; and different definitions are used under different circumstances (Lautrup, 2005; Epstein, 2012). For instance, Engineering Strain is well suited for solving one-dimensional problems where displacements are small (Table 2.1); but in three dimensions Lagrangian (or Eulerian) strain definitions are preferred (Epstein, 2012; Lautrup, 2005). In this document, strain refers to Engineering strain (defined in Equation 2.2) unless otherwise specified.

$$\varepsilon = \frac{\ell - \ell_0}{\ell_0} \tag{2.2}$$

Where ℓ is the current length of the tissue and ℓ_0 is its initial length, or gauge length. There are some weaknesses to this definition, for instance, it is difficult to generalize to three-dimensions. For the purposes of this thesis, which is predominantly an exploration of uni-axial strain, it is considered sufficient. Additionally, it is most commonly used throughout the literature, making results from this thesis more readily comparable to previous studies. Finally, it is still possible to generalize the Engineering strain to large-deformations in three-dimensions by way of the Biot strain tensor (Ogden, 1997), but that discussion is beyond the scope of this thesis.

Like strain, stress is also a tensor quantity; unlike strain, it does not directly quantify deformation (Lautrup, 2005; Epstein, 2012). Instead, stress is a measure of force through a material. Analogous to strain, there are many different definitions of stress, each with its own strengths and weaknesses. For the purposes of this thesis, only nominal stress—force

Table 2.1: Summary of strain definitions (in 1D), here ℓ_0 is the length in the undeformed state, or gauge length, and ℓ is the length in the deformed state (Summarized from (Epstein, 2012)).

Name	**Definition**
Engineering (Cauchy) Strain	$\frac{\ell-\ell_0}{\ell_0}$
True Strain	$\frac{\ell-\ell_0}{\ell}$ or $\frac{d\ell}{\ell}$
Green-Lagrange Strain	$\frac{\ell^2-\ell_0^2}{2\ell_0^2}$
Euler-Almansi Strain	$\frac{\ell^2-\ell_0^2}{2\ell^2}$
Stretch Ratio	$\frac{\ell}{\ell_0}$
Logarithmic Strain	$\ln\left(\frac{\ell}{\ell_0}\right)$

normalized by undeformed cross-sectional area—is considered.

$$\sigma = \frac{F}{S} \tag{2.3}$$

Where F is the force acting through the material and S is its cross-sectional area. σ represents the nominal (or first Piola-Kirchoff) stress, although the symbol σ more commonly refers to the Cauchy stress. While definitions of stress and strain are immensely useful in their own right, constitutive expressions enhance their utility by relating the amount of strain in a material to its stress. This is necessary because it closes the conservation equations from continuum mechanics.

In the limit of small-displacement analysis, all measures of strain converge on infinitesimal strain and all measures of stress reduce to the true stress. More importantly, the stress becomes a linear function of strain, which reads $\sigma = E\varepsilon$. In three-dimensions, for infinitesimal deformations of a linear anisotropic material, since stress and strain are second-order tensors, this reads:

$$\sigma_{ij} = C_{ijk\ell}\varepsilon_{k\ell} \tag{2.4}$$

Where $C_{ijk\ell}$ are the components of the fourth-order stiffness tensor, $\mathbb{C}$, and the summation

of repeated indices k and ℓ is omitted following Einstein's summation convention (Lautrup, 2005). Because both the stress (σ) and strain (ε) tensors are symmetric, the tensor $C_{ijk\ell}$ has 21 independent components for the case of a linear anisotropic material. Equation 2.4 is deceptively simple: the large quantity of parameters contained within it make the acquisition of C difficult to do experimentally.

As this thesis deals primarily with uni-axial stresses and strains, the other components of the strain tensor will not be explored, although the strain in other axes and planes are important for other applications. In the simplest case of Hooke's Law for a linear anisotropic material, the three dimensional constitutive equation is:

$$\sigma_{ij} = \left(\frac{E\nu}{(1+\nu)(1-2\nu)}\right)\varepsilon_{kk}\delta_{ij} + \left(\frac{E}{1+\nu}\right)\varepsilon_{ij} \tag{2.5}$$

Where E is the Young's modulus and ν is the Poisson's Ratio. The Poisson's ratio quantifies how much a material will change in length along a direction perpendicular to the principle direction of stretch. Most objects tend to thin as they are lengthened—a positive Poisson's Ratio—although some materials can exhibit a negative Poisson's Ratio. Even in the simplest case, the presence of Poisson's Ratio serves to emphasize that all of the elements of the strain tensor are inextricably linked to one-another.

2.3.2 Viscoelasticity

Viscoelasticity is a portmanteau of *viscous*—relating to viscosity of fluids—and *elasticity*—referring to the tenancy of solids to return to their original configuration. Mathematically, these materials portray a dependency on *both* the strain and strain-rate of the material.

Viscoelasticity of Biological Tissues

Most soft tissues—ligaments, tendons, and even annulus tissue—portray a characteristic force-deflection curve, sometimes renormalized to a stress-strain curve (Figure 2.5). There is a prominent non-linear toe-region, attributed to the progressive engagement of the fibres

as they begin to resist the external load, termed *uncrimping* (Chazal et al., 1985; Rigby, Hirai, Spikes, & Eyring, 1959; Fratzl et al., 1998). The stiffness gradually increases and becomes more constant as all the collagen fibres are recruited, giving rise to the linear portion of the curve. As the soft tissue continues to be stretched, there is a gradual failure of individual collagen fibres (Provenzano, Heisey, Hayashi, Lakes, & Vanderby Jr, 2002), eventually culminating in total rupture of the tissue. These three phases of the curve are often called the toe, linear, and trauma (or failure) regions, respectively. These force-deflection curves are ubiquitous across soft tissues, and have been observed in tendon (Lin, Cardenas, & Soslowsky, 2004; David, Grood, Noyes, Zernicke, et al., 1978), ligaments (Chazal et al., 1985; Mattucci, Moulton, Chandrashekar, & Cronin, 2012; Hashemi, Chandrashekar, Mansouri, Slauterbeck, & Hardy, 2008; Viidik, 1973), and AF (Holzapfel, Schulze-Bauer, Feigl, & Regitnig, 2005; Elliott & Setton, 2001; Schollum, Robertson, & Broom, 2010; Gregory, Veldhuis, Horst, Brodland, & Callaghan, 2011; Gregory & Callaghan, 2011).

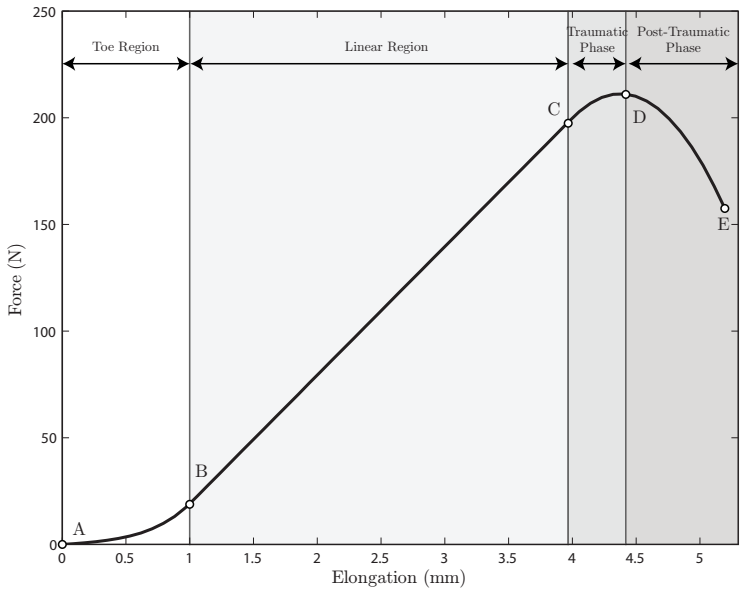

Figure 2.5: A typical force-deflection curve for ligaments, which exhibits the classic toe region, linear region, and traumatic regions. Figure adapted from Przybylski et al. (1996).

Of course, the properties of this curve are also dependent on all of the constituents of the ECM of the tissue in question. Ligaments, for example, which are abundant in

collagen—like the alar ligament in the cervical spine—tend to be stiffer and break at smaller magnitudes of strain relative to those whose ratio of elastin to collagen are higher—like the ligamentum flavum throughout the spine (Yoganandan, Kumaresan, & Pintar, 2000; Yoganandan et al., 1989; Przybylski et al., 1996). As this thesis is primarily concerned with tendons and the outermost layers of the AF, it is primarily concerned with the mechanics of type I collagen.

Classically, as the type I collagen fibrils of a soft tissue are strained beyond their failure threshold, they sequentially begin to fail (Knörzer et al., 1986; Wren, Lindsey, Beaupré, & Carter, 2003). This has been evidence by the accumulation of collagen fibril fragments preceding whole tendon rupture in rat tail tendons (Torp, 1975; Kastelic & Baer, 1980; Knörzer et al., 1986). However, recently, the idea of the gradual failure of collagen fibrils themselves has been brought into question. Veres, Harrison, and Lee (2013) used a scanning electron microscope to demonstrate that fibrils first undergo a plastic deformation. Once this plastic deformation has occurred, the fibrils themselves become more difficult to rupture. Mechanical damage to soft tissues represents a difficult property to quantify. The mathematical model used throughout this thesis attempts to quantify the proportion of 'in-tact' fibres, which progressively fail as the tissue is overloaded—as this is the classical picture of soft tissue failure.

Biological tissues exhibit a number of properties that Hooke's Law alone cannot reproduce. For instance, rate-dependence: the tendency of a material to have a strain-rate dependent Young's Modulus (Kenedi et al., 1975). As the rate of strain increases, so too does the measured Young's Modulus of the material (Figure 2.7). Rate-dependence is one instance of a larger class of viscoelastic properties; namely hysteresis, stress-relaxation, and creep (Fung, 1977, 1967, 1981).

Hysteresis is characterized by disagreement in the stress-strain relationships between loading and unloading a material—the area between these curves being proportional to the amount of energy dissipated (Fung, 1981). On a stress-strain curve, the area between the loading and unloading curves is in the same units as stress, Pascals. If this is multiplied by the volume of the material, one recovers the total energy dissipated, in Joules. Thus, on a stress-strain curve, the area described by hysteresis can be thought of as the energy

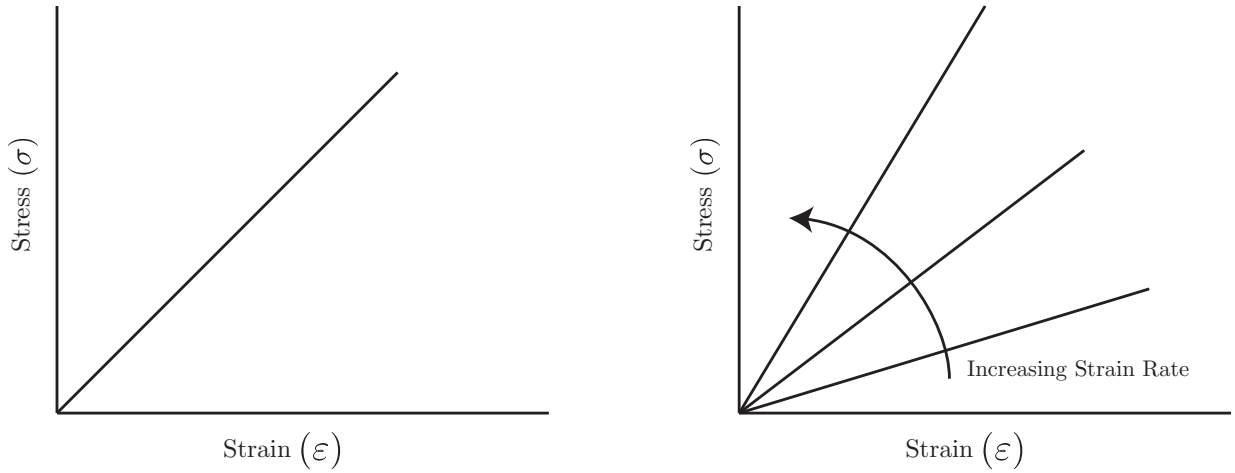

Figure 2.6: Examples of rate-dependence. On the left is the stress-strain curve for a purely elastic, linear material—one which obeys Hooke's Law. On the right, however, is a demonstration of the rate-dependence phenomenon. With increasing strain rate, so too the slope of the stress-strian curve—or Young's Modulus—increases.

dissipated per unit volume of the material—or the strain energy density removed from the system in a single cycle of loading.

Stress-relaxation is the reduction in stress of a tissue for a fixed strain (Figure 2.7). Conversely, continued deformation under constant load is referred to as creep (Figure 2.8) (Fung, 1981). These two tests distinguish solids from fluids. A fluid, under a constant stress, will continue to deform; whereas a solid will eventually reach a stable configuration. In opposite fashion, when stretched to a constant strain, solids will retain some stress, whereas the molecules in a fluid will eventually reach a configuration with zero stress. In the IVD, the layers of the annlulus are described well as viscoelastic solids, whereas the NP is a viscoelastic fluid (Iatridis, Weidenbaum, Setton, & Mow, 1996).

In the spine, viscoelastic effects have been demonstrated on ligaments (Bass et al., 2007; Jiang, Wang, & Peng, 2015; Lucas et al., 2009; Myers, McElhaney, & Doherty, 1991; Troyer & Puttlitz, 2011), IVDs (Guilak et al., 1999; Iatridis, Setton, Weidenbaum, & Mow, 1997; Keller, Spengler, & Hansson, 1987), and bone (Bembey, Oyen, Bushby, & Boyde, 2006), and scale to the level of the FSU (Bowman & Robbins, 1972; Wen, Lavaste, Santin, & Lassau, 1993; Yingling, Callaghan, & McGill, 1997; Barrett, Gooyers, Karakolis, & Callaghan, 2016). To some extent, creep is able to alter the proprioceptive information obtained from

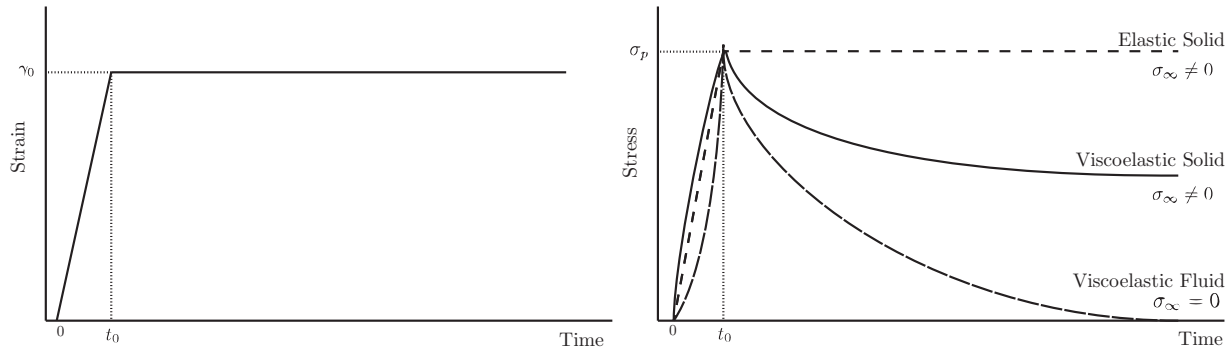

Figure 2.7: Stress-relaxation experiments involving solids and fluids, adapted from Fung (1981). In this case, under a constant strain, the stress will decrease in solids and fluids. Unlike fluids, solids will asymptotically approach a nonzero amount of stress under these conditions.

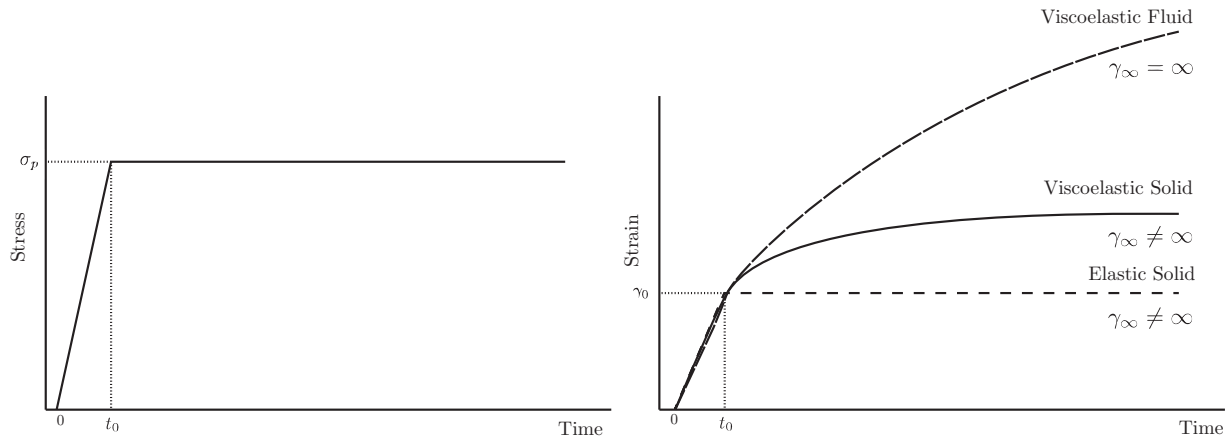

Figure 2.8: Creep experiments involving solids and fluids, adapted from Fung (1981). Here, γ represents the shear strain of a the solid, liquid, or viscoelastic solid. With a constantly held stress—as seen on the left panel—there is a corresponding increase in strain. Left under this constant tension, a viscoelastic fluid will continue to deform; whereas a solid will asymptotically settle into a final, deformed configuration.

ligaments, and may even be an instigator of inflammatory responses (Solomonow, 2004, 2006). In some cases, the inflammation brought on by creep is thought to contribute to sensitization of nociceptors (Walker & Williamson, 2009; Solomonow, Baratta, Zhou, et al., 2003; Aguggia, 2003).

2.4 Collagen

Etymologically speaking, the term collagen originates from Greek "kolla" meaning "glue" and "gen" for "generating", which reflects the utility of denatured collagen—or gelatin—to make glue (Myles, 1993). Collagens represent a family of structural proteins ubiquitous throughout the animal kingdom, and, at present, there are 28 distinct collagens known to exist (Karsdal, 2019). All collagens are trimers, consisting of three collagen molecular subunits. The presence of an α-helical domain composed of repeating Gly-X-Y residues (X is usually proline, and Y is usually hydroxyproline) in each of these molecular components is common among the collagens, and endows the trimer with its signature "triple-helix" (Karsdal, 2019; Welgus, Jeffrey, & Eisen, 1981; Fratzl, 2008), first elucidated in Crick (1954). Broadly speaking, they can be categorized into four major classes: fibril-forming collagens, fibril-associated collagens with interrupting triple helices (FACITs), network forming collagens, and membrane collagens.

Type I Collagen is a fibril-forming collagen, the most abundant of the collagen types *in vivo*, and the major constituent of most tensile connective tissues (Orgel et al., 2001; Karsdal, 2019). It is a very stable molecule with an ancient past; in fact, collagen recovered from dinosaur fossils bears a remarkable similarity to modern forms of collagen (Lingham-Soliar & Wesley-Smith, 2008). It is hetero-trimeric, meaning that its three macro-molecular components are not identical (Karsdal, 2019). Specifically, type I collagen is composed of two $\alpha 1(I)$ and one $\alpha 2(I)$ peptides, which are encoded on the COL1A1 (chromosome 17) and COL1A2 (chromosome 7) genes, respectively (Karsdal, 2019; Retief, Parker, & Retief, 1985). Mutations in these genes are associated with a variety of syndromes, including Ehlers-Danlos syndrome, osteogenesis imperfecta, and an increased propensity for IVD degeneration (Pluijm et al., 2004; Toktaş et al., 2015). Because of its constituent peptides, Type I Collagen is commonly notated as $[\alpha 1(I)]_2[\alpha 2(I)]_1$.

Tendon, for example, is a highly hierarchical tissue (Figure 2.9) composed of tendon fascicles, which are themselves composed of collagen fibres, which are then composed of fibrils, which are composed of microfibrils, which are, finally, composed of the polymerised collagen molecule (Sasaki & Odajima, 1996; Kastelic, Galeski, & Baer, 1978; Snedeker &

Foolen, 2017). The collagen molecule on its own is a cylindrical-shaped protein approximately 300 nm long, and 1.24 nm in diameter. The axial packing density of collagen molecules into the micro-fibril, and the micro-fibril into the fibril, have been the topic of controversy (Hulmes & Miller, 1979; Hulmes, 2008; Orgel et al., 2001; Okuyama, 2008); however, the longitudinal packing is generally consistent with the Hodge-Petruska model (Petruska & Hodge, 1964). This model was first used to explain the striated appearance of collagen micro-fibrils under scanning electron microscopy, with light-dark bands that repeat every 67 nm called the D-band. In this regime, there is a $0.54D$ gap between adjacent collagen molecules in the longitudinal direction; and each strand is staggered relative to one-another by 67 nm. This gives rise to distinct regions where the collagen molecules maximally overlap of length $0.46D$, and a gap-region of length $0.54D$.

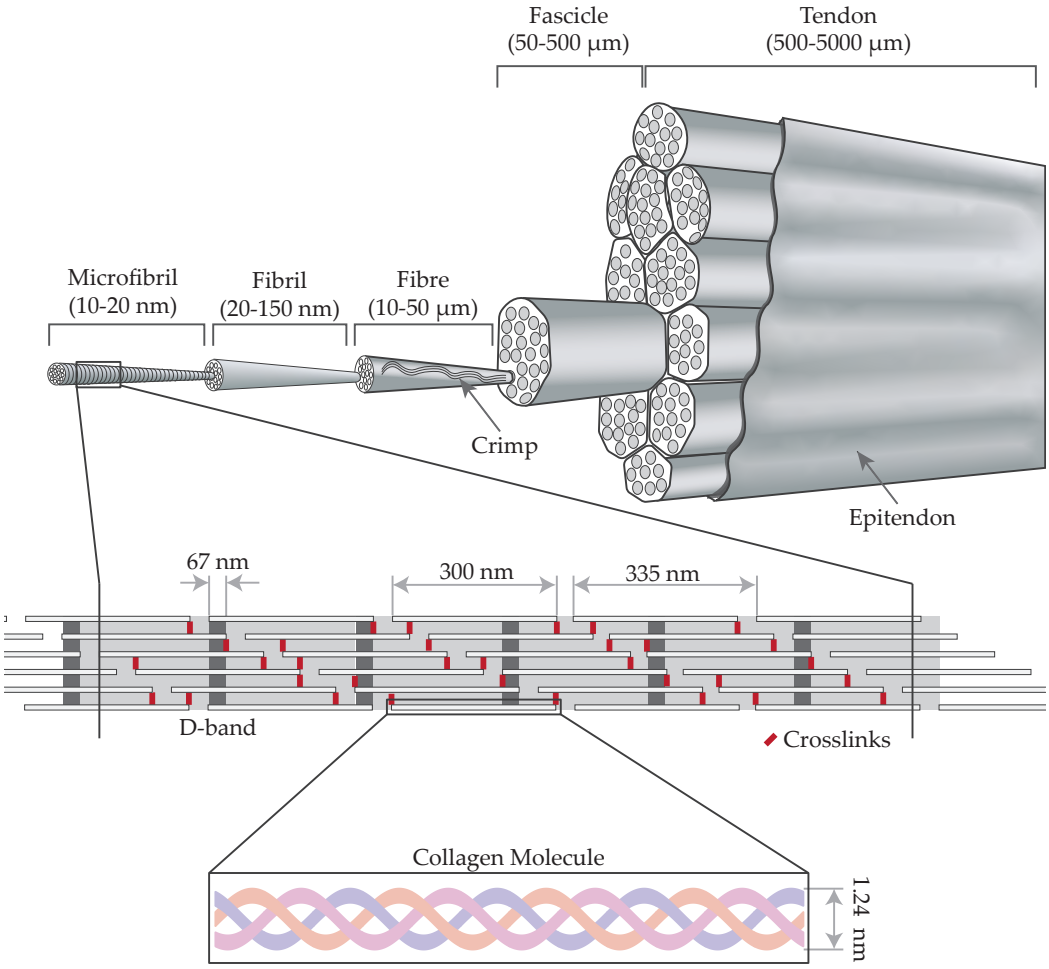

Figure 2.9: Hierarchical structure of tendon, ranging from tendons fascicles to microfibrils with the approximate radius of each level of the hierarchy indicated. The molecules are longitudinally arranged according to the Hodge-Petruska model.

2.4.1 Collagen Distribution Modelling

Mathematically modelling soft-tissue mechanics predominantly relies on deriving equations which match a tissue's force-deflection or stress-strain curve. These models have ranged from exponential (Lucas, Bass, Salzar, Shender, & Paskoff, 2006; Jamison, Marangoni, & Glaser, 1968; Troyer, Shetye, & Puttlitz, 2012), to piece-wise linear (Chandrashekar,

Hashemi, Slauterbeck, & Beynnon, 2008; Yoganandan et al., 2000), to piece-wise quadratic and linear, to interpolations of measured curves (Mattucci et al., 2012). They are highly effective for simulating loading ranges where the failure of a structure is not anticipated to occur: like gait (Marouane, Shirazi-Adl, & Hashemi, 2015; Adouni, Shirazi-Adl, & Shirazi, 2012), or lifting (McGill & Norman, 1986; Anderson, Chaffin, Herrin, & Matthews, 1985) movements. However, because these models typically omit the failure portion of the curve, they have proven difficult to use in situations where damage is likely to occur: for example, in whiplash simulations (Fice, Cronin, & Panzer, 2011; Brolin & Halldin, 2004). To adequately capture the failure portion of the curve requires a departure from this type of phenomenological thinking, and considering what occurs in the tissue from a mechanistic point-of-view.

Viidik (1968) first attempted to model the mechanical behaviour of collagenous tissues by considering the deformation in individual fibres rather than the entire tissue as a whole. By treating each fibre as a linear spring, each with its own resting length, Viidik (1968) was able to reproduce the toe and linear regions of a ligament's force-deflection curve. Later, Liao and Belkoff (1999) were able to use a similar framework to expand the initial model to include the failure portion of the curve by allowing each spring to fail once it had deformed by a prescribed amount. Like Viidik, Lee et al. (2014) were also able to reproduce the toe, linear, and failure portions of the curve using a discrete, experimentally derived collagen network with explicit attention given to cross-links between collagen fibrils. Bontempi (2009) considered a continuum approximation to the work of Viidik (1968). Here, the strain distribution through all of the constituent fibres is analogous to a height distribution of a population of humans. Instead of considering how the strain of an individual fibre changed, Bontempi (2009) considered how the whole distribution would change under static loads. Like Viidik (1968), Bontempi (2009) was able to reproduce the toe and linear regions of the curve.

There have since been two somewhat-related models which aim to expand the work of Bontempi (2009) to the failure portion of the force-deflection curve (Barrett & Callaghan, 2017; Bevan, Merabet, Hornsby, Watton, & Thompson, 2018). We will briefly derive the model of Barrett and Callaghan (2017), as it forms the foundation of the rest of this thesis.

We will let $\rho(x,t)$ denote the distribution of strain among the population of fibrils in a collagenous tissue, where x denotes the strain and t the time. Heuristically, $\rho(x,t)\Delta x$ can be thought of as proportion of collagen fibrils strained by x. Consequently, the proportion of fibrils strained between magnitudes a and b is then given by the integral:

$$\text{Fibrils strained between } a \text{ and } b = \int_a^b \rho(x,t)\,\mathrm{d}x \tag{2.6}$$

This can be thought of as an infinite sum of infinitesimal elements $\rho(x,t)\Delta x$ between a and b as Δx tends to zero. The rate of change of this proportion depends on the strain rate, v. In the absence of synthesis or destruction, the distribution $\rho(x,t)$ could slide between a and b as the whole soft tissue is deformed. For simplicity, we will assume that the entire macroscopic strain rate equally applies to all fibrils in the tissue. In addition, there could have been synthesis of new fibrils strained between these magnitudes, enzymatic degradation, or mechanical disruption. Written in mathematical notation we have:

$$\frac{\mathrm{d}}{\mathrm{d}t}\int_a^b \rho(x,t)\,\mathrm{d}x = v\rho(a,t) - v\rho(b,t) + \dot{S}(a,b) - \dot{C}(a,b) - \dot{D}(a,b) \tag{2.7}$$

Where $\dot{S}(a,b)$, $\dot{C}(a,b)$ and $\dot{D}(a,b)$ represent synthesis, catabolism, and mechanical disruption, respectively. The terms proportional to v denote the amount of the distribution that will either move into the region between a and b or out of it, depending on the strain rate, v. Using the Fundamental Theorem of Calculus, these terms can be combined, yielding the global conservation equation:

$$\frac{\mathrm{d}}{\mathrm{d}t}\int_a^b \rho(x,t)\,\mathrm{d}x = -v\int_a^b \frac{\partial \rho}{\partial x}\,\mathrm{d}x + \dot{S}(a,b) - \dot{C}(a,b) - \dot{D}(a,b) \tag{2.8}$$

Next, we suppose that there are local expressions for $\dot{S}(a,b)$, $\dot{C}(a,b)$ and $\dot{D}(a,b)$. For generality, we will assume that these are expressions of x, t and $\rho(x,t)$. The existence of

these relationships is a key assumption for the remainder of the model derivation:

$$\frac{\mathrm{d}}{\mathrm{d}t}\int_a^b \rho(x,t)\,\mathrm{d}x = -v\int_a^b \frac{\partial \rho}{\partial x}\,\mathrm{d}x + \int_a^b \dot{S}(x,t,\rho)\,\mathrm{d}x - \int_a^b \dot{C}(x,t,\rho)\,\mathrm{d}x - \int_a^b \dot{D}(x,t,\rho)\,\mathrm{d}x \quad (2.9)$$

Using the Leibniz Rule for differentiation under the integral sign, and bringing everything over to one side of the equation, this yields:

$$\int_a^b \frac{\partial \rho}{\partial t} + v\frac{\partial \rho}{\partial x} - \dot{S}(x,t,\rho) + \dot{C}(x,t,\rho) + \dot{D}(x,t,\rho)\,\mathrm{d}x = 0 \quad (2.10)$$

Finally, the only way for this expression to be true for every arbitrary interval $[a,b]$ is if and only if the entire integrand is zero for all x and t. This gives the Partial Differential Equation (PDE):

$$\frac{\partial \rho}{\partial t} + v\frac{\partial \rho}{\partial x} = \dot{S}(x,t,\rho) - \dot{C}(x,t,\rho) - \dot{D}(x,t,\rho) \quad (2.11)$$

Where $\dot{S}$, $\dot{C}$, $\dot{D}$ represent the synthetic, catabolic, and damage rates, respectively. Equation 2.11 is the most general form of the Collagen Distribution Model intended to be used for the remainder of this thesis. In words, this expression reads:

$$\frac{\partial \rho}{\partial t} + v\frac{\partial \rho}{\partial x} = (\text{synthetic rate}) - (\text{catabolic rate}) - (\text{damage rate}) \quad (2.12)$$

Where the left-hand-side of the equation can be, heuristically, thought of as "the rate of change of collagen."

Also important for this formalism, is the calculation of force (or stress) from knowledge of the distribution $\rho(x,t)$. The fibrils which are uncrimped are on the portion of the distribution to the right of $x = 0$. Assuming each fibril has a linear stiffness, k_f, and that

the total number of fibrils in the tissue is N, then the force can be calculated from:

$$F[\rho] = N \int_0^\infty k_f x \rho(x,t)\,\mathrm{d}x \tag{2.13}$$

This can be thought of as adding up the force contribution from each fibre in the population that is uncrimped, since each has force equal to $k_f x$ and there are $\rho(x,t)\Delta x$ stretched by x. The integral, then, plays the role of the sum over the whole distribution, which is multiplied by N since there are N total fibrils in the tissue.

Homogeneous Solution

It is often constructive, even to attain some intuition for a differential equation, to consider its behaviour under very simple situations. For Equation 2.11, the simplest non-trivial case would be under the condition that there are no sources or sinks of new collagen fibrils. Under these assumptions, the equation takes the simple form:

$$\frac{\partial \rho}{\partial t} + v(t)\frac{\partial \rho}{\partial x} = 0 \tag{2.14}$$

Specifying a solution to this differential equation requires also specifying an initial condition. For this we will assume that the fibrils form a Gaussian distribution with mean μ and standard deviation η. There is good reason to suggest a Gaussian for this problem. If the collagen fibrils can be thought of as being composed of discrete straight elements connected to one-another with ball-and-socket joints, then the slack lengths will naturally form a Gaussian as the length of the chain increases. This simply follows from the fact that there are more arrangements around the mean slack length than the extreme lengths. Further, since the total length of the polymer is the sum of the discrete elements, a Gaussian will emerge simply due to the Central Limit Theorem. Once the Gaussian is specified, the solution to Equation 2.14 is simply:

$$\rho(x,t) = \frac{1}{\sqrt{2\pi}\eta} \exp\left(-\frac{(x-\xi(t)-\mu)^2}{2\eta^2}\right) \tag{2.15}$$

Where $\xi(t)$ is the macroscopic strain so that $\dot{\xi}(t) = v(t)$. Calculating the force (or stress) from this expression also has an analytic expression:

$$F(\xi; k, \mu, \eta) = \frac{k\eta}{\sqrt{2\pi}} \exp\left(-\frac{(\xi-\mu)^2}{2\eta^2}\right) + \frac{k(\xi-\mu)}{2}\left[\operatorname{erf}\left(\frac{\xi-\mu}{\sqrt{2}\eta}\right) + 1\right] \tag{2.16}$$

Where $k = k_f N$ is the stiffness in the linear region of the curve, and ξ is, as before, the macroscopic strain. This expression matches experimental data very well, and represents an improvement over exponential modelling, as it accurately predicts the linear region of the curve. Unfortunately, since Equation 2.14 does not incorporate any mechanisms of failure or new collagen synthesis, Equation 2.16 can only be used in cases where failure is not expected to occur.

2.4.2 Mechanical Damage to Collagen Fibres

The classical picture of ordered rupture of collagen fibres as they are strained has recently come under some scrutiny (Veres et al., 2013; Veres, Harrison, & Lee, 2014). It has been documented that mechanical overload translates to the accumulation of fragmented collagen (Torp, 1975; Kastelic & Baer, 1980; Knörzer et al., 1986). However, it has also been shown that the same build-up of damaged collagen is preceded by a physical denaturing of the collagen fibrils (Willett, Labow, Avery, & Lee, 2007). On a biochemical level, the collagen proteins within fibrils undergo an uncoiling plastic deformation—much like a broken slinky (Veres et al., 2014). These deformed elements are regularly spaced throughout a collagen fibril, occurring every 240 nm or so, and have been coined as discrete plastic deformations (Veres et al., 2014). Fibrils that have undergone this conformational change tend to be stiffer than undeformed collagen fibrils, possibly due to a strain-hardening effect. Ultimately, it appears this mechanical change in the collagen fibril may have downstream effects on the macroscopic mechanics of collagenous tissues.

Mechanical overload of type I collagen may interact with the proteinases secreted by fibroblasts. Willett et al. (2007) used a bovine tail tendon model to show that, following mechanical overload, the collagen fibrils in the tendons were more susceptible to cleavage

by trypsin—a proteinase typically associated with gastric digestion. Similarly, Veres et al. (2014) found that mechanically overloaded collagen fibrils are still prone to this cleavage even when cooled to to temperatures optimal for collagen coiling, indicating that the denatured state induced by mechanical loading is thermodynamically stable. These authors concluded that, chemically, the α-chains of the collagen molecules are becoming uncoiled, termed micro-unfolding (Kadler, Hojima, & Prockop, 1988). This micro-unfolding facilitates their entry into the active site of protein cleaving enzymes (Veres et al., 2014). Additionally, fibres that had sustained discrete plasticity can be sensed by macrophages, which secrete inflammatory cytokines in turn (Veres, Brennan-Pierce, & Lee, 2015). Should the discrete plastic deformation enhance the ability of MMP to cleave collagens as well, then it may provide an additional mechanism by which mechanics can interact with the underlying physiology of collagenous tissues.

Some groups have also elucidated where rupture initiates in the collagen molecular structure. Using a molecular model, Rennekamp, Kutzki, Obarska-Kosinska, Zapp, and Gräter (2019) showed that the break of the collagen microstructure invariably begins at the cross-links between adjacent molecules. This result is consistent with Zitnay et al. (2020), who showed that in mechanical fatigue experiments, the mode of failure tends to be in the breakdown of cross-links, and eventual shearing, between the three constituent α-helices.

Discrete plasticity is not currently a feature present in the model (Equation 2.11); however, it could be considered depending on the experimental study outcomes. The methods by which this could be incorporated would be analogous to the different forms of binding between myosin and actin (Zahalak & Ma, 1990), or the incorporation of titin (Schappacher-Tilp, Leonard, Desch, & Herzog, 2015) in the Huxley muscle model. Rather than solely tracking the time-evolution of healthy collagen fibres ($\rho(\varepsilon, t)$), it would additionally track the time evolution of those which have undergone discrete plasticity ($\tilde{\rho}(\varepsilon, t)$). Rather than collagen fibrils being removed from the model when they fail—as they currently are—instead they serve as sources for the fibrils which have undergone discrete plasticity. While it may be enticing to include such detail in this thesis, it remains beyond of the proposed scope to create an initial model of Type I collagen response based on experimental studies of the 3 determining rate factors. The model will instead capture the classical picture of

soft tissue injury. Quantifying the rate of mechanical damage accumulation is the topic of **Study I** (Chapter 3).

2.5 Collagen Homeostasis

Soft tissues typically possess a population of fibroblasts which regulate their ECM. The ECM is the collection of proteins, glycosaminoglycans, and proteoglycans suspended in water which provide the scaffolding for fibroblasts to reside. Collagen is the most abundant protein in the ECM, and is one of the proteins responsible for imbuing tissues with their mechanical properties. The AF and NP of the IVD are examples of collagenous tissues, which must regulate the integrity of their collagen fibrils to maintain their mechanical function (Iatridis, MacLean, Roughley, & Alini, 2006; Stokes & Iatridis, 2004). They accomplish this task by managing the tug-of-war between fibril synthesis, catabolism, and degradation: the three terms in Equation 2.1.

This section begins by considering collagen fibril synthesis and catabolism in isolation. Since both are intimately linked to inflammation, particular attention is given to the inflammatory response of tissues and its influence on collagen fibril homeostasis.

2.5.1 Collagen Fibril Synthesis

There are 28 currently known different proteins classified as collagens in the human genome (Ricard-Blum, 2011). Collagens are trimeric proteins, consisting of three chains of collagen molecules (Karsdal, 2019; Fratzl, 2008). They can exist as homotrimers, meaning that all three chains are of the same molecule; or heterotrimers, indicating that at least one chain is different from the other two. The bulk of collagen synthesis is carried out by fibroblasts, which are usually specialized to their host tissues. Synethsis of collagen is a complex pathway, involving a vast array of post-translational modifications both inside and outside of the cell (Figure 2.10). In the endoplasmic reticulum of these cells, the three primary chains are combined to yield a procollagen molecule. Enzymes of the lysyl hydroxylase

family convert some lysine residues to hydoxylysine, which serve as sites for both intra- and inter-molecular cross-linking, either to other procollagens or to carbohydrates (Karsdal, 2019; Laurent, 1987; Hulmes, 2008). Formation of the cross bridges is integral to provide collagen its tensile strength (Siegmund, Allen, & Burr, 2008). Similarly, enzymes of the prolyl-hydroxylase family hydroxylize proline residues into hydroxyproline, which serves to stabilize the triple helix structure (Hulmes, 2008). A co-factor for the hydroxylation of both lysine and proline is Vitamin-C, a vitamin whose deficiency is famous for causing scurvy, a consequence of inadequate collagen synthesis (Padh, 1991; Myllylä et al., 2007; Tuderman, Myllylä, & Kivirikko, 1977).

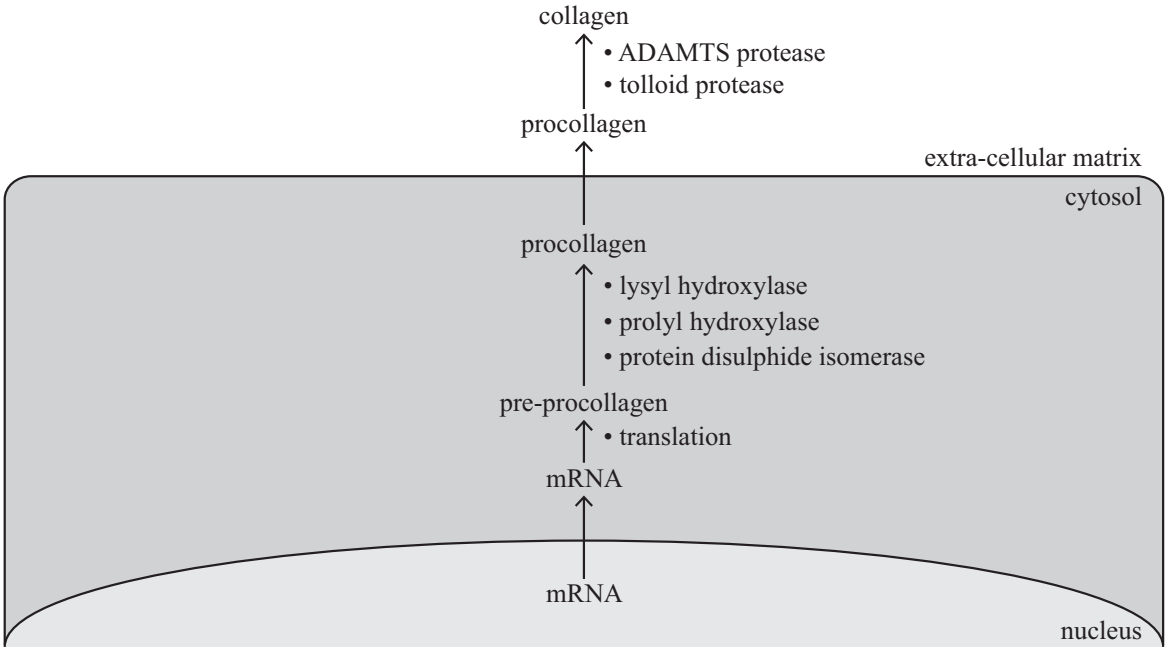

Figure 2.10: Physiological events leading from mRNA transcription to, ultimately, collagen integration into the extracellular matrix. This is a relatively simplified view of collagen synthesis.

Procollagen molecules are collected in vacuoles and excreted into the extracellular space. Once outside the cell, several—at least twenty—Heat Shock Protein 47 (HSP47) act as chaperone proteins to assist its incorporation into the existing collagen network (Nagata, 1998; Nakai, Satoh, Hirayoshi, & Nagata, 1992). Meanwhile, pro-peptide caps and tails—at

the carbon (C) and nitrogen (N) terminals of the protein—are cleaved by proteinases belonging to one of two families (Myllyharju, 2005). The N-terminal is cleaved by proteinases belonging to the family a disintegrin-like and metalloproteinase with thrombospondin type I motifs (ADAMTS) (Porter, Clark, Kevorkian, & Edwards, 2005); whereas the C-terminus is cleaved by those in the tolloid-like family (Hopkins, Keles, & Greenspan, 2007). Measurement of these liberated caps may provide an effective biomarker of collagen fibril synthesis (Karsdal, 2019). Defective cleavage of the N-terminus by ADAMTS-2, -3, or -14, leads to a hereditary disease in humans known as Ehlers-Danlos syndrome—characterized by excessive laxity in collagenous tissues (Le Goff & Cormier-Daire, 2011).

Type I collagen is the most abundant type of collagen in the outer layers of the AF (Sivan et al., 2014). It is composed of two α-1(I) chains and one α-2(I) chain, which together form a triple helix (Karsdal, 2019). While most of the residues in Type I collagen are of the form glycine-proline-hydroxyproline, the occasional hydroxylysine residue in the helical structure affords it the ability to cross-link to other proteins and proteoglycans (Karsdal, 2019; Hulmes, 2008). The final assembled molecule has a length of 300 nm and a width between 1 to 5 nm. Conversely, Type II collagen is the most abundant type of collagen for the inner annlulus fibrosis and NP (Sivan et al., 2014). It is a homotrimer, consisting of three identical α-1(II) chains. Like Type I collagen, the final assembled fibril is 300 nm in length, and over 1000 amino acids long (Karsdal, 2019; Hulmes, 2008). Procollagen molecules of both type I and II have their N-terminal telopeptides cleaved predominantly by ADAMTS-2, and C-terminus by tolloid proteinases (Porter et al., 2005).

2.5.2 Collagen Fibril Catabolism

The largest share of collagen turnover in the ECM is carried out by matrix metalloproteinases (MMP), a family of 23 metal (primarily zinc) and calcium containing proteinases which specialize in cleaving members of the ECM (Itoh, 2006; Birkedal-Hansen et al., 1993; Tschesche & Farr, 2000). MMPs, ADAMTS, and a third category of metalloproteinase, the ADAMs (a disintegrin and metalloproteinase), belong to a family of enzymes known as metzincins due to similarities in their bioechemical structure around their catalytic site

(Tschesche & Farr, 2000; Ho, Wylie, & Apte, 2014). Both ADAMTS and ADAMS enzymes interact with the ECM to some degree, however, they do so far less than do MMPs (Ho et al., 2014). While MMPs are capable of cleaving almost any constituent of the ECM, they each have a preferred substrate. For instance, MMP-1 and MMP-8 are very effective at degrading type I collagen; whereas MMP-13 portrays a high affinity for type II collagen (Nagase, 1996; Richardson, Freemont, & Hoyland, 2014).

Of the 23 types of MMPs, only three of them (MMP-1, MMP-8, and MMP-13) are classified as *collagenases*, and therefore have collagen as their preferred substrate. MMP-1, or collagenase-1, is manufactured by fibroblasts; whereas MMP-8 is primarily created by neutrophils—owing to their names as interstitial collagenase and neutrophil collagenase, respectively (Nagase, 1996). MMP-13 is primarily made by chondrocytes or the cells of the NP (Richardson et al., 2014). Another important class of MMPs are the *stromelysins*: MMP-3 and MMP-10. Stromelysins play a minor role in directly degrading ECM components; however, MMP-3 plays an major role in activating MMP-1 (Suzuki, Enghild, Morodomi, Salvesen, & Nagase, 1990). Ultimately, type I collagen catabolism is predominantly a function of only three MMPs: MMP-1, -8 and -3.

Synthesis and Action of MMPs

Like many other poteinases, synthesis MMP has an inactive precursor form, termed a zymogen (Nagase, 1996). For MMP-1, the precursor is pro-MMP-1, which is encoded on the 11^{th} chromosome (Pardo & Selman, 2005). The zymogen is activated, *in-vivo*, once it has been excreted into the ECM by MMP-3 (Suzuki et al., 1990), although other proteinases, including MMP-1, can be just as effective at activating it (Visse & Nagase, 2003) (Figure 2.11). The process involves removing a peptide-cap on its nitrogen terminal which normally blocks the active site of MMP1, thereby exposing the catalytic region (Visse & Nagase, 2003; Sekton, 2010).

MMP1 cleaves type I collagen between residues 775 and 776; and MMP8 cleaves it between residues 755 and 765 forming a collagen fragment known as C1M (Pardo & Selman, 2005; Karsdal, 2019). They are inhibited by tissue inhibitors of metalloproteinases (Tissue

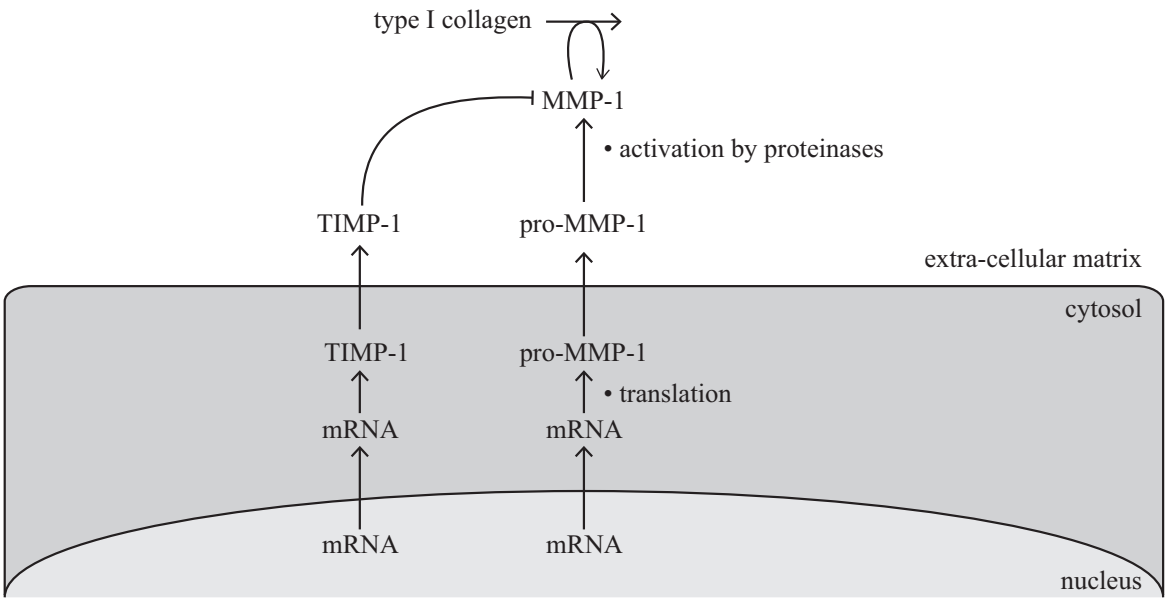

Figure 2.11: Physiological events leading from mRNA transcription to fully activated MMP-1. Additionally, its inhibitor, TIMP-1 follows a similar synthetic pathway, albeit devoid of a progenitor molecule step.

Inhibitors of Metalloproteinases (TIMP)). There are four types of TIMPs in mammals, each numbered in turn TIMP-1 through TIMP-4 (Murphy, 2011; Shingleton, 1996; Leppert, Lindberg, Kappos, & Leib, 2001). In addition to their regulatory role of inhibiting various MMPs, they also play a role in regulating ADAMTS—one of the family of enzymes responsible for activating pro-collagen into collagen. TIMPs act through competitive inhibition, binding one-to-one with an MMP at its active site (Brew & Nagase, 2010). Any of the TIMPs can inhibit any of the MMPs; however, they have low affinity for some specific MMPs depending on the TIMP in question (Baker, Edwards, & Murphy, 2002; Brew & Nagase, 2010). Expression of any TIMPs seems to be tissue-specific, with connective tissue expressing predominantly TIMPs-1 and TIMPs-2 (Karousou, Ronga, Vigetti, Passi, & Maffulli, 2008; Gardner, Arnoczky, Caballero, & Lavagnino, 2008).

This description of MMP-1 may paint the picture that MMPs indiscriminately obliterate matrix constituents with little regard for the overall health of the tissues they are

created in. More recent studies have discovered other substrates for MMPs, which may indicate that the picture of MMPs as bulldozers is too simplistic (McCawley & Matrisian, 2001). For instance, MMP-1 has been shown to cleave pro-Tumor Necrosis Factor-α (TNF-α) (pro-tumor necrosis factor-α), a precursor to TNF-α, a potent stimulator of inflammation (Gearing et al., 1995). Additionally, some ECM fragments created by MMPs are bioactive, term matricryptins, which often with cryptic downstream effects (Davis, Bayless, Davis, & Meininger, 2000; Ricard-Blum & Ballut, 2011). For instance, fragments of type I collagen cleaved by MMP-1 are potent attractors of immune cells, which respond to damage by initiating an inflammatory response (Weathington et al., 2006).

2.5.3 Inflammation

Inflammation is a complex physiological response to harmful stimuli. It is canonically the first response to injuries or pathogens, characterized by swelling, redness, sensitization, and increased local body temperature. It is a normal response to injury, and serves several functions including to promote the migration of immune cells to the affected regions and to stimulate local cells to initiate ECM-remodelling and scar formation. On a cellular level, inflammation is communicated by chemical messages called inflammatory cytokines. These cytokines bind to receptors on the cellular membranes of resident fibroblasts and immune cells, which leads to genetic expression of a range of different proteins involved in ECM remodelling.

Inflammatory cytokines refers to a broad family of small proteins used as chemical messengers between cells. For brevity, this review focuses on two families of inflammatory cytokines as they seem to be the most salient in the cellular response of fibroblasts to inflammation: tumor necrosis factors (TNFs) and interleukins (ILs). Cytokines of these classes map directly onto the genetic expression of MMPs, intimately tying the inflammatory response to the homeostasis of the ECM.

Interleukin-1

Of the interleukins, Interleukin-1 (IL-1) represents a class of 11 different cytokines ubiquitous in both acute and chronic inflammation (Dinarello, 2011; Arend, 2002). Of those cytokines in the interleukin-1 family, IL-1α and IL-1β, appear to play the largest role in propagating chronic tissue inflammation (Risbud & Shapiro, 2014; Freemont, 2008; Millar, Murrell, & McInnes, 2017; Arend, 2002). A third interleukin of this class, the interleukin-1 receptor agonist (IL-1Ra) provides the system with negative feedback, as it competitively inhibits the receptor in which IL-1α and IL-1β would normally bind.

Like MMPs, interleukins are first synthesized as a progenitor molecule: pro-IL-1 (α, β or Ra) (Figure 2.12). Typically, these precursor molecules are biologically inactive; however, a special case is pro-IL-1α, which possesses the ability to integrate with the cellular membrane and participate in cell-to-cell communication (Risbud & Shapiro, 2014; Arend, 2002). IL-1β, on the other hand, has its pro-peptide cleaved by intracellular caspase-1 or extracellular proteinases (Arend, 2002). Both IL-1α and IL-1β bind to the interleukin-1 receptor I (IL-1R1) which triggers a downstream Mitogen Activated Protein Kinase (MAPK) cascade, and can also interact with the nuclear factor κ-B (NF-κB) pathway (Figure 2.13) (Risbud & Shapiro, 2014; Weber, Wasiliew, & Kracht, 2010). These signalling pathways ultimately lead to the expression genes specific to the receptor, most notably, in the case of tissue inflammation, the upregulation of MMP1. There also exists a second receptor for IL-1α and IL-1β: IL-1R2. It is not biologically active, and is thus termed the 'decoy' receptor, as interleukins bound to it are inactive (Arend, 2002).

The Mitogen Activated Protein Kinase (MAPK) cascade is a complex intra-cellular signalling pathway which involves a series of phosphorylation and dephosphorylation events, culminating in the activation of transcription factors, proteins which encourage transcription of specific genes (Sabio & Davis, 2014). While many of these cascades exist in the cell, they all predominantly stem from three broad categories: the extracellular regulated kinases (ERK); the p38 MAP kinases; and the c-Jun NH_2-terminal kinases (JNK) (Sabio & Davis, 2014). The ERK pathway is predominantly activated by growth factors, and promotes cellular proliferation; whereas the other two are generally considered activated by

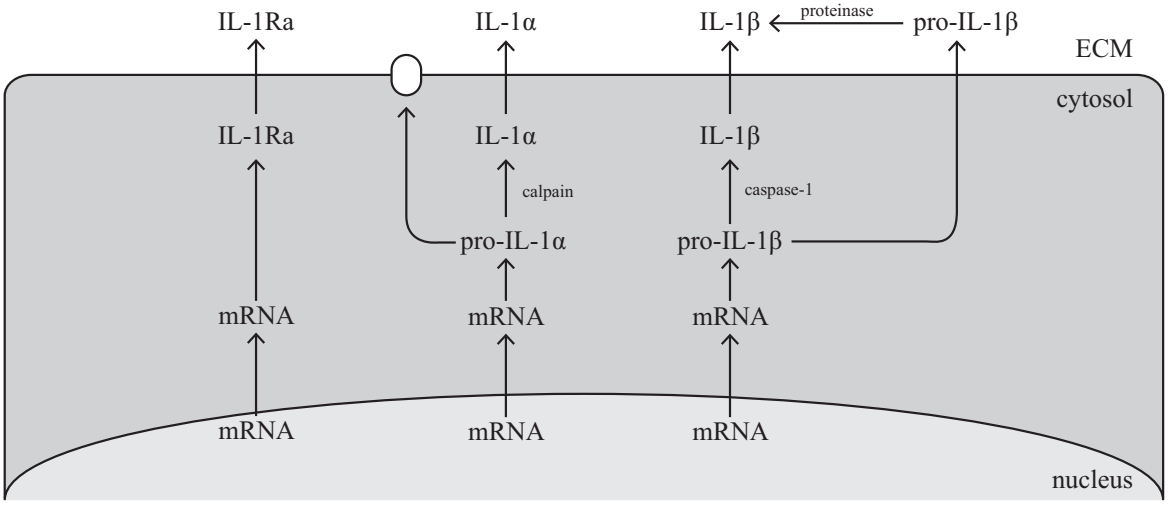

Figure 2.12: Synthesis of IL-1α, IL-1β and IL-1Ra. Pro-IL-1β is activated intracellularly by caspase-1, and extracellularly by proteinases (including MMP1). pro-IL-1α is activated intracellularly by calpain, but can also be integrated onto the cellular membrane and actively participate in cell-to-cell communication. Adapted from Risbud and Shapiro (2014)

stress. In the case of the IL-1R1, the sequence of events is quite complex, but ultimately leads to the expression of genes that promote an inflammatory response (Weber et al., 2010; Ozbabacan et al., 2014; Obata, Brown, & Yaffe, 2000).

Phosphorylation cascades like the MAPK-pathway serves to greatly amplify a small signal. It is much like a telephone sequence, where one person calls two people, and those two people each call two more people, and so-on. After only five iterations of this informing game, thirty-two people are being called in the bottom tier. In much the same way, a single molecule binding to a receptor can lead to several downstream activation events, owing to the fact that one activated product can activate several others in the tier below it. Because of this, cascades of this type can act like switches: rapidly turning on gene expression when the right conditions are met, and sequestering it otherwise. Huang and Ferrell (1996) used a mathematical model of the MAPK cascade to demonstrate this

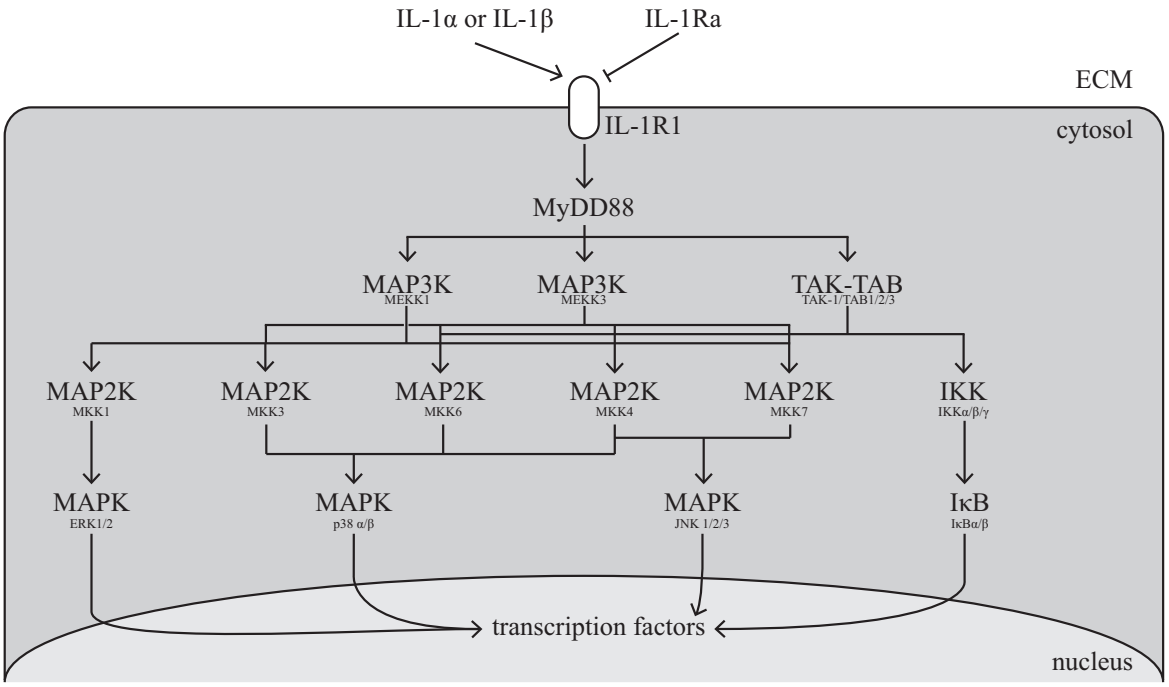

Figure 2.13: MAPK and NF-κB signalling pathways stemming from IL-1 stimulation. Adapted from Ozbabacan et al. (2014)

switch-like behaviour *in-silico*. They modelled the reaction rates of a three-tiered MAPK cascade and compared the steady-state input-output response to a single layer of activation. Indeed, with more layers in the cascade, the more the system approached the behaviour of an ideal switch. Similarly, Gunawardena (2005) demonstrated, using a similar modelling framework, that multiple phosphorylation events had the effect of changing the threshold-value of the biological switch. These are two separate mechanisms by which biological systems can control both the sharpness and threshold value of their response, independent of the properties of the enzymes.

There is some evidence linking these pathways, collectively known as the inflamosome, to collagen homeostasis. Fibroblast cultures treated with IL-1β increase expression of MMP-1, MMP-3, MMP-8, and, most cryptically, IL-1β and TNF-α (Likhitpanichkul et al., 2016). Additionally, IL-1β expression in the IVD seems to be correlated to disc degeneration (Le Maitre, Hoyland, & Freemont, 2007). Together these suggest an interplay

between the physiological state of a tissue and its potential mechanical properties.

Tumor Necrosis Factor-α

TNF-α is ubiquitous in the acute and chronic inflammatory response (Sabio & Davis, 2014; Séguin, Pilliar, Roughley, & Kandel, 2005; Allen et al., 2011; Le Maitre et al., 2007). Like IL-1, it is first synthesized as an inactive form: pro-TNF-α. Its pro-peptide is cleaved by either MMP-1 or other proteinases present in the ECM (Risbud & Shapiro, 2014). Once activated, TNF-α can bind to one of two receptors—TNF-α R1 or TNF-α R2—in either case, stimulating the same MAPK and NF-κB cascades that IL-1β does (Risbud & Shapiro, 2014), resulting in increased expression of MMP-1, IL-1β and pro-TNF-α (Sabio & Davis, 2014; Obata et al., 2000; Risbud & Shapiro, 2014).

For the IVD, TNF-α seems to be strongly correlated with the degree of disc degeneration implying that it may play a role in the degenerative pathophysiology (Bachmeier et al., 2007; Weiler, Nerlich, Bachmeier, & Boos, 2005; Le Maitre et al., 2007). The effect of mechancial stress on TNF-α concentration seems to portray a U-shaped dose-response curve, with both mechanical underuse (MacLean et al., 2003; Uchida et al., 2005) and overuse (Walter et al., 2015; Korecki, MacLean, & Iatridis, 2008; Gardner et al., 2008; Thornton et al., 2010) corresponding to elevated TNF-α levels. It may be the case that TNF-α is partially responsible for the atrophy and decreased tissue tolerance observed with underuse (Stokes & Iatridis, 2004).

Mathematical Models of Inflammation

There have been several previous models of acute inflammation based on systems biology (Clermont, Chow, Constantine, Vodovotz, & Bartels, 2004; Vodovotz et al., 2006; Scholma et al., 2014), but others have successfully modelled the series of reactions in the MAPK cascade, or similar signally pathways (Huang & Ferrell, 1996). In most cases, these models have aimed to reduce the complexity of the MAPK-cascade involved in signal transduction. Vodovotz et al. (2006) used a complex Ordinary Differential Equation (ODE) model

to simulate the effects of acute inflammation. They found their results could be reduced to a simpler set of equations, where the effect of immune cells and cytokines could be combined into a single term (Kumar, Clermont, Vodovotz, & Chow, 2004). In a similar vein, Scholma et al. (2014) simplified the entire cascade as a single step governed by mass action. They found that, with the right parameter selection, they were able to replicate the interactions between IL-1 signalling and a similarly abstracted negative feedback system in articular chondrocytes. A classic mathematical model of the MAPK-cascade demonstrated that such signalling pathways act as biological switches: turning on specific gene expression when specific requirements are met (Huang & Ferrell, 1996). In the case where detailed information on the state of each molecular constituent is not required down-to-the nanosecond, a quasi-steady state simplification can be reasonably applied. These models demonstrate that while it is possible to model the entire phosphorylation cascade, it may ultimately be unnecessary. Modelling a biological system requires carefully selecting a level of abstraction which adequately captures the behaviour of the system, without being so cumbersome and complex that it is impossible to apply or parameterize.

Inflammation and Cartilage

Painful changes to articular cartilage manifest most apparently in the cartilage of the knees, hip, and shoulder during osteoarthritis (OA). This pathology was classically associated with cumulative wear-and-tear; however, research in recent decades have provided a cellular mechanism for the propagation of the degenerative state of these tissues (Kapoor, Martel-Pelletier, Lajeunesse, Pelletier, & Fahmi, 2011; Fernandes, Martel-Pelletier, & Pelletier, 2002).

The biochemical changes seen in OA are initiated by mechanical damage, which ruptures the Type II collagen that make up the articular surface. Ruptured type II collagen is sensed by the resident fibroblasts, known as chondrocytes in the cartilage. Chondrocytes respond to the ruptured collagen by secreting inflammatory cytokines, IL-1β and TNF-α (Kapoor et al., 2011; Fernandes et al., 2002; Goldring & Goldring, 2004). These seem to have an intended paracrine effect, alerting surrounding chondrocytes to the localized dam-

age; however, they also exert a potent autocrine effect, causing the chondrocyte to secrete matrix metalloproteinase-13 (MMP-13) (Bonassar et al., 1997; Arner, Hughes, Decicco, Caterson, & Tortorella, 1998). MMP-13, secreted into the ECM begin cleaving type II collagen, producing yet more collagen fragments (Karsdal, 2019). This completes the cycle, as cleaved type II collagen fragments are once again sensed by the chondrocyte, causing them to respond with inflammatory cytokines (Klatt et al., 2009; Yasuda, 2014).

Inflammation and Tendons

Tenocytes, the resident fibroblasts of the tendon, are responsible for the synthesis and turnover of the ECM components where they reside. Type I collagens compose most of their basal synthetic activity, accounting for 65-80% of the ECM constituents of a tendon (Scott, Backman, & Speed, 2015). After an injurious event, tenocytes synthesize type III collagen, forming a callus scaffolding for future type I collagens to affix (Sharma & Maffulli, 2006; Maffulli, Ewen, Waterston, Reaper, & Barrass, 2000). Gradually, over the course of a year, type III collagen is replaced by type I collagen, completing the wound-healing cascade. The synthesized type III collagen by tenocytes accumulates with age, leading to a higher proportion of type III collagen in aged tendons (Torricelli et al., 2013). The synthesis of collagen by tenocytes mirrors that of other fibroblasts: pro-collagen molecules are extruded from the cell and integrated into the existing collagen network.

Tendinopathies are generally regarded as painful disorders of the tendon. Those which are accompanied by inflammation are termed tendonitis; whereas those where inflammation is difficult to detect—either through the lack of redness, swelling, or inflammatory biomarkers in the blood—are termed tendinosis (Abate et al., 2009; Maganaris, Narici, Almekinders, & Maffulli, 2004). Until recently, tendinosis was thought to be entirely devoid of a state of chronic inflammation. However, recent evidence suggests an insidious role for inflammation to play in the cascade of this condition.

Tendon overuse injuries are typically attributed to biomechanical origins. Cyclic strains at physiological levels—typically less than 4% strain—impart micro-damage to the collagen fibrils arranged in the tendon, which gradually culminate in the reduction of tissue toler-

ance (Maeda, Kuroyanagi, Ando, & Matsumoto, 2019; Sharma & Maffulli, 2006; Nakama, King, Abrahamsson, & Rempel, 2005). Micro-trauma induces two parallel events: (i) tenocytes secrete IL-1β, and (ii) macrophages are drawn to the site of damage (Sun et al., 2008). Increased tenocyte expression of MMP-1 is downstream of IL-1β stimulation, linking the inflammatory response to increased catabolism (Maeda et al., 2019; Tsuzaki et al., 2003; Thorpe et al., 2015; Archambault, Tsuzaki, Herzog, & Banes, 2002). Secondly, macrophages migrating to the site of damage respond by secreting their own IL-1β, either in response to the local response from tenocytes or in response to sensing microdamage to collagen fibrils (Veres et al., 2015). This provides a potential avenue by which mechanical exposure can propagate to an inflammatory response (Riley, 2003; Millar et al., 2017).

In addition to constructing their extracellular environment, tenocytes also secrete enzymes specialized for cleaving the two major constituents of their ECM: the collagens and the proteoglycans (Gardner et al., 2008; Thornton et al., 2010). Gene expression of these MMPs has been shown to be higher in both tendinosis and tendonitis. The expression of MMPs is downstream of the sensation of the inflammatory cytokines, IL-1 and IL-1β (Maganaris et al., 2004). In addition to increasing the synthesis of MMPs, IL-1β also reduces the expression of type I collagen. The other aspect of ECM degradation by tenocytes are enzymes beholden to the family A Disintegrin and Metalloproteinase (ADAM) with Thrombospondin (TS) motifs, termed ADAMTS (Maganaris et al., 2004). These enzymes are specialized for cleavage of the proteoglycans which compose the ECM; their genetic expression is also stimulated by IL-1β (Archambault et al., 2002; Tsuzaki et al., 2003).

Inflammation and the Intervertebral Disc

Inflammation has been shown to play a critical role in modulating both the synthesis and catalysis of collagen fibrils in the NP (Freemont, 2008; Zhang et al., 2020; Ashinsky et al., 2019). The NP is primarily Type II collagen, which smoothly transitions to a type I dominant phenotype in the outer annulus. The fibroblasts of the NP possess a similar feed-forward inflammatory response to chondrocytes. Recently, it was demonstrated that neutrophils are able to migrate through the end plate into the NP, and may induce the

runaway inflammatory cascade and promote the infiltration of nociceptors into the NP (Wiet et al., 2017). Once mast cell infiltration has commenced, it is possible that they can promote a state of chronic inflammation.

Additionally, several *in-vitro* studies have demonstrated the potential for a feed-forward catabolic cascade. Chen et al. (2016) used a rat tail intervertebral puncture model to study the time course of events following a puncture injury used to simulate a disc herniation. They found that there was an immediate expression of cytokines following puncture, consistent with other, similar studies (Ulrich, Liebenberg, Thuillier, & Lotz, 2007). Two weeks after this transient rise in inflammatory cytokines, there was a subsequent downstream upregulation of MMP-13 in the IVD. Further, exposure of cultured NP cells to TNF-α causes their genetic expression to abruptly change to one which promotes ECM catabolism, characterized by increased expression of IL-1β (Maidhof, Jacobsen, Papatheodorou, & Chahine, 2014). Meanwhile, nuclear cells show a marked increased expression of MMP-13, TNF-α, IL-1β in response to exposure to IL-1β (Le Maitre, Freemont, & Hoyland, 2005) or TNF-α (Séguin et al., 2005; Purmessur et al., 2013; Le Maitre et al., 2007). These result seem to suggest that, downstream from mechanical exposure, the cells of the NP can support a chronic, feed-forward state of inflammation that is deleterious to the integrity of the ECM.

In the annulus, the story is a little different. It seems that the intermediate layers of the AF have some capacity to mitigate the local inflammatory response (Wiet et al., 2017; Le Maitre et al., 2005), despite annular clefts and lesions being correlated to MMP-expression (Weiler, Nerlich, Zipperer, Bachmeier, & Boos, 2002). However, these studies were only considering intermediate layers of the AF, and not the outer-most. The layers of the outer one-to-two millimetres of AF have access to the vascular system (Urban, Smith, & Fairbank, 2004), which may permit the migration of immune cells, circumventing their access by way of the end plate. Thus, the outer AF may have the ability to sustain the deleterious chronic state of inflammation much like the NP, articular cartilage, or tendons. Since nociceptors are also sensitive to inflammatory cytokines, it may provide a different mechanism for discogenic pain generation in the absence of nuclear degeneration.

Inflammation and Nerves

Inflammatory signals have also been demonstrated to play a role in peripheral sensitization of nociceptors—nerves specialized to relay potentially harmful stimulii to the brain. The 'inflammatory soup', as it is referred to, consists of inflammatory peptides (bradykinins) and lipids (prostaglandins), which act in concert to lower the action potential threshold on nociceptors (Julius & Basbaum, 2001; Woolf & Salter, 2000). The lowered threshold makes these nerves more likely to relay nociceptive afferent signals to the brain, which may change a previously non-painful stimulus into a painful one. This sensitization in the wake of inflammation is what makes the tissue surrounding an open sore more sensitive, and is intended to inform the brain that tissue is undergoing healing.

The process can also occur in reverse: nerve cells can excrete inflammatory cytokines into the tissues they innervate (Black, 2002). This 'neurogenic inflammation' can alter how the tissues respond to damage, and can even occur if no damage has been endured. Sensory neurons have the capacity to release Substance P into their periphery, which has been shown to stimulate mast cell migration, and amplify the initial spread of inflammation. In addition, they may secrete other inflammatory cytokines, like interleukin-1.

2.6 Methodology

2.6.1 *in-vivo* Techniques

In Biomechanics, *in-vivo* methodology is typically restricted for human participants. However, for the purposes of this thesis, *in-vivo* is taken to be those methods which utilize a living animal. As the focus of **Study III** (Chapter 5) is to quantify how a mechanical environment interacts with collagen synthesis and degradation, it will need to use a type of *in-vivo* model. The choice of animal to use as a surrogate for human tissue is important, as animal anatomy differs, often significantly, from human. Additionally, there can be cellular differences between humans and animals; especially in the spine, where small animals—like rats or mice—retain their notochord cells in the NP for their whole lives, whereas large

animals—like humans, sheep, or cows—do not (Alini et al., 2008). This makes studying degenerative changes in the NP of small animals difficult to generalize to humans.

Animal models of intervertebral damage broadly fall under two categories: surgically induced disc degeneration, and those replicating the physiological state of the disc leading up to herniation. Most animal models fall under the former, typically using a disc puncture model to initiate disc degeneration (Michalek, Funabashi, & Iatridis, 2010; Korecki, Costi, & Iatridis, 2008; Masuda et al., 2005; Michalek & Iatridis, 2011; Gregory, Bae, Sah, & Masuda, 2014; Michalek et al., 2010; Norcross, Lester, Weinhold, & Dahners, 2003). The puncture mimics a disc herniation, circumventing the usual chronic exposure pathway needed to produce a herniation *in-vivo* (Tampier et al., 2007; Callaghan & McGill, 2001). The subsequent biological changes map quite well onto the changes seen with disc degeneration.

Animal models which aim to replicate the physiological state of the disc prior to herniation are relatively less common. Osti, Vernon-Roberts, and Fraser (1990) pioneered an annular lesion model where they used a wire-like needle to damage a goat lumbar IVD, taking great care not to disrupt the inner layers or the NP. Over the subsequent months, they observed changes in the disc reminiscent of disc degeneration: decreased contrast between annular and nuclear tissue, lesions in the inner annulus distal to where the incision was made, and eventual herniation. This technique has since been adapted to test various therapeutic modalities on an injured IVD, such as infilling the annular lesion with engineered tissue (Le Visage et al., 2006; Clouet, Fusellier, Camus, Le Visage, & Guicheux, 2018), or chondrocyte transplantation (Ganey et al., 2003). Further, it has been extended to other animals, like rabbit (Sobajima et al., 2005; Masuda et al., 2005; Nomura, Mochida, Okuma, Nishimura, & Sakabe, 2001), dogs (Ganey et al., 2003), cows (Korecki, MacLean, & Iatridis, 2008), or rats (Elliott et al., 2008). Rat *in-vivo* models exploring the effect of mechanical load, rather than surgically induced injury, are less common. MacLean, Lee, Alini, and Iatridis (2005) and Iatridis, Mente, Stokes, Aronsson, and Alini (1999) affixed a device to the rat tail which could cyclically load the disc *in-vivo* in compression. These models have been used to document physical changes in the IVD, like decreased stiffness and disc height (Stokes, Aronsson, Spence, & Iatridis, 1998), in addition to physiologi-

cal changes, like altered mRNA expression or protein markers of collagen synthesis and degradation (MacLean, Lee, Alini, & Iatridis, 2004; MacLean et al., 2005; Iatridis et al., 1999). To date, torsion is the other loading modality explored with this model (Barbir et al., 2011).

2.6.2 *in-vitro* Techniques

Mechanical Testing

In their most basic form, tissue tensile testing is uni-axial; simply combining a servo-motor in series with a load cell and the specimen in question, and recording both the tension and displacement of the tissue. The results from a mechanical test are visualized as a load-displacement plot, which is sometimes normalized to a stress-strain curve. Tests of this sort are commonplace when studying tendons (Butler, Kay, & Stouffer, 1986; Arya & Kulig, 2009; Lynch, Johannessen, Wu, Jawa, & Elliott, 2003), ligaments (Hewitt, Guilak, Glisson, & Vail, 2001; Mattucci et al., 2012, 2012; Myklebust et al., 1988; Yoganandan et al., 2000; Holmes, Howarth, Callaghan, & Keir, 2012), and AF (Gregory & Callaghan, 2011; O'Connell, Sen, & Elliott, 2012; Bass, Ashford, Segal, & Lotz, 2004).

One concern for mechanical testing of this sort is the number of freeze-thaw cycles a specimen endures prior to data collection. The formation of ice crystals during a freezing cycle can reasonably disrupt the alignment and integrity of the collagen fibrils which make up the tissue. Previous work has demonstrated that repeated freeze-thaw cycles did not alter the tensile behaviour of rat tail tendons (Lee & Elliott, 2017), nor human tissue (Lee et al., 2009; Huang, Zhang, Sun, Zhang, & Tian, 2011). However, these cycles have been shown to be fatal to the local cells, disqualifying frozen tissue as an *in-situ* model for *in-vivo* tissue (Suto et al., 2012).

Western Blotting

Western Blot Analysis is a semi-quantitative method for measuring the expression of proteins in tissues (Taylor & Posch, 2014; Mahmood & Yang, 2012). Broadly speaking, the

process begins with homogenization of tissues and cells, separating proteins by their masses and formal charge, transferring proteins to a polyvinyl difluoride (PVDF) membrane and, lastly, identifying proteins by way of antibody-antigen fluorescence.

Tissue homogenization ensures that all proteins in the sample are suspended in solution and available for subsequent electrophoresis. There are several techniques for accomplishing this, ranging from physical homogenization with a glass-homogenization, mortar and pestle, or automatic bead-homogenization, to chemical techniques where strong detergents or chaotropes (*e.g.* Guanidine Hydrochloride) are used to denature all of the proteins in a sample. The choice of homogenization technique ultimately depends on how fibrous the tissue of interest is; liver, for instance, can usually be easily homogenized by hand with a glass homogenizer. After homogenization, samples are suspended in a sample buffer, and remnant solid matter is removed using a centrifuge and aspirating the supernatant.

The protein concentration in the isolated protein samples is then established with a Bicinchoninic acid (BCA) assay (Walker, 2009). A small portion of the samples are diluted, and mixed with a 50:1 solution containing BCA and copper (II) sulphate, and incubated at 37°C for 30 minutes. Peptide bonds in the protein sample reduce Cu^{2+} cations to Cu^{+}, which subsequently chelate with the BCA. The final amount of Cu^{+} is directly proportional to the concentration of peptide bonds in the sample. Since the absorption spectra between these two copper ions is known, and apparent in the visual spectrum, protein content can be estimated from the measured absorption spectrum of the sample. The final step in this preparatory protocol is to dilute samples to a known concentration (typically 1 $\mu g/\mu L$) in a buffer containing sodium dodecyl-sulphate (SDS), a very strong detergent that keeps proteins denatured for long term storage.

Separation of proteins by their molecular weight is done by a process called *electrophoresis*, a phenomenon where charged particles suspended in a solution migrate when held under a uniform electric field (Taylor & Posch, 2014; Mahmood & Yang, 2012). First samples are placed in accessible wells in a polyacrylamide gel, immersed in electrophoresis buffer, and exposed to an electric current for 60 minutes. After which time, the polyacrylamide gel contains lanes of sample proteins each separated according to their molecular weight. The proteins are then transferred to a PVDF (or nitrocellulose) membrane by applying a

current orthogonal to the gel toward the membrane.

The final step, detection, first involves applying a primary antibody to the membrane and leaving it typically overnight. The primary antibody binds to the protein of interest, usually three to four amino acids. Then, a secondary antibody is applied which binds to the primary antibody. The secondary antibody is labelled with a binding site for the enzyme horshradish peroxidase, which catalyzes oxidation of luminol by hydrogen peroxide. This reaction produces UV light, which can be detected by a photodetector. The amplitude of UV light emission in a region of the membrane is directly related to the concentration of protein-primary-secondary complexes in that region (Taylor & Posch, 2014; Mahmood & Yang, 2012).

The method is only semi-quantitative, as the density of each blot is reported as a fold-change relative to a control group (Taylor & Posch, 2014; Mahmood & Yang, 2012). Western blots have been used previously to study the change in protein expression of rat tissue in response to mechanical loading and tissue degradation (Purmessur et al., 2013).

Immunohistology is a similar method that uses fluorescent antibodies which adhere to specific proteins. Like Western Blotting it is restricted to being semi-quantitative; however, it yields a more powerful spatial resolution, as the exact location of specific proteins can be identified. The real-time polymerase chain reaction (RT-PCR) is another analysis useful for studying the physiology of fibroblasts. Rather than Western Blotting, which aims to characterize the final expression of proteins, RT-PCR is useful for characterizing the expression of mRNA. RT-PCR has been previously used to measure the change in genetic expression of fibroblasts in response to mechanical loading and inflammatory cytokines (Tsuzaki et al., 2003; Korecki, MacLean, & Iatridis, 2008; MacLean et al., 2004). A limitation of RT-PCR is that it is only useful for quantifying the mRNA expression, which may or may not translate to downstream active protein expression—epsecially for proteins as highly regulated as MMPs. For instance, if MMP-1 mRNA production is up 10-fold, but so is TIMPs-1, it may not be that the increase in MMP-1 is all that significant; alternatively if MMP-1 mRNA production is up 10-fold, but there is little to no expression of MMP-3, then it is unlikely that much of the MMP-1 has been activated out of its pro-MMP-1 form, and is therefore inactive.

2.6.3 *in-silico* Techniques

This section aims to lay out the fundamental concepts for computational modelling of both mechanical and biological systems. It begins with an overview of biochemically relevant quantities: rate laws, in particular mass action and Michaelis-Menten kinetics.

Enzyme Kinetics

Most reactions throughout biology are catalyzed by enzymes. These have the advantage of accelerating the rate of reaction by reducing the activation energy. Unfortunately, enzyme catalyzed reactions are not particularly well described by the Law of Mass Action (Ingalls, 2013; Cleland, 1967; Johnson & Goody, 2011). To adequately capture the time evolution of an enzyme-catalyzed reaction requires considering the Mass Action in each step of the reaction. Suppose the enzyme, E, acts on a substrate, S; first E and S bind together to form a complex, C, after this, the complex relinquishes a product, P and the enzyme E. As a chemical equation the process is represented:

$$S + E \underset{k_-}{\overset{k_+}{\rightleftarrows}} C \overset{k_{\text{cat}}}{\rightarrow} P + E$$

Where the rate-constants for the Law of Mass Action are indicated by proximity to the arrows indicating the direction of the reaction. After employing the Law of Mass Action to these reactions we arrive at the system of differential equations describing the rate of change of each of the chemical species:

$$\frac{d[S]}{dt} = k_-[C] - k_+[S][E] \tag{2.17}$$

$$\frac{d[E]}{dt} = k_-[C] + k_{\text{cat}}[C] - k_+[S][E] \tag{2.18}$$

$$\frac{d[C]}{dt} = k_+[S][E] - k_-[C] - k_{\text{cat}}[C] \tag{2.19}$$

$$\frac{d[P]}{dt} = k_{\text{cat}}[C] \tag{2.20}$$

A simplifying assumption is to treat the complex, C, as existing in a steady state—the so-called quasi-steady state approximation (QSSA). Additionally, the total amount of enzyme $E_{\text{tot}} = [E] + [C]$ is conserved throughout the reaction. This gives rise to the differential-algebraic equation system:

$$\frac{d[S]}{dt} = k_-[C] - k_+[S][E] \tag{2.21}$$

$$\frac{d[E]}{dt} = k_-[C] + k_{\text{cat}}[C] - k_+[S][E] \tag{2.22}$$

$$\frac{d[P]}{dt} = k_{\text{cat}}[C] \tag{2.23}$$

$$0 = k_+[S][E] - k_-[C] - k_{\text{cat}}[C] \tag{2.24}$$

$$E_{\text{tot}} = [E] + [C] \tag{2.25}$$

The last two expressions can be rearranged for the steady state concentration of complex, $[C]$, as:

$$[C] = \frac{E_{\text{tot}}[S]}{[S] + \frac{k_- + k_{\text{cat}}}{k_+}} = \frac{E_{\text{tot}}[S]}{[S] + K_m} \tag{2.26}$$

Where we have defined the Michaelis-Menten constant, $K_m = \frac{k_- + k_{\text{cat}}}{k_+}$. Finally, this can be substituted back into the expressions to yield a simpler non-linear system:

$$\frac{d[S]}{dt} = -\frac{k_{\text{cat}} E_{\text{tot}}[S]}{K_m + [S]} \tag{2.27}$$

$$\frac{d[P]}{dt} = \frac{k_{\text{cat}} E_{\text{tot}}[S]}{K_m + [S]} \tag{2.28}$$

The hyperbolic term describing the rate of reaction represents the effective rate of conversion from substrates into products, often called Michaelis-Menten Reaction Kinetics (Johnson & Goody, 2011) (Figure 2.14). At low concentrations of substrate, the model predicts a linear conversion to products. However, as the concentration of substrate increase, there is diminishing returns, as it begins to asymptote at $k_{\text{cat}} E_{\text{tot}}$, sometimes abbreviated V_{max}. This represents where all of the available enzymes are constantly occupied

with the conversion of substrate into products. The constant rate of reaction at these high concentrations of substrate can be approximated by a zeroth-order ODE, with a constant rate of reaction. For these reasons, the Michaelis-Menten enzyme kinetic scheme captures a linear rate of reaction at low substrate levels, which transitions to a zeroth order reaction at high substrate concentrations.

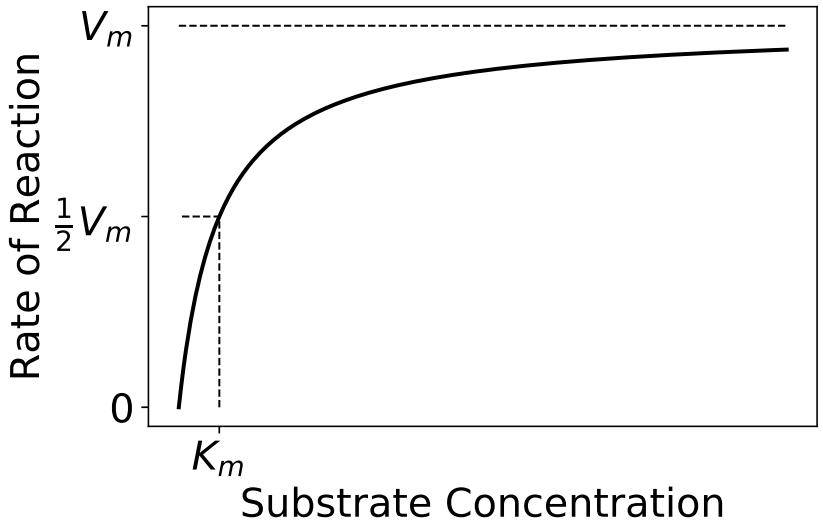

Figure 2.14: The Michaelis-Menten equation for the rate of reaction as a function of substrate concentration. At low concentrations the rate of reaction increases linearly with substrate concentration, which experiences diminishing returns beyond K_m, where the rate of reaction is half of V_m. The horiziontal asymptote of the equation is V_m, the maximum rate of reaction, where the enzymes are fully occupied in conversion from substrates to product.

Often times, enzymes cannot carry out their actions with impunity once they have been activated. Many enzymes, including MMP-1, are regulated by inhibitors (Cleland, 1967; Ingalls, 2013). There are three general types of inhibition throughout biochemistry, each having its own impact on the Michaelis-Menten kinetic equation derived above. Inhibitors can directly compete to inhibit enzyme by blocking the enzyme's active site: so-called competitive inhibition. Alternatively, inhibitors can bind to the complex formed between the substrate and enzyme, and prevent the conversion to product: uncompetitive inhibtion. Finally, an inhibitor can bind elsewhere on an enzyme entirely, and trigger a conformational change which deactivates the enzyme whether a substrate is bound or not: non-competitive

inhibition.

Competitive Inhibition. Under the competitive inhibition scheme, substrates S and inhibitors I both compete to bind to the enzyme E, forming one of two complexes: the complex with the substrate ES, which, like before, can be converted into products; and the complex with the inhibitor EI, which does nothing beyond unbinding. The various reactions are encapsulated below:

$$S + E \underset{k_-}{\overset{k_+}{\rightleftarrows}} ES \overset{k_{\text{cat}}}{\rightarrow} P + E$$

$$I + E \underset{k_{-i}}{\overset{k_i}{\rightleftarrows}} EI$$

A useful parameter for any inhibition scheme is the equilibrium constant, K_i, which is a ratio of the forward and reverse reaction coefficients (*i.e.* $K_i = \frac{k_i}{k_{-i}}$). After undergoing a similar derivation to the Michaelis-Menten scheme above, one arrives at the following expression for the rate of reaction (V):

$$V = \frac{V_{\max}[S]}{K'_m + [S]} \tag{2.29}$$

Where K'_m is the apparent Michaelis-Menten constant, given by:

$$K'_m = \left(1 + \frac{[I]}{K_i}\right) K_m = \alpha K_m \tag{2.30}$$

Where we have defined $\alpha = 1 + \frac{[I]}{K_i}$ as the inhibitory factor. Ultimately, this equation expresses that, under competitive inhibition, the maximum rate of reaction V_m remains unchanged. However, the Michaelis-Menten constant is increased with more inhibition. Intuitively, even with the inhibitor present, if the concentration of substrate is high enough, it is more likely for the enzyme to interact with proper substrate rather than inhibitor.

Uncompetitive Inhibition. Uncompetitive inhibition requires that the enzyme first binds with its substrate prior to enacting its inhibitory effect. In the reaction scheme

(Figure 2.15), this involves the inhibitor binding to the complex ES thereby preventing it from converting substrate into product. This type of inhibition is unique, since it requires the presence of substrate, unlike competitive or non-competitive inhibition. This type of inhibition manifests itself under Michaelis-Menten reaction kinetics by reducing both K_m and V_m. The reduction in K_m indicates an increased affinity for substrate and assemblage of the complex, ES. However, because some of the enzyme is occupied in the inhibited state, ESI, there is a subsequent reduction in V_m.

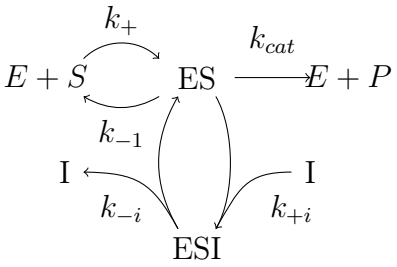

Figure 2.15: Reaction mechanism for uncompetitive inhibition. Under this reaction scheme, the inhibitor (I) can only bind to the enzyme once it is has bound to its substrate (ES-complex). The resulting complex is unable to catalyze the conversion to product, P.

Applying the Law of Mass Action and the QSSA to this reaction scheme results in a similar Michaelis-Menten equation:

$$v = \frac{\left(\frac{V_m}{\alpha}\right)[S]}{\left(\frac{K_m}{\alpha}\right) + [S]} \tag{2.31}$$

Where $\alpha = \left(1 + \frac{[I]}{K_i}\right)$, once again, is the inhibitory factor. This equation indicates that both the maximum velocity and the Michaelis-Menten constant are reduced in this type of inhibition. The reduction in K_m represents an increase in the enzyme's ability to bind to its substrate.

Non-Competitive Inhibition. In non-competitive inhibition, inhibitors can bind to either free enzyme or to the enzyme-substrate complex (Figure 2.16). In this scheme, the inhibitor has equal propensity for binding to the enzyme before or after it has already abound to the substrate. Like uncompetitive inhibition, non-competitive inhibition has

the effect of decreasing the maximum reaction velocity, V_m. However, it has no effect on the Michaelis-Menten constant (K_m).

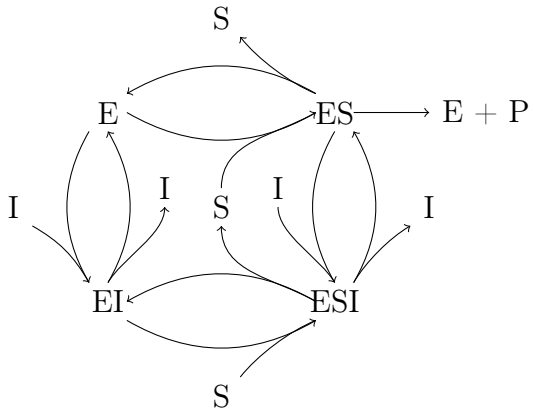

Figure 2.16: Reaction mechanism for non-competitive inhibition. Under this reaction scheme, the inhibitor (I) is able to bind to the enzyme or the enzyme-substrate complex. It is only the enzyme-substrate complex which is able to catalyze the conversion from substrate (S) to product (P). The rate constants for each reaction are omitted from this diagram for brevity.

In applying the same QSSA to the non-competitive inhibition scheme, we arrive at the Michaelis-Menten term for the reaction velocity:

$$v = \frac{\left(\frac{V_m}{\alpha}\right)[S]}{K_m + [S]} \tag{2.32}$$

Where $\alpha = \left(1 + \frac{[I]}{K_i}\right)$, as before. Like incompetitive inhibition, this factor effectively acts to reduce the maximum reaction velocity.

Mixed Inhibition. The final type of inhibition is known as 'mixed inhibition,' and it has the same reaction scheme as non-competitive inhibition (Ingalls, 2013). In fact, non-competitive inhibition can be seen as a special case of mixed inhibition where the association and dissociation constants for the inhibitor are the equal whether the substrate is bound or not. The cases where the enzyme has a higher affinity for inhibitor either before or after binding to substrate can alter reduce the Michaelis-Menten constant (K_m) or the maximum velocity (V_m) in any assortment of ways. It is called 'mixed' since it can portray elements of competitive inhibition if the enzyme binds to its inhibitor at a greater rate

prior to substrate attachment; or as incompetitive inhibition if the enzyme favors binding to the inhibitor after the substrate is attached.

Enzyme inhibition manifests itself by adjusting the parameters in the Michaelis-Menten equation: either V_m, K_m, or both. These mechanisms give cells some measure of control on how sensitive pathways may be to increases in the availability of substrate without waiting for old enzymes to degrade by natural means. Non-competitive inhibition affects the maximum reaction velocity by effectively reducing the amount of free enzyme available. Conversely, competitive inhibition acts to increase the K_m, reducing the efficiency by which enzymes can act on their substrate, but not the maximum reaction velocity.

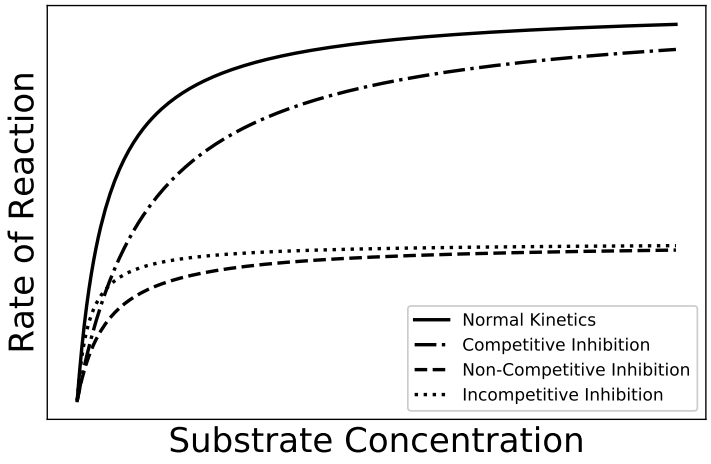

Figure 2.17: Example curves showing the consequence of various inhibition schemes on the resulting Michaelis-Menten kinetics. Competitive inhibition has the effect of increasing K_m and shifting the curve to the right, although the maximum reaction velocity (the asymptote of the expression) does not change. Incompetitive inhibition, by contrast, reduces the V_m of the enzyme while leaving K_m unchanged. Non-competitive inhibition has the effect of decreasing both the K_m and V_m.

Limitations of ODE Biological Models

It is important to clarify a few limitations of the ODE methods presented above (Ahn, Tewari, Poon, & Phillips, 2006; Kahlem et al., 2011). They often demonstrate a lot more promise than statistical models, providing predictions which are mechanistically driven. While this is enticing, they often require obtaining a tremendous number of parameters

from the literature. In the analysis of the Mitogen Activated Protein Kinase cascade alone, for example, there were 12 parameters. In requiring the accurate quantification of parameters, they are often difficult to validate. Additionally, in cases where parameter values cannot be obtained from the literature, they are tuned either by least-squares or using probabilistic techniques like Bayesian Inference.

Other biological models exist, like agent-based modelling or stochastic methods; but they do not provide the same intuitive modular structure contained in an ODE model. These ODE models provide an avenue of analyzing the response of biological systems to novel perturbations through classical stability analysis. In some cases, they even provide analogies into control theory. For instance, the response of the MAPK-cascade is similar to that of a switch, an easy analogy that can be made to control theory.

2.7 Summary

In basic terms, tissues experience damage when an applied load exceeds their tolerance. Assuming the tolerance is related to the number of collagen fibrils in the tissue, then the rate of change of the tissue tolerance is related to the interaction between three rates: synthesis, catabolism and mechanical disruption of collagen fibrils. This review sought to review the current understanding of each of these three characteristics.

The mechanical response of soft tissue to loading presents as three distinct phases. At first, as the collagen fibres begin to uncrimp, there is a toe region. Once all the fibres become uncrimped, the tissue's stiffness becomes constant, and the force-deflection curves enter a linear region. Finally, the fibres begin to rupture as they are stretched beyond their limits, heralding the failure portion of the curve. Once ruptured, these structures can no longer support force, reducing the tolerance of the tissue. The whole tissue tolerance is an emergent property stemming from the tolerances of all of the constituent fibrils. Plastic deformations in each of these structures tend to be a complex phenomenon, with the fibrils first developing distinct regions of discrete plasticity before complete rupture.

Both synthesis and catabolism are physiological events that depend on the expression

and translation of proteins like collagen, proteinases, and their inhibitors. After translation, three pro-collagen molecules are interwoven in the cytoplasmic reticulum before being extruded into the extracellular space where they integrate with the pre-existing fibril network. The telopeptides on the pro-collagen molecule are cleaved by proteinases. Cross-links are established by binding molecules, like sugars or other proteins, to the hydroxylysine residues on the collagen molecule. Catabolism may occur downstream of an inflammatory response and is carried out by matrix metalloproteinases, which selectively cleave collagen species.

Understanding each of these components is crucial for describing the adaptation of biological tissues to an applied load, and reductionist investigations have been tremendously productive in elucidating these mechanisms. However, it is still unclear how the whole system may behave to applied mechanical loads or if a rampant feedforward loop could develop in a living organ. Therefore, this thesis aims to fill this substantive gap by exploring the physiological response to an applied mechanical load and piecing these elements together in a cohesive mathematical model.

Chapter 3

Study I: Collagen Failure and Strain Rate

3.1 Introduction

The accuracy of large-scale biomechanical models is intrinsically tied to how they represent their constituent soft tissues. Historically, phenomenological models of soft tissue force-elongation, or stress-strain, curves have successfully described the properties of those tissues when operating within the toe and linear regions (Mattucci et al., 2012; Fratzl, 2008; Yoganandan et al., 2000; Troyer et al., 2012). These types of models, when coupled with quasi-linear viscoelastic (QLV) theory (Fung, 1967, 1977, 1981), form the backbone of soft tissue models used throughout biomechanics. They have been tremendously successful inside their domain of application; however, this treatment typically ignores the failure portion of the curve, which may be critical for injury prediction.

The failure portion of a soft tissue's force-elongation curve can be mathematically reproduced using a more mechanistic paradigm. This can be achieved by modelling an entire population of collagen fibrils as they uncrimp and are eventually strained to failure (Viidik, 1973; Liao & Belkoff, 1999; Bontempi, 2009). However, keeping track of potentially trillions of collagen fibrils in a macroscopic biomechanical model is computationally

prohibitive. Nevertheless, this can be accelerated, considerably, by following the rate of change of the distribution of strain among the collagen fibrils (Barrett & Callaghan, 2017; Bevan et al., 2018; Hamedzadeh, Gasser, & Federico, 2018).

From one perspective, ignoring the formation of new collagen fibrils and enzymatic degradation, the time-evolution of this distribution obeys a transport equation akin to the Huxley Muscle Model:

$$\frac{\partial \rho}{\partial t} + v\frac{\partial \rho}{\partial s} = -\dot{D}(s, t, \rho) \tag{3.1}$$

Where $\rho(s, t)$ is the strain-distribution over the collagen fibrils in the model such that $\rho(s, t)\Delta s$ can be thought of as the proportion of collagen fibrils in the tissue stretched by amount s at time t; v is the strain rate; and $\dot{D}$ is the rate of damage accumulation, termed the damage function.

In this context, it is unclear what the form of the breaking function should be, or rather, what is supported by experimental evidence. The rate of failure tends to be sudden and traumatic, as evidenced by some investigations instantaneously removing fibrils if they strain beyond a certain threshold altogether (Hamedzadeh et al., 2018; Liao & Belkoff, 1999). We initially assumed the damage function to be a scaled Heaviside step function (Barrett & Callaghan, 2017), but the resulting stress-strain curves at one strain rate do not generalize to different strain rates. In particular, it fails to reproduce the observation that, when tendons or ligaments are strained to failure at different rates, their failure strain remains more-or-less consistent despite the failure stresses being wildly different (Noyes, DeLucas, & Torvik, 1974; Mattucci et al., 2012; Woo, Peterson, Ohland, Sites, & Danto, 1990; Ng, Chou, Lim, & Chong, 2004).

Tobolsky and Eyring (1943) proposed a model of the rate of polymer breaking based on statistical mechanics, which Ellis (1978) applied to the creep failure of rat tail tendons. The Tobolsky-Eyring rate equation takes the form:

$$-\frac{1}{N}\frac{\mathrm{d}N}{\mathrm{d}t} = w_0 \exp\left(-\frac{U_0 - \gamma_0\sigma}{k_B T}\right) \tag{3.2}$$

Where N is the number of bonds in a cross-section of the material, U_0 is the activation

energy (in kcal/mol) for the breakage of covalent bonds, k_B is the Boltzmann constant, T is the absolute temperature (in K), and σ is the applied stress (in Pa). The parameters, w_0 and γ_0, are called the collision parameters, which borrows terminology from the classic Arrhenius equation in chemistry (Laidler, 1984; Arrhenius, 1889). For Equation 3.1, the number of bonds in a given cross-section is proportional to $\rho(s,t)$, and the stress experienced by those fibrils is $\sigma = E_f s$, where E_f is the fibril's modulus of elasticity. Therefore, after grouping redundant constants, the Tobolsky-Eyring theory implies a breaking function of the form:

$$\dot{D}(s,t,\rho) = \alpha \exp(\beta s)\, \rho(s,t) \tag{3.3}$$

Where $\exp(x)$ is the exponential function, and α and β are parameters that alter its shape. Putting everything together, this investigation was focused on the behaviour of the model:

$$\frac{\partial \rho}{\partial t} + v\frac{\partial \rho}{\partial s} = -\alpha \exp(\beta s)\, \rho(s,t) \tag{3.4}$$

For the failure-strain to be consistent across different strain-rates requires that the damage function, $\dot{D}$ in Equation 3.3, accounts for the strain rate. The independence of failure strain on strain rate also implies that, in the failure portion of the force-deflection curve, the number of collagen fibrils broken per unit stretch is independent of strain rates. This observation provides the starting point for dimensional analysis. Since the units for $\dot{D}$ is in collagen fibrils per unit time we have:

$$[\dot{D}] = \frac{[\text{collagen}]}{[T]} = [\text{collagen}] \times \frac{1}{[T]} \tag{3.5}$$

Where $[\cdot]$ represents the 'units' of whatever quantity is inside: T for time and [collagen] for number of collagen fibrils. This expression implies that the breaking function may be the product of collagen content and strain rate, which has units $\frac{1}{[T]}$. Therefore, we conclude that:

$$\dot{D} \propto v, \qquad \text{for } v > 0 \tag{3.6}$$

In other words, requiring that $\dot{D}$ is proportional to strain rate gives a sufficient condition for failure strain to be independent of strain rate. Therefore, the purpose of this investigation was to test the hypothesis that this proportionality would hold true under experimental conditions.

3.1.1 Specific Hypothesis

The breaking function is described by two parameters, α and β, where only α is in direct proportion. Both of these parameters can be quantified from a failure test using least-squares. Therefore, if the hypothesis is true, straining isolated rat tail tendon samples to failure at different rates would result in the parameter α, and not β, being proportional to the strain rate (Figure 3.1).

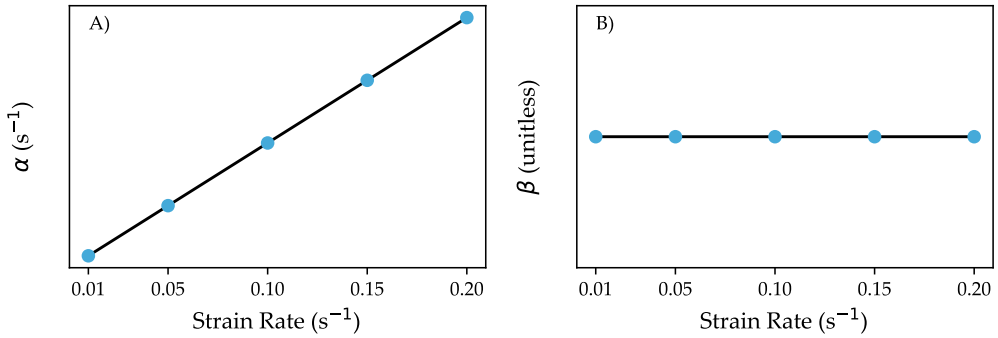

Figure 3.1: Hypothesis based on the dimensional analysis of a Tobolsky-Eyring rate equation and the independence of failure strain on strain rate. In (A) the parameter α, which the breaking function is directly proportional to, is expected to exhibit the proportionality with strain rate, whereas β, is not, as can be seen in (B).

3.2 Methods

Experimental Design

Fifty small longitudinal sections (length approximately 5 mm) of the extrinsic tendon between caudal vertebrae 1 and 10 were harvested from a single Sprague-Dawley rat (mass:

393.5 g; age: between 6 and 12 months). They were mounted along a single axis in a biaxial biological material testing system (BioTester, CellScale, Waterloo, Ontario), secured with stainless steel clamps lined with friction tape (Figure 3.2). The clamps were secured with a single M4 screw, which was tightened, by a torque wrench to 13.6 Nm for each specimen. Immediately post-mounting, specimens underwent a cyclic pre-condition test, consisting of a 1 Hz sinusoidal strain to 10% for 20 cycles (Bass et al., 2007), prior to failure tests. During the failure tests, specimens were elongated at one of five rates—0.01, 0.05, 0.10, 0.15, or 0.20 s^{-1}—to 300% strain which guaranteed failure. Force and displacement were continuously sampled at 100 Hz, and normalized to nominal stress and engineering strain post-collection. All specimens spent less than 4 h in 0.9% normal saline between harvesting and mechanical tests.

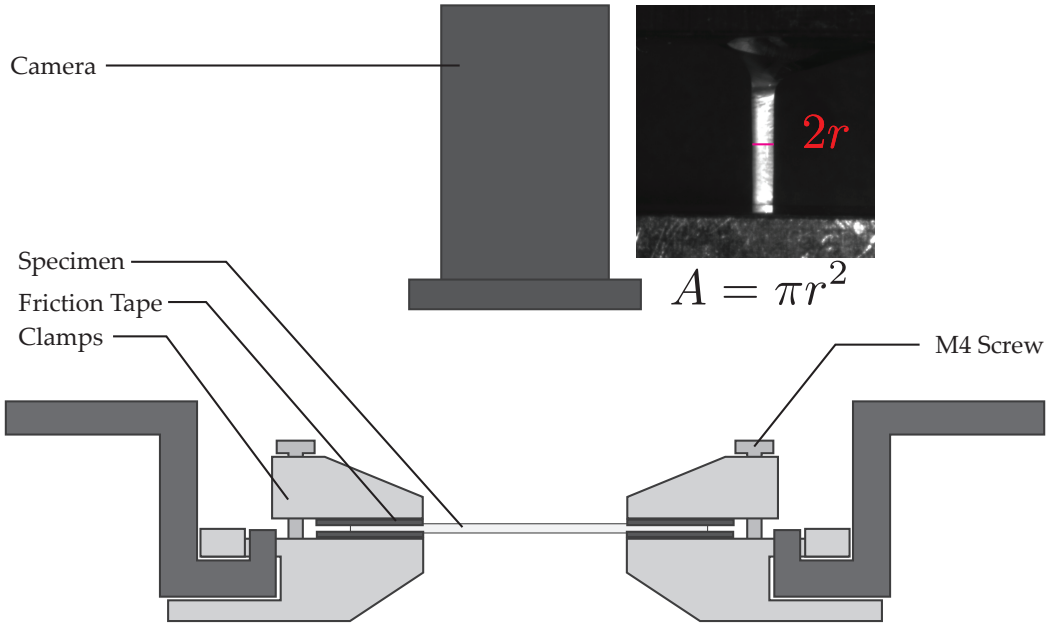

Figure 3.2: Uni-axial stress-strain test for this experiment. The CellScale clamps held the specimen at a gauge-length of 3500 μm while a top-down mounted camera sampled the failure tests. The cross-sectional area was estimated assuming a circular cross-section along with diameter measurements on the initial image.

Specimen cross-sectional areas were estimated from a top-down mounted camera. Images from the camera were calibrated using the 3500 μm gauge length to convert between pixels and width. The width was divided by two and the cross-sectional area was calcu-

lated assuming a circular cross-section. Using these quantities, force and deflection were normalized to nominal stress and engineering strain for subsequent model fitting.

Model Fitting

Since Equation 3.4 is a differential equation, its solution depends on specifying initial conditions. This was assumed to be a Gaussian distribution with mean μ and standard deviation η, which can be obtained from the toe and linear portions of the measured stress-strain curve along with E, the effective modulus of elasticity in the linear region (Barrett & Callaghan, 2018). The stress at a given time can then be calculated as:

$$\text{stress}(t) = E \int_0^\infty s\rho(s,t)\,\mathrm{d}s \tag{3.7}$$

The breaking function parameters, α and β, were then found by least-squares minimization between the predicted and measured stress using the `minimize` function in the `scipy` Python package (Virtanen et al., 2020). During this procedure, Equation 3.4 was numerically solved using the method of moments (Zahalak & Ma, 1990; Barrett & Callaghan, 2021), which reduces its complexity to a system of three ODEs. These equations were then integrated using the `odeint` function in `scipy` and the squared error between predicted and measured stresses were evaluated. A sample fit is shown in Figure 3.3. The overall root-mean-squared error (RMSE) was also calculated.

3.2.1 Data Reduction & Statistics

Dependent Variables

The two main dependent variables in this investigation were the breaking function parameters, α and β; although the other model parameters, like μ, η, and E were also calculated, but not used for subsequent statistical analysis. In addition, experimental measures like

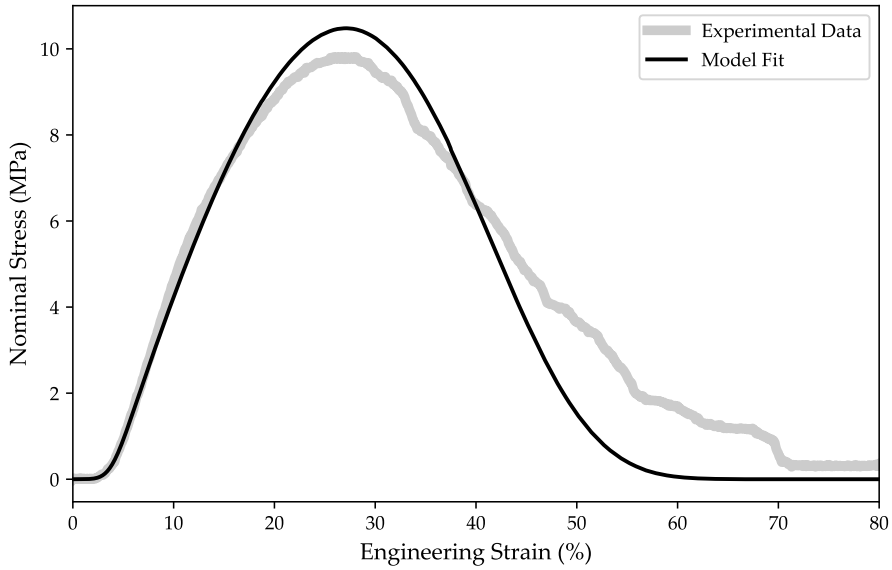

Figure 3.3: A typical model fit for this investigation with an RMSE was 0.89 MPa, slightly higher than the average RMSE of 0.79 MPa.

the ultimate tensile stress, strain at peak stress, peak force, and cross-sectional areas, were also evaluated for descriptive statistics.

Justification of Statistical Model

The main hypothesis here is that α will be proportional to the strain rate, while β is not. Both of these hypotheses can be addressed with simple linear regression. For this investigation, Bayesian Linear Regression was used, which required specifying any prior information that was known about α and β. Since little was known about them, relatively flat, or uninformed priors were used, which correspond with what Pierre Simon Laplace would call the Principle of Indifference (Jaynes, 1968).

Specifying model assumptions and prior distributions is a standard procedure in Bayesian inference, which is used extensively throughout this thesis. Nevertheless, the author has assigned a high prior probability that the reader is more familiar with Frequentist meth-

ods, so a little more detail is included for the first investigation. The interested reader is directed to McElreath (2020) for an accessible, yet comprehensive, introduction to the subject; or Gelman, Carlin, Stern, and Rubin (1995) for a more advanced treatment. The general procedure goes as follows:

1. State prior distributions of model parameters.
2. Use the data, along with Bayes' Theorem, to update those distributions in light of data.
3. Analyze the posterior distributions to make inferences.

We expect that the average magnitude of α will depend linearly on the strain rate, v, and that its measurement is associated with some error, σ. A common assumption, for both Bayesians and Frequentists, is that the error will be scattered around the average according to a Normal distribution. Written in probability notation:

$$\alpha \sim \text{Normal}(mv + b, \sigma)$$

Here the $\sim$ notation can be read 'distributed as,' so the first line states that α is a normally distributed random variable, whose mean is the regression line, $mv + b$, and whose standard deviation is σ. In a typical Frequentist analysis, as per the Null Hypothesis, m and b would be provisionally assigned no magnitude. Then, the probability of observing their magnitudes (or more extreme) would be calculated. If their measured magnitudes are unlikely under the Null, based on some *a priori* threshold, then that hypothesis is rejected. In a Bayesian analysis, rather than proposing a specific magnitude of m and b, they are assigned prior distributions which cover a wide range of hypotheses. Then, Bayes' Theorem is used to calculate which magnitudes of m and b are most likely given the observations. Since not much is known about them, using wide, or indifferent, priors are commonplace. Thus, the model that we are building now contains distributions for these

other parameters:

$$\begin{aligned}
\alpha &\sim \text{Normal}(mv + b, \sigma) \\
m &\sim \text{Normal}(0, 1) \\
b &\sim \text{Normal}(0, 1) \\
\sigma &\sim \text{Exponential}(1)
\end{aligned}$$

Now we have added that the parameters, m and b are also distributed according to a standard normal distribution. To aid in the fitting process, the dependent and independent variables are often 'standardized' (*i.e.* converted to z-scores) to facilitate stating priors like this. With respect to standardized magnitudes, a standard normal distribution contains relatively little information. We have also chosen to model σ according to an Exponential Distribution. This is simply because an Exponentially distributed random variable cannot be negative, which matches with the intuition that standard deviations are also non-negative.

These priors can be entered directly into a probabilistic programming language, which, for this thesis, will universally be the `PyMC3` Python package (Salvatier, Wiecki, & Fonnesbeck, 2016). Once provided with the observed data, the program updates the parameter distributions in light of these observations using Bayes' Theorem. This is commonly called calculating the posterior distribution, and it is the major conceptual difference between Bayesian and Frequentist inference: for Bayesians, the model parameters have a distribution (McLevey, 2021; McElreath, 2020).

The final caveat comes from the author's experience with α, and β, and has little to do with Bayesian Inference. These are parameters of an exponential model found by least-squares fitting to a differential equation. This least-squares procedure requires evaluating numeric gradients, and the behaviour of the differential equation, and thus the optimizer, can be very sensitive to their magnitudes. Thus, to allow for some more extreme parameter values, a Student's t Distribution with 5 degrees of freedom was used instead, whose wider tails are more forgiving of potential outliers. In the parlance of machine learning and data science, this is sometimes called 'Robust Linear Regression' due to its ability to improve

model performance in cross-validation studies (Lange, Little, & Taylor, 1989).

Hence, without further ado, the full statement of the statistical model for α was the following:

$$\alpha \sim \text{Student's } t_{\nu=5}\ (m_0 v + b_0, \sigma_0) \tag{3.8a}$$
$$m_0 \sim \text{Normal}(0, 1) \tag{3.8b}$$
$$b_0 \sim \text{Normal}(0, 1) \tag{3.8c}$$
$$\sigma_0 \sim \text{Exponential}(1) \tag{3.8d}$$

The model for β was essentially the same:

$$\beta \sim \text{Student's } t_{\nu=5}\ (m_1 v + b_1, \sigma_1) \tag{3.9a}$$
$$m_1 \sim \text{Normal}(0, 1) \tag{3.9b}$$
$$b_1 \sim \text{Normal}(0, 1) \tag{3.9c}$$
$$\sigma_1 \sim \text{Exponential}(1) \tag{3.9d}$$

Here we have indexed the parameters for the α parameter with 0, and the β model with 1. As previously mentioned, both models were fit using the `PyMC3` package in Python (Salvatier et al., 2016), with the No-U Turn Sampler (NUTS), which sampled the posterior distribution using a Hamiltonian Monte Carlo (HMC) method. Four trace chains were collected, each composed of 1000 tuning samples, and 2000 true samples. Typical diagnostics for the quality of the statistical fit were the effective number of samples collected from the traces, the Monte-Carlo Standard Error (MCSE) average and standard deviation, and the $\hat{r}$-statistic. The $\hat{r}$ statistic is the ratio of variance within a given chain with the between-chain variance. If the chains were independent and drawn from the same portion of the posterior distribution, this $\hat{r}$ will be close to unity. Since the converse of this statement does not hold, it was necessary to evaluate the trace-plots (parameter-magnitude versus sample number) to ensure that the posterior distributions had successfully converged.

Parameter statistics were evaluated from the resulting posterior distributions. This included their mean and standard deviation magnitudes, in addition to a 97% highest-

density interval (HDI). The 97% HDI is the narrowest interval which covers 97% of the probability mass in a given probability distribution. This gives a (typically asymmetric) interval which has the specified coverage probability, often called a credible interval to distinguish it from a Frequentist confidence interval (McElreath, 2020).

3.3 Results

There was considerable variability in the stress-strain curves, even within each rate condition (Figure 3.4). The parameters α and β were successfully computed for all specimens, with RMSEs that varied from 0.1 to 7.9 MPa, with an average of 0.8 MPa (Table 3.1). Moduli of elasticity were 94.0 (46.9) MPa, with an average failure stress of 14.9 (6.4) MPa. There was considerable variability throughout the obtained stress-strain (and force-deflection) curves in this experiment, but no experimental outcome seemed to vary dramatically with the strain rate (Table 3.1).

The variation between specimens also manifested in variability in the resulting model parameters, like E, μ, η, and β whose standard deviations were around 50% of their average values (coefficient of variation). By contrast, the collision parameter, α, exhibited a higher degree of variation, which reflects the variability of the failure portion of the stress-strain curves observed.

Table 3.1: Descriptive statistics for the all outcome measures in this investigation. Outcome measures are separated based on whether they were model parameters obtained through least-squares, or directly obtained from the experimental data. Units are given for each row as well. *Note that for the mean and standard deviation initial strains, magnitudes are provided in per mille rather than percent.*

Parameter	**Mean value (standard deviation)**				
Rate (s^{-1})	**0.01**	**0.05**	**0.10**	**0.15**	**0.20**
Model Parameters					
Effective Modulus (E) (MPa)	80.5 (32.4)	97.8 (59.4)	96.5 (52.8)	87.7 (34.1)	108.0 (44.9)
Standard Deviation (η) (‰)	9.1 (4.0)	8.4 (4.7)	10.0 (6.1)	10.6 (5.1)	12.5 (4.4)
Mean Initial Strain (μ) (‰)	36.2 (13.1)	65.6 (12.1)	59.2 (17.7)	74.8 (33.5)	80.2 (52.9)
Collision Parameter (α) (ms^{-1})	14.3 (26.4)	19.5 (13.5)	46.9 (28.3)	68.1 (53.6)	139.1 (83.6)
Exponential Parameter (β) (unitless)	9.4 (3.7)	11.1 (7.1)	10.7 (6.1)	10.3 (4.0)	10.2 (4.9)
Experimental Measures					
Ultimate Tensile Stress (MPa)	11.9 (4.1)	16.2 (7.0)	15.8 (7.7)	14.9 (5.5)	16.0 (6.3)
Strain at Peak Stress (%)	28.9 (6.8)	34.4 (11.0)	31.5 (7.0)	36.0 (7.9)	30.7 (9.6)
Area (mm^2)	0.41 (0.23)	0.46 (0.43)	0.48 (0.26)	0.41 (0.29)	0.47 (0.44)
Peak Force (N)	4.0 (1.2)	5.1 (1.6)	5.9 (2.0)	4.8 (2.4)	5.8 (3.3)

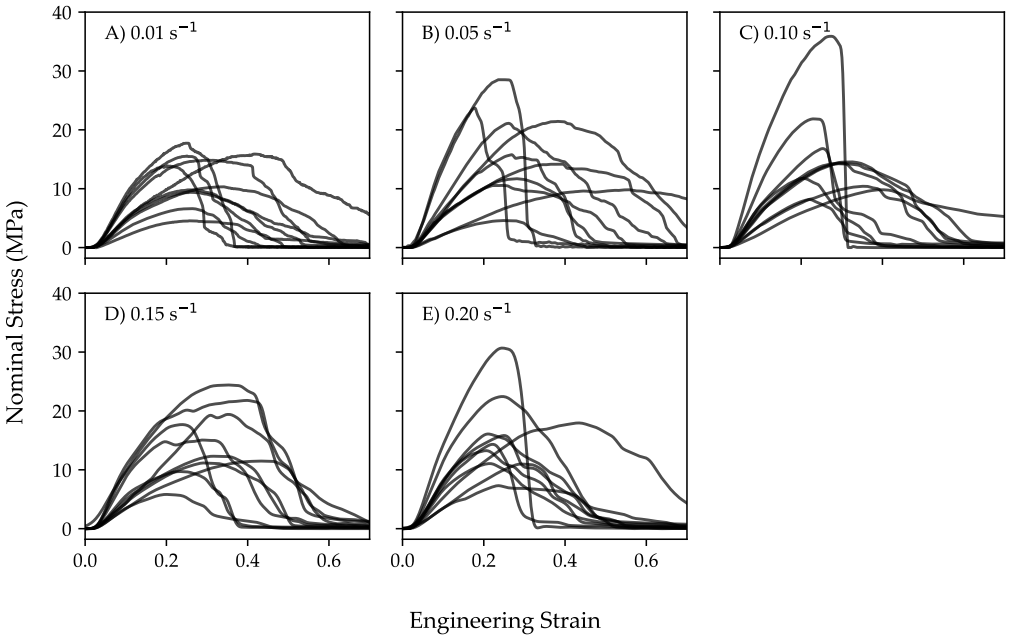

Figure 3.4: Resulting stress-strain curves for all strain rates in this investigation, starting from (A) at 0.01 s^{-1}, then (B) 0.05, (C) 0.10, (D) 0.15, and (E) 0.20 s^{-1}. There was considerable variability over all five conditions, which is also reflected in the failure parameters recorded.

The statistical models were able to successfully converge to a stable posterior distribution, as evidenced by high effective sample sizes, $\hat{r}$ magnitudes close to 1, low MCSE, and excellent trace plots, which are included in Appendix A.1. The plots of damage parameters against strain rate were highly suggestive that α exhibited some proportionality with strain rate, whereas β did not (Figure 3.5). The resulting regressions look remarkably similar to Figure 3.1.

There are a few inferences that can be drawn from the resulting statistical analysis. The first is that the notion of proportionality between α and the strain rate is very consistent with the statistical model: m_0 was never less than zero for any sample in the traces. This can also be seen graphically by the apparent positive slope in α versus the strain rate (Figure 3.5A). Further, there was strong evidence that the intercept can be treated as zero, as its posterior probability distribution was closely centred on zero. In fact, a model that omitted it exhibited a better Watanabe–Akaike information criterion (WAIC) of 75.4

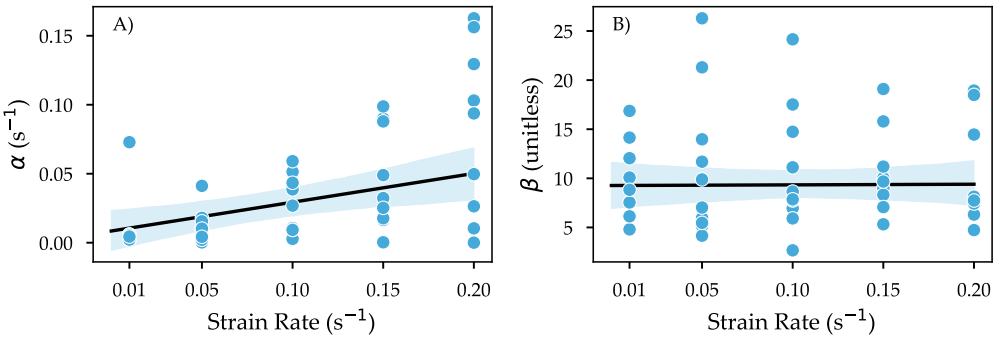

Figure 3.5: Results of the regression analysis for both breaking function parameters for (A) α and (B) β against strain rate. Points on the scatterplot represent observed magnitudes, the solid curve is the average regression line, and the shaded region is a 97% credible interval for the regression line. The scatter-plots are highly suggestive that α is more sensitive to strain rate than β is. The variability in estimates is also apparent on these plots, which is a combination of the variability observed in the measured stress-strain plots along with the sensitivity of the optimization routine.

versus 74.8.

Table 3.2: Results from the Hamiltonian Monte Carlo simulation for both α and β.

Parameter	**Mean (SD)**	**97% HDI**
α *Model*		
Intercept (b_0)	0.00 (0.01)	(-0.03, 0.02)
Slope (m_0)	0.57 (0.13)	(0.30, 0.84)
Standard Deviation (σ_0)	0.04 (0.01)	(0.03, 0.06)
β *Model*		
Intercept (b_1)	9.19 (1.08)	(6.77, 11.46)
Slope (m_1)	1.16 (8.30)	(-16.94, 19.27)
Standard Deviation (σ_1)	3.86 (0.47)	(2.90, 4.94)

The evidence was not nearly as strong for β being proportional to the strain rate, the probability mass for m_1 was roughly symmetric about zero, with only a slight positive shift. Like the intercept in the α-model, a model omitting the proportionality slope also had a slightly better WAIC: -156.2 versus -156.9. Indeed, the average positive slope is barely perceptible on the resulting plot (Figure 3.5B).

3.4 Discussion

This investigation found evidence that a collagen fibril recruitment model, combined with a Tobolsky-Eyring rate equation, yields biofidelic simulations of rupture for isolated rat tail tendon specimens. This analysis combined *in vitro* methods with a detailed *in silico* computational model, and found that, at least in the context of the tested model, the rate of damage accumulation is likely proportional to strain rate.

The measured failure stress, strain at peak stress, and Young's modulus in this investigation are slightly lower in magnitude than previous investigations. Haut (1983), for example, showed that the failure stress of rat-tail tendon specimens increased almost two-fold from 61 MPa to 108 MPa between lengthening velocities of 0.7 mm/s and 140 mm/s. On the other hand, Kato et al. (1989) found that rat tail tendon samples portrayed an ultimate tensile stress around 35 MPa, and a modulus of elasticity around 550 MPa—and neither substantially varied with strain rate. For comparison, failure stresses in this investigation were 14.9 (6.5) MPa, with moduli of elasticity around 94.0 (46.9) MPa. Differences may be accountable in terms of differences in cross-sectional area measurements, as the failure forces reported here are not much different from Haut (1983): 5.1 (2.3) N here versus 6 N.

Modelling the collagen fibril strain distribution among soft tissues may provide a fruitful avenue for quantifying their failure properties. Equipped with more comprehensive models of tendon damage and rupture, macroscopic biomechanical models may be able to improve their prediction of injury initiation in these tissues. In addition, similar principles may also apply to other soft tissues, like ligaments (Liao & Belkoff, 1999; Viidik, 1973) or vascular tissue (Bevan et al., 2018). Indeed, previous rheological models which have explicitly modelled the strain among a population of collagen fibrils have treated them as brittle materials which fracture when stretched beyond a prescribed threshold (Bontempi, 2009; Hamedzadeh et al., 2018; Liao & Belkoff, 1999). One advantage of this treatment is that it side-steps the breaking function entirely and at a seemingly little cost to model accuracy—at least in traumatic situations. This is also justifiable from a separation of timescales argument: the timescale of a collagen fibril rupture occurs on a much faster

timescale than the kinematics of human movement. Equivalently, if the breaking function is considered zero below a given threshold, this amounts to a quasi-steady state approximation to Equation 3.4. In situations where the rate of damage accumulation may be on a similar timescale to the movement, such as a cumulative loading scenario, modelling the accumulation of damage using the current model may be better justified. This topic is explored later on in **Study IV** (Chapter 6).

There was considerable variability in the breaking function parameters, α and β, as evidenced by Figure 3.5. This poses a considerable challenge for future modelling, especially since average magnitudes are usually assigned in macroscopic biomechanical models. However, it is equally important to acknowledge the variability observed in the *in vitro* failure data themselves (Figure 3.4). Other mechanical tests of ligamentous failure (Mattucci et al., 2012; Quinn & Winkelstein, 2007; Bass et al., 2007) have observed a similar variability in this region of the stress-strain curve, which suggests that the chaotic behaviour in this region is typical. It may be the case that traumatic failure is "predictably unpredictable," by its very nature, and that embracing the variability with Monte Carlo methods may be warranted.

The most substantial limitation of the current model is that it assumes that the soft tissue is only composed of one type of constituent: type I collagen. While type I collagen composes 65-80% of the dry mass of tendons (Kannus, 2000), the other constituents, like elastins, proteoglycans or glycosaminoglycans, are also contributing elements to the mechanical response of these tissues. In particular, there is good evidence to suggest that the viscous behaviour of connective tissues arises, predominantly, from these other matrix components (Karunaratne, Li, & Bull, 2018; Puxkandl et al., 2002). X-ray diffraction experiments, for instance, have demonstrated that the collagen fibrils only experience between 20-40% of the total macroscopic strain, with most viscoelastic deformations occurring not in the collagen fibrils themselves (Fratzl et al., 1998; Puxkandl et al., 2002). This observation directly conflicts with the model, which assumes that all fibrils experience the same strain rate equivalent to the macroscopic strain rate.

3.5 Conclusions

An exponential breaking function is supported by both statistical mechanics theory and empirical evidence. Overall this takes the form:

$$\dot{D}(s,t,\rho) = \alpha v \exp(\beta s)\, \rho(s,t) \text{ for } v > 0 \tag{3.10}$$

Where, for isolated rat tail tendon specimens, α is likely between 0.30 and 0.81 with an average of 0.57, and β is between 7.9 and 10.7 with an average of 9.3.

3.6 Toward Study II

The major goal of Study I is to empirically determine a form for the breakage of collagen depending on strain rate. This directly achieves part of one of the goals of this thesis: to determine the breakage properties of collagen fibrils.

Chapter 4

Study II: Collagen Catabolism and Strain

4.1 Introduction

The mobilization of the innate immune system to a site of injury is a fundamental process in the connective tissues (Liu, Smith, Zhang, Burns, & Li, 2012; Eming, Krieg, & Davidson, 2007). The infiltrated macrophages and neutrophils, along with the resident fibroblasts of the tissue, respond to damaged ECM components by secreting inflammatory cytokines (Abe et al., 2007; Peng et al., 2006; Wiet et al., 2017; Burke et al., 2002; Arroyo & Iruela-Arispe, 2010). These cytokines can in turn lead to the increased gene expression of Matrix Metalloproteinase (MMP), which break down collagen fibres (Vo et al., 2013; Johnson, Schoepflin, Choi, Shapiro, & Risbud, 2015). The response of resident fibroblasts to secrete enzymes that break down collagen molecules seems counter-intuitive. If the fibroblast is aiming to produce collagen fibres to replace the damaged ones, why also risk the destruction of the new filaments? This universal response to injury would only be useful if the MMPs were selective in the collagen fibrils they removed.

It has been observed that mechanical strain can inhibit the action of bacterial collagenases. Nabeshima, Grood, Sakurai, and Herman (1996) immersed rabbit patellar

tendon samples in a solution containing collagenase from *Clostridium histolyticum* (*C. histolyticum*) for 20 hours, and found that samples that were held taut retained more than 95% of their ultimate tensile strength compared to controlled samples. Ruberti and Hallab (2005) developed a collagen gel consisting of layers of collagen sheets, such that each layer was oriented orthogonal to its neighbours. When these gels were held in a uni-axial strain test aligned with half the collagen in the sample, only those in the orthogonal direction were selectively cleaved by collagenase. Other studies have verified that mechanical strain has been shown to protect isolated collagen fibrils from collagenase cleavage (Ruberti & Hallab, 2005; Flynn et al., 2010; Camp et al., 2011; Chang, Flynn, Ruberti, & Buehler, 2012), which seems to scale to the whole tissue (Camp et al., 2011; Nabeshima et al., 1996; Saini, Cho, Dooling, & Discher, 2020). This body of work suggests that exposure to mechanical strain may be a protective mechanism for essential fibrils.

The toe region in a soft tissue's force-deflection curve arises from the sequential engagement of collagen fibrils as the tissue is strained (Fratzl et al., 1998). In addition, from a theoretical perspective, the instantaneous stiffness in the toe region is reflective of the proportion of collagen fibrils which have been engaged (Barrett & Callaghan, 2017). This would suggest that loading tissue samples into various points of the toe region may provide the means of selectively tuning what proportion of collagen fibrils are in a crimped state. If only those fibrils which are crimped are susceptible to enzymatic cleavage by collagenases, then an applied load corresponding to a specific proportion of collagen being uncrimped would also inhibit the collagenase by that magnitude.

Therefore, the objectives of this project are twofold. The first major objective is to develop a quantitative model for how enzymatic cleavage of collagen occurs, and how that cleavage is affected by the degree of strain in the fibrils. The second is to test whether the strain-inhibition of collagenases is consistent with the established biomechanical mechanism of gradual collagen fibril engagement within the toe region.

4.1.1 Specific Hypothesis

The specific hypothesis for this investigation comes from analyzing the partial differential equation model which describes how a strain distribution among a population of collagen fibrils evolves over time. If we let $\rho(x,t)$ denote the instantaneous distribution of strain among the constituent collagen fibrils, then its time evolution is governed by the transport equation:

$$\frac{\partial \rho}{\partial t} + v\frac{\partial \rho}{\partial x} = -\frac{V_{\max}\kappa(x)\rho(x,t)}{K_m + \langle \kappa, \rho \rangle} - b(x,t)\rho(x,t) \tag{4.1}$$

Where we have defined the Michaelis-Menten parameters to be $V_{\max}$ and K_m, respectively, $\kappa(x)$ denotes the concentration of active binding (mM) sites per fibril as a function of displacement, and $b(x)$ denotes the breaking function. The first term on the right-hand side describes the loss of $\rho(x,t)$ resulting from enzymatic cleavage of collagen fibrils, whereas the second term describes the rate of collagen fibril failure as a function of fibril strain. Note that we have chosen to leave $\kappa(x)$ as a function of fibril strain, x, since we wish to directly test the hypothesis that enzymatic cleavage only occurs to fibrils that are crimped. Secondly, we have used the angled-brackets, $\langle \cdot, \cdot \rangle$, as shorthand notation for an "inner product", which, in this case, counts the total available binding sites among all of the collagen fibrils.

$$\langle \kappa, \rho \rangle = \int_{-\infty}^{\infty} \kappa(x)\rho(x,t)\,\mathrm{d}x \tag{4.2}$$

At an instant in time, if the soft tissue were to be loaded to failure, the stiffness would be given by:

$$k(t) = k_0 \int_{-\infty}^{\infty} \rho(x,t)\,\mathrm{d}x \tag{4.3}$$

Where k_0 is the stiffness of the virgin material—without any enzymatic cleavage or

mechanical disruption. Differentiating this and integrating, both with respect to time (between $0 \leq t \leq T$) gives:

$$k_T - k_0 = k_0 \int_0^T \int_{-\infty}^{\infty} \frac{\partial \rho}{\partial t} \, \mathrm{d}x \, \mathrm{d}t \tag{4.4}$$

This simplifies, somewhat, once the transport equation terms are substituted in for $\frac{\partial \rho}{\partial t}$. Further, bringing k_0 and k_T to the left-hand side of the equation, yields the model:

$$\frac{k_0 - k_T}{k_0} = \underbrace{\int_0^T \frac{V_{\max} \langle \kappa, \rho \rangle}{K_m + \langle \kappa, \rho \rangle} \, \mathrm{d}t}_{\substack{\text{Cumulative} \\ \text{Biochemical Degradation} \\ (C)}} + \underbrace{\int_0^T \langle b, \rho \rangle \, \mathrm{d}t}_{\substack{\text{Cumulative} \\ \text{Mechanical Disruption} \\ (M)}} \tag{4.5}$$

This defines a measurable outcome variable—the relative reduction in stiffness—as being composed of losses from biochemical (C) and mechanical (M) means. It is possible to quantify these two terms from simulations of a two-hour creep protocol where a prescribed proportion of collagen fibrils are engaged. These simulations predicted that if collagenase activity is inhibited by mechanical strain (*i.e.* $\kappa(x) = 0$ for $x > 0$), then the loss in stiffness decreases linearly with the proportion of crimped collagen fibrils. Conversely, when collagenase activity is unaffected by the magnitude of fibril strain (*i.e.* $\kappa(x)$ is constant for all values of x), then the magnitude of cumulative degradation is indifferent to the magnitude of strain until a threshold is met. At this point, the biochemical degradation is able to weaken the tissue's tolerance to the point where mechanical failure occurs in the middle of the creep protocol (Figure 4.1).

The results from this simulation (Figure 4.1) can be explained intuitively. If a tendon were held at a level of force corresponding to $p\%$ of the collagen population being uncrimped and exposed to collagenase over a long period of time; then, according to the strain inhibition hypothesis, $(1-p)\%$ of the collagen fibrils will be selectively cleaved by the

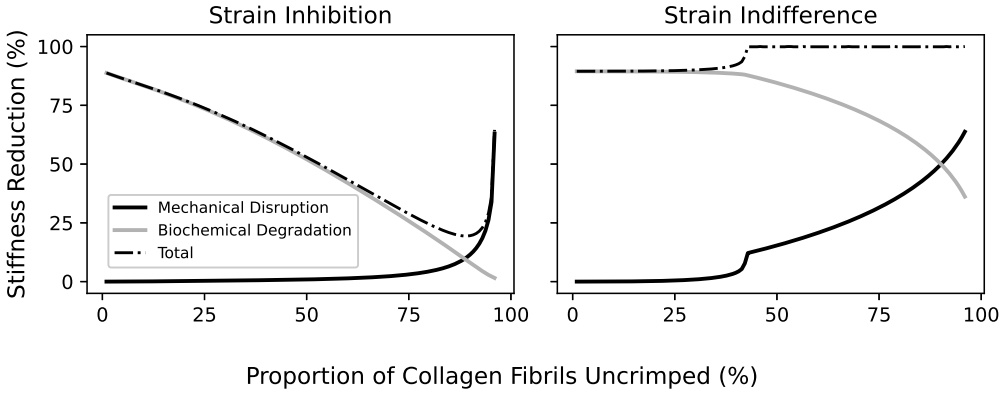

Figure 4.1: Computational model results demonstrating a potential relationship between the relative reduction in stiffness and collagen uncrimp percentage in the creep test. These tests either assume that the activity of collagenase is inhibited by mechanical strain in the fibrils (left) or strain indifference (right). This simulation used the unnormalized model with fourth order breaking function, $b(x) = b_4(x - x_0)^4$, $x_0 = 120.05$ μm, $b_4 = 1 \times 10^{-13}$ s^{-1}, and Michaelis-Menten dynamics for the enzymatic cleavage ($V_{\max} = 0.02$ mM s^{-1}, $K_m = 1$ mM).

enzyme. Therefore, we would expect a $(1 - p)\%$ reduction in the linear region stiffness of the tendon after exposure to collagenase, solely due to enzymatic degradation. Conversely, if collagenase is able to cleave collagen regardless of its level of strain, then one would expect a uniform reduction in stiffness across all levels of force. That is, until the enzyme degrades the tissue to the point where the applied load exceeds its tolerance. Beyond this point, the model expects there would be larger magnitudes of mechanical damage with increasing magnitudes of tissue strain.

4.2 Methods

4.2.1 Experimental Design

92 rat tail tendon specimens were obtained from three six-month old female rats (body mass: 298.2 - 350.4 g). The cross-sectional area of each specimen was measured with a 2D blue-laser profilometer (LJ-V7000 series, Keyence Company, Osaka, Japan). They were mounted for uni-axial strain tests on a biological materials testing system (Biotester, Cellscale, Waterloo, ON), held by stainless steel clamps and further secured by winding

them around a polylactic acid (PLA) hitch at a resting length of 3500 μm (Figure 4.2). Once mounted, specimens were immersed in a bath containing between 61 and 76 mL of isotonic Ringer's Solution (Table 4.1), heated to 37°C with a neutral pH of 7.0.

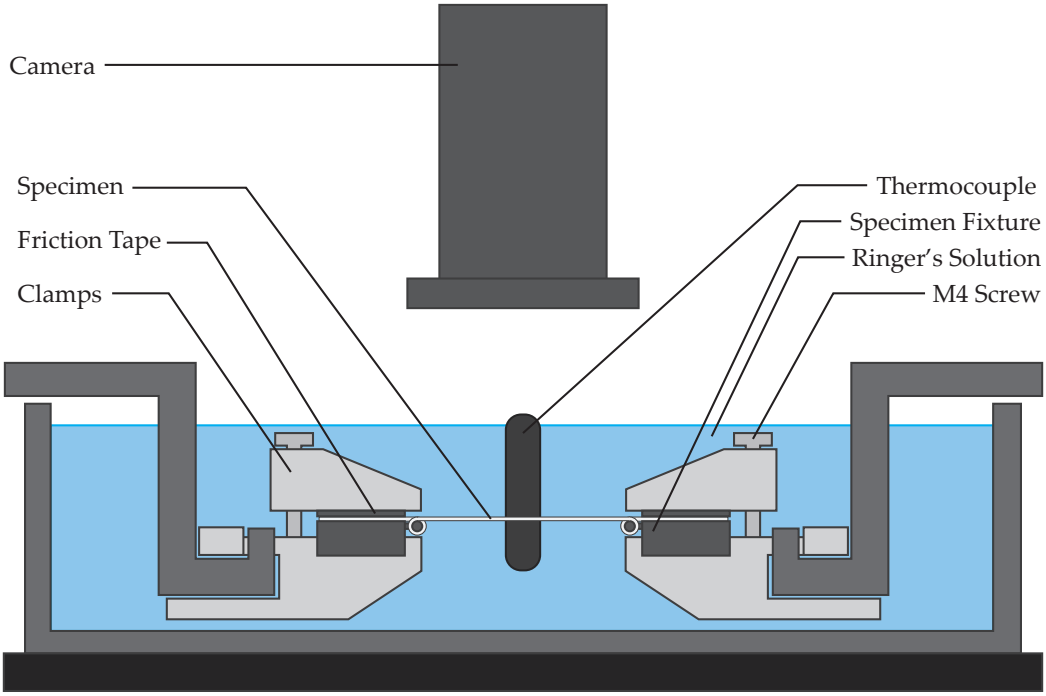

Figure 4.2: Experimental set-up for this study. The specimen was mounted along one axis of a biaxial tensile testing system, immersed in a temperature controlled bath atop a heated plate.

All specimens underwent pre-conditioning which consisted of 10 cycles of loading to 5 MPa, followed by 2 minutes and 30 seconds of rest, and terminated with a constant preload to 0.4 MPa. The length of each specimen under the 0.4 MPa preload was taken as its gauge length (Figure 4.3).

Following the pre-conditioning, specimens underwent three cycles of loading to 20 MPa, the last cycle of which was used to calculate preliminary fascicle stiffness (k) in the linear region, later normalized to modulus (Figure 4.4A). In addition, parameters corresponding to the average collagen fibril slack-length (μ) and standard deviation (η) were calculated. These parameters correspond to the assumed Gaussian distribution which is taken as the initial condition in the collagen distribution model and are used to relate the force sustained

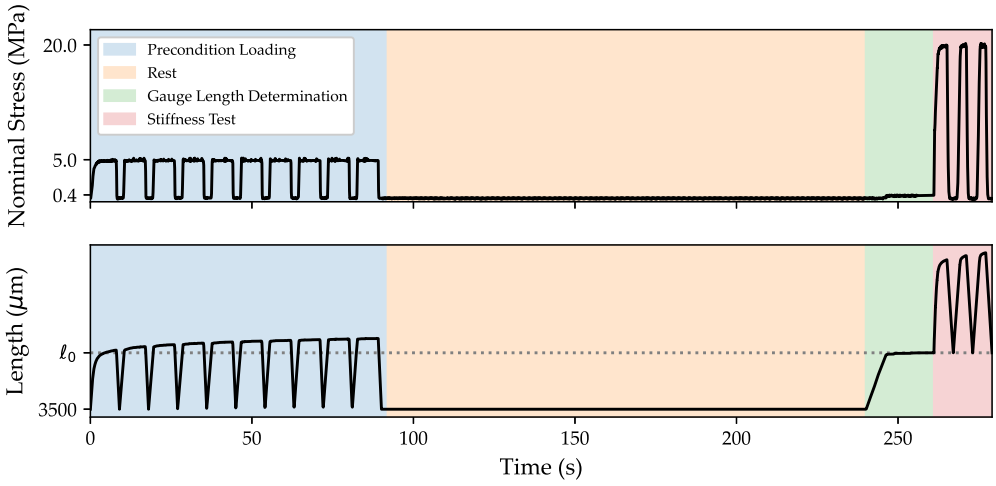

Figure 4.3: Example of the pre-conditioning used in this investigation. Specimens were initially mounted on the CellScale device at a fixed length of 3500 μm and immersed in a heated bath containing isotonic Ringer's solution, heated to 37°C. They then underwent preconditioning cycles (blue shaded region), where they completed ten cycles of loading to a nominal stress of 5 MPa. Following this, they rested at 3500 μm for 150 seconds, prior to gauge length determination, which was determined from the specimen length when held at 0.4 MPa. After this, they endured three cycles to 20 MPa, the last cycle of which was used for preliminary stiffness calculations.

by the specimen to the state of strain among the population of constituent collagen fibrils (Figure 4.4C).

Assuming that the strain distribution among the collagen fibrils follows a normal distribution with mean μ and standard deviation η, the displacement corresponding to $p\%$ collagen engagement can be calculated using:

$$z = \frac{x_p - \mu}{\eta} = \text{probit}(p) \qquad p \in (0, 1) \tag{4.6}$$

Where probit is the inverse of the normal distribution cumulative distribution function and x_p is the stain corresponding to $p\%$ of collagen fibrils being engaged. This strain can then be input into the ILS to solve for the corresponding level of force.

$$F(p) = k\eta \left(\frac{1}{\sqrt{2\pi}} \exp\left(-\frac{z^2}{2} \right) + zp \right) \tag{4.7}$$

Where $F(p)$ is the force-magnitude that corresponds to $p\%$ of collagen fibrils being in an

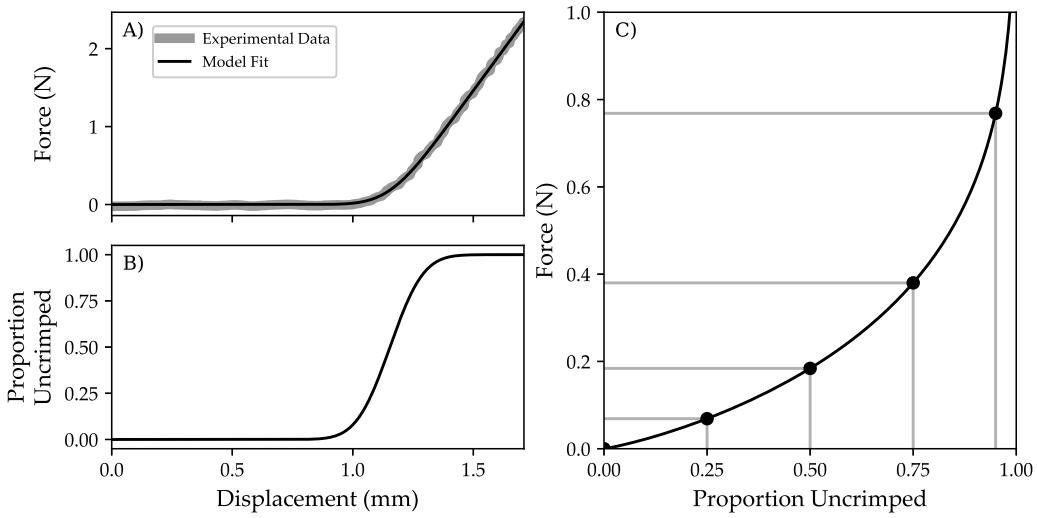

Figure 4.4: (A) Sample stiffness evaluation for this investigation. The last loading cycle to 20 MPa is isolated and used to tune the parameters for a collagen distribution model. The output of this model is a Gaussian distribution, which describes the proportion of uncrimped collagen fibrils as a function of displacement (B). This cumulative distribution is then plotted against the applied force (C), which is then used to calculate levels of force that correspond to specific proportions of uncrimp among the collagen fibrils. The corresponding algebraic process is described in the text.

uncrimped state. Unfortunately, this function is not defined when $p = 1$, so $p = 0.95$ was taken as a magnitude which represented 100% fibril uncrimp.

Specimens were separated into five groups, represented by these aforementioned approximated uncrimped levels: 0%, 25%, 50%, 75% and 100%. For the duration of testing, they remained submerged in Ringer's solution, with a small concentration of microbial Collagenase D (from *C. histolyticum*, EC 3.4.24.23, Sigma Aldrich catalog number: 11088866001) and held under constant tension analogous to a creep test for two hours (Barbir, Michalek, Abbott, & Iatridis, 2010). The chosen activity of Collagenase D (0.054 U/mL) was selected to digest approximately 95% of the collagen molecules in the 0% uncrimped condition over the course of two-hours. Briefly, the activity of the lipolized Collagenase D provided was 0.27 U/mg, as determined from the Wünsch collagenase assay (Wünsch & Heidrich, 1963). The number of collagen molecules in the rat tail tendon specimens was estimated using the Hulmes-Miller quasi-hexagonal axial packing structure of collagen molecules in a wet rat tail tendon (Lees, Pineri, & Escoubes, 1984; Hulmes & Miller, 1979), the Hodge-Petruska longitudinal packing model (Petruska & Hodge, 1964), and assuming a cylindrical tendon

geometry of length 3500 μm and 500 μm radius (Appendix B). Pilot specimens were used to confirm the expected loss in stiffness in the 0% condition.

Table 4.1: Concentration of molecular species in the Ringer's Solution. These molar concentrations were calculated from mass-concentrations of calcium chloride (0.48 g/L), potassium chloride (0.42 g/L), sodium bicarbonate (0.2 g/L), and sodium chloride (9 g/L).

Ion	**Concentration (mM)**
Na^+	156.38
K^+	5.63
Ca^{2+}	1.08
Cl^-	161.79

Following the two-hour creep protocol, specimens were loaded to failure at 0.2 s^{-1} while force and deflection were continuously measured. This was used to calculate the change in stiffness, expressed as a percentage of the initial stiffness. Control specimens in the 25, 50, 75 and 100% condition underwent the same protocol without exposure to Collagenase D in order to distinguish stiffness differences arising from the mechanical exposure from the collagenase D treatment.

4.2.2 Data Reduction & Statistics

Dependent Variables

The preliminary stiffness (k_0) and post-creep stiffness (k_{2h}) were quantified from the preliminary stiffness and failure tests, respectively. Both methods used a least-squares algorithm, combined with the homogeneous solution for the force-deflection curve. From these two measures, the detriment in stiffness was quantified as:

$$\delta k = \frac{k_0 - k_{2h}}{k_0} \tag{4.8}$$

Justification of Statistical Model

The statistical model for this investigation mirrored the scientific hypothesis about strain inhibition and the expected changes in δk, as a function of the proportion of uncrimped

fibrils during the creep test, u. The loss in stiffness model included the sum of two contributing terms which are themselves dependent on u: one for mechanical disruption, $M(u)$, and the other for enzymatic (or biochemical) degradation, $C(u)$. The specific form of these functions were chosen to be consistent with both the strain-inhibitory and strain-indifferent hypotheses. Lastly, we defined a variable to represent the enzyme exposure, E, which was either 1 if the tendon was in the experimental group, and 0 if it was in the control group. Writing this model, with priors, in statistical notation:

$$\delta k \sim \text{Normal}(\mu, \sigma) \tag{4.9a}$$

$$\mu(u) = \alpha + E \cdot C(u) + M(u) \tag{4.9b}$$

$$\sigma \sim \text{Exponential}(0.1) \tag{4.9c}$$

$$\alpha \sim \text{Normal}(0, 1.0) \tag{4.9d}$$

Where $C(u)$ and $M(u)$ were taken to be functions of the uncrimped percentage, and E is an indicator variable representing whether or not collagenase was present. Both the strain inhibition and strain indifference hypotheses expect to see a linear relationship between the u and the magnitude of biochemical degradation. More specifically, in the strain-indifferent hypothesis, the slope of this relationship is close to zero until the mechanical degradation term dominates (Figure 4.1), whereas it is a perfectly linear relationship with a slope of -1 for the strain-inhibition hypothesis. The form for this function, along with its priors are:

$$C(u) = \beta + \gamma(1 - u) \tag{4.10a}$$

$$\beta \sim \text{Uniform}(0,\ 1) \tag{4.10b}$$

$$\gamma \sim \text{Uniform}(0,\ 1) \tag{4.10c}$$

The hypothetical simulations earlier suggested that mechanical damage becomes exponentially more prevalent with u. However, since exponential functions can be extremely sensitive to their parameterizations, a simpler polynomial model was assumed for greater numerical stability. This model assumes that mechanical disruption is negligible when a small proportion of collagen fibrils are uncrimped, but grows to a parameter ω as the whole

population becomes engaged.

$$M(u) = \omega u^{1+\eta} \tag{4.11a}$$

$$\omega \sim \text{Uniform}(0,\, 1) \tag{4.11b}$$

$$\eta \sim \text{Exponential}(5) \tag{4.11c}$$

Model Fitting

The posterior distribution of the parameters in this model was estimated using a HMC algorithm, specifically the No U-Turn Sampler (NUTS) in the `PyMC3` Python library (Salvatier et al., 2016). The traces produced from the sampler used four chains, each containing 2000 samples. The mean, standard deviations and 97% highest-density intervals (HDIs) of the model parameters were evaluated from the estimated posterior distributions. Briefly, in any distribution, there are infinitely many intervals which cover a specified proportion of the distribution: the HDI is the shortest such interval. Additionally, posterior predictive checks were compared to the initial dataset to qualitatively assess that the observed data fell within a 67% quantile envelope of simulated data.

4.3 Results

Descriptive statistics of many of the outcome variables of the sample are available in Table 4.2. Overall, specimens had an average initial stiffness of 3.56 (SD: 1.03) mN/μm, with an average cross-sectional area around 60800 (26900) μm^2, and an initial length of 4855 (545) μm. Altogether, the average Young's Modulus in this sample was 323 (125) MPa.

The resulting strain-versus-time curves portray a substantial degree of variability (Figure 4.5), but with most specimens exhibiting a classic first-order response with most of the deformation occurring in the first 15 minutes of loading. In the 100% uncrimp group there were a substantial number of failures (4 controls; 5 experimental), which represent 44% and 50% of both samples in this group. These specimens exhibited an S-shaped curve with

Table 4.2: Descriptive statistics (means and standard deviations) of the outcome variables in this investigation. These include the sample size (n) within each group and the outcomes from the preliminary stiffness test: the initial stiffness k_0, the mean (μ) and standard deviation (η) parameters for the non-destructive tendon model, compared to the stiffness of the post-creep failure test k_{2h}. Finally, the geometric properties like the cross-sectional area (A) and gauge length (ℓ_0) are presented.

			Parameters					
Condition	**Group**	n	k_0 (mN/μm)	μ (μm)	η (μm)	k_{2h} (mN/μm)	A (μm^2)	ℓ_0 (μm)
Control	25	11	3.67(1.28)	683(341)	146(77)	3.15(1.11)	73300(30600)	4771(401)
	50	10	3.68(1.13)	589(232)	115(53)	3.12(1.10)	62900(41500)	5295(959)
	75	11	2.69(0.60)	577(246)	125(31)	2.68(0.53)	51900(16600)	5143(474)
	100	9	2.97(1.05)	432(940)	111(64)	1.42(1.37)	52900(33600)	4788(273)
Collagenase	0	10	3.51(0.99)	707(192)	87(24)	0.48(0.46)	61000(28300)	4753(606)
	25	10	4.00(0.66)	714(186)	82(20)	2.08(0.57)	55500(21300)	4758(486)
	50	10	4.11(0.84)	776(212)	93(18)	2.69(0.73)	66600(23600)	4830(545)
	75	11	3.79(0.83)	727(200)	89(26)	2.66(1.20)	54800(18200)	4683(451)
	100	10	4.00(0.78)	862(190)	99(14)	1.40(1.55)	62300(18700)	4691(339)

both a primary, secondary and tertiary creep strain-versus-time structure. One specimen in the 75% uncrimp condition ruptured mid-creep as well, but this was the only rupture outside of the 100% condition.

The HMC algorithm successfully converged on adequate model parameters, as evidenced through trace-plots (Appendix A.2), Monte Carlo standard errors, effective sample sizes, and the $\hat{r}$-parameter (Table 4.3). These indicated that both the model had sufficiently converged on a stationary posterior distribution and that there were no algorithmic pathologies in approximating those distributions. Sampling from the posterior distribution was able to adequately cover the observed dataset with a 67% prediction interval, roughly one standard deviation (Figure 4.6A), further reinforcing the quality of the statistical model fit. There was considerable variability in the estimates, with a standard deviation around 26% in terms of stiffness reduction.

The estimates of mechanical disruption and biochemical degradation from the model showed less variability (Figure 4.6B). Mechanical degradation followed a non-linear trend with very little involvement at low levels of uncrimped percentage and increasing dramatically when 100% of the fibrils were engaged. Biochemical degradation followed a decreasing linear trend, with most degradation occurring at lower levels of fibril engagement and dropping to approximately zero when the full population was engaged (Figure 4.6B). The slope of this relationship was on average -0.63, with a 97% highest density interval between -0.43 and -0.84, which is reflected in the estimates from the statistical model.

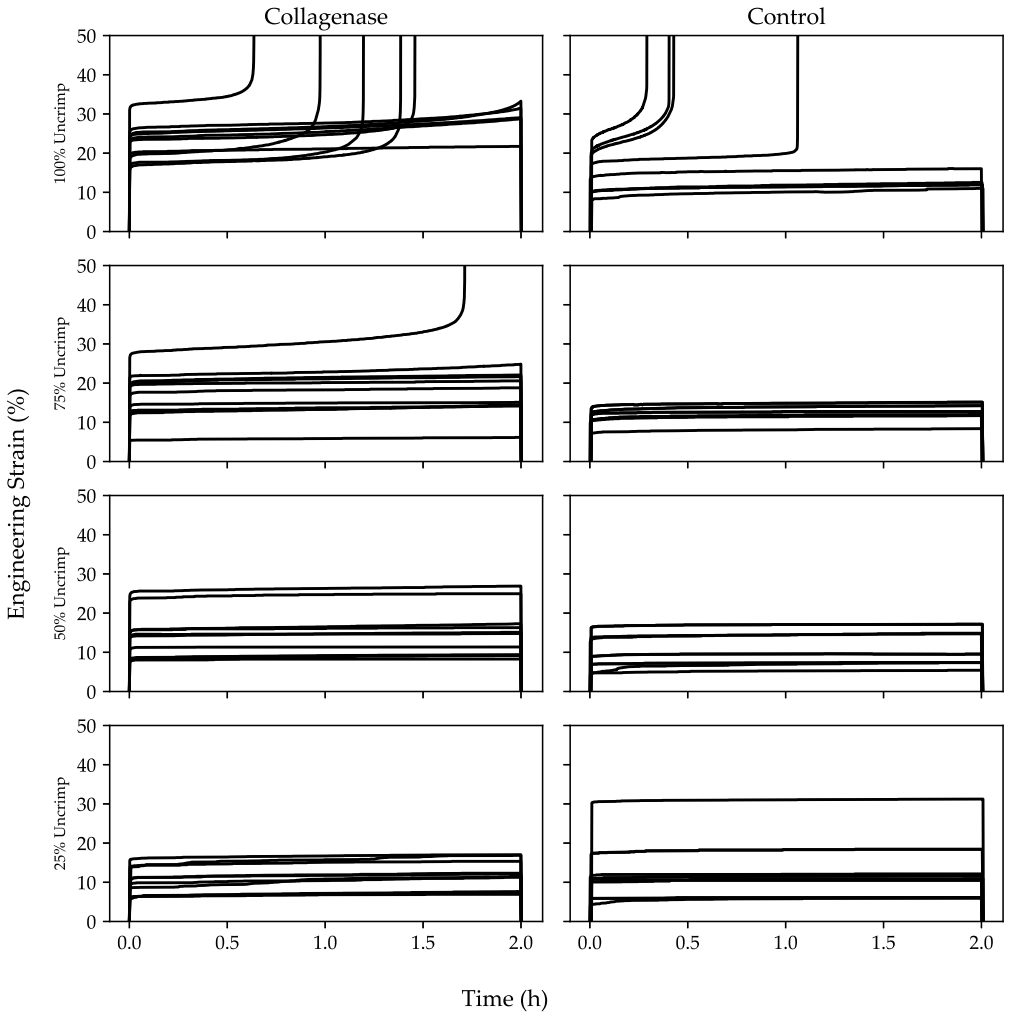

Figure 4.5: Strain-versus-time curves for all the specimens in this investigation. On the left-side are the samples exposed to collagenase, whereas control specimens are on the right. The bottom row indicates the 25% condition, moving to the 100% uncrimped condition at the top. Interestingly, a substantial number of specimens failed in the 100% condition, an observation which was similar between experimental and control groups.

4.4 Discussion

This investigation demonstrated that strain inhibition of bacterial collagenase is consistent with the uncrimping mechanism governing the toe region of a tendon's force-deflection curve. This is evidenced by the statistical models of mechanical disruption and biochemical

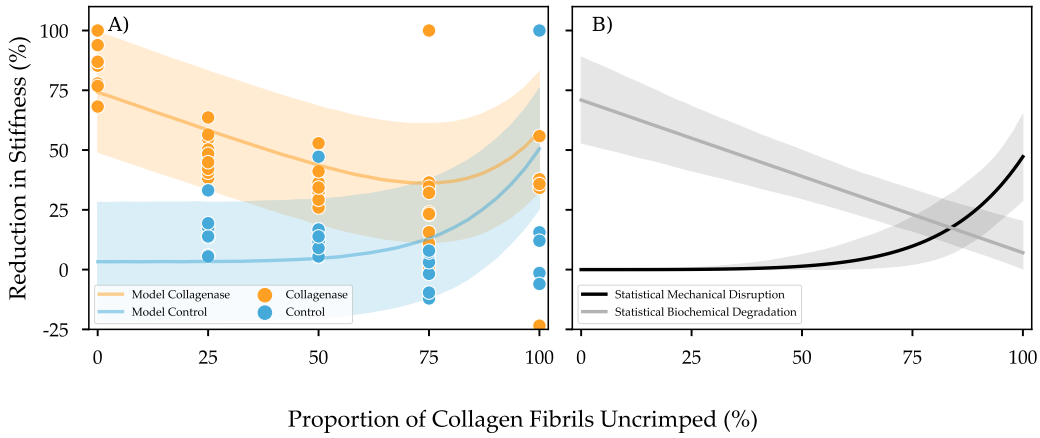

Figure 4.6: (A) Stiffness loss magnitudes for all samples in this investigation (scatterplot), where control specimens are blue and collagenase exposed specimens are orange. Superimposed on this plot is the 67% prediction interval from the posterior distribution of the statistical model (shaded region) along with its average value (solid line). (B) Posterior distribution of mechanical disruption and biochemical degradation functions along with their 97% credible intervals.

Table 4.3: Summary of the statistical fit resulting from the Hamiltonian Monte Carlo simulation using 4 chains with 2000 samples each. Tabulated here are the means and standard deviations for the 6 parameters in the statistical model along with their 95% Highest Density Interval (HDI). This interval is the shortest interval in their posterior distribution that covers 97% of its probability. Additionally, there are some diagnostics for the HMC algorithm itself, including the mean and standard deviation of the Monte Carlo Standard Error (MCSE), which measures the error in the mean estimate from the simulation. The second diagnostics are the effective sample size (ESS) both bulk and tail, which measure the number of effective independent samples in the draw (or the effiicency of the HMC algorithm). Finally, $\hat{r}$ measures the ratio of within chain-variance to between-chain variance in the simulation: a successful draw from the posterior distribution yields an $\hat{r}$ of unity, but the converse is not necessarily true.

Parameter	Mean (SD)	97% HDI	MCSE Mean (SD)	ESS Bulk	ESS Tail	$\hat{r}$
α (unitless)	0.03 (0.05)	(-0.06, 0.13)	0.00 (0.00)	1922	2281	1.0
β (unitless)	0.08 (0.05)	(0.00, 0.17)	0.00 (0.00)	1763	1324	1.0
γ (unitless)	0.63 (0.11)	(0.43, 0.84)	0.00 (0.00)	1735	1074	1.0
η (unitless)	4.66 (1.66)	(1.69, 7.80)	0.03 (0.02)	2816	2327	1.0
ω (unitless)	0.47 (0.09)	(0.31, 0.63)	0.00 (0.00)	1835	1353	1.0
σ (unitless)	0.26 (0.02)	(0.22, 0.29)	0.00 (0.00)	2757	2435	1.0

degradation (Figure 4.6) resembling the strain inhibition hypothesis more so than the strain indifference hypothesis (Figure 4.1). Further, the posterior distribution for the slope parameter, γ, predicted that magnitudes close to 0 are vanishingly likely, with a 97% highest density interval spanning 0.43 to 0.84. The results from the statistical model also generally agree with the predictions made from the computational model, suggesting that a Michaelis-Menten term, like the one in Equation 4.1, may be appropriate for future mechano-kinetic simulations.

A surprising observation in this investigation was that most of the specimens in the 100% uncrimp condition, for either experimental or control groups, ruptured during the creep exposure. The toe and early linear region are typically considered a soft tissue's physiological range (Arnoczky, Lavagnino, & Egerbacher, 2007; Wang et al., 2018), so a prolonged creep protocol within the toe region was not expected to result in substantial mechanical disruption. Previous investigations into creep failure of rat tail tendons have typically parameterized their loading conditions in terms of force or stress (Zitnay, Lin, & Weiss, 2021). Ellis (1978) examined the characteristic S-shaped curves of rat tail tendons undergoing creep until failure using a Tobolsky-Eyring kinetic model. They argued that the estimated activation energies (30.7 kcal/mol) strongly implied that the tendon rupture was related to the breakage of covalent bonds rather than a reorganization of matrix constituents. When a covalent bond is ruptured, the electron pair inhabiting that bond may also be separated, forming free radicals in a process called homolysis. The formation of these radicals by mechanical means, called mechanoradicals, are detectable by electron-paramagnetic resonance, even at physiological levels of stress (5 - 20 MPa) in rat-tail tendons (Zapp et al., 2020). For comparison, the levels of stress in the 100% uncrimp group ranged between 10 and 20 MPa, which is consistent with the observed scission of covalent bonds. These observations, in aggregate, suggest that prolonged loads on collagenous tissues, even within a so-called physiological range, may be associated with the accumulation of damage.

4.4.1 Enzyme Kinetics

Strain has been demonstrated to vastly decrease the ability of bacterial collagenase to cleave individual collagen molecules, a property that also scales up to a whole tissue (Ruberti & Hallab, 2005; Flynn et al., 2010; Camp et al., 2011; Nabeshima et al., 1996). The results of this investigation show that this finding is also consistent with the uncrimping mechanism within the toe region of a tendon's force-deflection curve. That is, if a tendon is held at a force corresponding to $p\%$ of its constituent fibrils being uncrimped, then $(1-p)\%$ of the total fibrils are susceptible to enzymatic cleavage.

The mechanism of strain inhibition is likely an emergent property of strain at the molecular level. The axial packing structure of collagen molecules into microfibrils endows them with a characteristic *D*-banding appearance, where regions of highly overlapping collagen molecules form dark-bands every 67 nm (Petruska & Hodge, 1964). Microfibrils exposed to strain do not exhibit a change in the width of their *D*-bands, but the relative lengths between them, suggesting that fibrillar strain is almost entirely due to collagen molecular strain (Sasaki & Odajima, 1996). It is likely the case that the physical deformation of collagen molecules disrupts their fit inside the catalytic site of bacterial collagenase (Chang et al., 2012).

While strain inhibition of bacterial collagenases has been repeatedly demonstrated, whether that observation carries to mammalian MMPs is still contested. Adhikari, Chai, and Dunn (2011), for example, showed that application of a 10-12 pN force to individual homotrimeric collagen molecules increased MMP-1 activity more than 100-fold. Similarly, the same authors found that MMP-1 catalytic activity was increased 8-fold in heterotrimeric type I collagen molecules (Adhikari, Glassey, & Dunn, 2012). On the other hand, Flynn et al. (2010) found, much like the previous investigations, that the mechanical strain of collagen fibrils inhibited their proteolysis by MMP-8. This latter result was substantiated by computational modelling, which predicted that mechanical strain stabilizes heterotrimeric type I collagen, suggesting that it would be protective (Chang et al., 2012). The inconclusive findings regarding strain inhibition of mammalian collagenases make generalizing the present study to human MMP challenging.

4.4.2 Davis' Law

Davis' Law predicates that soft tissues will respond to their mechanical loading environment. Unfortunately, the fundamental mechanisms behind these two phenomena are not well understood. Mathematical models of Wolff's Law, the equivalent statement for bone, have modelled osteoblasts that respond to the strain energy density in their immediate vicinity by increasing the bone mineral density (Mullender & Huiskes, 1995). In this simple mathematical model, the formation of complex structures, like trabechulae, was observed,

which the authors argued was an emergent property of bone through osteoblast activity. Despite this, the mechanism which leads to uniform alignment of type I collagen in the direction of tensile load, for both bone and soft tissues, remains elusive. One hypothesis, supported by our observations, is that the enzyme-driven degradation of collagen interacts with the mechanical state of the collagen fibres (Saini et al., 2020).

Previous studies have demonstrated that small amounts of strain have a potent inhibitory effect on collagenase activity (Camp et al., 2011; Ruberti & Hallab, 2005; Chang et al., 2012; Saini et al., 2020). Ruberti and Hallab (2005) conducted an experiment with an engineered collagen gel which consisted of concentric layers oriented orthogonal to one-another. The gel was held under tensile load in the direction of one of the two collagen orientations, while simultaneously exposed to the collagenase. They found that the collagenase was only able to break down collagen fibres in the orientation orthogonal to the direction of force application, indicating that strain may play a role in inhibiting the degradation ability of collagenases. On the molecular level, Camp et al. (2011) held individual collagen molecules under tension while exposing them to the same collagenase as Ruberti and Hallab (2005). They found that extremely small magnitudes of forces (> 3 pN, an elongation of roughly 258 nm) reduced the effectiveness of the enzyme to break down collagen molecules by 90%. To the author's knowledge, the current investigation was the first to control a mechanical exposure not in terms of macroscopic stress or strain, but in terms of the strain imparted to the constituent fibrils of the tissue. To that end, our results strongly agree with the previous investigations, and suggest that a graded, mechanically driven, inhibition of collagenases may be present when operating under physiological loads.

These investigations strongly demonstrate a potential interplay between collagen mechanics and biochemistry, and suggest a potential mechanism for collagen fibril alignment. Under the proposed mechanism fibres which are not loaded are selectively pruned by collagenases secreted by the resident fibroblasts. It would imply a nuanced restating of Davis' Law: the resident fibroblasts do not necessarily respond by creating fibrils aligned in the direction of load; rather, the direction of load prevents collagen fibrils in that direction from being destroyed by the fibroblasts.

A corollary of Davis' Law is the familiar "use it or lose it" colloquialism, referring to tissue atrophy. Mechanical load is essential to the homeostasis of soft tissues (Lavagnino, Gardner, & Arnoczky, 2013; Galloway, Lalley, & Shearn, 2013), and tenocytes deprived of mechanical load exhibit physiological changes characteristic of tendinopathy (Arnoczky et al., 2008). These adaptations involve the increased expression of MMPs (Lavagnino, Arnoczky, Tian, & Vaupel, 2003), aptoptosis (Monika Egerbacher, Arnoczky, Caballero, & Gardner, 2008), and, interestingly, a decreased organization of collagen fibril orientations (Arnoczky et al., 2007). It may be possible that inactivity would accelerate MMP-mediated collagen degradation, as there would likely be less strain inhibition associated with those low load magnitudes. This physiological mechanism may underlie the decreased tissue tolerances observed with immobilization or otherwise sedentary behaviour.

4.4.3 Limitations

The most significant limitation in this experiment is the use of a bacterial collagenase. In addition to the difficulties in replicating a strain-inhibition hypothesis on human MMPs raised earlier, the Collagenase D product contains two isoforms of collagenases, Collagenase-G and Collagenase-H, each with its own set of reactive properties (Eckhard et al., 2009; Eckhard, Schönauer, Nüss, & Brandstetter, 2012; Eckhard, Schönauer, & Brandstetter, 2013). In addition, bacterial collagenases of this type bear little resemblance to mammalian collagenases aside from their zinc-containing catalytic region (Eckhard et al., 2009). Bacterial collagenases tend to be much larger proteins than their mammalian counterparts—114 kDa versus roughly 58 kDa, respectively—and indiscriminately cleave collagens regardless of type at numerous sites along the molecule. By comparison, MMPs are typically half the molecular weight, are very selective of both the type of collagen they cleave and wherein the molecule they hydrolyze. MMP-1, for example, reliably produces two fragments of type I collagen-containing 1/4 and 3/4 of the total mass. The differences between bacterial and mammalian collagenases cannot be overstated.

An inherent assumption throughout this experiment and data analysis is the relationship between changes in stiffness and damage accumulation in a material. For well-behaved

materials, like polymers, the onset of damage is well related to a change in stiffness, owing to the destruction of fibres throughout the material. For biological tissues, which often exhibit both viscoelastic and viscoplastic responses, the relationship is not always clear. Some investigations have observed a decrease in stiffness following an injurious event (Panjabi & Courtney, 2001), and this would be supported by the modelling efforts throughout this investigation. However, there have also been a few investigations which have, paradoxically, found an increase in stiffness following a sub-maximal straining event (Panjabi, Moy, Oxland, & Cholewicki, 1999; Panjabi, Yoldas, Oxland, & Crisco III, 1996). Panjabi et al. (1999) excised the anterior cruciate ligaments (ACL) of rabbits for both the left and right sides. One side entered their control group, where it underwent a cyclic pre-loading condition in displacement control prior to being stretched to failure; the other side underwent the same failure protocol, but with a pre-condition where one displacement cycle went up to 80% of the failure displacement from the control group. Their results showed that the tangent stiffness halfway through the failure protocol (K_{50}) was increased in their experimental, submaximal loading condition, and they attributed this change to the rearrangement of matrix constituents in response to sub-maximal loading. This result is incongruous with the partial differential equation model which formed the basis of the hypothesis and statistical analysis in this investigation. This model cannot predict an increase in stiffness by any means other than the synthesis of additional collagen fibrils.

Finally, there may be explanations for the results other than strain inhibition. For instance, increasing the packing density of collagen fibrils has been shown to sterically hinder the effectiveness of collagenases (Perumal, Antipova, & Orgel, 2008). Biological tissue tends to narrow when lengthened due to the conservation of volume and Poisson effects. It is possible that this effect could also compress collagen fibrils closer together, which would interfere with the collagenase's ability to degrade tissues. This is one possible mechanism that would be difficult to untangle from the current investigation, however, others could also be possible. Retaining the strain inhibition hypothesis in this investigation is not as epistemologically valuable as falsifying it would have been.

4.5 Toward Study III

Thus far, both studies I and II have used rat tail tendons as their units of study. This may seem far removed from the goal of uncovering some of the aetiology of chronic low back pain, but it does provide methods for studying type I collagen fibrils in isolation. **Study III** aims to finally tackle the Mountain of a Mole Hill Hypothesis. Further, as we will see in **Study IV** (Chapter 6), the results from both **Study I** and **Study II** will be used to derive the holistic model.

Chapter 5

Study III: Creep and Inflammation in the Rat

5.1 Introduction

Low back pain is a tremendous socioeconomic issue, with more than 80% of people reporting low back pain at some point in their lives. Its etiology is multifaceted, complicated by biological, nutritional, psychosocial, and mechanical factors. These factors interplay with one-another, for instance mechanical load has been shown to influence the cellular response of fibroblasts in the intervertebral disc (IVD) (Korecki, MacLean, & Iatridis, 2008; Wuertz et al., 2009). Among the most insidious responses to mechanical load is inflammation and the downstream expression of matrix degrading enzymes like those in the Matrix Metalloproteinase (MMP) family (Le Maitre et al., 2005; Séguin et al., 2005; Purmessur et al., 2013; Le Maitre et al., 2007). After a mechanical insult, either through mechanotransduction or the sensation of damaged ECM constituents, the fibroblasts of the tissues secrete inflammatory cytokines: molecular messages which signal an inflammatory response (Wong, Akaishi, Longaker, & Gurtner, 2011). In addition to relaying the local inflammation—a paracrine effect—these cytokines also exude an autocrine effect, prompting the fibroblasts to begin synthesis of MMPs. The MMPs then degrade ECM components, like type I collagen, pre-

disposing the tissue for further injury. This metabolic effect has been detected in the blood following lifting tasks (Yang, Marras, & Best, 2011). Viscoelastic creep may also interact with mechanotransduction and inflammation of biological tissues (D'Ambrosia et al., 2010; Solomonow, Zhou, Baratta, & Burger, 2003; Solomonow, Zhou, Lu, & King, 2012). These investigations have usually been limited to human volunteers and surrogate measures of inflammation—like EMG-activity or algometers (Solomonow, Zhou, et al., 2003)—or feline models with indirect measures of inflammation, like neutrophil counts (Solomonow et al., 2012). Mechanistically it is plausible that sustained creep can impart some tissue damage, which may translate into an inflammatory response. Creep carries with it some other neurological consequences, as it diminishes the ability to relay proprioceptive information (Solomonow, 2006; LaBry, Sbriccoli, Zhou, & Solomonow, 2004), which may increase the likelihood of these tissues sustaining injury.

Previous *in-vivo* rat models have demonstrated the physiological response of annular tissues to mechanical loading. Iatridis et al. (1999) demonstrated that prolonged compression of a rat tail IVD translated to changes in disc mechanical properties: decreased stiffness and disc height. Using the same *in vivo* model, Wuertz et al. (2009) showed that consistent, low magnitude mechanical compression can lead to the accumulation of mild degenerative changes in the AF, as demonstrated by the increased expression of MMPs, decreased synthesis of type I collagen, and decreased expression of tissue inhibitors of metalloproteinases (TIMPs). These malicious physiological changes have even been documented downstream of a single compressive loading event (MacLean, Roughley, Monsey, Alini, & Iatridis, 2008). Similarly, prolonged torsion can also lead to the same downstream physiological changes (Barbir et al., 2011). Here, Barbir et al. (2011) used a torsion creep model, both cyclic and static, to induce an inflammatory response in rat tail IVDs. They found that, like the compression model before them, a significant up-regulation of matrix degrading enzymes and the cytyokines Interleukin-1 (IL-1)β and Tumor Necrosis Factor-α (TNF-α). The disproportionate response of the fibroblasts to relatively small amounts of damage is a pain-generating pathway this thesis refers to as the Mountain of a Mole Hill Hypothesis.

To date, there has yet to be an *in vivo* rat model using a flexion-creep modality; despite

the role of prolonged, cyclic flexion on the pathomechanics of disc herniation (Callaghan & McGill, 2001; Tampier et al., 2007). Therefore, the purpose of this investigation is to test whether flexion can exhibit the same physiological response as compression or torsion in a rat model. Additionally, as most studies examining the effect of creep on inflammation have been limited to human subjects and surrogate measures of inflammation, this study aims to demonstrate that viscoelastic creep can elicit an inflammatory response in the fibroblasts of disc-tissue *in vivo*.

5.2 Specific Hypothesis

The specific hypothesis for this investigation comes from analyzing a scientific model (Figure 5.1), with an accompanying set of differential equations, that reproduces a physiological response reminiscent of what was proposed following a repetitive compressive load of rat tail IVDs (MacLean et al., 2008). The input into the model is a variable, D, which represents an abstract form of 'damaged' or 'denatured' collagen. When this damage is sensed by the resident fibroblasts of the AF, they respond by secreting pro-inflammatory cytokines, represented in the model as P, for pro-inflammatory. These cytokines elicit an autocrine effect on the fibroblast that just secreted them, leading to the downstream expression of more pro-inflammatory cytokines, in addition to anti-inflammatory cytokines, represented as A, MMPs, represented as E, and tissue inhibitors of MMPs (TIMPs), represented as I. The MMPs expressed then remove the damaged collagen from the vicinity, returning the system to a neutral, steady state.

Using 'damaged' or 'denatured' collagen as the initial pro-inflammatory signal is based on a few investigations. Solomonow, Baratta, Zhou, et al. (2003), for instance, observed a many-fold increase in the expression of inflammatory cytokines downstream of a high-magnitude repetitive loading protocol in cat spinal ligaments. They postulated that exposure to mechanical creep may be associated with microscopic damage to tissues, evidenced by residual laxity in their ligaments several hours after exposure, which may have been driving the response they observed. Further substantiating their findings, these authors

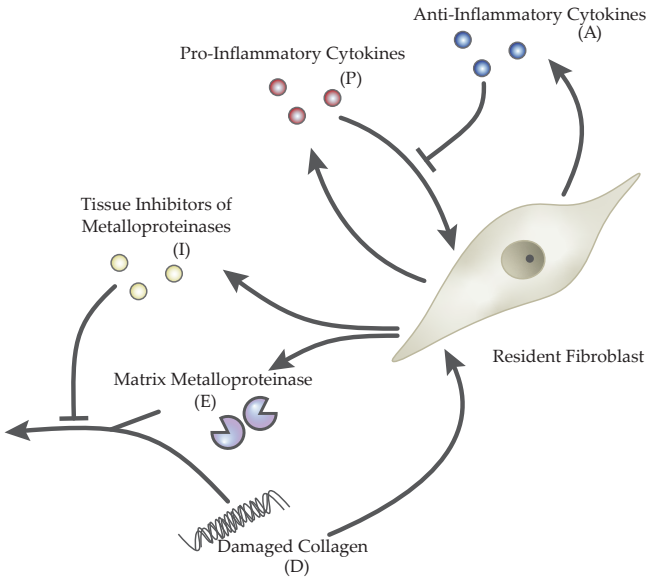

Figure 5.1: Schematic diagram of a scientific model detailing the expected initial feedforward, and eventual negative feedback, response of fibroblasts in response to sensed damage. In this model, damaged collagen (D) is sensed by a resident fibroblast, which responds by secreting pro-inflammatory cytokines (P). Pro-inflammatory cytokines in turn lead to the secretion of matrix metalloproteinases (E), tissue inhibitors of metalloproteinases (I), and an anti-inflammatory cyotkine signal (A).

later showed that the amplitude of the resulting inflammatory response was proportionate with the amount of applied load (D'Ambrosia et al., 2010). Similar studies restricted to loading rat tail IVDs have also shown a transient increase in inflammatory cytokines following repetitive compressive loading (LePage, Stoker, Kuroki, & Cook, 2021; Miyagi et al., 2012). On the cellular level, immune cells, in particular, appear to have the ability to discriminate between damaged and intact collagen. This is evidenced by the detection of MMP-1, produced by macrophages, in overloaded tendons (Veres et al., 2015; McCawley & Matrisian, 2001; Sternlicht & Werb, 2001). Taken together, these results suggest that damaged collagen, or another biomarker reflective of it, can elicit an inflammatory response downstream of a mechanical exposure.

IL-1β, MMP-1/8 and TIMP-1 expression all occur downstream of IL-1β signal transduction. The cascade of events from receptor binding to activation of transcription factors—

most notably through the Nuclear Factor κ B (NF-κB) and Mitogen Activated Protein Kinase (MAPK) cascades—effectively asks like a molecular switch, usually described by a Hill–Langmuir equation (Hill, 1910). Given a extracellular concentration of ligand, in this case IL-1β, the downstream steady state behaviour of transcription factors does not change dramatically until the concentration of ligand reaches a threshold.

The inclusion of a coincident anti-inflammatory response is necessary to damp and suppress the pro-inflammatory positive feedback loop. Aside from being a mathematical necessity, it also appears that some pro-inflammatory cytokines paradoxically trigger the expression of anti-inflammatory ones. For example, cultured fibroblasts increase the synthesis of the Interleukin-1 Receptor Antagonist (IL-1Ra) anti-inflammatory cytokine when stimulated with IL-1 or TNF-α (Martel-Pelletier, McCollum, & Pelletier, 1993). The need to dampen the IL-1 feedforward loop may be a possible explanation for the co-expression of these seemingly opposed signalling pathways.

Together with the conceptual model in Figure 5.1, one can formulate a differential equation model which captures these dynamics, explored extensively in **Study I**. Using the same variable names to describe the pro-inflammatory (P), anti-inflammatory (A), MMP (E) and TIMP (I) responses to Damage Associated Molecular Pattern (DAMP) (D), the differential equation takes the form:

$$\frac{\mathrm{d}P}{\mathrm{d}t} = \beta_P D + \frac{\alpha_P P^n}{k_P^n(1 + A/K_i)^n + P^n} - \delta_P P \tag{5.1a}$$

$$\frac{\mathrm{d}A}{\mathrm{d}t} = \frac{\alpha_A P^n}{k_A^n(1 + A/K_i)^n + P^n} - \delta_A A \tag{5.1b}$$

$$\frac{\mathrm{d}E}{\mathrm{d}t} = \frac{\alpha_E P^n}{k_E^n(1 + A/K_i)^n + P^n} - \delta_E E \tag{5.1c}$$

$$\frac{\mathrm{d}I}{\mathrm{d}t} = \frac{\alpha_I P^n}{k_I^n(1 + A/K_i)^n + P^n} - \delta_I I \tag{5.1d}$$

$$\frac{\mathrm{d}D}{\mathrm{d}t} = -\frac{k_{\mathrm{cat}} E D}{K_m\,(1 + I/K_I) + D} \tag{5.1e}$$

Where:

1. δ_P, δ_A, δ_E, and δ_I are degradation coefficients (related to half-life) for the pro- and anti-inflammatory cytokines, MMPs and TIMPs, respectively.

2. n is the Hill Coefficient for the IL-1β signal transduction pathway.

3. α_P, α_A, α_E, and α_I are the steady-state rates of transcription and translation for the pro- and anti- inflammatory cascades, MMPs and TIMPs, respectively.

4. k_P, k_A, k_E, and k_I are the half-steady-state concentrations for the transcription and translation for the pro- and anti- inflammatory cascades, MMPs and TIMPs, respectively.

5. K_i and K_I are the inhibition constants for the anti-inflammatory response and TIMPs on MMPs, respectively.

6. k_{cat} and K_m are the Michaelis-Menten parameters for the MMPs.

The dynamics of this model are highly non-linear and require specifying a staggering 17 parameters. Adding to the confusion, the sensitivity of this model on the underlying parameters can be quite substantial. In this case, it is helpful—and almost necessary—to non-dimensionalize the equation as much as possible. Doing so yields:

$$\frac{\mathrm{d}\hat{P}}{\mathrm{d}t} = \frac{\hat{\alpha}_P \hat{P}^n}{(1+\hat{A})^n + \hat{P}^n} + \hat{\beta}_P \hat{D} - \delta_P \hat{P} \tag{5.2a}$$

$$\frac{\mathrm{d}\hat{A}}{\mathrm{d}t} = \frac{\hat{\alpha}_A \hat{P}^n}{\hat{k}_A^n(1+\hat{A})^n + \hat{P}^n} - \delta_A \hat{A} \tag{5.2b}$$

$$\frac{\mathrm{d}\hat{E}}{\mathrm{d}t} = \frac{\hat{P}^n}{\hat{k}_E^n(1+\hat{A})^n + \hat{P}^n} - \delta_E \hat{E} \tag{5.2c}$$

$$\frac{\mathrm{d}\hat{I}}{\mathrm{d}t} = \frac{\hat{\alpha}_I \hat{P}^n}{\hat{k}_I^n(1+\hat{A})^n + \hat{P}^n} - \delta_I \hat{I} \tag{5.2d}$$

$$\frac{\mathrm{d}\hat{D}}{\mathrm{d}t} = -\frac{\hat{k}\hat{D}\hat{E}}{1+\hat{I}+\hat{D}} \tag{5.2e}$$

Where (and the chosen sample parameters are tabulated in Table 5.1):

$$\hat{P} = \frac{P}{k_P} \qquad \hat{A} = \frac{A}{K_i} \qquad \hat{E} = \frac{E}{\alpha_E} \qquad \hat{I} = \frac{I}{K_I} \qquad \hat{D} = \frac{D}{K_m}$$
$$\hat{\alpha}_P = \frac{\alpha_P}{k_P} \qquad \hat{\beta}_P = \frac{\beta_P K_m}{k_P} \qquad \hat{k}_A = \frac{k_A}{k_P} \qquad \hat{\alpha}_I = \frac{\alpha_I}{K_I}$$
$$\hat{k}_I = \frac{k_I}{k_P} \qquad \hat{k}_E = \frac{k_E}{k_P} \qquad \hat{k} = \frac{k_{\text{cat}}\alpha_E}{K_m}$$

Amazingly, this set of five ODEs captures—at least qualitatively—the kinetic behaviour postulated by MacLean et al. (2008) and Iatridis et al. (2006), as can be seen in Figure 5.2. Assuming that inflammation is a downstream event of viscoelastic creep, possibly mediated by microscopic damage to extracellular matrix components, one would expect to see a transient inflammation response local to the IVD following a creep exposure. This would be indicated by the expression, and subsequent secretion, of inflammatory cytokines like IL-1β. The hypothesis is that matrix metalloproteinase expression is a downstream autocrine consequence of this inflammatory response, and that increased proteinase expression will result in cleaved type I collagen. Both of these events follow the transient inflammatory response and will yield detectable increases in MMP-1/8. Therefore, the specific hypothesis is a time history of molecular actors as indicated in Figure 5.2, with a dose-dependent transient increase in inflammatory mediators and downstream MMP and TIMP expression. Based on previous work using a single compressive load, the transient inflammatory response is expected to be resolved after 72-hours, which will correspond with an increased tissue expression of MMP-1/8 (MacLean et al., 2008).

A more detailed analysis of this network is the topic of **Study I**, which will also connect it with the mechanical (**Study I**) and biochemical (**Study II**) models of collagens in fibrous tissues.

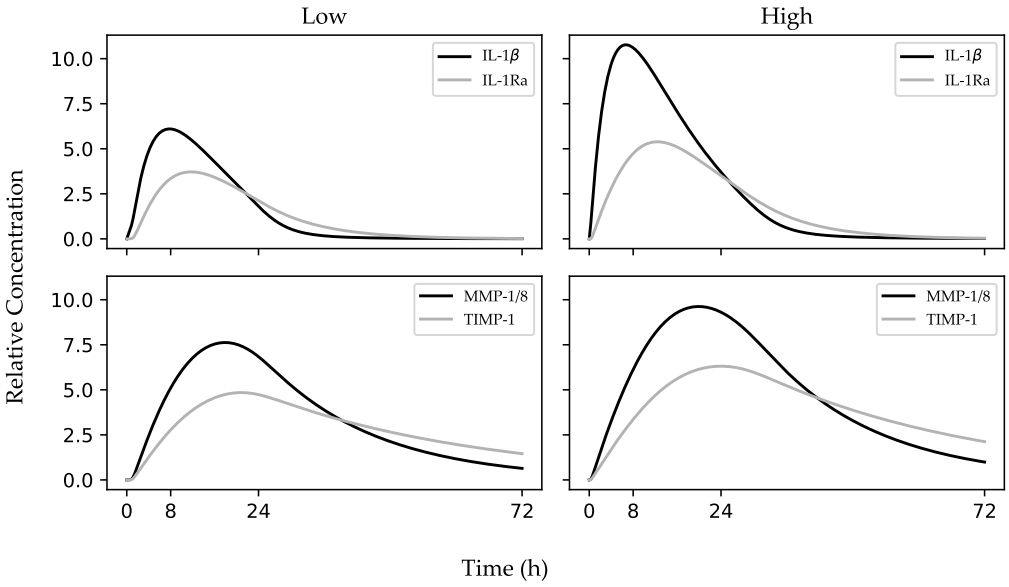

Figure 5.2: Numerical simulation which forms the basis of the scientific hypothesis for this investigation. In this plot, low refers to a low magnitude of DAMP stimulus, what is expected from a 15 Nmm creep exposure. By contrast, high refers to the 75 Nmm exposure used in this experiment.

Table 5.1: Sample parameters for the simulations in Figure 5.2. Degradation rates are based on the half-life of concentrations of IL-1β and IL-1Ra for pro- and anti-inflammatory cytokines, typically around 2.5 hours. Ratios of synthetic and equilibrium constants are very loosely derived from receptor association constants in the interleukin-1 system.

Parameter	**Magnitude**	**Description**
$\hat{\alpha}_P$ (h^{-1})	1.7	Normalized rate of pro-inflammatory synthesis
$\hat{\beta}_P$ (h^{-1})	3.0	Sensitivity to damage
$\hat{\alpha}_A$ (h^{-1})	1.0	Normalized rate of anti-inflammatory synthesis
$\hat{k}_A$ (unitless)	1.33	Normalized equilibrium coefficient for anti-inflammatory synthesis
$\hat{\alpha}_I$ (h^{-1})	0.5	Normalized rate of TIMP synthesis
$\hat{k}_I$ (unitless)	1.0	Normalized equilibrium coefficient for TIMP synthesis
$\hat{k}_E$ (unitless)	1.0	Normalized equilibrium coefficient for MMP synthesis
δ_A (h^{-1})	0.1	Degradation rate for anti-inflammatory cytokines
$\hat{k}$ (h^{-2} M^{-1})	0.2	Normalized MMP activity
δ_I (h^{-1})	0.025	Degradation rate for TIMPS
δ_P (h^{-1})	0.3	Degradation rate for pro-inflammatory cytokines
δ_E (h^{-1})	0.05	Degradation rate for MMPs
n (no units)	4	Hill coefficient

5.3 Methods

5.3.1 Animal Model

Sixty skeletally mature Sprague-Dawley rats (>4 months old, body mass: 344 ± 29 g) were divided into one of nine groups: one control group and eight experimental groups based on four time-point conditions and two load magnitude conditions (Table 5.2). The load magnitudes refer to the moment magnitude applied to motion segment between caudal vertebrae eight and nine (Ca8-9) for one hour, and are either low (15 Nmm) or high (75 Nmm). The time-point groups refer to how long post creep-exposure prior to sacrifice and tissue harvesting. The experimental protocol was approved by the animal ethics review board at the University of Waterloo (AUPP# 43195).

Table 5.2: Number of animals used in this experiment per group.

Group	Number	Group	Number
0-hour low	8	0-hour high	5
8-hour low	8	8-hour high	4
24-hour low	8	24-hour high	5
72-hour low	8	72-hour high	5
control	9		

5.3.2 Protocol

All animals were first induced with isoflurane anesthetic, then gently placed on a two-degree-of-freedom carriage. Their state of consciousness was assessed using a toe-pinch withdrawal test prior to carefully palpating the prezygapophysis and transverse processes of the coccygeal vertebrae, and labelling the approximate joint centres of Ca7-8, Ca8-9, and Ca9-10 with a permanent marker. Their tail was held in the mobile carriage by a clamp fixture, secured with four M3 screws, at the level of the eighth caudal vertebra. The clamping fixture was coated with a thin layer of plasticine to firmly cushion the tail while improving the friction between the clamp and specimen. A complimentary clamp on a six-degree-of-freedom robotic arm (Model MH5SII, Yaskawa, Mississauga, Ontario) held their ninth caudal vertebra in an analogous way (Figure 5.3), which interfaced with a

six-degree-of-freedom load cell (ATI IP65, ATI Industrial Automation, Apex, NC, USA). The load cell was connected to a 16-bit multifunction I/O device (NI USB-6210, National Instruments, Austin, TX, USA), which was sampled using the NI-DAQmx API in C# at 100 Hz. This arrangement of hardware achieved a moment resolution of 0.125 Nmm. The tightness of the clamps was adjusted to ensure no slippage, while also not noticeably blanching the distal tail, indicative of ischemia. The clamps on the carriage and robotic arms were designed so that rotation of the robotic arm's wrist joint would apply a rotation at the animal approximate Ca8-9 joint centre as identified through palpation. The angular resolution of the robotic arm's stepper motor was 0.0001° per step.

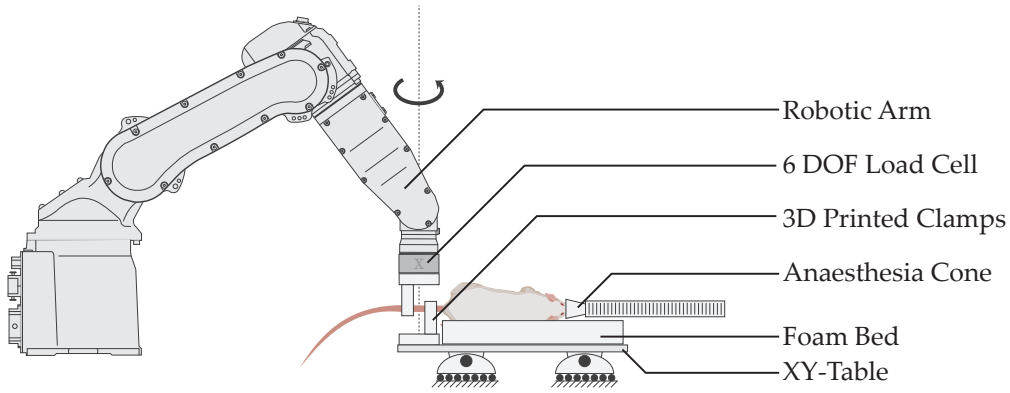

Figure 5.3: Experimental configuration for applying flexion-extension mechanical load to the Ca8-9 motion segment of an anesthetized animal. The robot applies an angular displacement about the Z axis, coincident with the motion segment's flexion-extension axis. At the same time, a six-degree-of-freedom load cell measures the moment, which facilitates quantifying the moment-angle curve. The anesthetized animal is on an XY table during this test, free to translate but not rotate.

After mounting in the test apparatus, animals underwent a preliminary passive range-of-motion test, where the robotic arm, in displacement control, cyclically flexed and extended the Ca8-9 joint at 4.0° per second until ±20 Nmm was achieved, which signalled direction reversal. The resulting moment-angle curve was used to calculate neutral-zone length according to the methods of Sarver and Elliott (2005). Briefly, a piecewise linear function with four breakpoints was fit to the last loading cycle measured. The region with the lowest stiffness was taken to be the neutral zone, and the borders on either side as the total neutral zone range (Figure 5.4).

After the preliminary stiffness test, control animals were sacrificed by open cardiac

puncture exsanguination and their Ca8-9 AF was harvested. The remaining animals endured an hour-long creep protocol where the robotic arm applied a fixed moment (15 Nmm or 75 Nmm) to the Ca8-9 joint, controlled using a proportional control algorithm. During this time, the angle of the motion segment was continuously measured at roughly 100 Hz. These data would later be used to evaluate viscoelastic creep parameters for the rat tail using a Prony Series with three relaxation times (Equation 5.3). Descriptive statistics for these data were obtained, but were not used for any statistical inference. Mathematically, this is described by the equation:

$$\theta(t) = C_0 + \sum_{i=1}^{3} C_i \left(1 - e^{-t/\tau_i}\right) \tag{5.3}$$

Where $\theta(t)$ is the flexion angle (degrees) at the Ca8-9 joint over time, and C_i, τ_i are the 7 parameters which characterize the creep response in units of degrees and time, respectively.

Immediately following this creep protocol, they underwent another passive range-of-motion test. Animals in the 0-hour time-point group were immediately sacrificed, while other animals were returned to the animal wing for 8, 24, or 72 hours—depending on their time-point group. After the intervening time, animals were again induced with isoflurane gas, underwent a final passive range-of-motion trial, and were sacrificed by open cardiac puncture exsanguination.

Annular samples were isolated from the Ca8-9 motion segment of all specimens. After sacrifice, the tail was severed at the level of approximately Ca7-8. Then, another cut was made at Ca9-10 with a pair of front cutters, ensuring not to completely sever the tendons. Tensile force was applied to the caudal segments from this level, which removed all tendons with no insertions onto caudal vertebra eight or nine. This isolated segment was then carefully skinned, exposing the osteoligamentous motion segment. Isolating the motion segment using this technique efficiently removed the tendons, which are otherwise tedious to reflect, exposing the IVD for subsequent dissection. The Ca8-9 AF was then harvested by cutting through the disc, removing the NP, and collecting the AF on the cranial and caudal segments of the segment. Samples were immediately plunged into

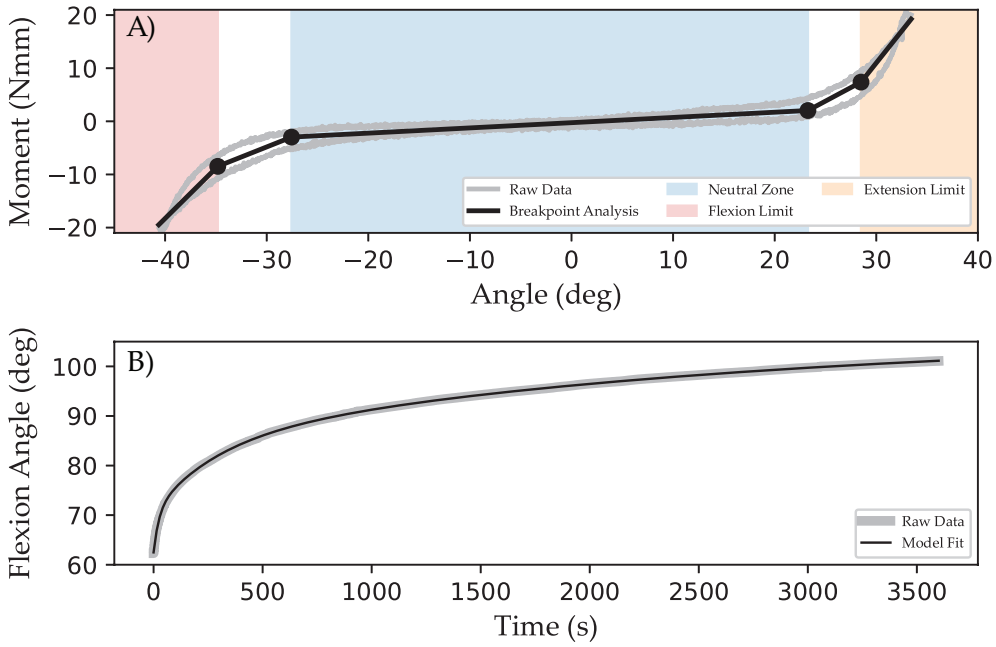

Figure 5.4: Mechanical outcome variables for this investigation. (A) A typical moment-angle curve measured from the passive range-of-motion trial, with the four-breakpoint piecewise linear fit to establish the limits of the neutral zone and the stiffness in flexion and extension. (B) A typical angle-versus-time curve during a one-hour creep protocol for a 75 Nmm applied moment. Superimposed on the flexion angle—which has been negated so that positive indicates more flexion—is the model fit from a triple time-constant creep function.

liquid nitrogen, and moved to a $-80°$ C freezer for storage until sample preparation for Western Blot analysis.

5.3.3 Western Blot

Tissue samples were suspended in 300 μL of muscle lysis buffer prior to homogenization on a bead homogenizer (TissueLyser II, Qiagen, Venlo, Netherlands) for 5 minutes at 20 Hz prior to 4°C centrifugation at 10,000g for 5 minutes, after which the supernatant was recovered. 5 μL of each sample, along with 20 μL of homogenized rat liver tissue, were collected into a tissue standard. A Bicinchoninic acid (BCA) assay was then used to establish the concentration of protein in sample extracts (Walker, 2009). Using this concentration, preserved samples in SDS were prepared ensuring a concentration of 1 μg/μL for subsequent

electrophoresis. Samples were boiled (Eppendorf Thermomixer R 5355, Mississauga ON, Canada) at 95°C for five minutes with constant agitation before storage in a -80° C freezer overnight. The following day, 40 μg of protein were loaded into a 12% polyacrylamide gel for gel electrophoresis. A power supply (PowerPac, Bio-Rad Laboratories, Montreal, QC, Canada) provided a voltage controlled current through the gel and electrophoresis buffer consisting of 100 V for 10 minutes, followed by 160 V for 50 minutes. A protein ladder (2.2 μg of Kaleidoscope precision plus) was also loaded in the leftmost lane (Mahmood & Yang, 2012).

Following electrophoresis, proteins between 50 and 75 kDa (high weight) and 20-37 kDa (low weight) were isolated and transferred to PVDF membranes (Immun-Blot PVDF Membrane, Bio-Rad Laboratories, Montreal, QC, Canada) with a dry-transfer technique. This consisted of a current-controlled (1.1 mA) power applied orthogonal to the gel, for 15 minutes. The membranes were then blocked with 5.0% bovine serum albumin (BSA) for one hour before incubation in a solution containing a 1:1000 dilution of primary antibody—MMP-1 for the high weight, and IL-1β for the low-weight—was applied overnight. The next day involved detection which involved soaking the membrane in a solution containing a 1:10000 dilution of secondary antibody for one hour, 3 repetitions of rinsing the membrane with TBS-T for 5 minutes, before the addition of an enhanced luminol chemiluminescent solution (ECL) and detection (Mahmood & Yang, 2012).

Membranes were then stripped with a mild stripping buffer (Eaton et al., 2014) at room temperature, re-incubated with secondary antibody to ensure the primary antibodies had been stripped, and re-incubated with primary antibodies for new proteins at 4° overnight: MMP-8 for the high weight and TIMP-1 for the low weight. Detection and visualization the following day mirrored the above. Ponceau was then applied to the membranes in order to quantify the intensity of all protein bands in the samples, and was used as a loading-control for all subsequent analysis.

Protein content was measured as the average intensity within a bounding box using an average of the lowest 10 intensity pixels as a representative background in AlphaView (ProteinSimple, Santa Clara, California). Within each gel, intensities were normalized to the control lane.

5.3.4 Outcome Measures

There were three mechanical outcome measures, each quantified from the passive range-of-motion tests conducted before the exposure, immediately following the exposure, and at the terminus of each time-point. Firstly, the neutral zone length, which has been reported as a sensitive measure of potential tissue disruption (Oxland & Panjabi, 1992). Then the second and third outcome measures were the extension and flexion stiffnesses at the same time-points.

In addition to the mechanical outcome measures, tissues were probed for four different biomarkers. IL-1β is a cytokine indicative of an inflammatory response. Downstream of this cytokine is the expression of zinc-containing proteinases, MMPs, which are usually expressed by neutrophils (MMP-1) or fibroblasts (MMP-8). Finally, the tissue inhibitors of MMPs, TIMPs, of which TIMP-1 was chosen to be a representative. Detection of these biomarkers would support a potential inflammatory response with deleterious long-term outcomes for the IVD (MacLean et al., 2003; Wuertz et al., 2009).

5.3.5 Justification for Statistical Model

Recovery from static mechanical creep is well described by a first-order, exponential decay function returning to baseline magnitudes. The time-constants for these recoveries tend to vary quite substantially, ranging from on the order of a few minutes (McGill & Brown, 1992) to the order of a few hours (Solomonow et al., 2000; Solomonow, Baratta, Banks, Freudenberger, & Zhou, 2003; King, Davidson, Zhou, Lu, & Solomonow, 2009). Typically, the recovery time from exposure is typically several times longer than the exposure itself. Motivated by these findings, the statistical model for all three mechanical exposures was

assumed to follow this first-order decay according to the probabilistic model:

$$y \sim \text{Normal}(\mu, \sigma) \tag{5.4a}$$
$$\mu = y_0 + M\left(\beta e^{-t/\tau} + \gamma\right) \tag{5.4b}$$
$$\beta \sim \text{Normal}(1, 0.5) \tag{5.4c}$$
$$\gamma \sim \text{Normal}(0, 1) \tag{5.4d}$$
$$\tau \sim \text{Lognormal}(1.7, 1) \tag{5.4e}$$
$$\sigma \sim \text{Exponential}(2) \tag{5.4f}$$

Where y_0 was the outcome measure from the preliminary test or its baseline measure, either neutral zone length or stiffness. M is the applied moment magnitude over the hour, either 15 or 75 Nmm. Equation 5.4b further implies that the initial post-exposure measure will be $y_0 + M(\beta + \gamma)$, and that the long term behaviour of the outcome measure will be $y_0 + M\gamma$. Therefore, the parameters, β and γ, parameterize the immediate and long-term recovery patterns. The parameter τ, the time constant for the exponential relaxation, represents the time duration corresponding to 36.8% of the recovery. Since recovery times are typically hours longer than the exposure itself, a Lognormal with a mode at 2 hours was chosen as the prior for this parameter. Full recovery was expected, so γ was given central tenancy around zero, and β was expected to be positive, indicative of an increase in the outcome variable.

The posterior distributions of these parameters was sampled using the HMC method with the No-U Turn Sampler (NUTS) in the `PyMC3` Python Package (Salvatier et al., 2016) using four chains, each with 1000 tuning samples and 2000 real samples. Convergence of the model was assessed from standard diagnostics: trace-plots, effective sample size, and the $\hat{r}$ statistic. These diagnostics are presented for the interested reader in Appendix A.3.

Unlike mechanical recovery, there is no single function that captured the expected physiological responses. Thus, the statistical model for the physiological outcome measures resembled a standard analysis of variance (ANOVA) with a Dunnett's post hoc test for comparing all experimental groups to control. There were eight experimental groups in

total, corresponding to the two loading magnitudes and four time-points, which, along with the control group, were represented as a cell-means model with nine cells. Because the measures in the Western Blot Analysis were normalized to the standard, prior distributions were taken as normal and centred around unity with a standard deviation of 0.5. The variance parameter had an initial exponential distribution with a unit rate. Wide priors were used since there was relatively little information available for the expected protein content downstream of a prolonged creep flexion exposure. Using conventional probability notation, the model, along with prior probabilities, was specified as:

$$y_c \sim \text{Normal}(\mu_c, \sigma) \qquad \text{Control Group} \tag{5.5a}$$

$$y_{ij} \sim \text{Normal}(\mu_{ij}, \sigma) \qquad \text{Experimental Groups} \tag{5.5b}$$

$$\mu_{ij} \sim \text{Normal}(1,\ 0.5) \qquad i = 0, 1; j = 0, 1, 2, 3 \tag{5.5c}$$

$$\mu_c \sim \text{Normal}(1, 0.5) \tag{5.5d}$$

$$\sigma \sim \text{Exponential}(1.0) \tag{5.5e}$$

Where μ_{ij} is the estimated group mean for the i^{th} loading magnitude ($i = 0$ for 15 Nmm, and $i = 1$ for 75 Nmm), and j^{th} time-point ($j = 0$ for 0-hours, up to $j = 3$ for 72-hours). Similarly, μ_c was the mean for the control group. The posterior distributions were estimated using the same NUTS sampler in the `PyMC3` Python package, again with four chains of 3000 samples (1000 tuning). From this data contrasts between μ_{ij} and μ_c were evaluated. The posterior distributions of these contrasts were used to calculate the inferential probability that a particular cell mean exceeded the average of the control group given the observed data:

$$\Pr(\mu_{ij} > \mu_c | X) = \text{Probability of increased expression given the data.} \tag{5.6}$$

Where the vertical bar notation is conventional for a conditional probability, which, in this case, is inferred based upon the observed data, X.

5.4 Results

5.4.1 Mechanical Data

A three-parameter relaxation function was able to adequately describe the creep response of the rat tail, with coefficients summarized in Table 5.3. The fastest characteristic times were between 13.4 and 28.2 seconds for high and low magnitude exposures, respectively. The middle relaxation time ranged between 1.5 and 3.25 minutes, and the largest was between 18 and 21 minutes. There was almost twice as much total creep in the 75 Nmm creep condition compared to the 15 Nmm, with total angular deviations of 35.4 (4.3) degrees and 16.6 (2.3) degrees, respectively.

Table 5.3: Summary of un-normalized creep function coefficients and total creep measured during the mechanical exposure. Low magnitude parameters refers to the average and standard deviations of the parameters obtained from least-squares on the low-magnitude, 15 Nmm, creep function, whereas high refers to the 75 Nmm condition. The total creep magnitude was the difference between the angle at the end of the creep protocol versus the beginning, once the applied moment was equal to the assigned applied moment.

Parameter	**Low Magnitude**	**High Magnitude**
C_0 (deg)	43.2 (6.2)	59.7 (5.5)
C_1 (deg)	3.1 (1.1)	5.9 (1.3)
C_2 (deg)	3.6 (1.6)	5.6 (2.1)
C_3 (deg)	10.1 (3.0)	23.7 (3.9)
τ_1 (s)	28.2 (26.7)	13.4 (6.2)
τ_2 (s)	192.2 (175.5)	106.3 (18.1)
τ_3 (s)	1273.9 (375.1)	1089.0 (189.5)
Creep Magnitude (deg)	16.6 (2.3)	35.4 (4.3)
Maximum Flexion Angle (deg)	59.6 (6.6)	95.3 (8.9)

The statistical models were able to converge for all three mechanical outcome variables, as evidenced by trace-plots and chain diagnostics summarized in Appendix A.3 and model parameters in Table 5.4. The resulting statistical models adequately cover the observed spread in the data with a 67% credible interval (Figure 5.5), with some noted deviations owing to the relatively small samples in some of the groups.

Virtually all mechanical outcome variables returned to baseline magnitudes within 8-hours, as evidenced by the high posterior probability that the relaxation coefficients (τ) were between 30 minutes and 8 hours (93.4% in the whole posterior distribution). Following the creep exposure, the length of the neutral zone increased quite substantially: by 12.0

(3.3) degrees in the low magnitude group and 25.9 (5.8) degrees in the high magnitude group. These were related, but not exactly equivalent to, the magnitudes of creep observed during the hour-long exposure.

In the posterior distribution, the stiffnesses for both flexion and extension had a high probability ($\Pr(\beta + \gamma < 0|X) \approx 100\%$) to decrease immediately following the creep protocol. The decrease was slight, however: in extension, an average decrease of 0.705 (0.064) Nmm/deg for every 100 Nmm applied moment during creep and 0.946 (0.062) Nmm/deg for flexion. This is consistent with the experimental averages, for which the extension stiffness decreased by 0.24 (0.29) Nmm/deg and 0.45 (0.21) Nmm/deg in the low and high magnitude conditions, respectively. Likewise, in flexion, the decreases were 0.21 (0.23) and 0.63 (0.24) Nmm/deg for the low and high magnitudes. These changes in stiffness likely did not persist beyond the 8-hour mark, however, as the relaxation times, τ, were similar to the neutral zone changes.

Table 5.4: Summary of statistical model parameters as means (standard deviations) and 97% highest density intervals (HDIs) for all three mechanical outcome variables. The units of these parameters depend on the units of the outcome variable of interest, degrees for the neutral zone length, and Nmm/deg for the flexion and extension stiffness magnitudes. The parameters β and γ are normalized to the applied moment magnitude, and can be scaled by 15 or 75 Nmm to yield their approximate magnitudes for the low and high loading conditions.

	Neutral Zone (deg)		**Flexion Stiffness** (Nmm/deg)		**Extension Stiffness** (Nmm/deg)	
Parameter	Mean (SD)	97% HDI	Mean (SD)	97% HDI	Mean (SD)	97% HDI
β (units / 100 Nmm)	34.2 (2.5)	(28.8, 39.4)	-0.88 (0.18)	(-1.14, -0.63)	-0.68 (0.11)	(-0.94, -0.44)
γ (units / 100 Nmm)	2.3 (2.1)	(-2.0, 6.7)	-0.067 (0.099)	(-0.28, 0.16)	-0.024 (0.094)	(-0.22, 0.20)
τ (hours)	2.61 (1.34)	(0.34, 5.53)	4.91 (3.32)	(0.32, 12.75)	3.58 (2.55)	(0.24, 9.73)
σ (units)	5.5 (0.34)	(4.79, 6.26)	0.23 (0.02)	(0.2, 0.27)	0.24 (0.02)	(0.21, 0.28)

Potential long-term residual effects, parameterized by γ in the statistical model, were inconsistent and had a very low likelihood of exceeding the estimated standard deviation. For context, according to the statistical model, an estimated 100 Nmm creep exposure had only a 2% probability of inducing a long-term change that exceeds σ. Models omitting γ still perform just as well, for example, for the neutral zone model including γ only increases the Akaike information criterion from -179.4 (5.7) to -179.0 (5.7). Overall, it is likely that there were no long-term residual changes in any of the three mechanical outcome measures.

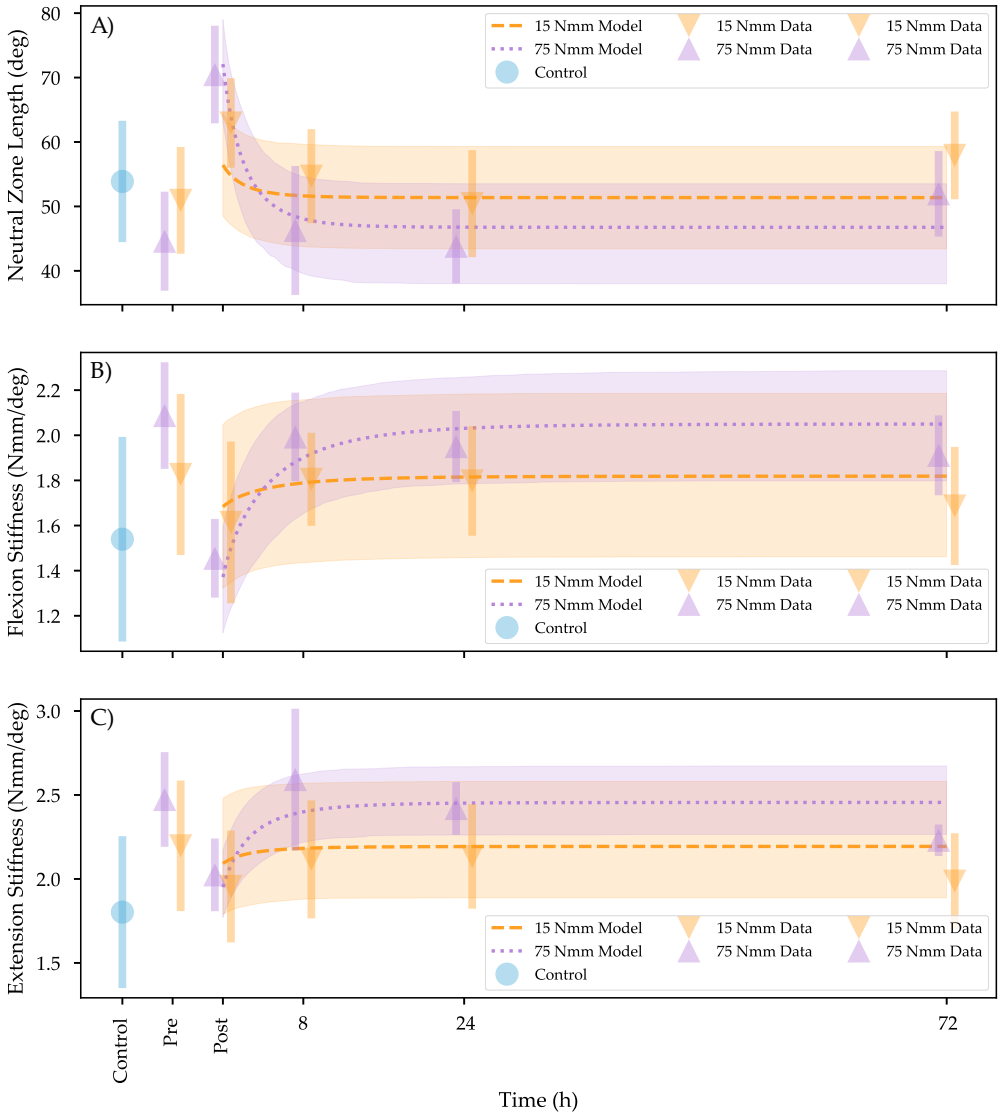

Figure 5.5: Results for the three mechanical measures tested in this investigation. Data averages and standard deviations are presented for each time-point condition, along with controls. Statistical model predictions for the recovery phase of the responses are also shown as lines with 67% credibility intervals as well. In (A) the NZ lengths, in deg, over time are presented. In (B) and (C) the flexion and extension stiffnesses in Nmm/deg are reported. For all measures, the statistical model predicted a rapid return to baseline levels, indicating the high likelihood that all or most animals recovered within 8-hours.

5.4.2 Western Blots

Proteins for all four biomarkers were detected for every group in the Western Blots (Figure 5.6), despite some potential unbalanced loading of each of the lanes. Total protein, as measured from Ponceau, was used to normalize each sample for the amount of protein loaded in each lane. The accompanying raw images of the blots are available in Appendix A.3.1.

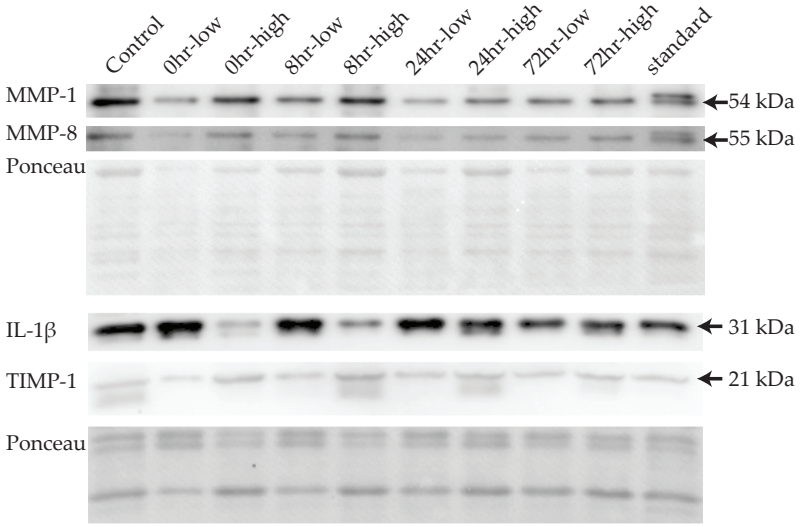

Figure 5.6: Sample blots for all four biomarkers evaluated in this investigation. The four time-point groups are marked as 0, 8, 24, or 72 hours, along with low magnitude (15 Nmm) and high (75 Nmm) creep exposures. Controls and tissue standards are also included on either side of the groups being blotted. In addition, loading controls, in this case total protein as shown by ponceau, is used to account for potential unavoidable differences in the amount of protein loaded into each lane.

The statistical model was able to converge on a steady state cell means model with no divergences for any of the outcome measures. Model diagnostics, along with trace-plots for each of the models, are included in the Appendix A.3.

There was no strong physiological response detected among any of the load magnitude or time-point groups compared to the controls for any of the biomarkers examined (Figure 5.7). In most cases their content trended negatively compared to controls. This result is reflected in the inferential probabilities, with the highest probability of an increased expression only at 78% for TIMP-1 high exposure beyond 8-hours of the 75 Nmm expo-

sure. Overall, none of the posterior distributions indicated a high plausibility of a lasting physiological response following the creep exposure.

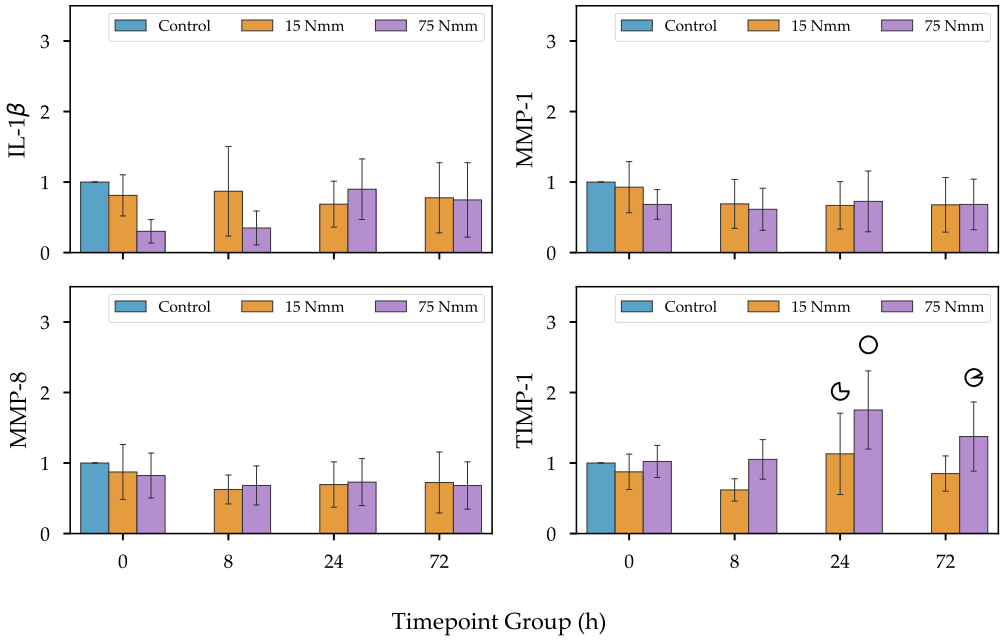

Figure 5.7: Outcome average protein densiometry measurements for IL-1β (top-left), MMP-1 (top-right), MMP-8 (bottom-left) and TIMP-1 (bottom-right) normalized to both the tissue standard and total protein (from Ponceau). Where the posterior probability was greater than 40% a circular fraction is indicated over the bar, indicating the inferential probability that that group's mean is greater than the control group. This only occurred three times in the whole dataset, and were for TIMP-1 expression in the 8, 24, and 72 hour groups.

5.5 Discussion

This investigation quantified the short-term mechanical and physiological responses to a prolonged static flexion load in the rat tail at two levels of applied moment: low (15 Nmm) and high (75 Nmm). The results were highly suggestive that (a) animals recovered from the mechanical exposure less than 8 hours post-exposure, and (b) there was likely no underlying inflammatory response in the IVD that was exposed to loading.

There was a substantial creep response—in terms of the flexion angle between caudal

vertebrae 8 and 9—in the low magnitude group. Over the duration of the exposure, this angle approached 59.6 (6.6) degrees, amounting to a 16.6 (2.3) degrees increase in flexion angle over one hour. This magnitude of creep was also reflected in an elongated neutral zone by 12.0 (3.3) degrees. Even these remarkable kinematic responses pale in comparison to the high-magnitude group, which saw staggering maximum flexion angles of 95.3 (8.9) degrees, and an immediate change in neutral zone length by 25.9 (5.8) degrees. The exposure may have also affected the flexion and extension end-range stiffnesses, which decreased by approximately 0.5 (0.3) Nmm/deg and 0.2 (0.3) Nmm/deg in the high and low-magnitude groups, respectively. Yet, despite these dramatic immediate mechanical changes, 8-hours after the exposure there was little evidence that the animals had been loaded at all. All three mechanical outcome variables had returned to baseline levels, with a high posterior probability (93.4%) that the relaxation time constant was between 30 minutes and 8 hours, within the 8-hours between the end of the exposure and the first non-zero time-point group. These observations were also reflected in the biomarkers assessed post-sacrifice. In particular, there was very little evidence from the Western Blot analysis which supported the hypothesis that an inflammatory response occurred downstream of the mechanical creep exposure. TIMP-1 was the only biomarker that saw any appreciable increases relative to the control group, and yet, the fold change of this molecule is not enough to be considered biologically significant (McCarthy & Smyth, 2009). Overall, this investigation did not see any notable long-term mechanical or physiological responses to a prolonged flexion creep protocol.

The mechanical recovery from creep within 8-hours is in agreement with previous investigations on human volunteers. McGill and Brown (1992) exposed human volunteers to 20 minutes of static trunk flexion and observed a nearly complete recovery approximately 30 minutes later, with an average relaxation time of approximately 10 minutes. In addition to mechanical consequences of creep, like an elongated neutral zone (Busscher et al., 2011), it also disrupts neuro-muscular reflexes (Solomonow, Baratta, Zhou, et al., 2003; Solomonow, 2012), and, potentially, pain sensitization (Viggiani & Callaghan, 2021). Recovery of these neurological responses occurs on a similar time-frame as the mechanical changes, ranging from tens of minutes to several hours, and tend to take longer for

cyclic loading rather than static loads (Toosizadeh, Nussbaum, Bazrgari, & Madigan, 2012; Solomonow, Baratta, Zhou, et al., 2003). Unfortunately, this investigation does not have the granularity of time data to definitively measure relaxation coefficients less than 8 hours, but it does seem plausible that this was the case. Changes in the neutral zone length, a sensitive measure for the induction of damage (Oxland & Panjabi, 1992), returned to baseline levels within this time frame. Given this evidence, it is very likely that the exposure, despite drastic mechanical changes immediately afterwards, imparted no long-term damage onto the IVD .

Mechanical creep is thought to initiate an inflammatory response, however, the results of this investigation suggest that this response may be mediated by tissue micro-damage, as postulated by Solomonow (2004), or by movement, as postulated by Barbir et al. (2011). Previous mechanical loading experiments on rat IVDs have focused on compression and have been similarly met with inconsistent physiological responses (Yurube et al., 2012; Barbir et al., 2011; Wuertz et al., 2009; MacLean et al., 2008, 2003; Iatridis et al., 2006). Miyagi et al. (2012), for instance, compared a disc puncture model to static loading applied to the Ca5-6 IVD. They found that puncture models responded with an immediate, transient, inflammatory response, but the dynamic compression condition took approximately two weeks to reach its peak. Similarly, Yurube et al. (2012) induced a chronic static compressive load on the rat tail disc and saw evidence of a chronic inflammatory response, and subsequent matrix remodelling, after 7 days of exposure. By contrast, LePage et al. (2021) exposed cultured rat tail IVDs to three days of 1 Hz cyclic compression at three loading magnitudes: 0.0, 0.5, and 1.0 MPa, thought to resemble habitual loads (Wilke, Neef, Caimi, Hoogland, & Claes, 1999). They found conflicting results in the cytokines IL-1β and TNF-α, as these two biomarkers did not increase between the middle and high loading conditions. Both the concentration and activity of MMP-8 mirrored the changes in these cytokines, which conflicted with the dose-dependent hypothesis the authors initially proposed. More pertinent to this analysis, Barbir et al. (2011) found substantial increases in the expression of IL-1β, TNF-α, and MMP-3, 24-hours following a 90-minute cyclic torsional exposure on the rat tail to 30 degrees, but not with a static hold. They argued that movement sensed by the resident fibroblasts could promote a downstream remodelling

response. Given the limited evidence of lasting mechanical disruption in this investigation, and the fact that the loading was not cyclic, our results would be consistent with either the mechanical damage or movement sensing hypotheses.

There remains the question: how much damage is enough to initiate an inflammatory response? As will be discussed in more detail in **Study IV**, the signal transduction pathways downstream of IL-1β binding to its receptor portray a switch-like behaviour (Huang & Ferrell, 1996; Kolch, Calder, & Gilbert, 2005). This is characterized by no cellular response at low concentrations of IL-1β until a threshold is reached, at which point gene expression is 'turned-on' at a constant rate. It may be the case that the cellular response to damage obeys a similar response and that the studies with disparate physiological responses to loading may be close to that threshold.

5.5.1 Limitations

Previous groups have used bone-pins or K-wires to rigidly adhere their testing device to their specimens (Miyagi et al., 2012; Iatridis et al., 1999; MacLean et al., 2005; Barbir et al., 2011). While this method ensures that there is no slippage of the clamps relative to the underlying bones, it also constitutes a much more invasive test than what was explored in this investigation. Using skintight clamps was chosen in favor of the bone-pin method to sidestep the invasive surgery installing the clamps, which may, on its own, produce a considerable inflammatory response. The downside of the non-invasive clamp protocol in this investigation is that the flexion angle measured may not be truly representative of the orientations of the bones beneath them. Deformations in the skin, for example, may bias measured angles to be larger. This may account for the large angles observed here, including a greater than 90 degree angle in the 75 Nmm exposure group, which is difficult to conceive would be possible without failure at one joint level alone. Despite these limitations, the exposure documented here is a repeatable one, and one that unquestionably resulted in deformation and creep at the Ca8-9 joint.

A challenging aspect of conducting Western Blot analyses on connective tissues like the IVD is that they are predominantly composed of insoluble, polymerized collagen. Thus, for

a given IVD mass, only a fraction of its protein content will be available for blotting. Using the entire AF from Ca8-9, for example, was able to yield enough protein to be detectable on the BCA assay, and therefore subsequent analysis. The exposure may have elicited an inflammatory response but in only part of the AF. After blotting, this local response may have been drowned out by the overwhelming majority of the disc not participating in that response.

5.5.2 Relevance to the Global Hypotheses

One of the global hypotheses was that an innocuous mechanical exposure could elicit a transient inflammatory response which may be responsible for some forms of low back pain. The results of this investigation would suggest that, at least in a rat model, a one-time flexion creep exposure does not seem to elicit a corresponding inflammatory response. Nor does it appear to tilt the phenotype of resident fibroblasts in favor of extracellular matrix catabolism.

5.5.3 Toward Study IV

Study I aims to synthesize the mechanical damage term from **Study I** and the rate of catabolism term from **Study II** using the experimental data from **Study III**. This involves deriving, simplifying and calibrating a holistic mathematical model that is capable of simulating a chronic exposure.

Chapter 6

Study IV: On Modelling Collagen Homeostasis

6.1 Introduction

At the most basic level, injuries occur when an applied load exceeds a tissue's tolerance (Kumar, 2001; McGill, 1997). For collagenous tissue, the tissue's tolerance is directly related to the number of collagen fibrils which can support the external load. These collagen fibrils are regulated by the fibroblasts, cells specialized in synthesizing components for the Extracellular Matrix (ECM). Therefore, the fibroblasts manage the interplay between mechanical damage, collagen fibril synthesis, and catabolism.

Biological tissues have a complicated mechanical behaviour, with the most well-described aspects being viscoelastic effects (Lucas et al., 2006; Jamison et al., 1968; Troyer et al., 2012). These include stress-relaxation, a decreased stress for a constantly applied strain; creep, an increasing strain for a constantly applied stress; hysteresis, characterized by a dissipation of energy upon cyclic loading; and rate-dependence, having a modulus that appears to vary with the applied strain-rate. In addition to these complex rate-sensitive measures, biological tissues are also hyper-elastic, meaning that their stress-strain curves

are highly nonlinear (Yoganandan et al., 2000; Mattucci et al., 2012). This curve typically begins with a toe region where the stiffness of the tissue gradually increases as more collagen fibrils become uncrimped, before a linear portion, where there is no subsequent increase in modulus. Plasticity, the tendency of tissues to sustain deformations that do not recover, complicates this behaviour by another wide margin.

In addition to this complex set of behaviours, biological tissues can accumulate damage from repeated events that induce micro-damage (Firminger & Edwards, 2021; Wren et al., 2003; Fung et al., 2010). This feature is especially apparent in creep-rupture and fatigue studies of tendons (Ellis, 1978; Wang & Ker, 1995; Wang, Ker, & Alexander, 1995) and ligaments (Chen et al., 2019; Jones, Beason, & Dugas, 2018). These experiments highlight a potential role of fatigue, the culmination of damage into rupture if enough cycles—or time under tension—is endured, in potential injury pathways. Together, the set of biological tissues' hyper-viscoelastic, plastic, and fatigue properties form the foundation of observations that any model of biological tissues should aim to reproduce.

Models of the mechanical response of soft tissues are relatively commonplace (Lucas et al., 2006; Jamison et al., 1968; Troyer et al., 2012; Chandrashekar et al., 2008; Yoganandan et al., 2000; Mattucci et al., 2012). However, there have only been a handful of attempts at modelling the complex set of reactions involved in tissue degradation by catabolic enzymes, often stopping at gene expression (Clermont et al., 2004; Vodovotz et al., 2006; Scholma et al., 2014; Huang & Ferrell, 1996). To date, there are few models which bridge the mechanical behaviour of these tissues with the underlying physiology. Therefore, the goal in developing this computational model is to bridge the gap between these two areas of literature.

This chapter is intended as a reflection of the three empirical studies which make up this thesis. It aims to synthesize the preceding chapters while also producing some inductive hypotheses. Further, it explores some other ramifications of the computational model, how they compare to other damage models, and whether those predictions are consistent with other experimental evidence. The structure of this chapter begins by laying out, in detail, the model assumptions and the ultimate form they take. Then, it summarizes some pertinent experimental work and compares their results to model predictions.

6.2 Mechanical Model

This section describes the mechanical model in detail and comprises slightly more manageable subsections. The first subsection describes the technical aspects of the model: what the model equations are, how they are solved, and what they mean in terms of macroscopic biomechanical variables. In short: linear viscoelastic theory captures viscoelastic phenomena, and a simplified form of the distribution model handles damage, fatigue and rupture. Further, the solution method depends on what we can assume about the system, which we dichotomize as knowing strain and calculating stress (the inverse problem) or the opposite (the forward problem).

The second subsection is less concerned with the theoretical underpinnings of the model and more so whether it is consistent with experiments. For instance, whether the model reproduces the recognized viscoelastic behaviours: creep, stress-relaxation and hysteresis. In addition, fatigue experiments have observed some foundational relationships between the magnitude of applied stress, frequency, number of cycles to failure and time to failure.

Finally, the third subsection elaborates on the shortcomings of the model. This presents some phenomena the model cannot reproduce, and discusses some potential limitations, like its growing complexity.

6.2.1 Model Description

The mechanical model contains two components arranged in series: a Voigt viscoelastic element and the collagen distribution model (Barrett & Callaghan, 2021). The viscoelastic element represents the non-collagenous ground substance of the tissue: the proteoglycans and glycosaminoglycans. Puxkandl et al. (2002) conducted an X-ray diffraction experiment on rat tail tendons undergoing elongation to failure at different strain rates. They showed that the strain in collagen fibrils is much less than the macroscopic strain, and argued that the cross-links and ground substance may be responsible for the creep phenomenon. This result would imply that the ground-substance of the ECM is a viscoelastic component in series with the collagen fibrils.

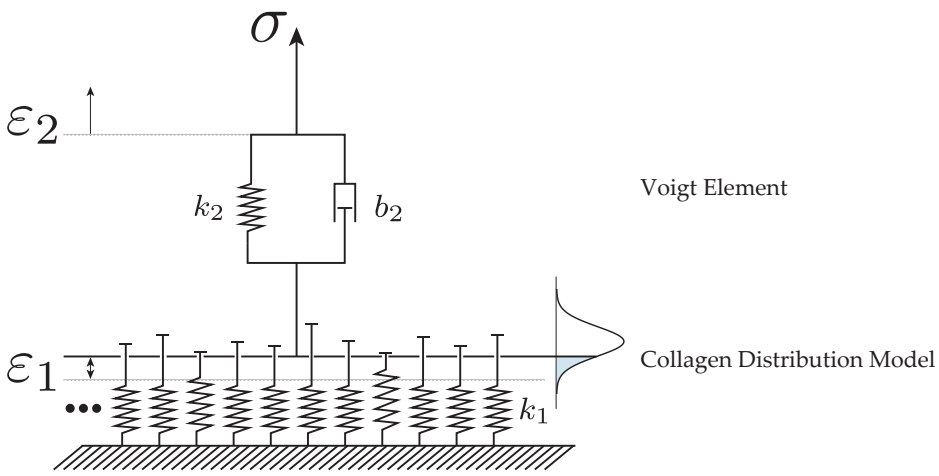

Figure 6.1: Depiction of the mechanical arrangement of collagen fibrils in the collagen distribution model with a Voigt element in series to represent the non-collagenous matrix elements.

Viidik (1968) was one of the first to consider the behaviour of a collagenous tissue composed of a population of fibrils arranged in parallel. By treating the fibrils as ropes, each with their own individual slack length, Viidik (1968) was able to reproduce the toe and linear portions of the force-elongation (or stress-strain) curve. For Viidik (1968), the stiffness of the material would increase in discrete increments as more fibrils become engaged, until all the fibrils in the tissue were sustaining force, at which point there was no subsequent increase in stiffness. Rather than model the time-evolution of potentially trillions of individual fibrils, it is somewhat easier to conceptualize the time-evolution of a distribution of strain among those fibrils, as others have done to reproduce the various elements of the force-elongation curve (Hamedzadeh et al., 2018; Bontempi, 2009; Bevan et al., 2018; Liao & Belkoff, 1999; Hooley & Cohen, 1979).

We consider the evolution of a distribution of strain in a population of collagen fibrils, $\rho(x,t)$. Heuristically, $\rho(x,t)\Delta x$ can be thought of as, roughly, the proportion of fibrils which are strained by x. The rate of change of the strain distribution among a population of collagen fibrils follows the Partial Differential Equation (PDE) given by Equation 2.11:

$$\frac{\partial \rho}{\partial t} + v\frac{\partial \rho}{\partial x} = \dot{S}(x,t,\rho) - \dot{C}(x,t,\rho) - \dot{D}(x,t,\rho) \tag{6.1}$$

Where v is the strain rate, $\dot{S}$, $\dot{C}$ and $\dot{D}$ describe the synthesis, catabolic degradation, and mechanical disruption rates, respectively. In **Study I** (Chapter 3), we argued that an appropriate functional form for $\dot{D}(x,t,\rho)$ was the Tobolsky and Eyring (1943) rate equation:

$$\dot{D}(x,t,\rho) = \alpha e^{\beta x}\rho(x,t) \tag{6.2}$$

Where α is the proportionality constant that may have strain-rate dependence, β is the exponential term related to the collision parameters and absolute temperature. In **Study I**, we argued that $\alpha = \alpha_0 + \alpha_1 v$, for positive, v.

In **Study II** (Chapter 4), we argued that a conventional Michaelis-Menten term would be inadequate for describing the rate of enzymatic degradation if mechanical strain can inhibit collagenases, although it is unclear whether this result translates directly to mammalian MMP. In mathematical notation, this statement reads:

$$\dot{C}(x,t,\rho) = \frac{k_{\text{cat}}E(t)\kappa(x)\rho(x,t)}{K_m + \langle \kappa, \rho \rangle} \tag{6.3}$$

Where k_{cat} and K_m are the Michaelis-Menten parameters, $E(t)$ is the molarity of collagenase at the time t, and $\kappa(x)$ describes the active sites in the crimped and uncrimped collagen as:

$$\kappa(x) = \begin{cases} r & x \leq 0 \\ 0 & x > 0 \end{cases} \tag{6.4}$$

This effectively turns off enzymatic activity on collagens once they have been uncrmiped. In other words, it encapsulates the strain-inhibition of collagenases. Finally, the notation $\langle \cdot, \cdot \rangle$ denotes an "inner-product," and is shorthand for the integral:

$$\langle \kappa, \rho \rangle = \int_{-\infty}^{\infty} \kappa(x)\rho(x,t)\,\mathrm{d}x \tag{6.5}$$

Without getting too theoretical, the inner product is a generalization of a dot product. In some respect, given the distribution of strain among collagen fibrils, the inner product with the function $\kappa(x)$ "measures" or "counts" all the available binding sites for collagenase. The inner product of two functions is a concept that comes from the mathematical discipline of Functional Analysis (Riesz & Nagy, 1955; Kolmogorov & Fomin, 1957).

Existence and Uniqueness

The proposed model is a PDE, and we would be remiss if we failed even to mention existence and uniqueness. Omitting synthesis, the partial differential equation model, so far, takes the form:

$$\frac{\partial \rho}{\partial t} + v\frac{\partial \rho}{\partial x} = -\frac{k_{\text{cat}} E(t)\kappa(x)\rho(x,t)}{K_m + \langle \kappa, \rho \rangle} - \alpha e^{\beta x}\rho(x,t) \tag{6.6}$$

Like algebraic equations, differential equations are sometimes haunted by questions of existence and uniqueness. Existence refers to whether or not a solution exists; for example, there does not exist a real number, x, for which $x^2+1=0$. Uniqueness refers to there being only one solution; for example, there is only one x for which $3x=9$. Unfortunately, there is no straightforward answer as to whether a solution to Equation 6.6 exists or is unique. We suspect that they exist since soft tissues do not cease to exist once forces are applied to them, but rigorous proofs of these qualities for PDEs are not trivial. For example, at the time of writing, proof of the existence of solutions to the Navier-Stokes Equations of fluid dynamics is currently worth one million dollars (Ladyzhenskaya, 2003).

As far as PDEs go, this one is already challenging. With the mechanical term alone, and when the displacement is prescribed, the method of characteristics can be used to give a unique solution. However, if a stress (or force) history is specified instead, then $v(t)$ is unknown and the distribution must also satisfy the condition:

$$\sigma(t) = \int_0^\infty kx\rho(x,t)\,\mathrm{d}x \tag{6.7}$$

Yielding two equations in two unknowns, $\rho(x,t)$ and $v(t)$, but the solution method is not trivial. Further, $\sigma(t)$ is required to satisfy at least the condition that it is strictly positive. It is still plausible that a solution would exist since the form of the equation is still a linear PDE, which are typically well-behaved. However, this type of boundary value problem does not have a conventional name to the author's knowledge. Interestingly, applying numerical techniques, like Galerkin's (Duncan, 1937) or Godunov's (Osher, 1985), or, as we will use in this chapter, the Distribution-Moment (DM) approximation (Donovan, 2020; Zahalak & Ma, 1990), reduces the stress controlled condition to a set of Differential Algebraic Equations (DAEs) which can be solved. This result does not pass for rigorous proof of existence but suggests that the solution one obtains from the approximation may be 'good enough' in an applied context.

Distribution Moment Approximation

Zahalak (1981) first developed the DM approximation to simplify the Huxley cross-bridge model from muscle physiology (Huxley, 1957). This simplification reduces the PDE to a series of three ODEs, which speeds up simulations several-fold (Zahalak & Ma, 1990). The process exploits the property that the solution must be a distribution, uniquely determined by its "raw moments," which are unnormalized generalizations of the mean, variance, skewness, and kurtosis. For a non-negative integer, λ, the λ^{th} raw moment of the strain distribution, $\rho(x,t)$, is denoted Q_λ, and is given by the integral:

$$Q_\lambda(t) = \int_{-\infty}^{\infty} x^\lambda \rho(x,t)\,\mathrm{d}x\,, \qquad \lambda = 0,1,2,\ldots \tag{6.8}$$

Zahalak (1981) assumed that the underlying distribution was Gaussian, and generalizations to other distributions have not necessarily improved performance of this method (Donovan, 2020). A Gaussian distribution is uniquely defined by its zeroth, first, and second raw moments; however, it is convenient to convert them to "central moments," namely the

mean and variance, whose formulae, in terms of the raw moments, are:

$$p(t) = \frac{Q_1}{Q_0} \qquad\qquad q^2(t) = \frac{Q_2}{Q_0} - \left(\frac{Q_1}{Q_0}\right)^2 \tag{6.9}$$

Where we have dropped the explicit dependence on time on the raw moments for brevity. Using these moments, one can construct a Gaussian distribution which approximates $\rho(x,t)$, which we will call $\tilde{\rho}(x,t)$. It takes the familiar form of a Gaussian, with a time-dependent mean, $p(t)$, and standard deviation, $q(t)$:

$$\rho(x,t) \approx \tilde{\rho}(x,t) = \frac{Q_0(t)}{\sqrt{2\pi}q(t)} \exp\left(-\frac{(x-p(t))^2}{2q^2(t)}\right) \tag{6.10}$$

This procedure gives us a way to go from a known distribution, $\rho(x,t)$, to an approximate Gaussian one, $\tilde{\rho}(x,t)$, using a statistical technique called the Method of Moments. Similarly, given the first three raw moments instead, we can approximate $\rho(x,t)$ using $\tilde{\rho}(x,t)$. This approximation motivates the next and most crucial step of the method: to use the PDE to derive equations that describe the rates of change of the raw moments. To do so, we multiply both sides of the PDE by x^λ and integrate over the whole real line. This yields:

$$\int_{-\infty}^{\infty} x^\lambda \left(\frac{\partial \rho}{\partial t} + v\frac{\partial \rho}{\partial x}\right) \mathrm{d}x = \int_{-\infty}^{\infty} x^\lambda \left(\dot{S}(x,t,\rho) - \dot{C}(x,t,\rho) - \dot{D}(x,t,\rho)\right) \mathrm{d}x \tag{6.11}$$

By the linearity of the integral, we can distribute it among each of the terms in this equation. At this point, there is not much that can be done with the right-hand side of the equation, so we will define the terms:

$$S_\lambda = \int_{-\infty}^{\infty} x^\lambda \dot{S}(x,t,\rho)\,\mathrm{d}x\,, \quad C_\lambda = \int_{-\infty}^{\infty} x^\lambda \dot{C}(x,t,\rho)\,\mathrm{d}x\,, \quad D_\lambda = \int_{-\infty}^{\infty} x^\lambda \dot{D}(x,t,\rho)\,\mathrm{d}x \tag{6.12}$$

And return to them later. Conversely, the left-hand side is more amenable to simplification. In the first term, for example, we can move the time-derivative outside of the integral. Then

we notice that the integral is what we defined as Q_λ:

$$\int_{-\infty}^{\infty} x^\lambda \frac{\partial \rho}{\partial t}\,\mathrm{d}x = \frac{\mathrm{d}}{\mathrm{d}t}\int_{-\infty}^{\infty} x^\lambda \rho(x,t)\,\mathrm{d}x = \frac{\mathrm{d}Q_\lambda}{\mathrm{d}t} \tag{6.13}$$

Similarly, we can use integration by parts on the second term to simplify it:

$$\int_{-\infty}^{\infty} x^\lambda \frac{\partial \rho}{\partial x}\,\mathrm{d}x = -\int_{-\infty}^{\infty} \lambda x^{\lambda-1} \rho(x,t)\,\mathrm{d}x = -\lambda Q_{\lambda-1} \tag{6.14}$$

Putting all these terms together, we have reduced the PDE model to:

$$\frac{\mathrm{d}Q_\lambda}{\mathrm{d}t} - v\lambda Q_{\lambda-1} = S_\lambda - C_\lambda - D_\lambda \qquad\qquad \lambda = 0, 1, 2, \ldots \tag{6.15}$$

The ODEs in 6.15 are generally valid for the time evolution of the (infinitely many) raw moments of the distribution, $\rho(x,t)$. However, the real strength of this method comes from the Gaussian approximation with which we started. With this approximation, we can truncate the series beyond $\lambda = 2$, as these are enough moments to approximate the distribution. Further, we can approximate the right-hand side as functions of those moments. For example, the breaking-function's moment can be approximated as:

$$D_\lambda \approx \tilde{D}_\lambda = \alpha \int_{-\infty}^{\infty} x^\lambda e^{\beta x} \tilde{\rho}(x,t)\,\mathrm{d}x \tag{6.16}$$

$$= \alpha \frac{Q_0}{\sqrt{2\pi}q} \int_{-\infty}^{\infty} x^\lambda \exp\left(-\frac{(x-p)^2}{2q^2} + \beta x\right)\mathrm{d}x \tag{6.17}$$

The resulting Gaussian integral can be evaluated through a series of variable substitutions, binomial expansions, and using a recursive relationship, explicitly derived in Zahalak (1981) and Barrett and Callaghan (2021). This simplification allows us to express the synthesis, degradation, and disruption terms as functions of the three raw moments of the distribution, Q_0, Q_1 and Q_2. Ultimately, this approximation reduces the PDE model to the three

ODEs:

$$\frac{\mathrm{d}Q_0}{\mathrm{d}t} = \tilde{M}_0(Q_0, Q_1, Q_2) \tag{6.18a}$$

$$\frac{\mathrm{d}Q_1}{\mathrm{d}t} = vQ_0 + \tilde{M}_1(Q_0, Q_1, Q_2) \tag{6.18b}$$

$$\frac{\mathrm{d}Q_2}{\mathrm{d}t} = 2vQ_1 + \tilde{M}_2(Q_0, Q_1, Q_2) \tag{6.18c}$$

Where we have defined $\tilde{M}_\lambda = \tilde{S}_\lambda - \tilde{C}_\lambda - \tilde{D}_\lambda$, which are all functions of the raw moments. The final piece to the model is the ability to calculate force (or stress) from the three moments, for which we just use the Gaussian approximation with Equation 6.7. Evaluating the integral yields:

$$\tilde{\sigma}(t) = \frac{kqQ_0}{\sqrt{2\pi}} \exp\left(-\frac{p^2}{2q^2}\right) + \frac{kpQ_0}{2}\left(1 + \operatorname{erf}\left(\frac{p}{\sqrt{2}q}\right)\right) \tag{6.19}$$

Where $\operatorname{erf}(\cdot)$ is the error-function, the integral of a Gaussian, which does not have an expression in terms of elementary functions, and k is the stiffness of the soft tissue in the linear portion of its force-deflection curve.

Equations 6.18a to 6.19 completely specify the DM approximation. To summarize, we have reduced the PDE model to a much more manageable set of three non-linear ODEs. These are faster to implement and solve and are not prone to some numeric stability issues afflicting PDEs. However, this comes with some cost, as the resulting distribution only estimates the actual distribution up to the first three raw moments.

The DM model can be thought of as a hyperelastic spring which is prone to damage accumulation and rupture, but not viscous behaviour. Conversely, the Voigt element is capable of reproducing the viscous behaviour like creep, stress relaxation, and hysteresis, but not damage. Solution techniques differ depending on what information is supplied: for example, if the goal is to calculate force from displacement (inverse problem) or vice-versa (forward problem). Both problems are outlined in Barrett and Callaghan (2021).

6.2.2 Model Analysis

This section compares simulations of the model against experimental results. The `solve_ivp` function in the `SciPy` Python environment numerically integrated the differential equations using parameter values in Table 6.1. The forward problem was stiff, and required an implicit Runge-Kutta method (Radau IIA) to solve (Hairer & Wanner, 1999). By contrast, the inverse problem was solved with a fourth-fifth order explicit Runge-Kutta method.

The parameter values are a compromise between **Study I** (Chapter 3) and **Study II** (Chapter 4), and were chosen because they: (*i*) yielded a failure stress of 69 MPa at 0.01 s^{-1} at 47% strain, consistent with **Study I**; and (*ii*) had a relaxation time of 60 s, was similar to what was observed in **Study II**; and (*iii*) resulted in a creep rupture after approximately 2 hours and 16 minutes at 30 MPa. This rupture time aligns with the specimens in **Study II** that experienced failure within 2 hours at magnitudes between 20 and 30 MPa.

Table 6.1: Mechanical parameters used in this investigation.

Parameter	Magnitude	Description	Reference
k_1 (MPa)	340.0	Tissue modulus	**Study II** and **Study I**
η (m/m)	0.02	Slack strain standard deviation	**Study II** and **Study I**
μ (m/m)	-0.06	Mean slack strain	**Study II** and **Study I**
k_2 (MPa)	180.0	Voigt elastic parameter	**Study II**
b_2 (MPa s)	10800	Voigt dashpot parameter	**Study II**
α_0 (s^{-1})	5.2×10^{-5}	Directly proportionate breaking	**Study I**
α_1 (unitless)	5.0×10^{-4}	Strain rate dependent breaking	**Study I**
β (unitless)	24.64	Exponential parameter for the breaking function	**Study I**

Viscoelastic Properties

The model exhibits rate-dependence (Figure 6.2A). The ultimate tensile stress increased from 69 MPa to 101 MPa between strain rates of 0.01 s^{-1} and 1.5 s^{-1}, respectively. This increase is similar to the results of Haut (1983), who found that the failure stresses of rat tail tendons increased from 61 MPa to 108 MPa following a 200-fold increase in the lengthening velocity.

Similarly, the apparent stiffness in the linear region increased with strain rate, from 275 to 339 MPa. This behaviour is consistent with the serial arrangement of rheological

elements. Theoretically, using the parameters in Table 6.1, this apparent stiffness could vary between 118 MPa, at 0 s^{-1}, to 340 MPa, at an infinite strain rate. Intuitively, as the strain rate gets larger, the dashpot in the Voigt element gets stiffer; consequently, the collagen distribution model incurs more of the total tendon strain. This trend is consistent with X-ray diffraction studies; Puxkandl et al. (2002), for instance, showed the strain in the collagen fibrils is often less than half that of the tendon. However, the collagen fibrils sustain a larger share of the total deformation with an increasing strain rate.

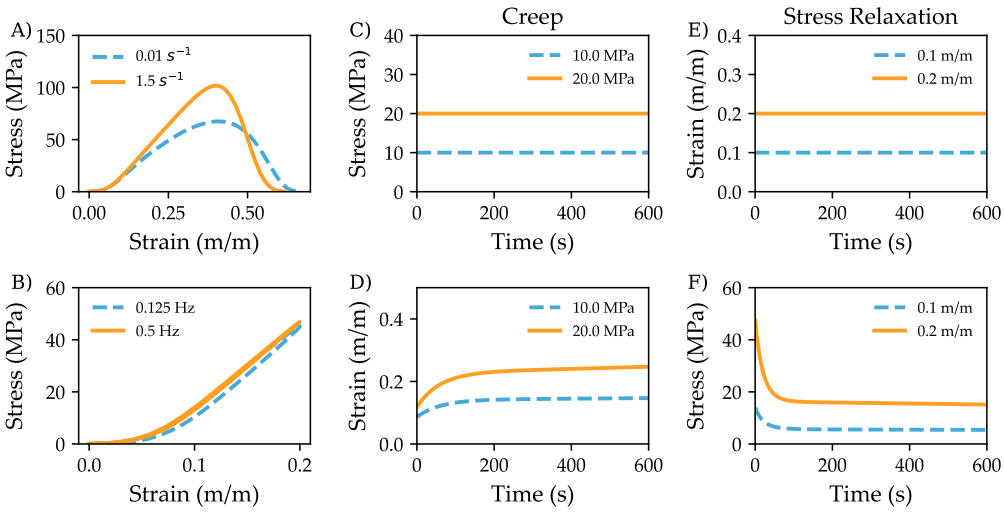

Figure 6.2: Demonstration of the viscoelastic behaviour exhibited by the model. (A) Strain-rate dependence of the resulting stress-strain curve. With a higher strain-rate the model predicts a larger magnitude of stress before complete rupture. (B) Hysteresis, for tendon, is around 1% at the higher frequency of 0.5 Hz compared to 12.2% at 1/8 Hz. (C) and (D) depict the creep response, where the applied stresses are shown in (C) and the resulting strain in (D). (E) and (F) show the same for stress-relaxation, where the applied strains are shown in (E) and the resulting stresses are in (F).

The model exhibited viscoelastic hysteresis (Figure 6.2B), which decreased from 12.2% to 0.1% with an increase of frequency from 1/8 Hz to 1 Hz, displacement controlled to 20% strain. This change also reflects the arrangement of rheological elements since higher frequency oscillations impose more substantial strain rates onto the tissue, and the collagen fibrils uptake most of the total displacement. Since they are purely elastic, they only dissipate energy if they rupture.

The model both creep (Figure 6.2C and 6.2D) and stress-relaxation (Figure 6.2E and 6.2F). The model predicted a first-order decay of strain to an approximate steady-state with a constantly applied stress. With a high-enough magnitude of stress, there is a slight linear trend in the steady-state, owing to the gradual rupture of constituent fibres, which eventually culminated in failure. There is extensive literature on tendons' creep failure, which we will discuss later. On the other hand, the model predicted an exponential decay of stress with a constantly applied strain. As some fibrils rupture at a higher applied displacement, the effective rate of decline appears to vary with the magnitude of applied strain. This effect is similar to what others have observed experimentally (Duenwald, Vanderby, & Lakes, 2009; Troyer et al., 2012); however, using a similar model, Shearer, Parnell, Lynch, Screen, and Abrahams (2020) argued that this phenomenon arises from the fibrils' viscoelasticity. Briefly, if each collagen fibril is capable of stress-relaxation, then when more of the distribution is uncrimped, there are more fibrils that can relax.

Creep Failure of Tendons

Tendons subjected to a constant load eventually rupture, and, at least for cyclic loading, there does not appear to exist an endurance limit: a load magnitude below which the tissue will never fail (Schechtman & Bader, 1997). Creep rupture of tendons manifests as a characteristic S-shaped strain-versus-time curve with three distinct portions. In the primary portion of the curve, the strain rate is substantial but rapidly approaches a minimum. Creep in this portion of the curve is thought to be purely viscoelastic, with very little damage imparted onto the tissue. Following this, there is a secondary creep phase, where the strain in the tissue increases linearly. Finally, there is a tertiary creep phase where the strain rate gradually increases until the tissue has ruptured. The response in cyclic loading is very similar, and the model exhibits both behaviours (Figure 6.3).

Ellis (1978) first applied the Tobolsky-Eyring rate law to the creep failure of rat tail tendons. This rate equation states that the rate by which bonds rupture in a polymer

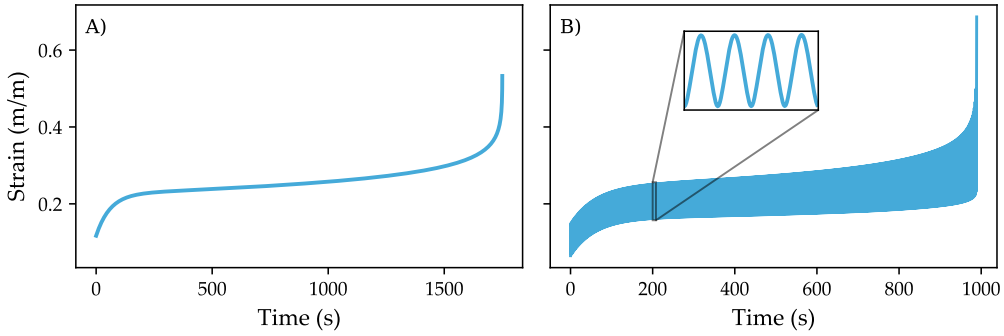

Figure 6.3: (A) creep rupture response of the model under 20 MPa constant applied load. (B) Creep rupture response of the model exposed to a cyclic force that oscillates between 5 and 30 MPa at 0.5 Hz.

grows exponentially with the applied stress according to:

$$-\frac{1}{N}\frac{\mathrm{d}N}{\mathrm{d}t} = w_0 \exp\left(-\frac{U_0 - \gamma_0\sigma}{k_B T}\right) \tag{6.20}$$

Where N is the number of bonds in the cross-section, U_0 is the activation energy required to rupture the chemical bonds, k_B is the Boltzmann Constant, and T is the absolute temperature. The parameters w_0 and γ_0 are called collision parameters due to their application in general chemical kinetics. By assuming that the number of bonds in a given cross-section remains approximately constant (*i.e.* N is constant), and that the lifetime is inversely proportional to the rate of of bond breaking (*i.e.* $t_f \propto (\mathrm{d}N\,/\,\mathrm{d}t)^{-1}$), Ellis (1978) arrived at the expression for the lifetime of a rat-tail tendon exposed to constant loading:

$$\frac{1}{t_f} = A_f \exp\left(-\frac{U_0 - \gamma_0\sigma}{k_B T}\right) \tag{6.21}$$

Which, he simplified to:

$$t_f = \exp\left(\beta_0 + \beta_1\sigma\right) \tag{6.22}$$

Where the experimenter can determine β_0 and β_1 through least-squares parameter estimation. By conducting creep-failure experiments at various temperatures, Ellis was able to

back-substitute to determine U_0 and γ_0 from his data. However, he found that this exponential equation had considerable difficulty fitting his data unless he included a quadratic term in the exponent. This solution was taken, by Ellis, as evidence discrediting the application of the Tobolsky-Eyring rate equation for biological tissues, like tendons (Ellis, 1978).

The current model uses the Tobolsky-Eyring rate equation as the functional form of the breaking function, without the quadratic correction postulated by Ellis. Despite this, when the model simulates creep-rupture experiments, the resulting times to rupture are in remarkable agreement with Ellis' experiment (Figure 6.4). This result suggests that the squared term is unnecessary if one considers the distribution of constituent fibrils in the tendon.

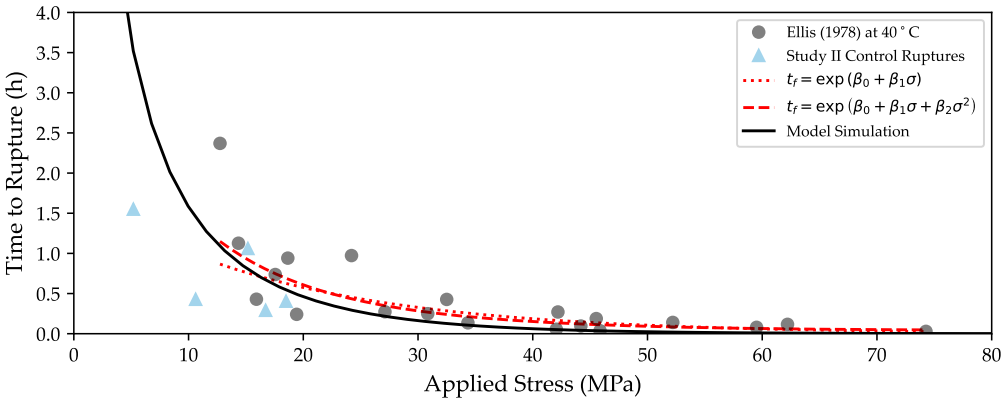

Figure 6.4: Comparison between various models against the data of Ellis (1978). The dotted line is the standard Tobolsky-Eyring theory, dashed is the quadratic exponential postulated by Ellis. In solid black are the simulations results from the current model, using standard Tobolsky-Eyring theory, calibrated with data from **Study I**. For further comparison, the control specimens which ruptured during the creep protocol in **Study II** are plotted as well as the blue triangles.

These simulations motivate the question: what did Ellis overlook in his analysis? In short, the stress in Equation 6.21 distributes among the remaining bonds in the polymer. As more bonds rupture, those remaining pick up the slack, which accelerates the overall rupture process (Ker, 2007). In addition to the paradoxical assumption that N is constant and its derivative is nonzero, Ellis' equation cannot account for this rupture mechanism. This phenomenon was known to Tobolsky and Eyring (1943), and the collagen distribution

model lends itself well to a similar analytic treatment. The intermediate integrals are challenging, but the result for the time to failure as a function of stress is:

$$t_f = -\frac{1}{A}\,\mathrm{Ei}\left(-B\sigma\right) \tag{6.23}$$

Where A and B are parameters related to the breaking function parameters and the effective modulus of the tissue, and $\mathrm{Ei}(\cdot)$ is the Exponential Integral, which does not have a closed-form in terms of elementary functions:

$$\mathrm{Ei}(x) = \int_{-\infty}^{x} \frac{e^t}{t}\,\mathrm{d}t \tag{6.24}$$

For positive x, this integral does not converge in a classical sense but is understood from a limiting process called the Cauchy Principal Value. Unlike the exponential expression that Ellis was working with, this equation rapidly tends to infinity as σ tends to zero. This asymptote is a desirable prediction from a fatigue model, since, intuitively, a material not subjected to any load should not exhibit mechanical failure. Importantly, this expression appears roughly linear on a semi-log plot, implying that the time-to-rupture would obey an exponential relationship with applied stress, an observation upon which many previous investigations have based their inference (Schechtman & Bader, 1997; Ellis, 1978; Wang & Ker, 1995; Wren et al., 2003; Caler & Carter, 1989).

What follows is a derivation of Equation 6.23: the rupture time while under a constant stress, σ, given the collagen distribution model. For simplicity, we will assume that the collagen fibril distribution is Gaussian with constant variance, q^2, whereas the average, $p(t)$, and area under the curve, $Q_0(t)$, vary with time. Under these assumptions, the distribution is approximated as:

$$\rho(x,t) = \frac{Q_0(t)}{\sqrt{2\pi}q}\exp\left(-\frac{(x-p(t))^2}{2q^2}\right) \tag{6.25}$$

Next we assume an effective fibril modulus of elasticity, k, and that all the fibrils are uncrimped, so that the stress in the tendon can be calculated from the integral:

$$\sigma = \int_{-\infty}^{\infty} kx\rho(x,t)\,\mathrm{d}x = kQ_0(t)p(t) \tag{6.26}$$

Where the second equality comes from substituting the Gaussian approximation for $\rho(x,t)$. Since the stress is constant, we have that:

$$p(t) = \frac{\sigma}{kQ_0(t)} \tag{6.27}$$

The rate of change of Q_0 can be found by integrating the PDE model over the whole real line, much like we did when we derived the differential equation for Q_0. This yields:

$$\frac{\mathrm{d}Q_0}{\mathrm{d}t} = -\int_{-\infty}^{\infty} \alpha\exp(\beta x)\rho(x,t)\,\mathrm{d}x \tag{6.28}$$

Substituting in the approximation for $\rho(x,t)$:

$$\frac{\mathrm{d}Q_0}{\mathrm{d}t} = -\frac{\alpha Q_0(t)}{\sqrt{2\pi}q}\int_{-\infty}^{\infty} \exp\left(-\frac{(x-p(t))^2}{2q^2} + \beta x\right)\mathrm{d}x \tag{6.29}$$

The resulting Gaussian integral can be simplified, considerably, to:

$$\frac{\mathrm{d}Q_0}{\mathrm{d}t} = -AQ_0e^{\beta p(t)} \tag{6.30}$$

Where we have defined A to be $\alpha e^{\beta^2q^2/2}$, collecting all the constants together. The final step uses Equation 6.27 to yield the ordinary differential equation:

$$\frac{\mathrm{d}Q_0}{\mathrm{d}t} = -AQ_0e^{B\sigma/Q_0} \tag{6.31}$$

Where $B = \beta/k$ is another grouped constant to clean up the resulting expressions. This equation is very similar to the one analyzed by Tobolsky and Eyring (1943). The appearance of Q_0 in the denominator of an exponential function reflects that the given external stress is resisted only by the remaining collagen fibrils. As more fibrils break, and since the external stress is constant, those that remain necessarily sustain more stress and are thus more likely to rupture. Amazingly, this equation is separable and amenable to integration between 0 and the rupture time, t_f. Doing so, and noting that $Q_0(0) = 1$ and $Q_0(t_f) = 0$, yields the integral:

$$\int_1^0 \frac{1}{Q_0} e^{-B\sigma/Q_0} \, \mathrm{d}Q_0 = -At_f \tag{6.32}$$

This can be evaluated using the substitution $y = -B\sigma/Q_0$, and using the definition of the exponential integral function. The end result is Equation 6.23, as required.

$$t_f = -\frac{1}{A} \operatorname{Ei}(-B\sigma) \tag{6.33}$$

Comparison to Reactive Damage Mechanics

There is a very close relationship between the present mechanical model and conventional reactive damage mechanics theory. Briefly, this theory tracks the time-evolution of a damage parameter, D, which ranges from 0, indicating an intact specimen, and 1, indicating complete rupture. Definitions of this parameter that relate to experimentally measurable quantities are not unique, but a common choice is the ratio of stiffness between the current state of the material and its initial state (Firminger & Edwards, 2021). A similar measure was used in **Study II** to quantify the overall enzymatic degradation of rat tail tendons. This quantity is also directly relatable to the area under the collagen fibril distribution, assuming a unit initial condition:

$$D(t) = 1 - \frac{E(t)}{k} = 1 - Q_0(t) \tag{6.34}$$

Where k is the modulus of the undamaged tissue, $E(t)$ is its instantaneous modulus, and $Q_0(t)$ is the zeroth moment in the DM. Wang and Ker (1995), using an extensive set of experimental observations on wallaby tail tendons, were able to derive a phenomenological relationship for the initial rate of change of the damage parameter and the initially applied stress. After grouping redundant constants, the expression they arrived at was:

$$\left.\frac{\mathrm{d}D}{\mathrm{d}t}\right|_{t=0} = Ae^{B\sigma_0} \tag{6.35}$$

Where σ_0 is the initially applied stress, the vertical bar denotes "evaluated at $t = 0$," and A and B are shape parameters. In their original treatment, Wang and Ker (1995) related these shape parameters to the empirical relationships between the applied stress and the minimum strain rate in the creep experiment, and the applied stress and the magnitude of plastic deformation. Using the relationship between $D(t)$ and $Q_0(t)$, this can be rewritten as:

$$\left.\frac{\mathrm{d}Q_0}{\mathrm{d}t}\right|_{t=0} = -Ae^{B\sigma_0} \tag{6.36}$$

This is precisely what is stated in Equation 6.31, evaluated at $Q_0(0) = 1$, where A and B are related, now, to the breaking parameters and standard deviation of the distribution. To generalize this expression to other times, Wang and Ker (1995) hypothesized that the functional relationship between the applied stress and the rate of damage accumulation would be the same. After applying their arguments for Q_0, the equation for its time-evolution would be:

$$\frac{\mathrm{d}Q_0}{\mathrm{d}t} = -Ae^{B'\sigma/Q_0} \tag{6.37}$$

Where $B' = B/k$. This expression is similar to Equation 6.31, but misses the direct proportionality term with Q_0. This result goes hand-in-hand with their assumption that the form of Equation 6.35 generalizes to other magnitudes of stress. Historically, Wang and Ker (1995) numerically solved this expression for the time to rupture; however, it can

be done analytically as well. One obtains:

$$t_f = \frac{1}{A}\left(e^{-B'\sigma} + B'\sigma \mathrm{Ei}(-B'\sigma)\right) \tag{6.38}$$

Where $\mathrm{Ei}(\cdot)$ is, once again, the exponential integral function. Within the magnitudes of stress that Wang and Ker (1995) were exploring, there is little practical difference between this expression and Equation 6.33 (Figure 6.5). Indeed, when the two relationships are plotted using the parameters reported by Wang and Ker (1995), they are almost identical within the 20 to 120 MPa corridor. However, as the applied stress approaches zero, the distribution model predicts that the time to failure will approach infinity. This notably diverges from the continued linear trend of Equation 6.38 on a semi-log plot. Interestingly, Wang and Ker (1995) had a data point that appeared to be on this upward trajectory around a 10 MPa creep exposure, which they omitted from the subsequent analysis.

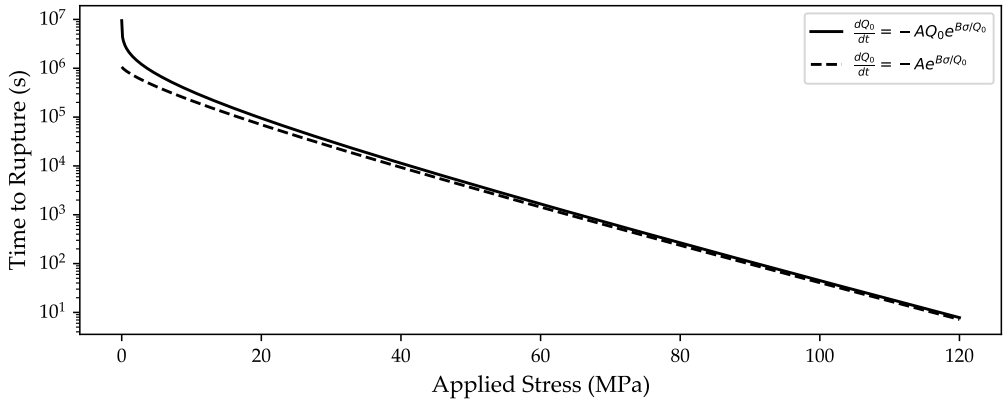

Figure 6.5: Times to rupture predicted from the two differential equation models for the rate of change of Q_0. The solid line comes from approximations based on the collagen distribution model, whereas the dashed line follows from the insightful experimental work of Wang and Ker (1995). Both curves used constants determined from that experiment, $A = 9.38 \times 10^{-7}$ s^{-1} and $B = 0.079$ MPa^{-1}.

Fatigue in Cyclic Loading

Unfortunately, the model is not amenable to similar cyclic loading analyses, but we can analyze numeric simulations. For these simulations, the applied stress oscillates between

a minimum and maximum stress, $\sigma_{\min}$ and $\sigma_{\max}$, respectively, with a frequency f in Hz. The minimum stress was selected to 5 MPa, although other investigations normally use around 10 MPa (Wren et al., 2003; Wang et al., 1995). The minimum is typically chosen to be just outside of the toe region to facilitate the calculation of cycle-varying stiffness (Wang et al., 1995), which, for Wallaby tendons, is around 10 MPa. This magnitude of stress is quite substantial for rat tail tendons, so we selected 5 MPa to be the minimum stress. Additionally, in cyclic loading, we tested two magnitudes of frequency: 0.5 Hz and 2.0 Hz, in order to determine the effect of frequency on the fatigue life predicted by the model.

An S-N curve typically summarizes the results of a cyclic fatigue experiment, where the applied stress (S) is plotted against the number of cycles tolerated until failure (N_f) or the time until rupture (t_f). For tendons, these S-N curves appear linear on a semi-log plot, indicating an exponential relationship (Edwards, 2018; Wren et al., 2003; Wang et al., 1995; Schechtman & Bader, 1997). Additionally, increasing the loading frequency decreases the time to rupture, which is notably different from bone, where the time to rupture is independent of frequency (Zioupos, Currey, & Casinos, 2001; Caler & Carter, 1989). Wang et al. (1995) argued that the mechanism of decreasing time to failure implies a damage mechanism in tendons that may be velocity dependent. To test this hypothesis, we toggled whether α_1 in the model was zero. In other words, we explored what effect the velocity-dependent breaking from **Study I** had on the time until failure under cyclic loading.

The results of this simulation suggest that Wang et al. (1995) may be correct, there may be a velocity-dependent failure mechanism accentuated in cyclic loading compared to static creep (Figure 6.6). Interestingly, when the velocity dependence was omitted from the model, even though the cycles to failure generally increased with frequency, the time-to-failure was unaffected. By contrast, with the velocity-dependent breaking function, though the number of cycles also increased with frequency, the time to failure generally decreased. Unfortunately, experimental work has not been conclusive about this observation. Surprisingly, Wang et al. (1995) report both decreased-time and equal-time observations with increasing frequency. However, a decreased time and increased cycles to failure is entirely

consistent with the experimental work of Zitnay et al. (2020).

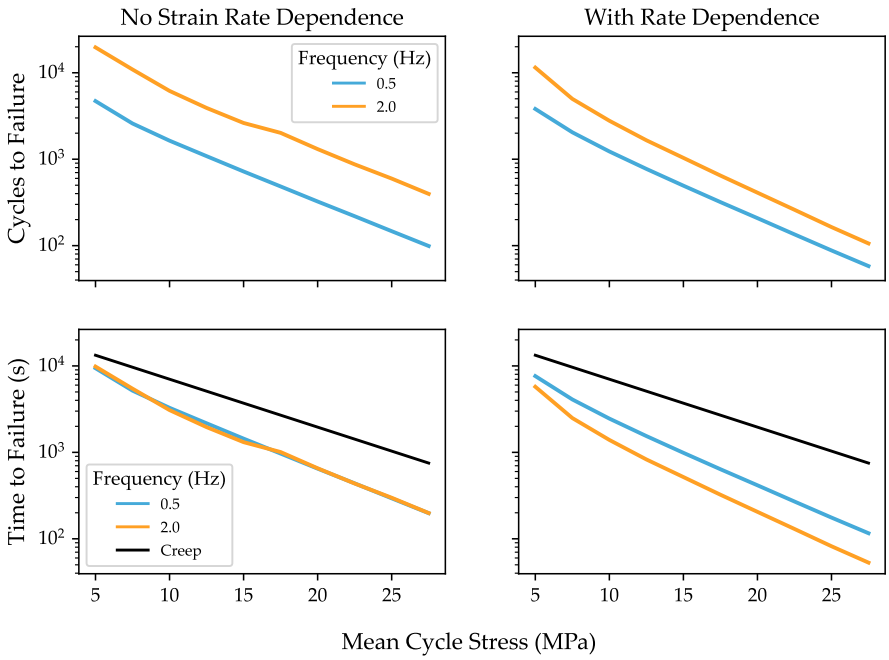

Figure 6.6: Fatigue response of the model to cyclic loading. Top panels depict the number of cycles tolerated until rupture, and the bottom two are time until failure. On the left are the conditions where α_1 was zero, indicating strain-rate independence in the breaking function. Conversely, on the right, the strain-rate dependent term is turned on.

Another standard outcome measure for cyclic fatigue experiments has been cyclic hysteresis and stiffness (Firminger & Edwards, 2021; Wren et al., 2003; Fung et al., 2010). These investigations have typically used a secant-modulus to represent the cyclic stiffness, the linear slope between the minimum and maximum cycle stresses on a stress-strain curve. Since tendons are non-linear, choosing the minimum cycle stress inside the linear region simplifies the secant modulus calculation, as there is no need to account for the toe region. On the other hand, hysteresis is the area between loading and unloading stress-strain curves. It represents the magnitude of dissipated energy per unit volume. We calculated these conventional outcome measures from simulated data to facilitate comparisons to other experiments.

Experiments on cyclic tendon fatigue universally observed a gradual decrease in the cycle stiffness until an abrupt rupture occurred (Firminger & Edwards, 2021; Wren et al., 2003), an observation that usually justified using a change in stiffness as a representative damage parameter. Similarly, Zitnay et al. (2020) explored the accumulation of collagen denaturation throughout the fatigue lifetime of tendons. Their results showed that denatured collagen gradually increased linearly during a fatigue test until rupture, which was remarkably similar to the observed decline in cycle stiffness in Wren et al. (2003). This result is consistent with the current model as well. As the simulated tendon endured more cycles, there was a linear decrease in the effective cycle stiffness, which dramatically decreased once rupture ensues (Figure 6.7). At the same time, the quantity of intact collagen, Q_0, also decreased linearly until the rupture. These simulation results are consistent with the decrease in stiffness and the increase in denatured collagen from these experimental studies.

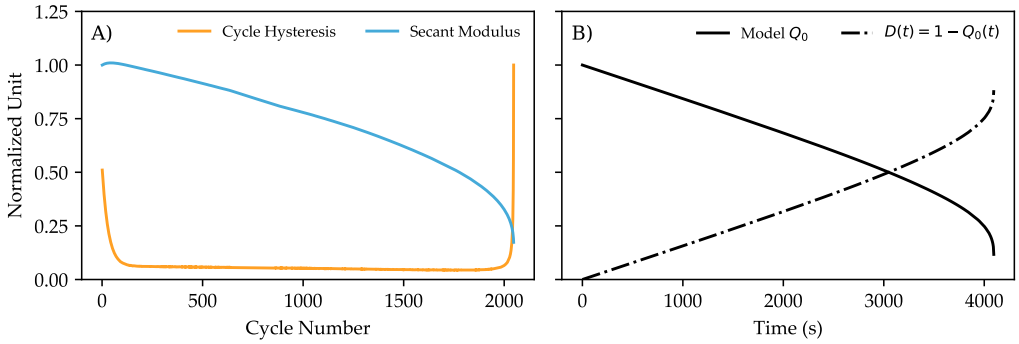

Figure 6.7: Analysis of a cyclic fatigue simulation between 5 and 15 MPa at 0.5 Hz. (A) The gradual decrease in secant modulus until a rupture, along with the U-shaped behaviour of hysteresis. (B) The model parameters, $Q_0(t)$, and the damage parameter, $D(t) = 1 - Q_0(t)$.

Experiments have shown that cyclic hysteresis typically follows a U-shape response, with an initial, rapid decrease in hysteresis through the primary creep phase (Firminger & Edwards, 2021). This decline is followed by a prolonged steady-state through the second phase before an abrupt increase immediately before rupture. The model's response is consistent with these observations (Figure 6.7), where the primary decline in hysteresis was due to elongation in the Voigt element until it reached a steady-state length. At this

point, every subsequent cycle dissipated energy by denaturing or disrupting the collagen fibrils in the model. This observation appeared to be consistent with Zitnay et al. (2020), though these authors measured collagen denaturation without hysteresis. This gradual disruption continued until rupture, which coincided with the beginning of the tertiary phase of creep.

Predictors of Fatigue-Life

Wang and Ker (1995) observed exponential relationships between the minimum strain rate during static creep and the initial peak strain, with the time to rupture for wallaby tendons under constant load. In addition, Firminger and Edwards (2021) quantified the relationship between the number of cycles endured until rupture and a plethora of outcome variables thought to relate to fatigue life. Among these were the creep rate and the median initial strain, similar outcome measures to minimum strain rate and initial strain from Wang and Ker (1995). Here, Firminger and Edwards (2021) defined creep rate as the average rate of change of peak strain in the secondary creep phase. In addition, they explored fatigue life against the peak cyclic stress and the initial damage rate, which Firminger and Edwards (2021) quantified from the ratio of current secant modulus to initial. The role of loading frequency was absent from the analysis of Firminger and Edwards (2021), so we included it to test whether the expected relationships, if present, were constant across loading frequencies. We used the case where the damage had a velocity-dependent component for all these tests.

Taken as a whole, the experimental results from Wang and Ker (1995) and Firminger and Edwards (2021) are suggestive of six empirical relationships, which we divide into exponential or power-law relationships. They suggest that the relationship between fatigue life and initial strain, median initial strain, and peak stress is exponential, much like the earlier work of Ellis (1978). Although, based on the creep-life analysis earlier, it is plausible that the distribution model would predict the relationship between fatigue-life and peak cyclic stress would follow an exponential-integral relationship. Similarly, they also suggest that power-law relationships exist between fatigue life and the minimum strain rate, creep

rate, and initial damage rate. These latter relationships would manifest as linear trends on a semilog plot, whereas the former three would be curvilinear. Using the creep and fatigue simulations from earlier, we tested whether these relationships are consistent with the model.

The relationship between the minimum strain rate in a creep test and the time to rupture was roughly a power-law relationship (Figure 6.8A). Like the exponential-integral type relationship, as the minimum strain rate approached zero, the expected time to rupture tended to infinity. However, there appeared to be a considerable linear trend beyond this asymptote. The time to failure also had a strong relationship with the initial strain (Figure 6.8B), which was roughly exponential, but approached a critical strain for which the tissue failed instantaneously.

The fatigue simulations results were similar to the creep test. Fatigue life and creep rate (Figure 6.8C), like the minimum strain rate in creep, exhibited a roughly power-law relationship that varied with the applied frequency. Similarly, fatigue life was roughly exponentially related to the median initial strain (Figure 6.8D). Fatigue life and peak cyclic stress also exhibited an frquency-dependent exponential relationship (Figure 6.8F). Overall, the only relationship that seemed to be independent of frequency was the power-law relationship between fatigue life and the initial damage rate (Figure 6.8E).

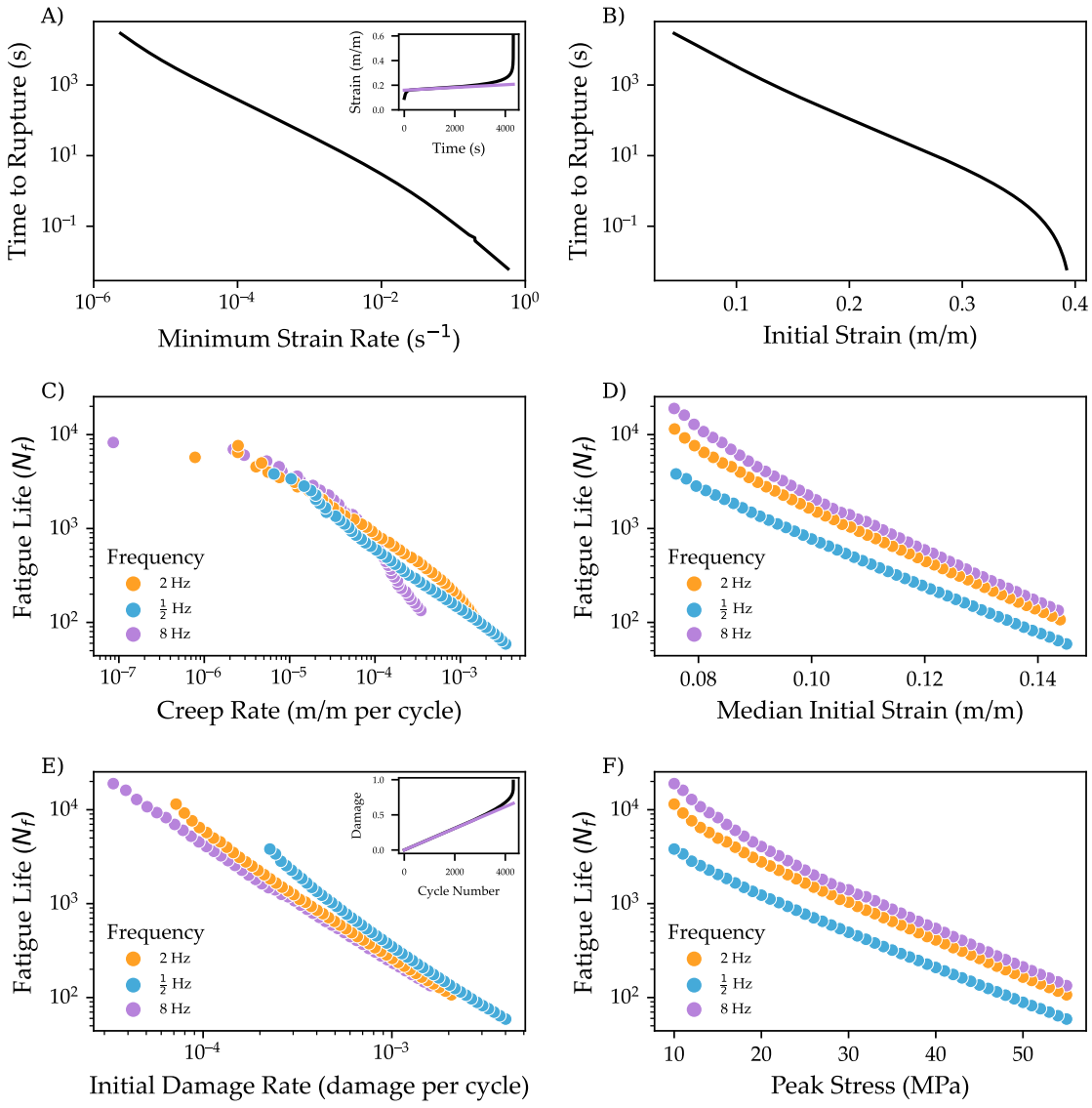

Figure 6.8: Model predictions between the outcome variables assessed in Wang and Ker (1995) and Firminger and Edwards (2021). (A) The quasi-power law relationship between minimum strain rate during the creep simulation and the time to rupture. (B) The predicted exponential relationship between initial initial strain and time to rupture. (C) The (frequency dependent) power-law relationship between creep rate and fatigue-life. (D) The (frequency dependent) exponential relationship between median initial strain and fatigue life. (E) The power-law relationship between fatigue-life and initial damage rate. (E) Exponential relationship between peak cyclic stress and the fatigue life.

6.2.3 Shortcomings

The overall predictions of this model are not egregiously different from the experimentally observed phenomenological relationships. However, the model does make some predictions that are not necessarily in line with published experimental results.

The first is the observation that the relaxation parameters in a stress-relaxation experiment vary with the magnitude of applied strain. Troyer et al. (2012) developed and used a non-linear viscoelastic theory to explain precisely this phenomenon. Similarly, Shearer et al. (2020) showed, using another collagen fibril recruitment-based model, that the macroscopic strain-dependent relaxation behaviour may be an emergent property stemming from relaxation in the fibrils. Supporting this model prediction, Gupta, Seto, Krauss, Boesecke, and Screen (2010) documented stress-relaxation at the fibril level. They suggested that a Voigt-element may represent the fibril-level stress relaxation with the non-collagenous components described as serially attached Maxwell elements. The current model reproduces the strain-dependent relaxation times phenomenon, provided that the magnitude of strain is substantial enough to induce failure in some of the constituent fibrils; however, this is not the currently accepted mechanism. Generalizing the collagen distribution model to more accurate descriptions of fibril-level viscoelasticity remains a potential avenue for future improvement.

Experimental results are suggestive that, with an increased loading frequency, the number of cycles to failure increases, but the time to failure decreases. This analysis showed that having a component of the breaking function directly proportional to the strain rate may be a sufficient condition to produce this effect. This result may be taken, along with the findings from **Study I**, as evidence favouring this velocity-driven component. However, there may be more to this story than simply velocity-dependent rupture. Zitnay et al. (2021) showed that the accumulation of denatured collagen over a fatigue protocol depends on the strain rate. Here, they cyclically loaded rat tail tendon samples to 10% of the (strain rate controlled) ultimate tensile stress at one of three strain rates and measured the magnitude of denatured collagen using fluorescent collagen hybridizing peptide (CHP). This peptide has a fluorescent head and a tail that effectively binds to damaged,

or otherwise denatured, collagen triple helices. At the end of the fatigue-life, they found less denatured triple helices in the highest strain rate condition. This experimental result is not consistent with the present model, which predicts that all the collagen fibrils would be damaged after a rupture, regardless of strain rate.

One possible explanation could be that Zitnay et al. (2021) showed that the mode of collagen damage changes with strain rate. The CHP technique for quantifying denatured collagen is only sensitive to triple helices with one of their constituent alpha-helices sheared. It may be the case that, as the strain rate increases, the failure increasingly occurs at the cross-links, breaking the collagen fibril but leaving the triple helix intact. Another explanation may be that by controlling for the strain rate in the ultimate tensile stress, Zitnay et al. (2021) inadvertently increased the corresponding load on the collagen fibrils in their high strain-rate condition. This imbalance may have biased their highest strain rates toward accruing more mechanical damage.

6.2.4 Summary

This section described the mechanical collagen distribution model. It began with a brief but detailed derivation of the distribution moment approximation to the full PDE model and the inclusion of the serial Voigt-element. Through simulations with some representative parameters, this section also demonstrated that the model produces the hyper-viscoelastic, fatigue, and rupture behaviour characteristic of biological soft tissues. Finally, we reflected on some limitations or shortcomings of the current model and some of its potentially controversial predictions.

The goal of every mechanistic model is to explain more while assuming less, whereas phenomenological models often adapt known empirical relationships in their construction. For example, to make a phenomenological tendon model, one could start by measuring the average stress-strain curve. They could measure the relaxation function and combine it with quasi-linear viscoelastic theory to account for viscoelasticity. To include damage, they could add a damage parameter that evolves in time according to expressions like the one

derived in Wang et al. (1995). As they add more empirical relationships to their model, it becomes more biofidelic, gradually making better predictions.

The current model is neither purely mechanistic nor phenomenological. It makes assumptions about how strain distributes among the collagen fibrils in soft tissues and their non-collagenous matrix viscoelastic properties. Further, it assumes that strain is imparted among the constituent fibrils equally and that they will obey a Tobolsky-Eyring rate equation as they rupture. From these assumptions, the current model predicts a hyper-elastic macroscopic stress-strain curve, viscoelasticity from the non-collagenous matrix constituents, and creep-failure and fatigue properties reminiscent of natural biological tissues. To that end, the inputs to a phenomenological model are generally outputs of a mechanistic one.

We will now touch on the physiological model in much the same way. Unfortunately, there is not as much detailed information on the precise response of fibroblasts to various stimuli, mainly because measuring the concentrations of different biochemical species is extremely difficult. Nevertheless, we will try to explore the specific pathways between damage-sensing and collagen adaptation.

6.3 Biochemical Model

This section describes the development of a simplified mathematical model of a fibroblast based on Systems Biology. Much more detailed models exist in the literature (Zeigler, Richardson, Holmes, & Saucerman, 2016), but they are often so complicated or include so much detail that they are not amenable to analysis. This derivation is also where the current iteration of the model takes a more phenomenological tone, often simplifying entire families of chemical species into one variable. Several investigations have used similar reduced models to investigate the behaviour of an acute inflammation response to a pathogen (Reynolds et al., 2006; Day et al., 2006; Clermont et al., 2004; Schroer, Ryzhova, & Merryman, 2014).

6.3.1 Model Description

In a nutshell, the model tracks the time evolution of seven chemical species. The first is a biomarker of damage, which we call $\hat{D}$, that drives the downstream physiological response. After sensing $\hat{D}$, fibroblasts respond by secreting a pro-inflammatory signal, $\hat{P}$. These molecules usually rally the innate immune system to the potential injury site to fight off possible microbial invaders. Fibroblasts also express receptors for pro-inflammatory molecules, whose activation leads to their feedforward expression. In addition, in this pro-inflammatory milieu, fibroblasts increase the expression of proteases and their inhibitors, which the model calls $\hat{Y}$ and $\hat{I}$, respectively, and decreases the expression of collagen, which the model tracks as $\hat{S}$. Paradoxically, activation of these pathways also seems to increase the secretion of an anti-inflammatory signal, which we call $\hat{A}$. This abstracted anti-inflammatory signal combines growth factors and inhibitors of the feedforward pro-inflammatory signal and leads to the downstream expression of protease inhibitors and collagen. For simplicity, we assume that the proteases break down the initial damaging biomarker, as they do in the case of decorin (Anders & Schaefer, 2014), enabling the system to turn itself off. Decorin is one of the myriad glycoproteins that inhabits the ECM and typically forms a complex with collagen—hence it decorates the collagen (Vu et al., 2018). It also happens that free decorin is a potent stimulator of inflammation.

We derive equations for the time-evolution of these six chemical species, $\hat{P}$, $\hat{I}$, $\hat{D}$, $\hat{A}$, $\hat{Y}$, and $\hat{S}$ using a Systems Biology approach based on the reaction network summarized in Figure 6.9. The final, seventh member of this model, not shown on the figure, is the existing collagen fibrillar network, $\hat{C}$, that newly synthesized collagen can incorporate with and which is vulnerable to deterioration by MMPs.

Each of the lines connecting species and arrows in Figure 6.9 corresponds to a specific type of enzyme or receptor interaction whose governing equations obey a Michaelis-Menton or Hill-equation (Ingalls, 2013). This derivation will step through all the sub-models of the system, starting with $\hat{D}$ promoting the self-amplification of $\hat{P}$, and gradually account for all the interactions depicted in that network. Analyzing some of the sub-models can be enlightening for exploring the behaviour of the fully assembled model.

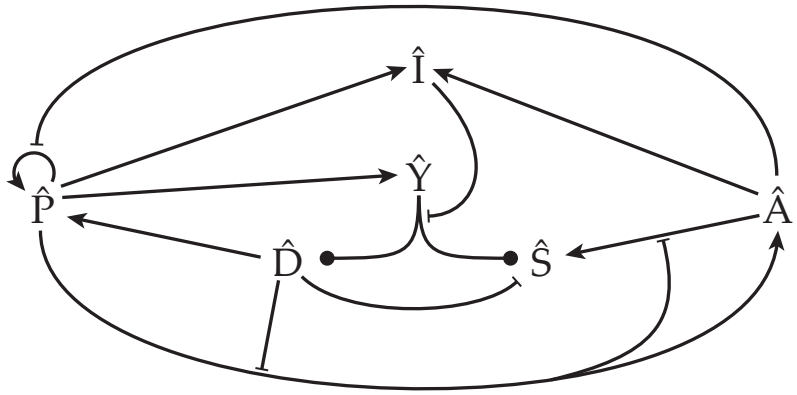

Figure 6.9: A network diagram demonstrating the complicated web of interactions among the six species in the biochemical model. Normal arrows between two species, for example $A \to B$, can be read as "A increases the expression of B". Arrows ending with $\perp$ can be read "A inhibits this reaction." Arrows ending dots indicate degradation.

Biochemical studies are excellent for isolating the specific arrows in the reaction network; however, due to the nested series of interactions, it can be relatively challenging to intuit how the fully assembled system may behave. On the other hand, physiological studies excel at observing the global systemic response to a stimulus but are somewhat limited by what inferences they can place on specific reactions. Systems Biology bridges these gaps by using quantitative techniques to predict how the reaction network, with its counter-intuitive sets of responses, will respond to a given stimulus.

Sensing and Responding to Mechanical Damage

To maintain homeostasis, resident fibroblasts of connective tissues—like tendons, ligaments and IVD—need to sense the presence of damage. This treatment will focus on an inflammation-mediated hypothesis, but precisely how fibroblasts detect damage is still uncertain.

Fibroblasts are honourary members of the immune system (Correa-Gallegos, Jiang, & Rinkevich, 2021). They express toll-like receptors (TLR) (Krock et al., 2016; Jang, Park, Won, Yun, & Kim, 2012; Huebener & Schwabe, 2013), which enable them to sense both Damage Associated Molecular Pattern (DAMP) and pathogen-associated molecular patterns (PAMP). In this way, fibroblasts play the role of sentinels for the immune system,

early detectors of potential damage and microbial infection. They respond, in turn, by secreting pro-inflammatory cytokines, which have the effect of summoning the patrolling cells of the innate immune system: macrophages, neutrophils and natural killer cells. In addition, fibroblasts also express receptors for these cytokines, leading to a self-activation or autocrine effect (Newton & Dixit, 2012; Kessler-Becker, Krieg, & Eckes, 2004; West-Mays, Strissel, Sadow, & Fini, 1995).

Proteoglycans, like decorin, typically form a complex with type I collagen. Mechanical damage to collagen liberates these proteoglycans from their complexes, which the fibroblast, using their TLR-receptors, can sense as DAMPs (Roh & Sohn, 2018; Newton & Dixit, 2012). This mechanism may occur in conjunction with another hypothesis for damage-sensing, mechanotransduction (Arnoczky, Tian, Lavagnino, & Gardner, 2004; Archambault et al., 2002), but we will neglect this mechanism for now. Other molecules may also play the role of DAMP for damage sensing, like free fibronectin. This glycoprotein adheres resident fibroblasts to the collagen network of the ECM (Roh & Sohn, 2018).

Downstream of TLR-mediated sensing of DAMPs, the fibroblast secretes pro-inflammatory cytokines (Roh & Sohn, 2018). To mathematically model this relationship, we will let $\hat{D}$ represent the (dimensionless) concentration of DAMPs in the ECM . Later, this will be the avenue for combining the mechanical and biochemical models. Further, we will let $\hat{P}$ represent the amount of pro-inflammatory cytokines. There are many such cytokines, the most ubiquitous of which are IL-1α, IL-1β and TNF-α. It suffices to group them into a single, representative, pro-inflammatory cytokine for this reduced mathematical model. So far, assuming that the receptor-binding and downstream signalling obeys a Hill-function, the differential equation for $\hat{P}$ is:

$$\frac{\mathrm{d}\hat{P}}{\mathrm{d}t} = \frac{\beta_D \hat{D}^m}{1+\hat{D}^m} + \frac{\alpha_P \hat{P}^n}{1+\hat{P}^n} - \delta_P \hat{P} \tag{6.39}$$

Where $\hat{\alpha}_P$ represents the maximum expression rate of $\hat{P}$ from the autocrine signalling, and $\hat{\beta}_D$ is that downstream of DAMP sensing. The last parameter in this expression, δ_P, is the decay constant for the pro-inflammatory signal, which, for IL-1β, gives a half-life of approximately 4 hours (Hazuda, Lee, & Young, 1987). The Hill-coefficients, n and

m, describe the *ultra-sensitivity* of the intracellular signalling pathways (Huang & Ferrell, 1996): the higher these powers, the more the pathway behaves like an ideal switch. Hill coefficients for the Mitogen Activated Protein Kinase (MAPK) cascade downstream of IL-1β and toll-like receptors are typically around 3 or 4 (Dower & Qwarnstrom, 2003). For the initial model in this derivation, we will use 4.

This single differential equation possesses some desirable properties of the interleukin-1 system. The first, as mentioned above, is ultra-sensitivity or a step-like response to increasing amounts of pro-inflammatory cytokines. The second is hysteresis, which refers to history-dependent behaviour much like mechanical hysteresis (Figure 6.10). In this case, the loading and unloading curves refer to increasing and decreasing concentrations of the DAMP, $\hat{D}$. With no DAMPs present, Equation 6.39 has one steady state corresponding to no expression of pro-inflammatory cytokines. However, as $\hat{D}$ increases, eventually, three steady states become viable, following what mathematicians would call a saddle-node bifurcation (shown on Figure 6.10A) (Strogatz, 2018; Ingalls, 2013). Two of these steady states are stable and correspond to high and low expressions of inflammatory cytokines; meanwhile, the third is between the two and is unstable.

When the amount of pro-inflammatory cytokines is low and increasing, the system evolves toward the low-inflammation steady state, with no obvious way to cross over to the high-concentration equilibrium (Figure 6.10B). This pattern continues until the system reaches a critical magnitude of DAMP concentration, at which point another saddle-node bifurcation occurs, and the low-concentration node vanishes. The system rapidly equilibrates at the high-concentration stable, steady-state, indicating a change to a pro-inflammatory phenotype. Decreasing the concentration of DAMPs from this point does not automatically return the fibroblast to low-inflammation. Instead, the magnitude of DAMPs must decrease beyond the first bifurcation when the system had a single steady-state and no inflammation present. This process manifests as a hysteresis loop since the system's evolution depends on its history (Figure 6.10B).

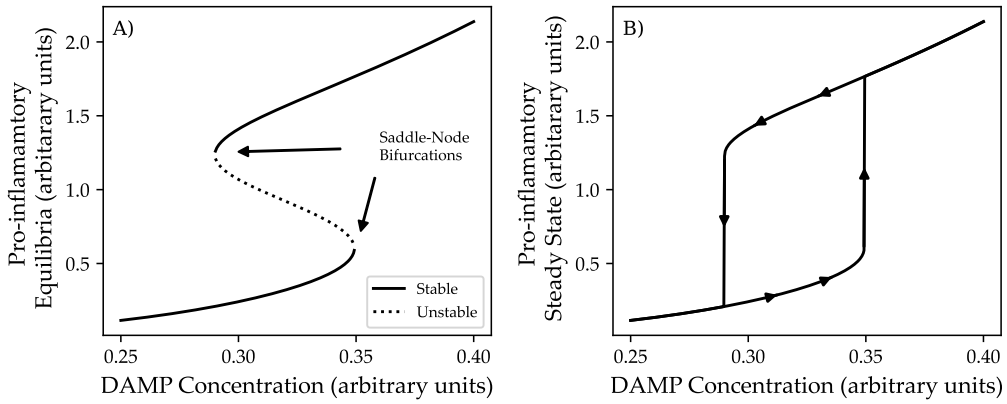

Figure 6.10: Ultrasensitivity and hysteresis in the pro-inflammatory cascade, holding $\beta_D = 5.0$, $\alpha_P = 0.25$, and $\delta_P = 0.17$. (A) depicts a bifurcation diagram for Equation 6.39 with varying magnitudes of $\hat{D}$. Stable steady-states are represented by the solid lines and the unstable equilibrium with the dotted line. In (B) numerical simulations with increasing and decreasing $\hat{D}$ demonstrating a considerable hysteresis loop.

The Anti-Inflammation Signal

Anti-inflammatory chemokines are expressed downstream of pro-inflammatory cytokines , including growth factors like transforming Transforming Growth Factor-β (TGF-β) (Lu, Tian, Han, Vogelbaum, & Stark, 2007) and the anti-inflammatory cytokines, IL-10 and IL-1Ra (Martel-Pelletier et al., 1993). These anti-inflammatory chemicals inhibit the feed-forward expression of pro-inflammatory cytokines (de Waal Malefyt, Abrams, Bennett, Figdor, & De Vries, 1991; Choi et al., 2006; Ozbabacan et al., 2014) but are themselves inhibited by DAMPs, for instance decorin (Droguett, Cabello-Verrugio, Riquelme, & Brandan, 2006; Zhang et al., 2009). Converting these observations to differential equations requires modifying the pro-inflammatory signal slightly to account for this complicated inhibition web.

$$\frac{\mathrm{d}\hat{P}}{\mathrm{d}t} = \frac{\beta_D \hat{D}^n}{1+\hat{D}^n} + \frac{\alpha_P \hat{P}^n}{\left(1+\frac{\hat{A}}{\gamma_A}\right)^n + \hat{P}^n} - \delta_P \hat{P} \tag{6.40a}$$

$$\frac{\mathrm{d}\hat{A}}{\mathrm{d}t} = \frac{\alpha_A \hat{P}^n}{\left(1+\frac{\hat{D}}{\gamma_D}+\frac{\hat{A}}{\gamma_A}\right)^n + \hat{P}^n} - \delta_A \hat{A} \tag{6.40b}$$

Where β_D, α_P and δ_P are, as before, the maximum expression rate, feedforward rate and degradation rate for the pro-inflammatory cytokines. In addition, similar parameters exist for the anti-inflammatory signal as well: α_A and δ_A describe the maximum expression and the decay rates. Two more parameters, γ_D and γ_A, represent the normalized inhibition concentrations for the two inhibitors in this pathway. The first, γ_D, quantifies the potency of DAMP inhibition on the expression of anti-inflammatory metabolites. The second, γ_A, represents the normalized inhibition constant for the anti-inflammatory pathway on the pro-inflammatory feedforward loop.

Being a normalized coefficient, γ_D is the ratio of the association constant between decorin and TGF-β, between 92 and 200 nM (Baker et al., 2009; Hildebrand et al., 1994), and the association constant between decorin and the TLR-2 receptor, on the order of 59 nM (Merline et al., 2011). The minuscule concentrations represented by these parameters are illustrative of the sensitivity of these pathways to changes in decorin levels. For comparison, using the 40 kDa molar mass of decorin, the TLR-2 receptor would be half-activated by half a gram of decorin, roughly a grain of sand, in a single cup of coffee.

The last inhibitory parameter, γ_A, is normalized in a similar way to γ_D; defined as the inhibitory concentration normalized to the receptor's half-concentration. For example, the anti-inflammatory cytokine, IL-1Ra, is a competitive inhibitor for the IL-1β receptor. Further, that receptor's affinity to IL-1Ra is on the order of 270 pM (Arend et al., 1994). Another element to the anti-inflammatory signal is TGF-β, which is a family of three growth factors, that roughly bind to their receptor with half-concentrations around 30 pM (Frolik, Wakefield, Smith, & Sporn, 1984).

Note that the two variables, $\hat{A}$ and $\hat{P}$, are normalized to their respective receptor's half-concentrations, ligand concentrations that correspond to half-occupation of relevant receptors. Binding affinities for IL-1β are on the order of 110 pM (Kasai et al., 1990), which is a similar order of magnitude to that of TGF-β, 30 - 140 pM (Frolik et al., 1984; Massague & Like, 1985). Working with dimensionless variables is often more convenient since having two or three variables at substantially different orders of magnitude can make interpreting simulations daunting. In addition, this normalization lends a physiological interpretation to a variable being around 1.0. This threshold is roughly the concentration

necessary to activate the downstream signal transduction without an inhibitor.

The parameters δ_P and δ_A represent the decay rates of the two inflammation signals. They are related to the half-lives of the species by $t_{1/2} = \frac{\ln 2}{\delta}$, which in the blood is roughly 1 to 4 hours for both IL-1β and TGF-β (Jin, Han, Berger, Dai, & Lindsey, 2011). Mathematical models which have lumped biochemical species similar to what we have done here typically extended these half-lives to account for other cellular processes that are abstracted away; for instance, the migration of leukocytes which amplify and extend these signals (Day et al., 2006). For this reason, we have selected a 3-hour half-life for the pro-, and a 5-hour half-life for the anti-inflammatory signals (Kudlow, Cheung, & Bjorge, 1986).

Collagen Synthesis and Degradation

Before including collagen in the model, it is essential to distinguish between the existing, fully polymerized collagen network in the ECM and newly synthesized monomeric collagen. Monomeric collagen is the most accessible place to start since fibroblasts manufacture collagen downstream of growth-factor sensing (Millar et al., 2017; Arend, 2002), a process substantially inhibited by pro-inflammatory cytokines (Dinarello et al., 2002). Further, new collagen can be cleaved by MMPs in a process well-described by standard Michaelis-Menten kinetics, where one molecule of MMP-1 can cleave between 25 and 54 molecules of collagen every hour (Welgus, Jeffrey, Stricklin, Roswit, & Eisen, 1980; Amar, Smith, & Fields, 2017; Tzafriri, Bercovier, & Parnas, 2002). Taken together, this implies an appropriate form for the synthesis of collagen monomers as:

$$\frac{\mathrm{d}\hat{S}}{\mathrm{d}t} = \frac{\alpha_S \hat{A}^n}{\left(1 + \frac{\hat{P}}{\gamma_P}\right)^n + \hat{A}^n} - \frac{h_{cat}\hat{Y}\hat{S}}{1 + \hat{I} + \hat{S} + \frac{\hat{D}}{\varepsilon_D} + \kappa\hat{C}} - \beta_S \hat{S} \tag{6.41}$$

Here, the first term represents the synthesis of collagen downstream of growth-factor stimulation, where the maximum rate of synthesis is given by α_S, approximately six-minutes per collagen molecule (Vuust & Piez, 1972). As indicated, the pro-inflammatory

signal inhibits this process, with a normalized inhibition constant of γ_P. Much like the previous two inhibition parameters, γ_P is the inhibition concentration of pro-inflammatory molecules normalized to the half-concentration of their receptor. This part of the model is challenging to infer since the pro-inflammatory signal does not explicitly inhibit the anti-inflammatory one in traditional ways. Instead, the pro-inflammatory influence over its opposing pathway occurs intra-cellularly by interfering with the common signal transduction pathways. Nevertheless, Graham, Willey, Adams, Yager, and Diegelmann (1996) showed that a dose of 100 pM of IL-1β downregulated type I collagen synthesis by 85%. Using a Hill-coefficient of 4, as we are using in the model, we estimate an inhibitory concentration of 164 pM, which we will take as a representative magnitude for this parameter.

The middle term represents the familiar Michaelis-Menten governed cleavage of new collagen by MMPs ($\hat{Y}$) with catalytic efficiency h_{cat}, the enzyme's activity divided by the Michaelis constant, between 25 and 54 μM^{-1} h^{-1} (Welgus et al., 1980; Amar et al., 2017; Tzafriri et al., 2002). This process is prone to competitive inhibition by the presence of TIMPs, $\hat{I}$, the existing collagen network, $\hat{C}$, and DAMPs, $\hat{D}$. The DAMP concentration is normalized by ε_D, which is a non-dimensionalized Michaelis-Menten constant. The final term represents the rate at which newly synthesized collagen incorporates into the fibrillar network. The formation of fibrils by fibrillar collagens occurs spontaneously, although chaperone proteins, namely heat-shock protein 47, made by the fibroblast, accelerate the process (Nagata, 1996). By this mechanism, roughly half of the newly synthesized collagen is incorporated into the network every 40-50 minutes (Kreger et al., 2010).

The final constant in Equation 6.41 is $\kappa(x)$, and it represents the fraction of collagen molecules in the fibrillar network that are susceptible to MMP-mediated cleavage. MMPs cannot freely diffuse into the microfibrils' tightly packed fibrillar network; therefore, only a tiny fraction, arguably about 10% (Welgus et al., 1980), of the total collagen in tissue is available for degradation. However, based on the ratio of the average fibril radius (250 nm) to that of the collagen molecule (602 pm) (Hulmes & Miller, 1979), we estimate that this fraction is closer to 1% (Figure 6.11). Tzafriri et al. (2002) conducted a similar analysis and even accounted for the decrease in fibril radius as degradation occurs. This analysis leads to two differential equations rather than one, and it is not immediately apparent how

to account for the presence of inhibitors. For collagen concentrations much larger than $K_m \approx 1.0$ μM, a constant fibril radius approximation closely matches Tzafriri et al. (2002), but we note that the model's accuracy is questionable at low collagen concentrations. What is apparent is that unadjusted Michaelis-Menten kinetics leads to an unphysiologically rapid decrease in collagen content (Figure 6.11).

To estimate κ, we analyze a single cylindrical fibril with radius R_f (250 nm) and length L (Figure 6.11), composed of collagen molecules with radius r_{col} (602 pm) and volume v_{col} (335 nm^3) that pack into the fibril with packing density ϱ (between 37 and 80% (Hulmes, Wess, Prockop, & Fratzl, 1995)). The total volume of the fibril is $\pi R_f^2 L$, which implies that it contains $n_{\text{total}} = \pi \frac{\varrho}{v_{col}} R_f^2 L$ total collagen molecules. To first order, the outer shell of this fibril with thickness $2r_{col}$ has an approximate volume of $4\pi R_f r_{col} L$. Thus, it contains roughly $n_{\text{grey}} = 4\pi \frac{\varrho}{v_{col}} R_f r_{col} L$ collagen molecules, which represent those that are vulnerable to enzymatic cleavage. The parameter, κ, is then the ratio of n_{grey} to n_{total}, or:

$$\kappa = \frac{n_{\text{grey}}}{n_{\text{total}}} = 4\left(\frac{r_{col}}{R_f}\right) \approx 9.6 \times 10^{-3} \tag{6.42}$$

The model can now incorporate adaptations to the existing collagen network with this correction factor in mind. The rate of change of collagen in the network is simply the rate of newly synthesized collagen incorporated into the network, less the rate of degradation by MMPs. Collagen in a soft-tissue fibrillar network is incredibly stable, with an estimated half-life of almost 200 years (Thorpe et al., 2010), which is prolonged even longer once mineralized. Amazingly, dinosaur fossils still exhibit an appreciable amount of intact mineralized collagen from their skin (Lingham-Soliar & Wesley-Smith, 2008). Neglecting natural decay, the differential equation takes the form:

$$\frac{\mathrm{d}\hat{C}}{\mathrm{d}t} = \beta_S \hat{S} - \frac{\kappa h_{cat} \hat{Y} \hat{C}}{1 + \hat{I} + \hat{S} + \frac{\hat{D}}{\varepsilon_D} + \kappa \hat{C}} \tag{6.43}$$

Where h_{cat}, ε_D, and β_S are, as before, the catalytic efficiency, dimensionless Michaelis-constant for DAMPs, and the rate constant for collagen network incorporation.

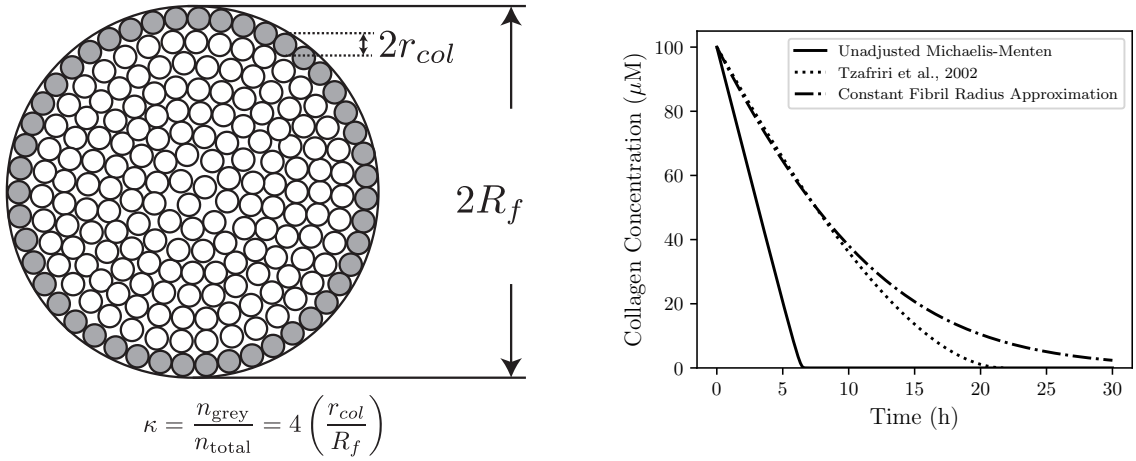

Figure 6.11: Only the collagen molecules on the fibril periphery are accessible to MMPs (left), and the fraction that are can be approximated from the ratio of the fibrillar radius to that of the molecule. Accounting for this accessibility leads to a very different predicted concentration-versus-time curve (right), which is further complicated by accounting for the potential decrease in fibrillar radius. Simulations assume a 250 nm fibrillar radius, a 602 pm molecular radius, 400 nM concentration of MMP-1, k_{cat} =54 h^{-1}, $K_m = 1.0$ μM, and an initial concentration of 50 μM collagen.

MMP and TIMPs

MMPs are expressed downstream of pro-inflammatory cytokine stimulation and inhibited by anti-inflammatory molecules (Arend et al., 1994; Tsuzaki et al., 2003), generally following the rule that most chemicals fall into one of the two pathways. TIMPs are the only exception to this rule, upregulated by both pro- and anti-inflammatory stimuli (Kunisch, Kinne, Alsalameh, & Alsalameh, 2016; Ciechomska, O'Reilly, Suwara, Bogunia-Kubik, & van Laar, 2014). These two species explicitly interact, since the role of TIMPs is to directly inhibit MMP activity through competitive inhibition. Together, these observations imply the structure of three differential equations for these species:

$$\frac{\mathrm{d}\hat{I}}{\mathrm{d}t} = \frac{\alpha_I \hat{A}^n}{\left(1+\frac{\hat{P}}{\gamma_P}\right)^n + \hat{A}^n} + \frac{\beta_I \hat{P}^n}{\left(1+\frac{\hat{A}}{\gamma_A}\right)^n + \hat{P}^n} - \delta_I \hat{I} \tag{6.44a}$$

$$\frac{\mathrm{d}\hat{Y}}{\mathrm{d}t} = \frac{\alpha_Y \hat{P}^n}{\left(1+\frac{\hat{A}}{\gamma_A}\right)^n + \hat{P}^n} - \delta_Y \hat{Y} \tag{6.44b}$$

Where α_I and β_I are the rates of synthesis of TIMPs from the pro- and anti-inflammatory pathways, reciprocally inhibited by each other. Similarly, α_Y is the maximum synthetic rate for MMPs downstream of inflammation. Like intact collagen, newly synthesized collagen is also susceptible to enzymatic cleavage by MMPs. TIMPs directly inhibit this turnover, and since MMPs also process the DAMP signal, to too do DAMPs. The parameter ε_D is a normalized version of the Michaelis-Menten constant for DAMP processing by MMPs. It is the ratio of the unnormalized Michaelis-Menten half-rate concentration, between 0.2 and 10 μM (Imai, Hiramatsu, Fukushima, Pierschbacher, & Okada, 1997; Mayne & Robinson, 1999), and the association constant with the TLR-receptor, roughly 59 nM (Merline et al., 2011).

Finally, the parameters, δ_I and δ_Y, describe the degradation rates for TIMPs and MMPs, respectively. MMPs tend to be long-lasting proteins with half-lives on the order of two-days or longer (Escuer, Martínez, McGinty, & Peña, 2019; Boyle, Lennon, & Prendergast, 2011). By contrast, TIMPs are short-lived, and some efforts have been made to extend their half-lives in the serum for therapeutic applications (Batra et al., 2012), but it is not clear how long they would last in the tissues in the absence of renal processing. We chose a 48-hour half life, since this gave a TIMP-response that was reminiscent of some physiological work (Knight et al., 2019).

Resolution of DAMPs

Due to the ongoing expression of potentially damaging enzymes, it is imperative to turn off the inflammatory response. To do this, the initiating biomarker, the DAMP, must be exterminated. In the case of decorin, MMP processing renders it ineffective, which comes at the cost of cleaving undamaged collagen. TIMPs and, through competitive inhibition, newly synthesized collagen inhibits MMP's activity on the intact collagen network. Together, these assumptions close the equations by describing the rate of change of the

DAMP:

$$\frac{\mathrm{d}\hat{D}}{\mathrm{d}t} = \frac{\kappa v_{cat}\hat{Y}\hat{C}}{1+\hat{I}+\hat{S}+\frac{\hat{D}}{\varepsilon_D}+\kappa\hat{C}} - \frac{k_{cat}\hat{Y}\hat{D}}{1+\hat{I}+\hat{S}+\frac{\hat{D}}{\varepsilon_D}+\kappa\hat{C}} - \delta_D\hat{D} \tag{6.45}$$

Here, the first term represents the production of new DAMPs from the action of MMPs on the native collagen population in the tissue. Similarly, the second term is the depletion of DAMPs from their processing by MMPs. The parameter, ε_D, is as before, a renormalized kinetic constant for DAMPs being processed by MMPs. Likewise, the constant k_{cat} is the catalytic efficiency, normalized to the half-concentration. Finally, v_{cat} describes the rate of production of new DAMPs from MMP-mediated cleavage of the existing collagen network. Here, we have grouped the stoichiometric ratio between collagen and decorin into v_{cat}. Based on the decorin content of tendons (Matuszewski et al., 2012), we estimate the collagen-to-decorin ratio to be roughly 651:1.

Assembling the Whole Reaction Network

The fully assembled reaction network takes the form of seven ordinary differential equations, using Hill-functions to represent receptor and signal transduction pathways and Michaelis-Menten kinetics for enzymatic degradation. The final, fully assembled system

takes the form (with parameters summarized in Table 6.2):

$$\frac{\mathrm{d}\hat{P}}{\mathrm{d}t} = \frac{\beta_D \hat{D}^n}{1+\hat{D}^n} + \frac{\alpha_P \hat{P}^n}{\left(1+\frac{\hat{A}}{\gamma_A}\right)^n + \hat{P}^n} - \delta_P \hat{P} \tag{6.46a}$$

$$\frac{\mathrm{d}\hat{I}}{\mathrm{d}t} = \frac{\alpha_I \hat{A}^n}{\left(1+\frac{\hat{P}}{\gamma_P}\right)^n + \hat{A}^n} + \frac{\beta_I \hat{P}^n}{\left(1+\frac{\hat{A}}{\gamma_A}\right)^n + \hat{P}^n} - \delta_I \hat{I} \tag{6.46b}$$

$$\frac{\mathrm{d}\hat{D}}{\mathrm{d}t} = \frac{\kappa v_{cat} \hat{Y} \hat{C}}{1+\hat{I}+\hat{S}+\frac{\hat{D}}{\varepsilon_D}+\kappa\hat{C}} - \frac{k_{cat} \hat{Y} \hat{D}}{1+\hat{I}+\hat{S}+\frac{\hat{D}}{\varepsilon_D}+\kappa\hat{C}} - \delta_D \hat{D} \tag{6.46c}$$

$$\frac{\mathrm{d}\hat{A}}{\mathrm{d}t} = \frac{\alpha_A \hat{P}^n}{\left(1+\frac{\hat{D}}{\gamma_D}+\frac{\hat{A}}{\gamma_A}\right)^n + \hat{P}^n} - \delta_A \hat{A} \tag{6.46d}$$

$$\frac{\mathrm{d}\hat{Y}}{\mathrm{d}t} = \frac{\alpha_Y \hat{P}^n}{\left(1+\frac{\hat{A}}{\gamma_A}\right)^n + \hat{P}^n} - \delta_Y \hat{Y} \tag{6.46e}$$

$$\frac{\mathrm{d}\hat{S}}{\mathrm{d}t} = \frac{\alpha_S \hat{A}^n}{\left(1+\frac{\hat{P}}{\gamma_P}\right)^n + \hat{A}^n} - \frac{h_{cat} \hat{Y} \hat{S}}{1+\hat{I}+\hat{S}+\frac{\hat{D}}{\varepsilon_D}+\kappa\hat{C}} - \beta_S \hat{S} \tag{6.46f}$$

$$\frac{\mathrm{d}\hat{C}}{\mathrm{d}t} = \beta_S \hat{S} - \frac{\kappa h_{cat} \hat{Y} \hat{C}}{1+\hat{I}+\hat{S}+\frac{\hat{D}}{\varepsilon_D}+\kappa\hat{C}} \tag{6.46g}$$

Despite the complexity of these equations, we have systematically derived them using Michaelis-Menten kinetics for enzyme behaviour and Hill functions to represent cell-surface receptors and their downstream signalling cascades. Where possible, we have made parameter definitions and their interpretations transparent. Unfortunately, many are not available, nor are there appropriate data available to fully calibrate the model. We will, for now, note that tuning many of the parameters, primarily the production rates, is a task that lies ahead. Nevertheless, we will analyze some of the behaviour using a set of parameters that, at least qualitatively, reproduces the accepted sequence of events during acute inflammation.

Table 6.2: Selected parameters for the mostly non-dimensionalized biochemical model, with a brief explanation of each parameter.

Parameter	Magnitude	Description & Justification
Production Rates[a]		
β_D (h^{-1})	5.0	Production rate of pro-inflammation upon DAMP sensing.
α_P (h^{-1})	0.5	Normalized rate of pro-inflammatory synthesis.
α_I (h^{-1})	10.0	Normalized TIMP expression from anti-inflammatory stimulus.
β_I (h^{-1})	0.5	Normalized TIMP expression from pro-inflammatory stimulus.
α_A (h^{-1})	1.0	Normalized peak anti-inflammatory rate.
α_Y ($\mu M\ h^{-1}$)	3.5×10^{-3}	Peak MMP expression rate.
α_S (h^{-1})	3.0	Normalized rate of collagen synthesis.
Decay Rates		
δ_P (h^{-1})	0.23	Decay rate for pro-inflammatory signal; 3-hour half-life (Hazuda et al., 1987).
δ_I (h^{-1})	0.014	Decay rate for TIMPs; 24-hour half-life, based on Knight et al. (2019).
δ_D (h^{-1})	2.1×10^{-3}	Decay rate for DAMPs; 14-day half-life.
δ_A (h^{-1})	0.087	Decay rate for anti-inflammation (Laraia et al., 2012; Kudlow et al., 1986)[b].
δ_Y (h^{-1})	0.014	Decay rate for MMPs; 48-hour half-life (Escuer et al., 2019).
β_S (h^{-1})	1.04	Rate of collagen integration into fibrillar network (Kreger et al., 2010).
MMP Properties		
$k_{cat}^{(D)}$ (h^{-1})	300	Rate constant for MMP cleavage of decorin (Imai et al., 1997).
$k_{cat}^{(S)}$ (h^{-1})	25	Rate constant for MMP cleavage of native collagen (Amar et al., 2017).
$K_m^{(D)}$ (μM)	8.0	K_m for MMP-proteoglycan (Imai et al., 1997; Mayne & Robinson, 1999).
$K_m^{(S)}$ (μM)	1.0	K_m for collagen (Amar et al., 2017).
Inhibition Properties		
$K_i^{(I)}$ (nM)	39	Inhibition constant for TIMP-1 and MMP-1 (Troeberg et al., 2002).
$K_i^{(D)}$ (nM)	92	Inhibition constant for DAMPs on TGF-β (Baker et al., 2009).
$K_i^{(A)}$ (pM)	270	Inhibition constant for IL-1Ra on IL-1R1 (Arend et al., 1994).
$K_i^{(P)}$ (pM)	164	Inhibition of collagen synthesis by IL-1β (Graham et al., 1996)[c].
Receptor Properties		
$K_R^{(P)}$ (pM)	110	Half-concentration for IL-1β on IL-1R1 (Kasai et al., 1990).
$K_R^{(A)}$ (pM)	90	Half-concentration for TGF receptor (Frolik et al., 1984; Massague & Like, 1985).
$K_R^{(D)}$ (nM)	59	Half-concentration for decorin and TLR-2 (Merline et al., 2011).
Normalized Constants		
r (unitless)	(1/651)	Decorin:Collagen ratio (approximated from (Matuszewski et al., 2012)).
γ_P (unitless)	1.49	$\gamma_P = K_i^{(P)}/K_R^{(P)}$, normalized pro-inflammatory inhibition strength.
γ_A (unitless)	3.00	$\gamma_A = K_i^{(A)}/K_R^{(A)}$, normalized anti-inflammatory inhibition strength.
γ_D (unitless)	1.56	$\gamma_D = K_i^{(D)}/K_R^{(D)}$, normalized DAMP inhibition strength.
ε_D (unitless)	135.6	$\varepsilon_D = K_m^{(D)}/K_R^{(D)}$, normalized Michaelis-Menten concentration.
k_{cat} ($\mu M^{-1}\ h^{-1}$)	37.5	$k_{cat} = k_{cat}^{(D)}/K_m^{(D)}$, catalytic efficiency of MMP on decorin.
v_{cat} ($\mu M^{-1}\ h^{-1}$)	0.65	$v_{cat} = r k_{cat}^{(S)}/K_R^{(D)}$, rate of production of DAMPs from collagen.
h_{cat} ($\mu M^{-1}\ h^{-1}$)	25.0	$h_{cat} = k_{cat}^{(S)}/K_m^{(S)}$, catalytic efficiency of MMP on collagen.
n (unitless)	4	Approximate Hill coefficient for MAPK cascades (Dower & Qwarnstrom, 2003).
κ (unitless)	9.6×10^{-3}	Fraction of fibrillar collagens available for MMP.

[a] These properties are dependent on many factors, like the number of fibroblasts and immune cells, for which it is difficult to find references. For this investigation, values were estimated based on current literature.

[b] The actual half-life for anti-inflammatory cytokines is roughly 3-hours, roughly equivalent to the pro-inflammatory mediators (Fuchs et al., 1996). We chose a half-life more representative of physiological data for this model.

[c] Estimated assuming a Hill-coeffiicent of 4.

6.3.2 Model Analysis

Modelling the Acute Inflammatory Response

Once the fibroblast has detected enough DAMPs to trigger an inflammatory response, a complex orchestra between matrix metalloproteinases, their inhibitors, pro- and anti-inflammatory cytokines begins to take form (Maruyama et al., 2020; Huebener & Schwabe, 2013; Eming et al., 2007; Sekton, 2010). This response starts with the feedforward secretion of the pro-inflammatory molecules, IL-1β and TNF-α, that peak roughly 4 to 8 hours after the injury (Manning et al., 2014; Dinarello, 2011; Hope & Saxby, 2007). Together, these molecules signal the fibroblast to begin manufacturing MMPs and, to a lesser extent, their inhibitors, TIMPs. They also down-regulate type I collagen and up-regulate type III collagen, where type III collagen rapidly constructs a collagen scaffold that eventually becomes scar tissue. Paradoxically, these cytokines trigger an anti-inflammatory response initially suppressed by the toll-like receptors detecting DAMPs (Lu et al., 2007; Martel-Pelletier et al., 1993). Once activated, the MMPs begin indiscriminately cleaving anything that looks like a DAMP in the vicinity, catching healthy collagen in the cross-fire. The extracellular milieu is mainly catabolic, arguably doing more harm than good as the fibroblast desperately tries to thwart a potential microbial infection.

Eventually, the MMPs have cleaned up the DAMPs to the point where there is no more prolonged suppression of the anti-inflammatory growth factors and inhibitors, like IL-10, TGF-β and IL-1Ra (Eming et al., 2007; Maruyama et al., 2020). This change ushers in the second wave of the acute inflammatory response: the transition phase. The fibroblast releases a burst of anti-inflammatory cytokines that signal to itself to begin synthesizing new collagen, more TIMPs, and very strongly inhibit the self-amplifying pro-inflammatory loop that has dominated the first wave of this response. This effect continues as the original pro-inflammatory cytokines decay, leaving only the MMPs, TIMPs and newly synthesized collagen.

In the last phase of this response, the remodelling or resolution phase (Hope & Saxby, 2007), the TIMPs synthesized in the transition phase protect the newly synthesized collagen from MMP-cleavage (Eming et al., 2007). Fibrillar collagens spontaneously form

fibrils, which integrate with the existing collagen network. Eventually, the MMPs decay away, either through normal protein breakdown or diffusion out of the tissue. Homeostasis emerges again, and, depending on the strength of the stimulus, there may have been an accumulation of collagen.

The model's response to a unit input of DAMPs, enough to activate half of the TLRs on the fibroblast's membrane, is remarkably consistent with the canonical description of the acute inflammatory response (Figure 6.12). A three-day-long simulation demonstrates these three waves of the inflammatory response, each characterized by peaks in $\hat{P}$, then $\hat{A}$ and $\hat{S}$. These species are the primary drivers of the initial pro-inflammatory, transition, and remodelling phases. Correspondingly, there is a rapid synthesis of proteases in the initial inflammatory phase, leading to a rapid decrease in DAMP concentrations. This decline ushers in the second phase, where the peaking anti-inflammatory cytokines increase the TIMP concentration. These inhibitors remain after the anti-inflammatory wave subsides and protects the newly formed collagens as the MMPs slowly decline.

We can operationalize the acute inflammatory response as three distinct waves, each corresponding to a peak in the phase's primary driver (Figure 6.12). The initial pro-inflammatory phase, which we call the P-wave, is characterized by the expression of cytokines like IL-1β and TNF-α. It is primarily catabolic, with coincident increases in the synthesis of MMPs, which break down DAMPs, newly synthesized collagen, and the existing collagen network. It stands to reason that factors that may prolong this phase could result in more collagen destruction than the subsequent remodelling phase, which we will explore in the next section. The middle-phase, the A-wave, is championed by anti-inflammatory mediators, like TGF-β, IL-10, and IL-1Ra. This phase is characteristically anabolic, with a rapid synthesis of TIMPs to sequester the potentially damaging effects from the MMPs synthesized in the P-wave. These inhibitors are in preparation for the S-wave, where the fibroblast has, for better or worse, returned to resting activity levels. Surviving collagen is free to integrate with the intact collagen network as the TIMPs and MMPs gradually decay.

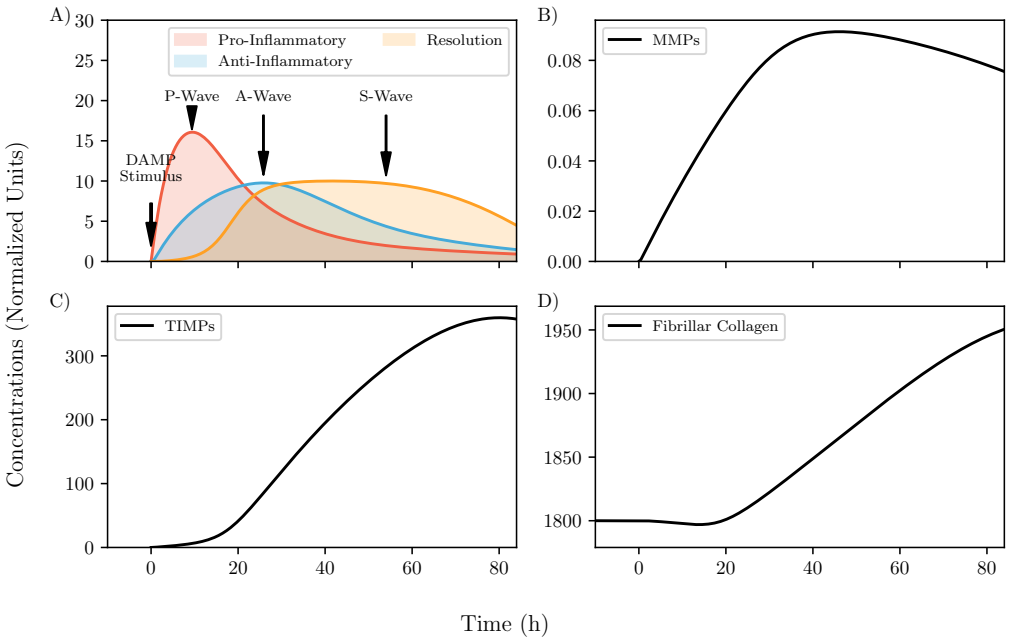

Figure 6.12: (A) Breakdown of the acute inflammatory response into three distinct waves corresponding to the primary driving molecules within each wave. In the P-wave, the governing cytokines are ($\hat{P}$) pro-inflammatory, and contribute to a net-catalytic environment. In the A-wave ($\hat{A}$) , there is a shift to anti-inflammatory cytokines and growth factors which promotes recovery. Finally, in the remodelling wave, newly synthesized collagen ($\hat{S}$) is integrated into the ECM. Other species during these waves are (B) the MMPs ($\hat{Y}$), (C) TIMPs ($\hat{I}$), and (D) the total collagen in the network ($\hat{C}$).

Comparison With Experiments

It is challenging to compare model predictions to experimental results for two reasons. The first is that most physiological studies report outcome variables as fold-changes relative to a control group. This normalization is understandable since it gives otherwise esoteric units of measurement direct physiological interpretation. We can also directly address this limitation by first calculating the raw concentration of the various components of the model and then normalizing them to the reported concentrations of those biomarkers in an unloaded tissue. The second is that this model predicts the downstream inflammatory response from sensing DAMPs, which would require knowing the concentration of DAMPs either following an injury or as a prescribed dose into a tissue. To the author's knowledge, only one study has directly examined the immune-stimulatory effect of a decorin injection

on the IVD (Zwambag et al., 2020). So while full validation is not yet possible, a comparison of results may lend some face validity to the model prediction.

Zwambag et al. (2020) used a 5 μg/mL doses of decorin to probe for a downstream inflammatory response. Using the 90 kDa molecular weight of decorin, and normalizing to the TLR's half-concentration, this amounts to a normalized initial conditions for $\hat{D}$ of 0.94. LePage et al. (2021) measured the total pro-inflammatory cytokine profile in unloaded cultured rat tail IVDs, which amounted to approximately 1,265 pg/mL. Assuming that the average pro-inflammatory molecule has a molar mass of 28 kDa, and using the half-concentration coefficient for IL-1β in the model, we converted between normalized model concentrations and pg/mL. Then, we normalized the cytokine concentration to that reported by LePage et al. (2021), yielding a fold-change to compare to Zwambag et al. (2020).

The results indicate that over 24 hours, the model's P-wave qualitatively follows what Zwambag et al. (2020) detected in the experiment, however delayed in time by approximately two-hours (Figure 6.13A). Further, the response more closely follows MCP-1 and MIP-2, two cytokines that are directly associated with recruiting the innate immune system (Zhang & An, 2007). Because of their movement inducing role in immune cells, they fall under a subclass of cytokines called chemokines. Unfortunately, this comparison is incomplete since those authors also measured TNF-α at negligible levels throughout the investigation. In addition, they did not directly measure IL-1β, the cytokine which $\hat{P}$ is most comparable. Nevertheless, it does provide some confidence that the model's response is somewhat physiologically justifiable during the P-wave portion of its acute inflammatory response. Unfortunately, experimental time-series data during the transition and resolution phases of the inflammatory response are not yet available.

Zwambag et al. (2020) also observed mechanical changes in their FSUs indicative of MMP-mediated ECM destruction, namely a decrease in stiffness and an increase in neutral zone length. The current model predicts the opposite of this (Figure 6.13B); six days after the injection, the amount of new collagen downstream of the pro-inflammatory stimulus exceeds what is lost by enzymatic degradation. This incongruence likely results from the uncalibrated nature of the model. Future work with similar tissue-culturing methods

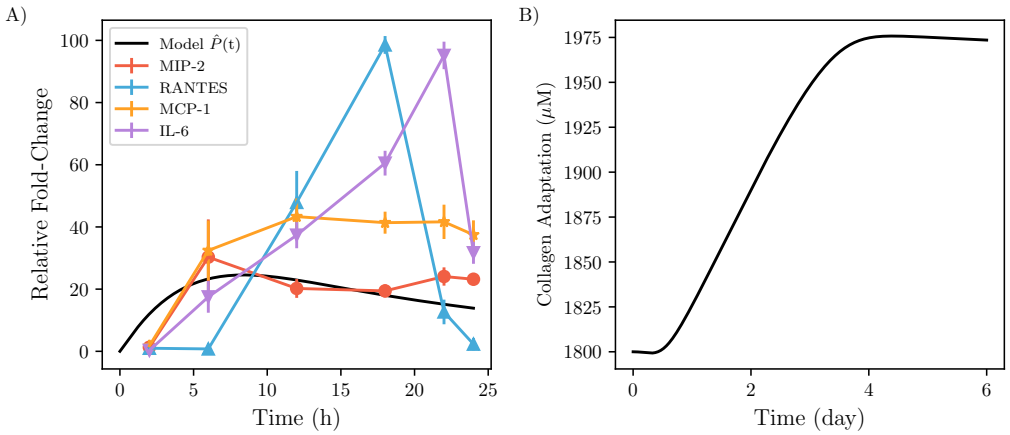

Figure 6.13: (A) Approximated fold-change of the current model (black line) against the fold-changes reported in Zwambag et al. (2020). The relative magnitudes are roughly comparable, however, the physiological response in the model appeared to begin roughly two-hours sooner. (B) The expected collagen response from the model, which predicts a remodelling that would increase the stiffness of specimens after six days. This response is not consistent with what Zwambag et al. (2020) observed, which was a significant decrease in specimen stiffness and an increase in neutral zone length.

may precisely quantify the acute inflammatory response downstream of prescribed DAMP dosages. Such data would be invaluable for calibrating the model for more accurate sensitivity analyses.

Dose-Independent Adaptations?

Despite the model being uncalibrated, it is still worthwhile to conduct a sensitivity analysis to gain intuition about its behaviour. In addition, a more detailed local sensitivity analysis can quantify how dependent model outputs are on parameter magnitudes. These results may help inform the future model calibration.

One readily apparent parameter to analyze is the initial concentration of DAMPs, like decorin, which initiates the inflammatory response. This parameter is also the direct relationship this current model has to mechanical load since, after all, it takes soft tissue overload to produce DAMPs. We first simulated a 10-day response to increasing magnitudes of $\hat{D}(0)$, from 0.5 to 5 and finally 50, in normalized units. These corresponded to 29.5, 295, and 2950 nM of decorin in the extracellular space (Figure 6.14).

There was a marked change in signal amplitude on all species when moving from the 0.5 to 5 $\hat{D}(0)$ initial conditions. This amplitude change did not occur in the shift from 5 to 50 $\hat{D}(0)$, where the only substantial difference is a slight shift in the onset of the A-wave and a slight increase in the magnitude of MMPs manufactured. This MMP increase follows from the stretching of the P-wave in time, which remained elevated until the resolution of the DAMP signal. Interestingly, new collagen synthesis also shifted but maintains the same magnitude throughout the S-waves. This response implies that, beyond a threshold stimulus, the fibroblast responds by manufacturing the same amount of new collagen.

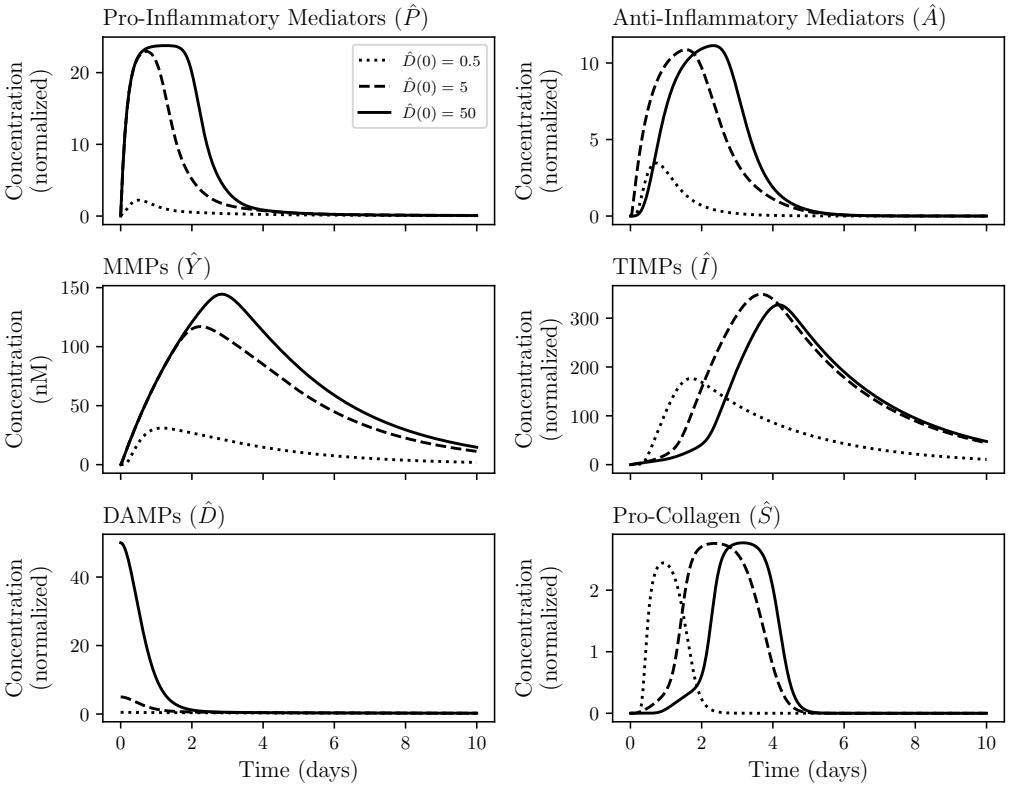

Figure 6.14: Ten-day acute inflammatory-responses to varying levels of initial DAMP concentration, corresponding to 29.5 (dotted), 295 (dashed), and 2950 (solid) nM of decorin ($\hat{D}$). Increasing the amount of DAMPs present has the effect of prolonging the P-wave ($\hat{P}$), which stretches out to accommodate more MMP synthesis ($\hat{Y}$) and eventual resolution of the instigator signal. The anti-inflammatory signal ($\hat{A}$) gets appropriately shifted in time to allow the catalytic P-wave to resolve, downstream is a burst of TIMP ($\hat{I}$) and collagen synthesis ($\hat{S}$). The amount of collagen synthesized in the resolution phase does not appear to be affected in any substantial way by the magnitude of DAMPs initially present.

We can explore the potential threshold-constant collagen response more explicitly by varying the magnitude of the initial stimulus with finer granularity and observing the net change in collagen integrated into the network after a two-week period. Further, it may be helpful to convert from the unnormalized DAMP signal to the equivalent concentration of destroyed collagen to elicit the same response. We can multiply the unnormalized initial DAMP concentration by its stoichiometric ratio with native collagen, approximately 651:1. Using a tendon collagen concentration of about 1.8 mM, we can even convert this magnitude to a percentage of collagen molecules destroyed.

Conducting this analysis does indeed reveal a stepwise response with a small amount of fibrillar collagen lost to MMPs for sub-threshold stimuli (Figure 6.15A). After the threshold, the amount of new collagen rapidly settles to a constant, roughly 150 μM. This analysis assumes the creation of DAMPs spontaneously in the ECM without the fibrillar network sustaining any damage. Accounting for initial damage raises an interesting question: at some point, would the 150 μM of newly synthesized collagen be insufficient to replace all the collagen lost in producing the original DAMP signal?

We get an answer by subtracting the initially damaged collagen from those newly synthesized. With the given model parameters, there appears to be a magnitude of inflammatory stimulus that is 'adaptive' (Figure 6.15B). Here, adaptive means that the amount of newly synthesized collagen exceeds the initially damaged amount. This term contrasts with a 'maladaptive' response, where the amount of new collagen is less than that destroyed. The adaptive portion of this response forms a roughly triangular waveform, with the optimal return on investment occurring just after the threshold needed to elicit the inflammatory response. After this threshold, it linearly tapers until it reaches another maladaptive portion, where the damage imparted to the tissue exceeds the 150 μM replacement.

Interestingly, there is another maladaptive portion of this response at low damage magnitudes. This portion refers to situations where the amount of damage imparted onto the tissue is not substantial enough to trigger the full might of the P, A, and S-waves but leads to a slight increase in MMP synthesis. In essence, according to this model of fibroblast behaviour, the inflammatory response may be considered approximately all-or-nothing.

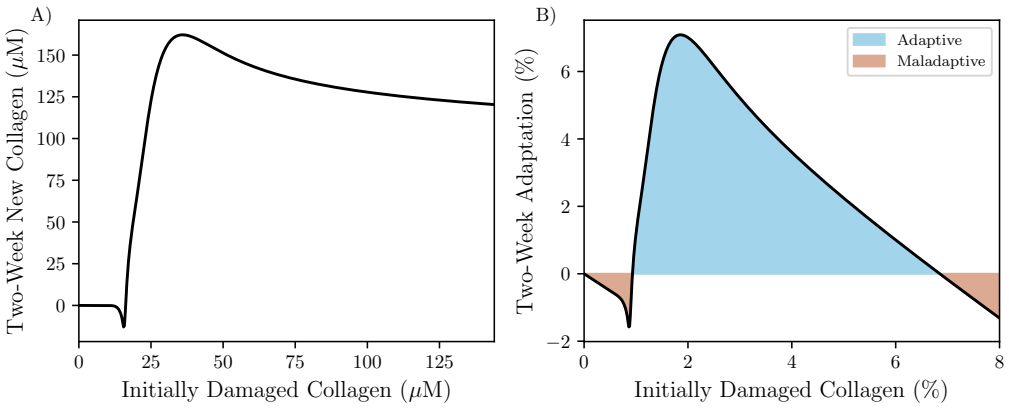

Figure 6.15: (A) Total synthesis of new collagen in response to damaged collagen (estimated from the molar ratio between decorin and collagen). there is a threshold magnitude of decorin needed to elicit the P- and A-waves, below-which there is hardly any synthesis of new collagen, and a slight net decrease stemming from a small amount of MMP-synthesis. Once the threshold is reached, there is a rapid change, where the fibroblasts synthesizes around 150 μM of collagen regardless of the amount of collagen initially damaged. (B) Subtracting this initial damage out to get the overall adaptation reveals a triangular-waveform with an optimal amount of damage to promote adaptation, surrounded by two maladaptive responses where the amount of collagen synthesized following the injury does not replace what was damaged.

The culprits for this stepwise synthetic response are the familiar saddle-node bifurcations that we encountered while deriving the differential equation for $\hat{P}$. Looming in that equation is another Hill function, representing the toll-like receptors, that responds like a switch once the normalized DAMP concentration exceeds unity. Once beyond this threshold, the fibroblast begins shifting toward a pro-inflammatory homeostasis characteristic of the P-wave, which it approaches in an approximately first-order fashion. The fibroblast will maintain this inflammatory phenotype—synthesizing MMPs, downregulating type I collagen, and slowly creating TIMPs—until the original DAMP signal abates. The A-wave initiates once the concentration of DAMPs is no longer strong enough to suppress the expression of growth factors; however, at this point, the system has retained no memory of how severe the original DAMP signal was. Therefore, the downstream response is roughly equivalent, whether the initial DAMP concentration was 2, 5 or 500. The only caveats that interfere with the resolution phase are the remaining MMPs from the P-wave, which leads to a gradual decline in net adaptation with increasing $\hat{D}(0)$. This mechanism leads to the dose-independent collagen synthesis downstream of DAMP sensing. There is no experiment documenting this type of response to the author's knowledge so it may represent

a novel hypothesis. It is a consequence of the structure of the equations, mainly the Hill functions, and might be present over a wide range of model parameters. An experiment like Zwambag et al. (2020) on cultured fibroblasts with varying initial concentrations of DAMPs would be the most direct way to falsify this hypothesis, which would also provide valuable data for calibration. If the response to DAMP stimuli is graded instead of threshold constant, the current model may have overlooked critical cellular mechanisms.

Local Sensitivity Analysis

Local sensitivity analysis is a method for quantifying the sensitivity of a model's steady-state to changes in parameter magnitudes. It can help flag parameters that substantially influence model responses (Zi, 2011). In addition, in the context of a systems biological model like this one, it may provide some guidance in developing therapeutic interventions. For example, if the model is not overly sensitive to producing a specific cytokine, targeting that in therapy may be a wasted effort.

Because the model contains a complex web of excitations and inhibitions, intuiting the model's sensitivity to a given parameter can be challenging. This difficulty is where the local sensitivity coefficient, a normalized partial derivative of the desired outcome variable, can be helpful. For the current model, we will consider the steady-state behaviour of the total collagen, $\hat{C}^{ss}$, as this gives some indication of the fibroblasts' adaptation to a given stimulus. As an initial condition, we will use 5 units of normalized decorin, 1.8 mM of initial fibrillar collagen, and the rest zero. The local sensitivity coefficient of steady-state collagen with respect to a model parameter, p, is given by:

$$S_p = \frac{p}{\hat{C}^{ss}} \frac{\partial \hat{C}^{ss}}{\partial p} = \frac{\partial \log \hat{C}^{ss}}{\partial \log p} \tag{6.47}$$

Where the last equality is why these parameters are sometimes called log-gains (Ingalls, 2013), they represent the percent change in the outcome variable in response to a percent change in parameter magnitude. In practice, we changed one parameter by 1% at a time and quantified the corresponding change in the net collagen deposition. These changes

were then normalized by $\frac{\hat{C}^{ss}}{p}$ to yield the normalized local sensitivity coefficient (Figure 6.16).

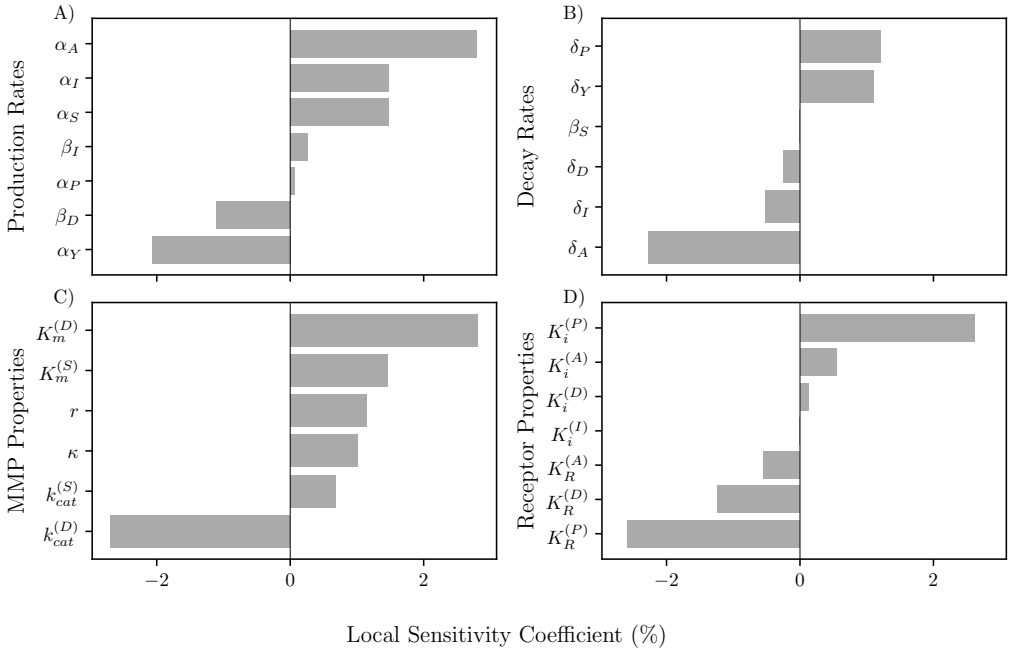

Figure 6.16: Resulting local sensitivity coefficients for (A) the production rate parameters, (B) the decay rate parameters, (C) the properties of MMPs, including the decorin:collagen ratio and the fraction of available collagen, and (D) the receptor parameters, including inhibition concentrations.

Most of the sensitivity coefficients are between -2.5 and 2.5%, indicating that the model is not overly sensitive to one parameter. The sensitivities for the production, decay, and receptor parameters jive well with intuition. For example, increasing the production rate for MMPs decreased the net collagen adaptation, whereas increasing the synthetic rate for collagen increased it. These results highlight the potential role of anti-inflammatory cytokines since their production and decay rates exhibited the highest magnitude local sensitivity coefficients. Correspondingly, administration of TGF-β in a collagen scaffold seems to accelerate wound healing (Pandit, Ashar, & Feldman, 1999). The properties associated with TLR-DAMP interactions, β_D and $K_R^{(D)}$, were also relatively large in magnitude. This result is encouraging since TLR antagonists have shown promise in alleviating inflammatory disorders (Abdollahi-Roodsaz et al., 2007).

The MMP-related properties are both surprising and counter-intuitive. Increasing the MMP catalytic efficiency for cleaving collagen, $k_{cat}^{(S)}$, somehow increased the net collagen adaptation. Similarly, increasing the rate by which MMPs cleave DAMPs, the primary negative-feedback mechanism in this reaction network, somehow led to less collagen deposition. The last parameter exhibited the highest magnitude local sensitivity coefficient of all those we explored. Counter-intuitive results like this are the hallmark of complex systems, like the one under investigation, where reductionist reasoning is not always correct. For instance, the reason why increasing $k_{cat}^{(S)}$ increased the net adaptation is that it slightly increased the number of DAMPs liberated from the existing collagen network. The slightly drawn-out inflammatory stimulus corresponded to slightly longer P- and A-waves, the latter driving collagen synthesis. In this case, the synthesis of new collagen more than made up for the increased rate by which MMPs degrade the fibrillar network. A similar mechanism is at play for the change in $k_{cat}^{(D)}$: speeding up the destruction of DAMPs led to a more rapid resolution of the DAMP signal, characterized by a narrower A-wave, which in turn led to less net collagen synthesis. To summarize, DAMPs indirectly stimulate collagen production through a complex signalling network. For the current (uncalibrated) model parameters, turning off the DAMP signal too quickly decreased the net collagen adaptation.

6.3.3 Shortcomings

The major shortcoming of the current iteration of this model is that it is uncalibrated. Because a full dataset sufficient to calibrate the model does not exist yet, to the author's knowledge, we have restricted the discussion of model properties to qualitative behaviour that is less likely to be sensitive to model parameters. Predictions from this model still come with a sizeable caveat that the exact magnitudes of each biomarker are not to scale, and that a more robust sensitivity analysis will need to be done once it has been properly calibrated. Future investigations will need to refine those parameters.

In addition to the lack of calibration, there may be other critical physiological mechanisms that the model has overlooked. The most apparent abstraction is reducing a rich

diversity of cytokines and chemokines into two homogeneous categories, $\hat{P}$ and $\hat{A}$. However, the criticism of physiological mechanisms can be more nuanced than this. For example, some investigations have documented that MMPs directly cleave IL-1β (Ito et al., 1996), which would provide this network with another means of negative feedback aside from the awakening of the A-wave. Another is the apparent liberation of TGF-β from MMP-cleaved decorin (Imai et al., 1997), which provides another avenue for dampening the feedforward P-wave. Related to this concern is the mechanism by which decorin inhibits TGF-β; it does not appear to be conclusive whether it acts as a competitive inhibitor on the growth factor's receptor or as a mixed inhibitor by forming complexes with TGF-β in the ECM (Baker et al., 2009; Hausser, Gröning, Hasilik, Schönherr, & Kresse, 1994; Hildebrand et al., 1994). The exact mechanism is unknown but implies slightly different structures in the differential equations.

Thirdly, during the P-wave, the fibroblast is frantically assembling a type III collagen scaffold, a response that may influence the long-term mechanical behaviour of the tissue, but not one considered here (Maffulli et al., 2000). Fourthly, the recruitment of the innate immune system to the site of inflammation was, in some sense, overlooked. Since the activation and deactivation of this response mirrors that of the P- and A-waves, it is plausible that those two differential equations, once calibrated, could account for this limitation. As a final example, the IL-1β system has another negative feedback strategy, the decoy receptor (Garlanda, Riva, Bonavita, Gentile, & Mantovani, 2013), that may produce non-competitive inhibition. This type of inhibition would directly affect the amount of pro-inflammatory cytokines available to induce downstream cellular signals, adding an inhibition term to the numerator rather than the denominator in Equations 6.46a to 6.46g (Ingalls, 2013). The sequence of events during acute inflammation is extraordinarily complex and reducing that complexity to a set of seven ordinary differential equations necessarily abstracted away many of the details. Future sensitivity analyses may be fruitful in determining the effect of including more of these mechanisms on the behaviour of the fibroblast-ECM system.

There do not appear to be any initial conditions that lead to chronic inflammation for the set of parameters explored here. Elucidating the cellular mechanisms behind chronic in-

flammation may be indispensable for developing therapies or preventative strategies for inflammatory disorders like tendonitis, tenosynovitis, or degenerative disc disease (Freemont, 2008; Risbud & Shapiro, 2014). The parameters selected and analyzed here reproduce, to some extent, an acute inflammatory response with ECM-remodelling. It may be the case that varying the production rates, potentially through the infiltration of the innate immune system into the tissue, or the receptor sensitivities, through the expression of additional receptors, may result in the development of a stable, inflamed, steady-state. Because the model has yet to be calibrated, exploring the parameter space for the existence of a chronically inflamed phenotype was outside this investigation's scope.

The model equations (Equations 6.46a to 6.46g) are both high-dimensional and non-linear, stemming from the bountiful use of Hill functions and Michaelis-Menten constitutive laws. A common co-morbidity of non-linearity is chaotic behaviour, importantly characterized by sensitivity to initial conditions. A popular example of chaos is a double pendulum, whose governing differential equations can be easily derived from mechanics. Troubling, however, is that initial conditions separated by the radius of a hydrogen atom, a magnitude that is impossible to comprehend, rapidly diverge within 30 seconds of simulation. There are other important numerical ramifications since the integration technique, step size, and floating-point number precision can lead to wildly different simulation results. This result strongly suggests that it is impractical to use these equations to predict the motion of the double pendulum since one would need state-of-the-art equipment, beyond what currently exists, to measure the initial conditions and a very high-order numerical scheme to integrate them. Even equipped with this meticulous measurement, simulation results would only be valid for tens of seconds.

There is no shortage of examples of chaos in nature, and this property substantially limits the predictability of chaotic ordinary differential equations. It would be nice to know if the model derived here is chaotic. If so, it would be well worth documenting the approximate timescale that solutions are valid over. A typical method for quantifying sensitivity to initial conditions is the system's maximum Lyapunov Exponent, whose inverse represents the system's limit of predictability, the approximate timescale before trajectories diverge by e. We numerically calculated this quantity using the methods described in

Sandri (1996). Fortunately, the current model with its uncalibrated model parameters is not chaotic, with a maximum Lyapunov exponent of -0.014. After the model has undergone a full calibration, it may be necessary to recalculate the Lyapunov exponent to ensure that the system has not transitioned to a chaotic one.

6.4 Combined Model

We now have the two building blocks for creating a fully mechano-biological model of soft tissue: the mechanical model from Section 6.2 and the physiological model from Section 6.3. This section presents a brief description of the intercommunication between these two models, followed by some short model predictions, specifically how they relate to the classical injury theory. Since the physiological model is still uncalibrated, this section focuses on the qualitative behaviour of the combined model rather than its specific predictions.

6.4.1 Model Description

The most challenging aspect of linking the two models is keeping track of units. The mechanical model describes the rates of change of three normalized moments, whereas the physiological model tracks the time-evolution of dimensionless concentrations. The critical relationship that binds the two together is in the initial conditions, precisely that $Q_0(0)$ corresponds to the initial concentration of collagen in the physiological model, $\hat{C}(0)$. Using this relationship, we arrive at:

$$\frac{Q_0(t)}{Q_0(0)} = \frac{\hat{C}(t)}{\hat{C}(0)} = \frac{\mathcal{C}(t)}{\mathcal{C}_0} \tag{6.48}$$

This expression helps maintain consistency between the two models, it acts as a conversion factor between Q_0 and $\hat{C}$, and it is what we will use to eliminate the $\hat{C}$ differential equation from the physiological model. We have also introduced $\mathcal{C}(t)$, the unnormalized concentration, with initial condition $\mathcal{C}_0$, related to the dimensionless form by $K_m^{(S)}\hat{C}(t) = \mathcal{C}(t)$. From

Study I, and our initial analysis, we will continue to use the Tobolsky-Eyring rate law for mechanical fibril disruption. From **Study II**, the Michaelis-Menten equation may be appropriate for describing catalysis in the partial differential equation model. The final term to describe mathematically is the rate of integrating newly synthesized collagen into the fibrillar network. We will assume that all the new collagen gets incorporated into $\rho(x,t)$ is proportional to the initial strain distribution: a Gaussian centred at μ with standard deviation η. Thus, the partial differential equation model takes the form:

$$\frac{\partial \rho}{\partial t} + v\frac{\partial \rho}{\partial x} = \frac{\beta_S \hat{S}}{\sqrt{2\pi}\eta} e^{-\frac{(x-\mu)^2}{2\eta^2}} - \frac{v_{cat}\hat{Y}\kappa(x)\rho(x,t)}{1+\hat{I}+\hat{S}+\frac{\hat{D}}{\varepsilon_D}+\langle\kappa,\rho\rangle\hat{C}_0} - \alpha e^{\beta x}\rho(x,t) \tag{6.49}$$

This equation is already tying together several components of the physiological model, $\hat{Y}$ is the concentration of MMPs, $\hat{S}$ is the free collagen, $\hat{I}$ is the TIMP concentration, and $\hat{D}$ is that of decorin. The final piece to the puzzle is determining $\kappa(x)$. Using the steric factor from earlier, along with the strain inhibition hypothesis from **Study II**, we find that:

$$\kappa(x) = \begin{cases} \kappa' & x \leq 0 \\ 0 & x > 0 \end{cases} \tag{6.50}$$

Where κ', with no dependence on x, is the fraction of fibrillar collagen available for collagenolysis, which we derived in Equation 6.42. Proceeding as we did for the DM-approximation in Section 6.2.1, we find that:

$$s_\lambda = \frac{1}{\sqrt{2\pi}\eta}\int_{-\infty}^{\infty} x^\lambda e^{-\frac{(x-\mu)^2}{2\eta^2}}\,\mathrm{d}x = \begin{cases} 1, & \text{for } \lambda = 0 \\ \mu, & \text{for } \lambda = 1 \\ \mu^2+\eta^2, & \text{for } \lambda = 2 \end{cases} \tag{6.51}$$

Further, we define the quantities:

$$C_\lambda = \int_{-\infty}^{\infty} x^\lambda \kappa(x)\rho(x,t)\,\mathrm{d}x \qquad\qquad \lambda = 0,1,2 \tag{6.52}$$

This yields the DM-approximation:

$$\frac{\mathrm{d}Q_\lambda}{\mathrm{d}t} = v\lambda Q_{\lambda-1} + \beta_S s_\lambda \hat{S} - \frac{v_{cat}\hat{Y}C_\lambda}{1+\hat{I}+\hat{S}+\frac{\hat{D}}{\varepsilon_D}+\hat{C}} - D_\lambda, \qquad \lambda = 0,1,2 \tag{6.53}$$

Where $\hat{C} = \hat{C}_0 C_0$, is the initial (normalized) concentration of collagen times the zeroth moment defined in Equation 6.52. Unfortunately, both collagen and catalysis begin with the same letter. It represents the total collagen available for collagenolysis, normalized to its Michaelis constant after accounting for strain-inhibition and the fibril geometry. The quantities C_λ and D_λ are approximated using the Gaussian approximation described in Section 6.2.1. These equations, more specifically when $\lambda = 0$, ultimately replace the equation for $\hat{C}$ in the physiological model. The final term to include in the model is the production of DAMPs from damage to this fibrillar network, which is related to the term D_0, the net loss of collagen by mechanical means. Including that in the DAMP equation gives:

$$\frac{\mathrm{d}\hat{D}}{\mathrm{d}t} = \hat{r}D_0 + \frac{v_{cat}\hat{Y}\hat{C} - k_{cat}\hat{Y}\hat{D}}{1+\hat{I}+\hat{S}+\hat{C}+\frac{\hat{D}}{\varepsilon_D}} - \delta_D \hat{D} \tag{6.54}$$

Where $\hat{r} = r\hat{C}_0/K_R^{(D)}$ is a normalized stoichiometric ratio between decorin and collagen. With these relatively minor adjustments, the model now accounts for the liberation of DAMPs from the existing collagen network. The fibroblast model responds by initiating an inflammatory response and downstream remodelling. Viscoelasticity can be incorporated in the same way as the mechanical model, along with force and displacement controlled conditions. Therefore, the fully assembled final model is a set of nine ordinary differential equations, with one algebraic constraint for either force or displacement.

Most of the model parameters remained the same as the previous two sections, with a few minor adjustments (listed in Table 6.3). Most notably, changes to the mechanical breaking parameters, and turning off mechanical damage for crimped collagen. More precisely tuning these parameters with additional experimental data is still necessary to test specific model predictions.

Table 6.3: Model parameters that were changed for the combined model.

Production Rates		Decay Rates		Mechanical Parameters	
β_D (h^{-1})	5.0	δ_P (h^{-1})	0.23	α_0	2.1×10^{-7}
α_P (h^{-1})	3.5	δ_I (h^{-1})	0.087	α_1	5.0×10^{-6}
α_I (h^{-1})	10.0	δ_D (h^{-1})	0.029	β	40.56
β_I (h^{-1})	0.5	δ_A (h^{-1})	0.039		
α_A (h^{-1})	10.0	δ_Y (h^{-1})	0.014		
α_Y ($\mu M\ h^{-1}$)	3.5×10^{-3}	β_S (h^{-1})	1.04		
α_S (h^{-1})	2.0				

6.4.2 Model Analysis

Thresholding Adaptation

Now equipped with the physiological one, the mechanical model can adapt and remodel to an applied load. This adaptation exhibits a rather abrupt thresholding behaviour; as little as a few MPa of applied stress can distinguish between signalling the fibroblast to trigger an inflammatory response or not. In addition, relatively minor damage, only 2% of the total collagen population, exacts the complete adaptive response from the fibroblast, which puts down roughly 7.5% more collagens over a 4-5 day recovery period (Figure 6.17). Similar threshold-constant observations have been made in tendons recovering from exercise, where the measured mRNA response to load is much higher than rest but does not vary tremendously with the number of repetitions endured (Magnusson, Langberg, & Kjaer, 2010). Unfortunately, the review by Magnusson et al. (2010), which synthesized three distinct loading paradigms, appears to be the only investigation that has (informally) documented a dose-response in collagen synthesis following applied load.

This thresholding may explain why there was no evidence of an inflammatory response in **Study III** (Chapter 5). If the creep magnitude did not induce enough damage to stimulate the fibroblasts into remodelling, it would explain why there was no evidence of either mechanical changes or a downstream inflammatory response. The thresholding behaviour appears to constitute a novel hypothesis generated from the physiological model.

An extreme corollary to this threshold-constant adaptation response is that, as noted in the physiological model, the fibroblasts of the soft tissue will synthesize roughly the

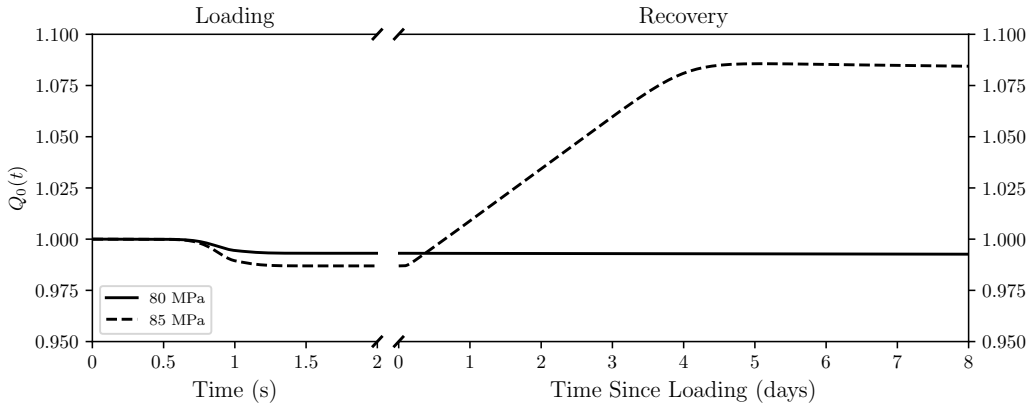

Figure 6.17: On the left is a decrease in Q_0 with an applied load of either 80 or 85 MPa over a 2 second time-interval via $\sigma(t) = \frac{A}{2}(1 - \cos(\pi t))$ (A is either 80 or 85 MPa). On the right is the 8-day recovery period from that applied load. The combined model exhibits the same thresholding property as the physiological model.

same amount of new collagen regardless of the severity of the initial insult. Simulating a one-hour creep at 10, 25, and 40 MPa, for example, led to three distinct responses (Figure 6.18). The low magnitude load, 10 MPa, did not induce enough damage to trigger remodelling and resulted in a small accumulation of damage that persists 8-days later with no healing. Conversely, a 25 MPa constantly applied load accumulated enough DAMPs over the hour-long exposure to trigger a remodelling response that exceeded the initial collagen concentration 8-days later. By contrast, the 40 MPa exposure, which was 12-seconds from the complete rupture at the end of the hour-long exposure, accumulated enough DAMPs to elicit the downstream remodelling response. However, the amount of new collagen synthesized by the fibroblasts was not enough to return the tissue to its initial state. These results may provide clinical insight into healing, where an injury near-miss, even after recovery, still needs to be rehabilitated to recover its total capacity.

Comparison with Classical Injury Theory

The classical conceptual model for injury pits the load applied to a tissue against its tolerance, with an injury occurring when the former exceeds the latter (McGill, 1997). This concept challenges the current model, which never explicitly defines a parameter to

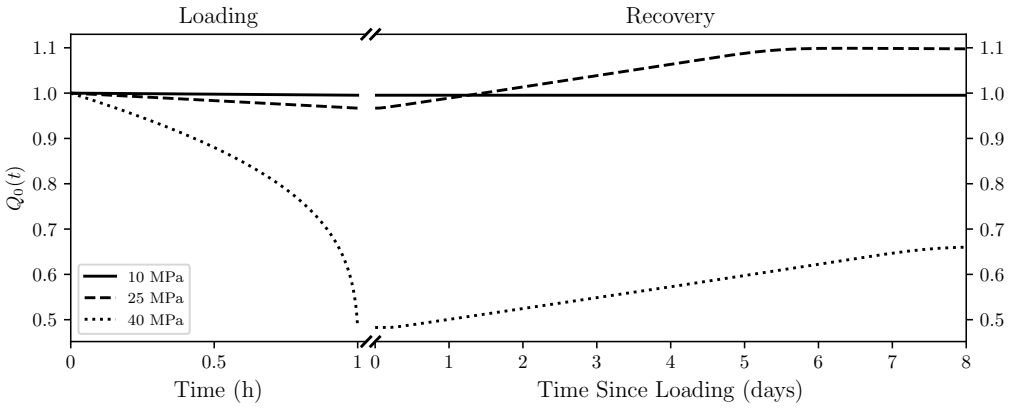

Figure 6.18: On the left is a decrease in Q_0 with a constantly applied load of 10, 25, or 40 MPa over an hour long exposure. On the right is the 8-day recovery period from that applied load. Again there is thresholding, and the downstream adaptation is roughly similar regardless of the magnitude of the damage stimulus.

represent 'tolerance.' If it is the ultimate tensile stress, then it is not a single unique value, but a function of strain rate. Therefore, we will define the context-dependent tissue tolerance at a given strain rate, $\hat{\sigma}(v)$, to be the maximum stress attained on a failure test at the specified strain rate, v. We can tease out an analytic expression for this quantity from our model equations using a similar approximation to the constant variance assumption. Further, we define the overall tissue tolerance (σ_{tol}) as the limiting magnitude of $\hat{\sigma}(v)$ as v tends to infinity, should that limit approach a finite value. We will show that this tissue tolerance is directly proportional to $Q_0(t)$.

For this derivation, we will make the slightly stronger assumption that the distribution's variance is zero, making our approximating distribution a Dirac-delta function positioned at $p(t)$. Further, we assume that the derivative of $p(t)$ is the strain rate, v. This simplification will make the resulting integrals much more tractable and does not substantially alter the result. With these assumptions, we approximate $\rho(x,t)$ as:

$$\rho(x,t) \approx Q_0(t)\delta(x - p(t)), \qquad p(t) = vt \tag{6.55}$$

And, assuming that this failure test is carried out at such a rate that synthesis and

catabolism are negligible, the derivative of Q_0 is given by the differential equation:

$$\frac{\mathrm{d}Q_0}{\mathrm{d}t} = -(\alpha_0 + \alpha_1 v) Q_0 e^{\beta p(t)} \tag{6.56}$$

Where we have re-introduced the parameters α_0 and α_1 as the rate independent and dependent parts of the breaking function. Using the assumption that $p(t) = vt$, we can solve this equation for $Q_0(t)$:

$$Q_0(t) = Q_0(0) \exp\left(\frac{\alpha_0 + \alpha_1 v}{\beta v}\left(1 - e^{\beta v t}\right)\right) \tag{6.57}$$

Where $Q_0(0)$ is the initial magnitude of Q_0 when the failure test commences. Like previously, the stress is simply:

$$\sigma(t) = \int_0^\infty kx\rho(x,t)\,\mathrm{d}x \approx kQ_0(t)p(t) \tag{6.58}$$

As t increases, the stress will initially increase with $p(t)$; however, Q_0 will also begin decreasing at a more dramatic rate, leading to an eventual decline in stress with increasing strain. The maximum occurs when the time-derivative of $\sigma(t)$ is identically zero, thus, from the chain rule we have:

$$\frac{\mathrm{d}\sigma}{\mathrm{d}t} = k\left(\frac{\mathrm{d}Q_0}{\mathrm{d}t}p(t) + Q_0\frac{\mathrm{d}p}{\mathrm{d}t}\right) \tag{6.59}$$

Substituting the differential equation for Q_0 (Equation 6.56), the assumption that $p(t) = vt$, setting the resulting expression equal to zero and solving for time yields the time of maximum stress, which we denote $\hat{t}$:

$$\hat{t} = \frac{1}{\beta v} W\left(\frac{\beta v}{\alpha_0 + \alpha_1 v}\right) = \frac{1}{\beta v} W(\tau) \tag{6.60}$$

Where $W(x)$ is the Lambert W function, the inverse function of $f(x) = xe^x$ which, much like the exponential integral, does not have a closed form in terms of elementary functions.

For convenience, τ is the argument of the Lambert W function, the ratio of breaking function parameters. Plugging this time into Equation 6.58, and using $p(t) = vt$ and the solution for $Q_0(t)$ in Equation 6.57, yields an approximation for the peak stress as a function of strain rate, which we have defined as the context-dependent tissue tolerance:

$$\hat{\sigma}(v) = \frac{kQ_0(0)}{\beta} W(\tau) \exp\left(\frac{1}{\tau}\left(1 - e^{W(\tau)}\right)\right), \qquad \tau = \frac{\beta v}{\alpha_0 + \alpha_1 v} \tag{6.61}$$

Efficient implementations of the Lambert W function are accessible through any commonly available scientific computing library, for example `lambertw` in `SciPy`. This zero-variance approximation is a decent estimate of the tissue tolerances obtained from simulating failure tests (Figure 6.19). As we initially suspected, the tissue tolerance is sensitive to the strain rate and is therefore context-dependent, but appears to approach a limiting magnitude for very rapid strain rates. It is precisely this limit that we define as the tissue's tolerance:

$$\sigma_{\text{tol}} = \lim_{v \to \infty} \hat{\sigma}(v) = \frac{kQ_0(0)}{\beta} W\left(\frac{\beta}{\alpha_1}\right) \exp\left(\frac{\alpha_1}{\beta}\left(1 - e^{W\left(\frac{\beta}{\alpha_1}\right)}\right)\right) \tag{6.62}$$

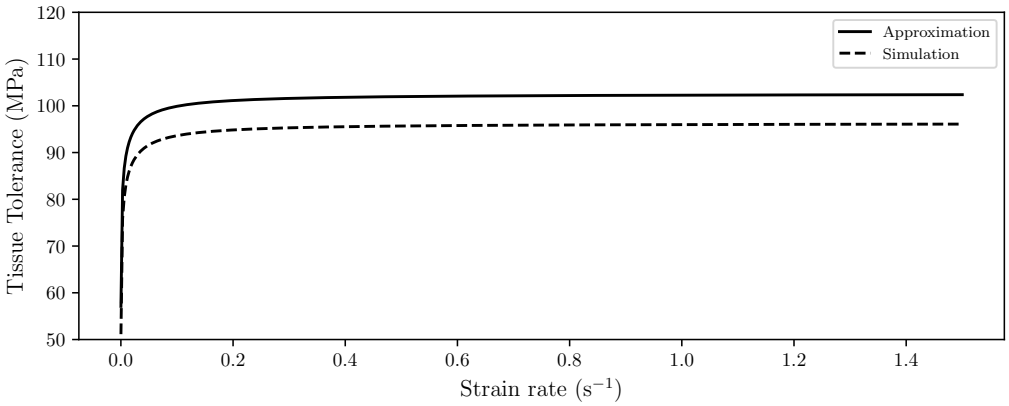

Figure 6.19: Approximation of the tissue tolerance with Equation 6.62 compared to simulated results. The tissue tolerance rapidly approaches a limiting value as the applied strain rate increases. The zero-variance approximation tends to be 6% higher than the full simulation.

These equations contain a noteworthy prediction. If there were no velocity-dependent

component to the breaking function, or if $\alpha_1 = 0$, then this limit is not defined. In this regime, the context-dependent tissue tolerance would continue to increase with the strain rate indefinitely. Indirectly, the experimental observation that the ultimate tensile strength of tendons and ligaments also seems to plateau with rising strain rates (Ng et al., 2004; Kato et al., 1989; Crisco, Moore, & McGovern, 2002) supports the rate-dependence of the breaking function.

We now consider that Q_0 could have evolved according to some other loading process that was halted at the time of tolerance measurement. In this case, the tissue's tolerance is also a function of time and is directly proportional to the instantaneous $Q_0(t)$, as we have shown. This quantity would represent the approximate tolerance one would measure if they harvested the tissue and failed it at the instant, t. We will define the proportionality constant to be ω, which, for the set of parameters in the current model, is 103.5 MPa:

$$\sigma_{\text{tol}}(t) = \omega Q_0(t), \qquad \omega = \frac{k}{\beta} W\left(\frac{\beta}{\alpha_1}\right) \exp\left(\frac{\alpha_1}{\beta}\left(1 - e^{W\left(\frac{\beta}{\alpha_1}\right)}\right)\right) \tag{6.63}$$

Equipped with a notion of tissue tolerance, we simulated both acute and chronic injuries using the same model, only changing the load condition for the forward problem (Figure 6.20). In line with the classical theory, an injury coincided with where the applied load exceeded the tissue tolerance. In the case of a chronic injury, a previously non-injurious magnitude of loading, 75 MPa in this case, when applied repeatedly, reduced the tissue tolerance to the point where it becomes injurious.

As a final comparison to the conceptual model, we also simulated recovery from a cyclically applied load (Figure 6.21). One cycle of the applied load would not have triggered an adaptive response in isolation, as it was below the 85 MPa threshold explored earlier. However, through cyclically loading, the DAMPs accumulated and reached the threshold to induce remodelling of the ECM. Even though the reduction in tissue tolerance occurred over a few seconds, the remodelling phase lasted several days. The imbalance between damage and recovery timescales is well established. Future directions may be to provide more quantitative insights into this phenomenon in the clinic, workplace, and sport.

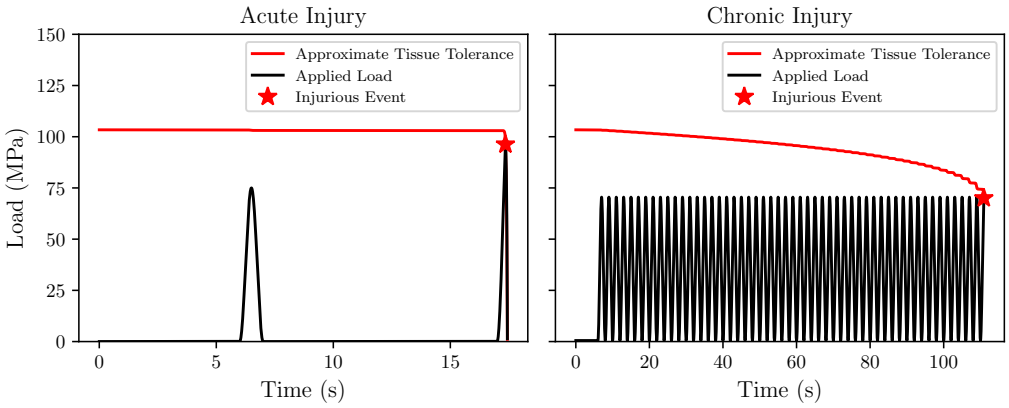

Figure 6.20: With the approximated tissue tolerance, the current model reproduces features associated with acute and chronic injuries, similar to those presented in Figure 2.1.

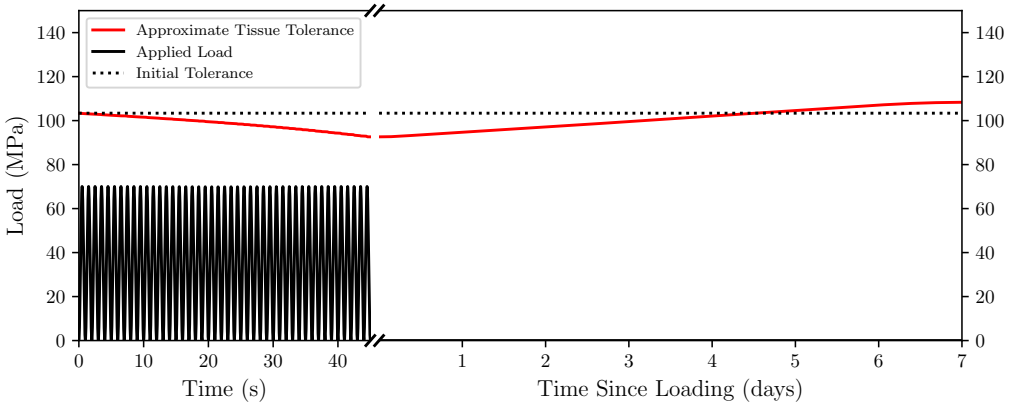

Figure 6.21: In this simulation, the magnitude of applied load, in isolation, would not have induced a downstream remodelling response. However, the accumulation of DAMPs through cyclic loading is enough to trigger downstream remodelling.

6.5 Discussion

This chapter detailed the development of a mechanical model for describing damage to biological tissues and a biochemical one that represented their downstream adaptation, but neither model could explain the complete set of complex behaviours that soft tissues exhibit in isolation. Therefore, connecting the two submodels led to a holistic model whose qualitative behaviour is similar to a classical injury theory.

Combining a collagen fibril recruitment model with a Tobolsky-Eyring rate law, and reducing complexity with a distribution moment approximation, resulted in a mechanical model that reproduced a variety of empirical relationships. Along with the salient features of viscoelasticity, this also included some of the more challenging aspects of fatigue, like the S-N curve for cyclic loading and the rupture-time results from creep-rupture experiments. In addition, we were able to derive some expected relationships directly from the model equations, which may benefit future parameter estimation and calibration endeavours.

The biochemical model was developed based on Michaelis-Menten enzyme kinetics and Hill functions for receptor-mediated signalling cascades, structured according to the proposed cellular response to DAMP recognition. While there was no available data for rigorously calibrating or validating the model, it qualitatively reproduced the tri-phasic inflammatory response, the initial phase of which agreed with experimental results. Combining this model with the mechanical one resulted in an in silico model of biological tissues that adapted to damage with inflammation and remodelling. However, it still suffers from requiring calibration to improve predictions.

We have already discussed the model's implications and shortcomings alongside the analysis of its subcomponents. Thus, this discussion synthesizes the main hypotheses, future directions, and limitations uncovered in deriving and analyzing the current model.

6.5.1 Hypotheses from the Model

Three main model predictions warrant further discussion. The first is a distinction between cumulative load and cumulative damage made by the model. This difference may provide some nuance to the popular cumulative load theory of injuries, by explicitly separating the notions of "load" and "damage." The second is the paradoxical statement that chronic injuries occur suddenly, which manifests most apparently on creep-rupture tests. The third is the switch-like behaviour of the inflammatory signalling cascades. This observation, in particular, demonstrates that the inflammatory system is, in some respects, hard to turn on and hard to turn off. Some of these are established properties of biological tissues; however, the model makes these predictions explicit and brings them to the forefront.

Cumulative Load is not Cumulative Damage

The cumulative load hypothesis was one among several postulated by Kumar (2001) that may underpin workplace injuries. Since then, measuring cumulative load has become a popular proxy for mechanical damage in ergonomic assessment (Norman et al., 1998; Holmes, Hodder, & Keir, 2010; Callaghan, Salewytsch, & Andrews, 2001), predicting osteoarthritis from habitual loading (Maly, 2008; Tateuchi et al., 2017), and sports injuries (Miller, 2017). The current model refutes this hypothesis somewhat since cumulative load and cumulative damage are distinct quantities related to time and strain integrals of the collagen distribution, $\rho(x,t)$, but with substantially different weighting factors. In particular, they are:

$$\text{Cumulative Load} = \int_0^T \langle kx, \rho(x,t) \rangle \, \mathrm{d}t \tag{6.64}$$

$$\text{Cumulative Damage} = \int_0^T \langle \alpha e^{\beta x}, \rho(x,t) \rangle \, \mathrm{d}t \tag{6.65}$$

Where $\langle \cdot, \cdot \rangle$ is the same inner product defined earlier, $\alpha e^{\beta x}$ is the breaking function and k is the stiffness. The cumulative load integral is simply the integral of the stress predicted from the model over time. This concept contrasts with the cumulative damage, which is the integral of the mechanical damage term, $\alpha e^{\beta x} \rho(x,t)$, over the whole strain distribution and time. The integrands in these two expressions are different, suggesting that these two quantities are distinct.

Of course, separating these two terms is not a new idea; both Edwards (2018) and Carter and Caler (1985) distinguish cumulative damage from load based on the Palmgreen-Miner rule. This rule states that the cumulative damage from cycles of varying load magnitudes is the weighted average of their predicted damage from the S-N curve. But, in practice, Edwards (2018) accounts for this by raising the force to a power, p, before integration, then calculating the p^{th} root of the final sum. Therefore, this normalization is more sensitive to higher magnitudes of force, and leads to more sensible predictions, but

is not reconcilable with how the current model distinguishes between cumulative damage and load. More empirically, Parkinson and Callaghan (2007) developed a method that applies a dimensionless scale factor to the force before integration, where they derived the scale factor from fatigue studies on FSUs. Similarly, Johnen, Mertens, Nitsch, and Brandl (2022) showed that experimental conditions, each with the same integrated spine compression, can have vastly different cardiovascular and psychophysical demands. Even though these methods disagree on how exactly cumulative load and cumulative damage are different, they agree that simply using cumulative load as a proxy for damage may be somewhat simplistic.

Chronic Injuries Occur Suddenly

The model exhibits the classic tri-phasic creep curve when subjected to a constantly applied load (Wren et al., 2003; Wang & Ker, 1995; Ellis, 1978; Firminger & Edwards, 2021). A rapid, initial, viscoelastic response reaches a steady-state within the first minute, which ushers in the second phase of the creep response. For the viscoelastic element in the model, the secondary creep phase is uneventful: the force applied to it is not changing, nor is its displacement. This tranquillity is in stark contrast to the fibril recruitment model. There is a constant ebb and flow of fibrils rupturing, engagement of new fibrils, and currently recruited fibrils extending to higher force magnitudes. This delicate balance is maintained until fibril damage begins to exceed the rate of new fibril engagement. With no further reinforcements, it is up to the existing fibrils to resist the applied force, initiating a traumatic feedforward cycle: the fibrils sustaining the most force rupture and the other fibrils pick up the slack, but that increases their rate of rupturing, therefore the cycle repeats until the tissue breaks. This acceleration is the hallmark of the tertiary creep phase, where failure is imminent.

Interestingly, there is very little mathematical evidence about when the second phase will end and the tertiary phase will begin. The best predictors tend to be the strain rate during secondary creep or the magnitude of initial strain among the collagen fibrils (Wang & Ker, 1995; Wren et al., 2003; Firminger & Edwards, 2021). The creep-rate result is

intuitive since it indirectly measures the rate at which recruited fibrils strain to make up for the ruptured ones. Similarly, the initial strain is intuitive since it implies a higher initial average strain among the constituent fibrils. However, it is difficult to say when the linear trend in the secondary phase will end even with this information. When it does, it proceeds to rupture very quickly. This chaotic phenomenon may partially explain why *in vivo* investigations with serendipitous injuries often have difficulty finding kinematic evidence that the injury was about to occur (Gooyers, Frost, McGill, & Callaghan, 2013; Cholewicki & McGill, 1992).

Inflammation is All-or-None

The saddle-node bifurcations in the pro-inflammatory differential equation endowed the physiological model with an ultra-sensitive switch-like behaviour (Kolch et al., 2005; Huang & Ferrell, 1996). More specifically, below a threshold concentration of ligand, the system did not respond with the feedforward expression of pro-inflammatory cytokines. The fibroblast maintained this state of inaction until the DAMP stimulus crossed that threshold. At that point, the system rapidly shifted to an inflammatory phenotype, characterized by the synthesis of MMPs and the inhibition of type I collagen synthesis. The limiting behaviour of this pathway with increasing DAMP concentrations asymptotically approaches a maximum expression of cytokines along with a correspondingly high expression of MMPs. Because of this switch-like behaviour, reaction networks of this kind are often simplified to conventional logic gates in a circuit diagram (Manesh et al., 2009). Much like how logic gates emit one of two states, the fibroblast either initiates a downstream remodelling response or does not. In this way, the inflammatory response is approximately an all-or-none.

The second implication of the saddle-node bifurcations is hysteresis (Kolch et al., 2005): to sequester the rampant feedforward pro-inflammatory response to DAMPs, their concentration needs to be much lower than the initial threshold. The hysteresis loop ensures that the fibroblast will commit to an initiated inflammatory response and that it will continue to do so until the stimulus diminishes, but it increases the risk of collateral damage to the

existing collagen network. Therefore, this mechanism may provide some means of promoting a chronic state of inflammation. However, future analyses on a fully calibrated model, or global sensitivity analysis of the entire parameter space, may further elucidate which parameter magnitudes are more susceptible to promoting chronic inflammation. Chronicity does not appear to be a concern for the model parameters explored in this investigation.

6.5.2 Future Directions

The future model could generate novel hypotheses and test potential therapeutic interventions for inflammatory disorders, but it first needs to be more rigorously validated. Therefore, the first major hurdle for the model requires more substantive calibration efforts. Ideally, this would involve culturing tendons or other easily accessible biological tissue and measuring approximate time series as the tissue responds to various stimuli, mechanical or otherwise. The distribution of model parameters can then be determined using Bayesian Inference directly from the experimental data (Chen et al., 2010). The differential equation model would be a causal statistical model for these investigations, and causal inferences could be directly tied to the posterior parameter distributions. This analysis was the initial goal for **Study III**; however, we did not observe an inflammatory response to the applied mechanical loads.

The model predicts that tissue remodelling occurs beyond a threshold and that the downstream remodelling takes approximately a whole week, but these predictions have yet to be tested. Therefore, another test of the model would be to explore whether a thresholding behaviour exists and to measure the approximate adaptation timeline. The threshold-constant behaviour of the model, which Magnusson et al. (2010) informally suggested may be the case for tendons, may have implications for optimal training programs. Targetting the magnitude of DAMP stimulus needed to provoke an inflammatory and remodelling response—and not much beyond that—would result in the most adaptation possible.

6.5.3 Limitations

There are many limitations of the current model, some of which were discussed earlier. For instance, the mechanical model fails to account for discrete plasticity (Veres et al., 2013) and strain-dependent relaxation times (Shearer et al., 2020; Troyer et al., 2012) but still predicts many of the features associated with fatigue and failure (Firminger & Edwards, 2021; Wang & Ker, 1995; Wang et al., 1995; Zitnay et al., 2020). Similarly, the physiological model may omit some established biochemical mechanisms, like MMP-mediated cleavage of IL-1β (Ito et al., 1996) and the activation of MMPs and IL-1β from their inactive precursors, but still captures, at least qualitatively, the tri-phasic inflammatory response to noxious stimuli (Eming et al., 2007). Unfortunately, there is not yet sufficient data available to fully calibrate the model; thus, this remains one of the model's most significant limitations.

6.6 Conclusions

This chapter documented the derivation and analysis of a holistic mathematical model of biological tissues. It required synthesizing the insights of the three experimental studies in this thesis and generated some novel hypotheses, but it still needs more model calibration and, therefore, still has room for improvement. **Study I** determined that the breaking function of the mechanical model may benefit from having a rate-dependent component and that its form may be the Tobolsky-Eyring rate law. In analyzing the model, we showed that this rate dependence might also explain the plateau of ultimate tensile strength with increasing strain rates and the decrease in time-to-failure with higher loading frequencies in cyclic fatigue tests. **Study II** showed that mechanical strain of collagen fibrils might inhibit their cleavage by MMPs, which was critical for deriving the Michaelis-Menten term for describing enzymatic degradation. **Study III** showed that even a dramatic creep exposure in the rat tail that produced a substantial magnitude of tissue strain did not induce a downstream inflammatory response. The model suggests that it likely did not damage the disc collagen and therefore did not produce enough DAMPs to warrant a response by the

fibroblasts. This thresholding behaviour and uniform response to varying magnitudes of stimuli represent novel hypotheses from the model, which may have significant ramifications in kinesiology, specifically training and rehabilitation.

Chapter 7

Conclusions

7.1 Problem Restatement

The classical theory of injury contrasts the loads applied to a tissue against its tolerance, with an injury arising from the former exceeding the latter. It has been tremendously helpful at elucidating acute and chronic injuries, both in work and sport. However, it has difficulty explaining LBP arising from otherwise innocuous exposures, like sedentary work, where the load magnitudes do not seem sufficient to disrupt or degrade soft tissues. Therefore, this thesis aimed to expand this theory's scope into the mechanical and physiological mechanisms so that it may better describe injuries.

7.2 Specific Thesis Objectives: Revisited

This thesis considered four minor goals in addition to its two overarching objectives. The first was to develop a quantitative model for the rate of collagen fibril failure as a function of both strain and strain rate. This model relates to the first global objective, as one of the terms of the collagen homeostasis equation is mechanical damage. **Study I** was able to show that a Tobolsky-Eyring rate law, when combined with the collagen fibril

recruitment model, adequately described the toe, linear, and eventual failure portions of a tendon's stress-strain curve. Further, this investigation supported a breaking function that is directly proportional to strain-rate.

The second minor objective was to develop a mathematical model for collagen fibre destruction by matrix-degrading enzymes and to explore how strain interacts with the rate of catabolism of fibrils. This goal, once again, relates to the first global thesis objective, as molecular catabolism is yet another term in the generalized rate of change of collagen equation. **Study II** showed that mechanical strain might inhibit the activity of these enzymes and that a Michaelis-Menten equation captures the kinetics of collagen catabolism, but it was not able to test this on mammalian collagenases. Therefore, though the final holistic model assumes that strain inhibits collagenases, there may be room for further improvement.

The third was to explore the role of inflammation in the synthesis of new collagen and matrix-degrading enzymes following a mechanical creep exposure. **Study III** subjected a cohort of sixty rats to a prolonged flexion creep protocol at one joint level in their tails and harvested their discs to probe for a downstream inflammatory response. However, despite an extreme magnitude of mechanical creep and staggering initial mechanical changes, the animals fully recovered less than eight hours following the protocol. Therefore, it may require more substantial exposures, or repetitive exposures, to induce a downstream inflammatory response.

The final minor objective was to synthesize mechanical and physiologic responses to injury and creep into a holistic mathematical model. **Study IV** attempted to produce this model, which took the form of nine coupled ordinary differential equations. The model's behaviour reproduced several established phenomena and produced a series of novel hypotheses, but remains uncalibrated. Nevertheless, this model substantially contributes to the classical theory of injuries by expanding its scope to include more physiological mechanisms.

7.3 Global Thesis Objectives: Revisited

This thesis had two overarching objectives. The first was to advance the understanding of collagen homeostasis in soft tissues and summarize this behaviour in a mathematical model. Unfortunately, this model could not be adequately calibrated. Therefore, its specific numeric predictions are undoubtedly imprecise, and parameter estimates require further refinement. Nevertheless, the holistic model was capable of describing the tissue response to disruption and generated a handful of novel hypotheses. These included an estimated all-or-none inflammatory response, an explanation for the abruptness of injuries, and formal distinction between cumulative load and cumulative damage.

The secondary objective was to test this thesis's hypothesis called "The Mountain of a Mole Hill Hypothesis." This hypothesis stated that the fibroblasts and immune systems in soft tissue respond to damage by dispatching a disproportionate inflammatory response and matrix-degrading enzymes. The results from **Study II** supported the notion that uncrimped collagen may be broken down faster by matrix-degrading enzymes, but the results from **Study III** demonstrated that even a modest creep exposure did not result in a substantive inflammatory response. Another refutation came from the computational model in **Study IV**, which argued that the fibroblast response is all-or-none, requires a stimulus that exceeds a given threshold, and is not a graded response like the original hypothesis requires. Ultimately, there was very little evidence supporting this hypothesis from either the theoretical or empirical studies contained in this thesis.

7.4 Conclusions

Study I demonstrated that strain rate might be an essential factor to consider when describing the failure properties of biological tissues. This rate sensitivity agrees with the consistency of failure strain across strain rates for ligaments and tendons (Noyes et al., 1974; Woo et al., 1990; Ng et al., 2004), appears to scale up to joint fatigue experiments (Zehr, Buchman-Pearle, & Callaghan, 2020), and may also explain the changes in the fatigue life of tendons loaded at disparate frequencies (*c.f.* **Study IV**). However, the mechanism for this

effect has not been fully elucidated beyond its phenomenological description in this thesis. Future investigations may seek to uncover the mechanisms responsible for rate-dependent failure properties.

Study II showed that strain-inhibition of bacterial collagenase is consistent with the uncrimping mechanism in the toe region of a tendon's force-deflection curve. This study provided a more granular picture of this phenomenon in native tendons beyond investigations that have explored strained versus unstrained conditions(Nabeshima et al., 1996; Saini et al., 2020). Further, it may have some critical ramifications in describing precisely how soft tissues remodel when responding to mechanical load. However, it is still unclear if strain inhibition is a feature of mammalian MMPs or whether the duration of strain magnitudes endured *in vivo* would be enough to inhibit them to an appreciable degree. Nevertheless, more investigations with MMPs, or those with cultured tissues, may be warranted to support or refute this hypothesis.

Study III determined that even extreme, sub-injurious magnitudes of creep during a one-time mechanical exposure to the rat-tail IVD may not be enough to induce an inflammatory response. This finding is inconsistent with prolonged cyclic compressive loading in the same tissue (Wuertz et al., 2009; MacLean et al., 2008, 2003), suggesting that cyclic loading, or compression, may uniquely stimulate the fibroblasts to secrete inflammatory cytokines. Exploring the downstream physiological responses to loads remains a fruitful line of inquiry into chronic diseases such as osteoarthritis, tenosynovitis, or, more pertinent to this thesis, chronic LBP.

Study IV culminated with an ambitious model that reproduced many of the mechanical behaviours of soft tissues and qualitatively described the sequence of events during an acute inflammatory response. However, the model remains uncalibrated and has substantial room for improvement. Nevertheless, its theoretical framework appears to have expanded the classical theory to include the biomechanical and biochemical mechanisms of collagen synthesis and turnover that may underpin acute and chronic injuries.

References

Abate, M., Silbernagel, K. G., Siljeholm, C., Di Iorio, A., De Amicis, D., Salini, V., ... Paganelli, R. (2009). Pathogenesis of tendinopathies: inflammation or degeneration? *Arthritis research & therapy*, *11*(3), 235.

Abdollahi-Roodsaz, S., Joosten, L. A., Roelofs, M. F., Radstake, T. R., Matera, G., Popa, C., ... van den Berg, W. B. (2007). Inhibition of toll-like receptor 4 breaks the inflammatory loop in autoimmune destructive arthritis. *Arthritis & Rheumatism: Official Journal of the American College of Rheumatology*, *56*(9), 2957–2967.

Abe, Y., Akeda, K., An, H. S., Aoki, Y., Pichika, R., Muehleman, C., ... Masuda, K. (2007). Proinflammatory cytokines stimulate the expression of nerve growth factor by human intervertebral disc cells. *Spine*, *32*(6), 635–642.

Adhikari, A. S., Chai, J., & Dunn, A. R. (2011). Mechanical load induces a 100-fold increase in the rate of collagen proteolysis by mmp-1. *Journal of the American Chemical Society*, *133*(6), 1686–1689.

Adhikari, A. S., Glassey, E., & Dunn, A. R. (2012). Conformational dynamics accompanying the proteolytic degradation of trimeric collagen i by collagenases. *Journal of the American Chemical Society*, *134*(32), 13259–13265.

Adouni, M., Shirazi-Adl, A., & Shirazi, R. (2012). Computational biodynamics of human knee joint in gait: from muscle forces to cartilage stresses. *Journal of biomechanics*, *45*(12), 2149–2156.

Aguggia, M. (2003). Neurophysiology of pain. *Neurological Sciences*, *24*(2), s57–s60.

Ahn, A. C., Tewari, M., Poon, C.-S., & Phillips, R. S. (2006). The limits of reductionism in medicine: could systems biology offer an alternative? *PLoS medicine*, *3*(6), e208.

Alini, M., Eisenstein, S. M., Ito, K., Little, C., Kettler, A. A., Masuda, K., ... Wilke, H. J. (2008). Are animal models useful for studying human disc disorders/degeneration? *European Spine Journal*, *17*(1), 2–19.

Allen, K. D., Shamji, M. F., Mata, B. A., Gabr, M. A., Sinclair, S. M., Schmitt, D. O., ... Setton, L. A. (2011). Kinematic and dynamic gait compensations in a rat model of lumbar radiculopathy and the effects of tumor necrosis factor-alpha antagonism.

Arthritis research & therapy, *13*(4), R137.

Amar, S., Smith, L., & Fields, G. B. (2017). Matrix metalloproteinase collagenolysis in health and disease. *Biochimica et Biophysica Acta (BBA)-Molecular Cell Research*, *1864*(11), 1940–1951.

Anders, H.-J., & Schaefer, L. (2014). Beyond tissue injury—damage-associated molecular patterns, toll-like receptors, and inflammasomes also drive regeneration and fibrosis. *Journal of the American Society of Nephrology*, *25*(7), 1387–1400.

Anderson, C. K., Chaffin, D. B., Herrin, G. D., & Matthews, L. S. (1985). A biomechanical model of the lumbosacral joint during lifting activities. *Journal of Biomechanics*, *18*(8), 571–584.

Antoniou, J., Steffen, T., Nelson, F., Winterbottom, N., Hollander, A. P., Poole, R. A., ... Alini, M. (1996). The human lumbar intervertebral disc: evidence for changes in the biosynthesis and denaturation of the extracellular matrix with growth, maturation, ageing, and degeneration. *The Journal of clinical investigation*, *98*(4), 996–1003.

Archambault, J., Tsuzaki, M., Herzog, W., & Banes, A. J. (2002). Stretch and interleukin-1β induce matrix metalloproteinases in rabbit tendon cells in vitro. *Journal of orthopaedic research*, *20*(1), 36–39.

Arend, W. P. (2002). The balance between il-1 and il-1ra in disease. *Cytokine & growth factor reviews*, *13*(4-5), 323–340.

Arend, W. P., Malyak, M., Smith, M., Whisenand, T. D., Slack, J. L., Sims, J. E., ... Dower, S. K. (1994). Binding of il-1 alpha, il-1 beta, and il-1 receptor antagonist by soluble il-1 receptors and levels of soluble il-1 receptors in synovial fluids. *The Journal of Immunology*, *153*(10), 4766–4774.

Arner, E. C., Hughes, C. E., Decicco, C. P., Caterson, B., & Tortorella, M. D. (1998). Cytokine-induced cartilage proteoglycan degradation is mediated by aggrecanase. *Osteoarthritis and cartilage*, *6*(3), 214–228.

Arnoczky, S. P., Lavagnino, M., & Egerbacher, M. (2007). The mechanobiological aetiopathogenesis of tendinopathy: is it the over-stimulation or the under-stimulation of tendon cells? *International journal of experimental pathology*, *88*(4), 217–226.

Arnoczky, S. P., Lavagnino, M., Egerbacher, M., Caballero, O., Gardner, K., & Shender,

M. A. (2008). Loss of homeostatic strain alters mechanostat "set point" of tendon cells in vitro. *Clinical orthopaedics and related research*, *466*(7), 1583–1591.

Arnoczky, S. P., Tian, T., Lavagnino, M., & Gardner, K. (2004). Ex vivo static tensile loading inhibits mmp-1 expression in rat tail tendon cells through a cytoskeletally based mechanotransduction mechanism. *Journal of Orthopaedic Research*, *22*(2), 328–333.

Arrhenius, S. (1889). Über die dissociationswärme und den einfluss der temperatur auf den dissociationsgrad der elektrolyte. *Zeitschrift für physikalische Chemie*, *4*(1), 96–116.

Arroyo, A. G., & Iruela-Arispe, M. L. (2010). Extracellular matrix, inflammation, and the angiogenic response. *Cardiovascular research*, *86*(2), 226–235.

Arya, S., & Kulig, K. (2009). Tendinopathy alters mechanical and material properties of the achilles tendon. *Journal of applied physiology*, *108*(3), 670–675.

Ashinsky, B. G., Gullbrand, S. E., Bonnevie, E. D., Mandalapu, S. A., Wang, C., Elliott, D. M., ... Smith, H. E. (2019). Multiscale and multimodal structure–function analysis of intervertebral disc degeneration in a rabbit model. *Osteoarthritis and Cartilage*, *27*(12), 1860–1869. Retrieved from https://doi.org/10.1016/j.joca.2019.07.016 doi: 10.1016/j.joca.2019.07.016

Bachmeier, B. E., Nerlich, A. G., Weiler, C., PAESOLD, G., Jochum, M., & Boos, N. (2007). Analysis of tissue distribution of tnf-α, tnf-α-receptors, and the activating tnf-α–converting enzyme suggests activation of the tnf-α system in the aging intervertebral disc. *Annals of the New York Academy of Sciences*, *1096*(1), 44–54.

Baker, A. H., Edwards, D. R., & Murphy, G. (2002). Metalloproteinase inhibitors: biological actions and therapeutic opportunities. *Journal of cell science*, *115*(19), 3719–3727.

Baker, S., Sugars, R., Wendel, M., Smith, A., Waddington, R. J., Cooper, P., & Sloan, A. J. (2009). Tgf-β/extracellular matrix interactions in dentin matrix: a role in regulating sequestration and protection of bioactivity. *Calcified tissue international*, *85*(1), 66–74.

Barbir, A., Godburn, K. E., Michalek, A. J., Lai, A., Monsey, R. D., & Iatridis, J. C. (2011). Effects of torsion on intervertebral disc gene expression and biomechanics,

using a rat tail model. *Spine*, *36*(8), 607.

Barbir, A., Michalek, A. J., Abbott, R. D., & Iatridis, J. C. (2010). Effects of enzymatic digestion on compressive properties of rat intervertebral discs. *Journal of biomechanics*, *43*(6), 1067–1073.

Barrett, J. M., & Callaghan, J. P. (2017). A mechanistic damage model for ligaments. *Journal of biomechanics*, *61*, 11–17.

Barrett, J. M., & Callaghan, J. P. (2018). A procedure for determining parameters of a simplified ligament model. *Journal of biomechanics*, *66*, 175–179.

Barrett, J. M., & Callaghan, J. P. (2021). A one-dimensional collagen-based biomechanical model of passive soft tissue with viscoelasticity and failure. *Journal of Theoretical Biology*, *509*, 110488.

Barrett, J. M., Gooyers, C. E., Karakolis, T., & Callaghan, J. P. (2016). The impact of posture on the mechanical properties of a functional spinal unit during cyclic compressive loading. *Journal of biomechanical engineering*, *138*(8), 081007.

Bass, C. R., Lucas, S. R., Salzar, R. S., Oyen, M. L., Planchak, C., Shender, B. S., & Paskoff, G. (2007). Failure properties of cervical spinal ligaments under fast strain rate deformations. *Spine*, *32*(1), E7–E13. doi: 10.1097/01.brs.0000251058.53905.eb

Bass, E., Ashford, F., Segal, M., & Lotz, J. (2004). Biaxial testing of human annulus fibrosus and its implications for a constitutive formulation. *Annals of biomedical engineering*, *32*(9), 1231–1242.

Batra, J., Robinson, J., Mehner, C., Hockla, A., Miller, E., Radisky, D. C., & Radisky, E. S. (2012). Pegylation extends circulation half-life while preserving in vitro and in vivo activity of tissue inhibitor of metalloproteinases-1 (timp-1). *PLoS One*, *7*(11), e50028.

Bembey, A. K., Oyen, M. L., Bushby, A. J., & Boyde, a. (2006). Viscoelastic properties of bone as a function of hydration state determined by nanoindentation. *Philosophical Magazine*, *28*(1), 5691–5703. Retrieved from http://discovery.ucl.ac.uk/43731/{%}5Cnhttp://www.tandfonline.com/doi/abs/10.1080/14786430600660864 doi: 10.1080/14786430600660864

Bevan, T., Merabet, N., Hornsby, J., Watton, P. N., & Thompson, M. S. (2018). A biome-

chanical model for fibril recruitment: Evaluation in tendons and arteries. *Journal of biomechanics*, *74*, 192–196.

Birkedal-Hansen, H., Moore, W., Bodden, M., Windsor, L., Birkedal-Hansen, B., DeCarlo, A., & Engler, J. (1993). Matrix metalloproteinases: a review. *Critical Reviews in Oral Biology & Medicine*, *4*(2), 197–250.

Black, P. H. (2002). Stress and the inflammatory response: a review of neurogenic inflammation. *Brain, behavior, and immunity*, *16*(6), 622–653.

Bogduk, N. (1983). The innervation of the lumbar spine. *Spine*, *8*(3), 286–293.

Bonassar, L. J., Sandy, J. D., Lark, M. W., Plaas, A. H., Frank, E. H., & Grodzinsky, A. J. (1997). Inhibition of cartilage degradation and changes in physical properties induced by il-1β and retinoic acid using matrix metalloproteinase inhibitors. *Archives of biochemistry and biophysics*, *344*(2), 404–412.

Bontempi, M. (2009). Probabilistic model of ligaments and tendons: quasistatic linear stretching. *Physical Review E*, *79*(3), 030903.

Bowman, B. M., & Robbins, D. H. (1972, feb). Parameter Study of Biomechanical Quantities in Analytical Neck Models.. Retrieved from http://papers.sae.org/720957/ doi: 10.4271/720957

Boyle, C. J., Lennon, A. B., & Prendergast, P. J. (2011). In silico prediction of the mechanobiological response of arterial tissue: application to angioplasty and stenting. *Journal of biomechanical engineering*, *133*(8).

Brew, K., & Nagase, H. (2010). The tissue inhibitors of metalloproteinases (timps): an ancient family with structural and functional diversity. *Biochimica et biophysica acta (BBA)-molecular cell research*, *1803*(1), 55–71.

Brolin, K., & Halldin, P. (2004). Development of a finite element model of the upper cervical spine and a parameter study of ligament characteristics. *Spine*, *29*(4), 376–385.

Bruehlmann, S. B., B. Rattner, J., R. Matyas, J., & A. Duncan, N. (2002). Regional variations in the cellular matrix of the annulus fibrosus of the intervertebral disc. *Journal of anatomy*, *201*(2), 159–171.

Buckwalter, J. A., Cooper, R., & Maynard, J. (1976). Elastic fibers in human intervertebral

discs. *The Journal of bone and joint surgery. American volume*, *58*(1), 73–76.

Burdorf, A., Naaktgeboren, B., et al. (1993). Occupational risk factors for low back pain among sedentary workers. *Journal of occupational medicine.: official publication of the Industrial Medical Association*, *35*(12), 1213–1220.

Burke, J., Watson, R., McCormack, D., Dowling, F., Walsh, M., & Fitzpatrick, J. (2002). Intervertebral discs which cause low back pain secrete high levels of proinflammatory mediators. *The Journal of bone and joint surgery. British volume*, *84*(2), 196–201.

Busscher, I., van Dieën, J. H., van der Veen, A. J., Kingma, I., Meijer, G. J., Verkerke, G. J., & Veldhuizen, A. G. (2011). The effects of creep and recovery on the in vitro biomechanical characteristics of human multi-level thoracolumbar spinal segments. *Clinical biomechanics*, *26*(5), 438–444.

Butler, D. L., Kay, M. D., & Stouffer, D. C. (1986). Comparison of material properties in fascicle-bone units from human patellar tendon and knee ligaments. *Journal of biomechanics*, *19*(6), 425–432.

Caler, W. E., & Carter, D. R. (1989). Bone creep-fatigue damage accumulation. *Journal of biomechanics*, *22*(6-7), 625–635.

Callaghan, J. P., & McGill, S. M. (2001). Intervertebral disc herniation: studies on a porcine model exposed to highly repetitive flexion/extension motion with compressive force. *Clinical Biomechanics*, *16*(1), 28–37.

Callaghan, J. P., Salewytsch, A. J., & Andrews, D. M. (2001). An evaluation of predictive methods for estimating cumulative spinal loading. *Ergonomics*, *44*(9), 825–837.

Camp, R. J., Liles, M., Beale, J., Saeidi, N., Flynn, B. P., Moore, E., ... Ruberti, J. W. (2011). Molecular mechanochemistry: low force switch slows enzymatic cleavage of human type i collagen monomer. *Journal of the American chemical society*, *133*(11), 4073–4078.

Carter, D., & Caler, W. (1985). A cumulative damage model for bone fracture. *Journal of Orthopaedic Research*, *3*(1), 84–90.

Cassidy, J., Hiltner, A., & Baer, E. (1989). Hierarchical structure of the intervertebral disc. *Connective tissue research*, *23*(1), 75–88.

Cassidy, J. D., Carroll, L. J., & Côté, P. (1998). The saskatchewan health and back pain

survey: the prevalence of low back pain and related disability in saskatchewan adults. *Spine*, *23*(17), 1860–1866.

Chandrashekar, N., Hashemi, J., Slauterbeck, J., & Beynnon, B. D. (2008). Low-load behaviour of the patellar tendon graft and its relevance to the biomechanics of the reconstructed knee. *Clinical Biomechanics*, *23*(7), 918–925.

Chang, S.-W., Flynn, B. P., Ruberti, J. W., & Buehler, M. J. (2012). Molecular mechanism of force induced stabilization of collagen against enzymatic breakdown. *Biomaterials*, *33*(15), 3852–3859.

Chazal, J., Tanguy, A., Bourges, M., Gaurel, G., Escande, G., Guillot, M., & Vanneuville, G. (1985). Biomechanical properties of spinal ligaments and a histological study of the supraspinal ligament in traction. *Journal of biomechanics*, *18*(3), 167–176.

Chen, C.-H., Chiang, C.-J., Wu, L.-C., Yang, C.-H., Kuo, Y.-J., Tsuang, Y.-H., & Tsai, T.-H. (2016). Time course investigation of intervertebral disc degeneration in a rat-tail puncture model. *Life sciences*, *156*, 15–20.

Chen, J., Kim, J., Shao, W., Schlecht, S. H., Baek, S. Y., Jones, A. K., ... Wojtys, E. M. (2019). An anterior cruciate ligament failure mechanism. *The American journal of sports medicine*, *47*(9), 2067–2076.

Chen, Y., Lawless, C., Gillespie, C. S., Wu, J., Boys, R. J., & Wilkinson, D. J. (2010). Calibayes and basis: integrated tools for the calibration, simulation and storage of biological simulation models. *Briefings in bioinformatics*, *11*(3), 278–289.

Choi, K.-C., Lee, Y. S., Lim, S., Choi, H. K., Lee, C.-H., Lee, E.-K., ... Park, S. H. (2006). Smad6 negatively regulates interleukin 1-receptor–toll-like receptor signaling through direct interaction with the adaptor pellino-1. *Nature immunology*, *7*(10), 1057–1065.

Cholewicki, J., & McGill, S. (1992). Lumbar posterior ligament involvement during extremely heavy lifts estimated from fluoroscopic measurements. *Journal of biomechanics*, *25*(1), 17–28.

Ciechomska, M., O'Reilly, S., Suwara, M., Bogunia-Kubik, K., & van Laar, J. M. (2014). Mir-29a reduces timp-1 production by dermal fibroblasts via targeting tgf-β activated kinase 1 binding protein 1, implications for systemic sclerosis. *PloS one*, *9*(12),

e115596.

Cleland, W. (1967). Enzyme kinetics. *Annual review of biochemistry*, *36*(1), 77–112.

Clermont, G., Chow, C. C., Constantine, G. M., Vodovotz, Y., & Bartels, J. (2004). Mathematical and statistical modeling of acute inflammation. In *Classification, clustering, and data mining applications* (pp. 457–467). Springer.

Clouet, J., Fusellier, M., Camus, A., Le Visage, C., & Guicheux, J. (2018). Intervertebral disc regeneration: From cell therapy to the development of novel bioinspired endogenous repair strategies. *Advanced drug delivery reviews*.

Correa-Gallegos, D., Jiang, D., & Rinkevich, Y. (2021). Fibroblasts as confederates of the immune system. *Immunological reviews*, *302*(1), 147–162.

Crick, F. (1954). A structure for collagen. *The Journal of Chemical Physics*, *22*(2), 347–348.

Crisco, J. J., Moore, D. C., & McGovern, R. D. (2002). Strain-rate sensitivity of the rabbit mcl diminishes at traumatic loading rates. *Journal of Biomechanics*, *35*(10), 1379–1385.

David, L., Grood, E. S., Noyes, F. R., Zernicke, R. E., et al. (1978). Biomechanics of ligaments and tendons. *Exercise and sport sciences reviews*, *6*(1), 125–182.

Davis, G. E., Bayless, K. J., Davis, M. J., & Meininger, G. A. (2000). Regulation of tissue injury responses by the exposure of matricryptic sites within extracellular matrix molecules. *The American journal of pathology*, *156*(5), 1489–1498.

Day, J., Rubin, J., Vodovotz, Y., Chow, C. C., Reynolds, A., & Clermont, G. (2006). A reduced mathematical model of the acute inflammatory response ii. capturing scenarios of repeated endotoxin administration. *Journal of theoretical biology*, *242*(1), 237–256.

de Waal Malefyt, R., Abrams, J., Bennett, B., Figdor, C. G., & De Vries, J. E. (1991). Interleukin 10 (il-10) inhibits cytokine synthesis by human monocytes: an autoregulatory role of il-10 produced by monocytes. *The Journal of experimental medicine*, *174*(5), 1209–1220.

Dinarello, C., et al. (2002). The il-1 family and inflammatory diseases. *Clinical and experimental rheumatology*, *20*(5; SUPP/27), S1–S13.

Dinarello, C. A. (2011). Interleukin-1 in the pathogenesis and treatment of inflammatory diseases. *Blood*, *117*(14), 3720–3732.

Donovan, G. M. (2020). Generalized distribution-moment approximation for kinetic theories of muscular contraction. *Mathematical Biosciences*, *329*, 108455.

Dower, S., & Qwarnstrom, E. (2003). Signalling networks, inflammation and innate immunity. *Biochemical Society Transactions*, *31*(6), 1462–1471.

Droguett, R., Cabello-Verrugio, C., Riquelme, C., & Brandan, E. (2006). Extracellular proteoglycans modify tgf-β bio-availability attenuating its signaling during skeletal muscle differentiation. *Matrix Biology*, *25*(6), 332–341.

Duenwald, S. E., Vanderby, R., & Lakes, R. S. (2009). Viscoelastic relaxation and recovery of tendon. *Annals of biomedical engineering*, *37*(6), 1131–1140.

Duncan, W. J. (1937). *Galerkin's method in mechanics and differential equations* (Tech. Rep.). HM Stationery Office.

D'Ambrosia, P., King, K., Davidson, B., Zhou, B. H., Lu, Y., & Solomonow, M. (2010). Pro-inflammatory cytokines expression increases following low-and high-magnitude cyclic loading of lumbar ligaments. *European Spine Journal*, *19*(8), 1330–1339.

Eaton, S. L., Hurtado, M. L., Oldknow, K. J., Graham, L. C., Marchant, T. W., Gillingwater, T. H., ... Wishart, T. M. (2014). A guide to modern quantitative fluorescent western blotting with troubleshooting strategies. *JoVE (Journal of Visualized Experiments)*(93), e52099.

Eckhard, U., Schönauer, E., & Brandstetter, H. (2013). Structural basis for activity regulation and substrate preference of clostridial collagenases G, H, and T. *Journal of Biological Chemistry*, *288*(28), 20184–20194. doi: 10.1074/jbc.M112.448548

Eckhard, U., Schönauer, E., Ducka, P., Briza, P., Nüss, D., & Brandstetter, H. (2009). Biochemical characterization of the catalytic domains of three different clostridial collagenases. *Biological Chemistry*, *390*(1), 11–18. doi: 10.1515/BC.2009.004

Eckhard, U., Schönauer, E., Nüss, D., & Brandstetter, H. (2012). Europe PMC Funders Group Structure of collagenase G reveals a chew and digest mechanism of bacterial collagenolysis. , *18*(10), 1109–1114. doi: 10.1038/nsmb.2127.Structure

Edwards, W. B. (2018). Modeling overuse injuries in sport as a mechanical fatigue phe-

nomenon. *Exercise and sport sciences reviews*, *46*(4), 224–231.

Elliott, D. M., & Setton, L. A. (2001). Anisotropic and inhomogeneous tensile behavior of the human anulus fibrosus: experimental measurement and material model predictions. *Journal of biomechanical engineering*, *123*(3), 256–263.

Elliott, D. M., Yerramalli, C. S., Beckstein, J. C., Boxberger, J. I., Johannessen, W., & Vresilovic, E. J. (2008). The effect of relative needle diameter in puncture and sham injection animal models of degeneration. *Spine*, *33*(6), 588–596.

Ellis, D. G. (1978, nov). Creep Failure of Rat Tail Tendon. *Journal of Biomechanical Engineering*, *100*(4), 229–234. Retrieved from https://asmedigitalcollection.asme.org/biomechanical/article/100/4/229/439625/Creep-Failure-of-Rat-Tail-Tendon doi: 10.1115/1.3426215

Eming, S. A., Krieg, T., & Davidson, J. M. (2007). Inflammation in wound repair: molecular and cellular mechanisms. *Journal of Investigative Dermatology*, *127*(3), 514–525.

Epstein, M. (2012). *The elements of continuum biomechanics*. John Wiley & Sons.

Escuer, J., Martínez, M. A., McGinty, S., & Peña, E. (2019). Mathematical modelling of the restenosis process after stent implantation. *Journal of the Royal Society Interface*, *16*(157), 20190313.

Evans, J., & Nachemson, A. (1968). Some mechanical properties of the third lumbar interlaminar ligament. *J Biomech*, *1*, 211–220.

Fernandes, J. C., Martel-Pelletier, J., & Pelletier, J.-P. (2002). The role of cytokines in osteoarthritis pathophysiology. *Biorheology*, *39*(1, 2), 237–246.

Fice, J. B., Cronin, D. S., & Panzer, M. B. (2011). Cervical spine model to predict capsular ligament response in rear impact. *Annals of biomedical engineering*, *39*(8), 2152–2162.

Firminger, C. R., & Edwards, W. B. (2021). Effects of cyclic loading on the mechanical properties and failure of human patellar tendon. *Journal of Biomechanics*, *120*, 110345.

Flynn, B. P., Bhole, A. P., Saeidi, N., Liles, M., DiMarzio, C. A., & Ruberti, J. W. (2010). Mechanical strain stabilizes reconstituted collagen fibrils against enzymatic

degradation by mammalian collagenase matrix metalloproteinase 8 (mmp-8). *PLoS One*, *5*(8), e12337.

Fratzl, P. (2008). Collagen: structure and mechanics, an introduction. In *Collagen* (pp. 1–13). Springer. doi: 10.1007/978-0-387-73906-9_1

Fratzl, P., Misof, K., Zizak, I., Rapp, G., Amenitsch, H., & Bernstorff, S. (1998). Fibrillar structure and mechanical properties of collagen. *Journal of structural biology*, *122*(1-2), 119–122.

Freemont, A. (2008). The cellular pathobiology of the degenerate intervertebral disc and discogenic back pain. *Rheumatology*, *48*(1), 5–10.

Frolik, C. A., Wakefield, L. M., Smith, D. M., & Sporn, M. B. (1984). Characterization of a membrane receptor for transforming growth factor-beta in normal rat kidney fibroblasts. *Journal of Biological Chemistry*, *259*(17), 10995–11000.

Fuchs, A. C., Granowitz, E. V., Shapiro, L., Vannier, E., Lonnemann, G., Angel, J. B., ... others (1996). Clinical, hematologic, and immunologic effects of interleukin-10 in humans. *Journal of clinical immunology*, *16*(5), 291–303.

Fung, D. T., Wang, V. M., Andarawis-Puri, N., Basta-Pljakic, J., Li, Y., Laudier, D. M., ... Flatow, E. L. (2010). Early response to tendon fatigue damage accumulation in a novel in vivo model. *Journal of biomechanics*, *43*(2), 274–279.

Fung, Y. C. (1967). Elasticity of soft tissues in simple elongation. *The American journal of physiology*, *213*(6), 1532–1544.

Fung, Y. C. (1977). A first course in continuum mechanics. *Englewood Cliffs, NJ, Prentice-Hall, Inc., 1977. 351 p.*, 329. Retrieved from http://adsabs.harvard.edu/abs/1977ph...book.....F{%}5Cnhttp://www.goodreads.com/book/show/1970414.First{_}Course{_}in{_}Continuum{_}Mechanics. doi: 10.1017/CBO9780511619571

Fung, Y. C. (1981). *Biomechanics: Mechanical Properties of Living Tissues, 2nd ed.* (Second ed.). Springer Science and Business Media.

Gabbett, T. J. (2016). The training—injury prevention paradox: should athletes be training smarter and harder? *Br J Sports Med*, *50*(5), 273–280.

Galloway, M. T., Lalley, A. L., & Shearn, J. T. (2013). The role of mechanical loading in

tendon development, maintenance, injury, and repair. *The Journal of bone and joint surgery. American volume*, *95*(17), 1620.

Ganey, T., Libera, J., Moos, V., Alasevic, O., Fritsch, K.-G., Meisel, H. J., & Hutton, W. C. (2003). Disc chondrocyte transplantation in a canine model: a treatment for degenerated or damaged intervertebral disc. *Spine*, *28*(23), 2609–2620.

Gardner, K., Arnoczky, S. P., Caballero, O., & Lavagnino, M. (2008). The effect of stress-deprivation and cyclic loading on the timp/mmp ratio in tendon cells: an in vitro experimental study. *Disability and Rehabilitation*, *30*(20-22), 1523–1529.

Garlanda, C., Riva, F., Bonavita, E., Gentile, S., & Mantovani, A. (2013). Decoys and regulatory "receptors" of the il-1/toll-like receptor superfamily. *Frontiers in immunology*, *4*, 180.

Gearing, A., Beckett, P., Christodoulou, M., Churchill, M., Clements, J., Crimmin, M., ... others (1995). Matrix metalloproteinases and processing of pro-tnf-α. *Journal of leukocyte biology*, *57*(5), 774–777.

Gelman, A., Carlin, J. B., Stern, H. S., & Rubin, D. B. (1995). *Bayesian data analysis*. Chapman and Hall/CRC.

Goldring, S. R., & Goldring, M. B. (2004). The role of cytokines in cartilage matrix degeneration in osteoarthritis. *Clinical Orthopaedics and Related Research (1976-2007)*, *427*, S27–S36.

Gooyers, C. E., Frost, D. M., McGill, S. M., & Callaghan, J. P. (2013). Partial rupture of the achilles tendon during a simulated fire ground task: Insights obtained from a case report for the prevention and reporting of musculoskeletal injury. *Clinical Biomechanics*, *28*(4), 436–440.

Graham, M. F., Willey, A., Adams, J., Yager, D., & Diegelmann, R. F. (1996). Interleukin 1 beta down-regulates collagen and augments collagenase expression in human intestinal smooth muscle cells. *Gastroenterology*, *110*(2), 344–350.

Gregory, D. E., Bae, W. C., Sah, R. L., & Masuda, K. (2014). Disc degeneration reduces the delamination strength of the annulus fibrosus in the rabbit annular disc puncture model. *The Spine Journal*, *14*(7), 1265–1271.

Gregory, D. E., & Callaghan, J. P. (2011). A comparison of uniaxial and biaxial mechan-

ical properties of the annulus fibrosus: a porcine model. *Journal of biomechanical engineering*, *133*(2), 024503.

Gregory, D. E., Veldhuis, J. H., Horst, C., Brodland, G. W., & Callaghan, J. P. (2011). Novel lap test determines the mechanics of delamination between annular lamellae of the intervertebral disc. *Journal of biomechanics*, *44*(1), 97–102.

Guilak, F., Ting-Beall, H. P., Baer, a. E., Trickey, W. R., Erickson, G. R., & Setton, L. a. (1999). Viscoelastic properties of intervertebral disc cells. Identification of two biomechanically distinct cell populations. *Spine (Phila Pa 1976)*, *24*(23), 2475–2483. Retrieved from http://www.ncbi.nlm.nih.gov/entrez/query.fcgi?cmd=Retrieve{&}db=PubMed{&}dopt=Citation{&}list{_}uids=10626310

Gunawardena, J. (2005). Multisite protein phosphorylation makes a good threshold but can be a poor switch. *Proceedings of the National Academy of Sciences*, *102*(41), 14617–14622.

Gupta, H., Seto, J., Krauss, S., Boesecke, P., & Screen, H. (2010). In situ multi-level analysis of viscoelastic deformation mechanisms in tendon collagen. *Journal of structural biology*, *169*(2), 183–191.

Hairer, E., & Wanner, G. (1999). Stiff differential equations solved by radau methods. *Journal of Computational and Applied Mathematics*, *111*(1-2), 93–111.

Hamedzadeh, A., Gasser, T. C., & Federico, S. (2018). On the constitutive modelling of recruitment and damage of collagen fibres in soft biological tissues. *European Journal of Mechanics-A/Solids*, *72*, 483–496.

Hashemi, J., Chandrashekar, N., Mansouri, H., Slauterbeck, J. R., & Hardy, D. M. (2008). The human anterior cruciate ligament: sex differences in ultrastructure and correlation with biomechanical properties. *Journal of orthopaedic research*, *26*(7), 945–950.

Hausser, H., Gröning, A., Hasilik, A., Schönherr, E., & Kresse, H. (1994). Selective inactivity of tgf-β/decorin complexes. *FEBS letters*, *353*(3), 243–245.

Haut, R. (1983). Age-dependent influence of strain rate on the tensile failure of rat-tail tendon. *Journal of biomechanical engineering*, *105*(3), 296–299.

Hayes, A. J., Benjamin, M., & Ralphs, J. R. (2001). Extracellular matrix in development of the intervertebral disc. *Matrix Biology*, *20*(2), 107–121.

Hazuda, D. J., Lee, J. C., & Young, P. R. (1987). The kinetics of interleukin-1 secretion from activated monocytes. *The Journal of Biological Chemistry*, *263*(17).

Hewitt, J., Guilak, F., Glisson, R., & Vail, T. P. (2001). Regional material properties of the human hip joint capsule ligaments. *Journal of Orthopaedic Research*, *19*(3), 359–364.

Hildebrand, A., Romaris, M., Rasmussen, L., Heinegård, D., Twardzik, D., Border, W., & Ruoslahti, E. (1994). Interaction of the small interstitial proteoglycans biglycan, decorin and fibromodulin with transforming growth factor β. *Biochemical Journal*, *302*(2), 527–534.

Hill, A. V. (1910). The possible effects of the aggregation of the molecules of haemoglobin on its dissociation curves. *j. physiol.*, *40*, 4–7.

Ho, J. C., Wylie, J., & Apte, S. S. (2014). The role of the adamts proteins in the intervertebral disc. In *The intervertebral disc* (pp. 125–135). Springer.

Holm, S., Maroudas, A., Urban, J., Selstam, G., & Nachemson, A. (1981). Nutrition of the intervertebral disc: solute transport and metabolism. *Connective tissue research*, *8*(2), 101–119.

Holmes, M. W., Hodder, J. N., & Keir, P. J. (2010). Continuous assessment of low back loads in long-term care nurses. *Ergonomics*, *53*(9), 1108–1116.

Holmes, M. W., Howarth, S. J., Callaghan, J. P., & Keir, P. J. (2012). Biomechanical properties of the transverse carpal ligament under biaxial strain. *Journal of orthopaedic research*, *30*(5), 757–763.

Holzapfel, G. A., Schulze-Bauer, C., Feigl, G., & Regitnig, P. (2005). Single lamellar mechanics of the human lumbar anulus fibrosus. *Biomechanics and modeling in mechanobiology*, *3*(3), 125–140.

Hooley, C. J., & Cohen, R. E. (1979). A model for the creep behaviour of tendon. *International Journal of Biological Macromolecules*, *1*(3), 123–132. doi: 10.1016/0141-8130(79)90028-X

Hope, M., & Saxby, T. S. (2007). Tendon healing. *Foot and ankle clinics*, *12*(4), 553–567.

Hopkins, D. R., Keles, S., & Greenspan, D. S. (2007). The bone morphogenetic protein 1/tolloid-like metalloproteinases. *Matrix Biology*, *26*(7), 508–523.

Huang, C.-Y., & Ferrell, J. E. (1996). Ultrasensitivity in the mitogen-activated protein kinase cascade. *Proceedings of the National Academy of Sciences*, *93*(19), 10078–10083.

Huang, H., Zhang, J., Sun, K., Zhang, X., & Tian, S. (2011). Effects of repetitive multiple freeze–thaw cycles on the biomechanical properties of human flexor digitorum superficialis and flexor pollicis longus tendons. *Clinical Biomechanics*, *26*(4), 419–423.

Huebener, P., & Schwabe, R. F. (2013). Regulation of wound healing and organ fibrosis by toll-like receptors. *Biochimica et Biophysica Acta (BBA)-Molecular Basis of Disease*, *1832*(7), 1005–1017.

Hulmes, D. (2008). Collagen diversity, synthesis and assembly. In *Collagen* (pp. 15–47). Springer.

Hulmes, D., Wess, T. J., Prockop, D. J., & Fratzl, P. (1995). Radial packing, order, and disorder in collagen fibrils. *Biophysical journal*, *68*(5), 1661–1670.

Hulmes, D. J., & Miller, A. (1979). Quasi-hexagonal molecular packing in collagen fibrils. *Nature*, *282*(5741), 878–880. doi: 10.1038/282878a0

Humzah, M., & Soames, R. (1988). Human intervertebral disc: structure and function. *The Anatomical Record*, *220*(4), 337–356.

Huxley, A. F. (1957). Muscle structure and theories of contraction. *Prog. Biophys. Biophys. Chem*, *7*, 255–318.

Iatridis, J. C., MacLean, J. J., Roughley, P. J., & Alini, M. (2006). Effects of mechanical loading on intervertebral disc metabolism in vivo. *The Journal of bone and joint surgery. American volume*, *88*(0 2), 41.

Iatridis, J. C., Mente, P. L., Stokes, I. A., Aronsson, D. D., & Alini, M. (1999). Compression-induced changes in intervertebral disc properties in a rat tail model. *Spine*, *24*(10), 996–1002.

Iatridis, J. C., Setton, L. A., Weidenbaum, M., & Mow, V. C. (1997, oct). The viscoelastic behavior of the non-degenerate human lumbar nucleus pulposus in shear. *Journal of Biomechanics*, *30*(10), 1005–1013. Retrieved from http://linkinghub.elsevier.com/retrieve/pii/S0021929097000699 doi: 10.1016/S0021-9290(97)00069-9

Iatridis, J. C., Weidenbaum, M., Setton, L. A., & Mow, V. C. (1996). Is the nucleus

pulposus a solid or a fluid? mechanical behaviors of the nucleus pulposus of the human intervertebral disc. *Spine*, *21*(10), 1174–1184.

Iizuka, Y., Iizuka, H., Mieda, T., Tsunoda, D., Sasaki, T., Tajika, T., ... Takagishi, K. (2017). Prevalence of chronic nonspecific low back pain and its associated factors among middle-aged and elderly people: an analysis based on data from a musculoskeletal examination in japan. *Asian spine journal*, *11*(6), 989.

Imai, K., Hiramatsu, A., Fukushima, D., Pierschbacher, M. D., & Okada, Y. (1997). Degradation of decorin by matrix metalloproteinases: identification of the cleavage sites, kinetic analyses and transforming growth factor-β 1 release. *Biochemical Journal*, *322*(3), 809–814.

Ingalls, B. P. (2013). *Mathematical modeling in systems biology: an introduction*. MIT press.

Ito, A., Mukaiyama, A., Itoh, Y., Nagase, H., Thøgersen, I. B., Enghild, J. J., ... Mori, Y. (1996). Degradation of interleukin 1β by matrix metalloproteinases. *Journal of Biological Chemistry*, *271*(25), 14657–14660.

Itoh, Y. (2006). Mt1-mmp: A key regulator of cell migration in tissue. *IUBMB life*, *58*(10), 589–596.

Jamison, C., Marangoni, R., & Glaser, A. (1968). Viscoelastic properties of soft tissue by discrete model characterization. *Journal of Biomechanics*, *1*(1), 33–46.

Jang, S., Park, J.-S., Won, Y.-H., Yun, S.-J., & Kim, S.-J. (2012). The expression of toll-like receptors (tlrs) in cultured human skin fibroblast is modulated by histamine. *Chonnam medical journal*, *48*(1), 7–14.

Jaynes, E. T. (1968). Prior probabilities. *IEEE Transactions on systems science and cybernetics*, *4*(3), 227–241.

Jiang, Y., Wang, Y., & Peng, X. (2015). A visco-hyperelastic constitutive model for human spine ligaments. *Cell biochemistry and biophysics*, *71*(2), 1147–56. Retrieved from http://www.ncbi.nlm.nih.gov/pubmed/25347987 doi: 10.1007/s12013-014-0322-9

Jin, Y.-F., Han, H.-C., Berger, J., Dai, Q., & Lindsey, M. L. (2011). Combining experimental and mathematical modeling to reveal mechanisms of macrophage-dependent

left ventricular remodeling. *BMC systems biology*, *5*(1), 1–14.

Johnen, L., Mertens, A., Nitsch, V., & Brandl, C. (2022). Why cumulative loading calculated using non-weighted integration may not be suitable for assessing physical stress of the lower back: an empirical investigation of strain during lifting and lowering tasks. *Ergonomics*, *65*(1), 134–146.

Johnson, E., Chetty, K., Moore, I., Stewart, A., & Jones, W. (1982). The distribution and arrangement of elastic fibres in the intervertebral disc of the adult human. *Journal of anatomy*, *135*(Pt 2), 301.

Johnson, K. A., & Goody, R. S. (2011). The original michaelis constant: translation of the 1913 michaelis–menten paper. *Biochemistry*, *50*(39), 8264–8269.

Johnson, Z. I., Schoepflin, Z. R., Choi, H., Shapiro, I. M., & Risbud, M. V. (2015). Disc in flames: Roles of tnf-α and il-1β in intervertebral disc degeneration. *European cells & materials*, *30*, 104.

Jones, C. M., Beason, D. P., & Dugas, J. R. (2018). Ulnar collateral ligament reconstruction versus repair with internal bracing: comparison of cyclic fatigue mechanics. *Orthopaedic Journal of Sports Medicine*, *6*(2), 2325967118755991.

Julius, D., & Basbaum, A. I. (2001). Molecular mechanisms of nociception. *Nature*, *413*(6852), 203.

Kadler, K. E., Hojima, Y., & Prockop, D. (1988). Assembly of type i collagen fibrils de novo. between 37 and 41 degrees c the process is limited by micro-unfolding of monomers. *Journal of Biological Chemistry*, *263*(21), 10517–10523.

Kahlem, P., Di Cara, A., Durot, M., Hancock, J., Klipp, E., Schchter, V., ... Mendoza, L. (2011). Strengths and weaknesses of selected modeling methods used in systems biology. *Systems and Computational Biology—Bioinformatics and Computational Modeling*.

Kandel, R., Hamilton, D., Seguin, C., Li, S.-Q., Arana, C., & Pilliar, R. (2007). An in vitro tissue model to study the effect of age on nucleus pulposus cells. *European Spine Journal*, *16*(12), 2166–2173.

Kannus, P. (2000). Structure of the tendon connective tissue. *Scandinavian journal of medicine & science in sports*, *10*(6), 312–320.

Kapoor, M., Martel-Pelletier, J., Lajeunesse, D., Pelletier, J.-P., & Fahmi, H. (2011). Role of proinflammatory cytokines in the pathophysiology of osteoarthritis. *Nature Reviews Rheumatology*, *7*(1), 33.

Karousou, E., Ronga, M., Vigetti, D., Passi, A., & Maffulli, N. (2008). Collagens, proteoglycans, mmp-2, mmp-9 and timps in human achilles tendon rupture. *Clinical orthopaedics and related research*, *466*(7), 1577.

Karsdal, M. (2019). *Biochemistry of collagens, laminins and elastin: structure, function and biomarkers*. Academic Press.

Karunaratne, A., Li, S., & Bull, A. M. (2018). Nano-scale mechanisms explain the stiffening and strengthening of ligament tissue with increasing strain rate. *Scientific Reports*, *8*(1), 1–9.

Kasai, K., Hiraiwa, M., Emoto, T., Kuroda, H., Hattori, Y., Mochizuki, Y., ... Shimoda, S.-I. (1990). Presence of high affinity receptor for interleukin-1 (il-1) on cultured porcine thyroid cells. *Hormone and metabolic research*, *22*(02), 75–79.

Kastelic, J., & Baer, E. (1980). Deformation in tendon collagen. In *Symposia of the society for experimental biology* (Vol. 34, pp. 397–435).

Kastelic, J., Galeski, A., & Baer, E. (1978). The multicomposite structure of tendon. *Connective Tissue Research*, *6*(1), 11–23. doi: 10.3109/03008207809152283

Kato, Y. P., Christiansen, D. L., Hahn, R. A., Shieh, S.-J., Goldstein, J. D., & Silver, F. H. (1989). Mechanical properties of collagen fibres: a comparison of reconstituted and rat tail tendon fibres. *Biomaterials*, *10*(1), 38–42.

Keller, T. S., Spengler, D. M., & Hansson, T. H. (1987). Mechanical behavior of the human lumbar spine. I. Creep analysis during static compressive loading. *Journal of orthopaedic research*, *5*(4), 467–78. Retrieved from http://www.ncbi.nlm.nih.gov/pubmed/3681521 doi: 10.1002/jor.1100050402

Kenedi, R. M., Gibson, T., Evans, J. H., & Barbenel, J. C. (1975, sep). Tissue mechanics. *Physics in Medicine and Biology*, *20*(5), 001. Retrieved from http://stacks.iop.org/0031-9155/20/i=5/a=001?key=crossref.540e3c771716730781c15811ee6748f6 doi: 10.1088/0031-9155/20/5/001

Ker, R. F. (2007). Mechanics of tendon, from an engineering perspective. *International*

Journal of Fatigue, *29*(6), 1001–1009.

Ker, R. F., Wang, X. T., & Pike, A. (2000). Fatigue quality of mammalian tendons. *Journal of Experimental Biology*, *203*(8), 1317–1327.

Kessler-Becker, D., Krieg, T., & Eckes, B. (2004). Expression of pro-inflammatory markers by human dermal fibroblasts in a three-dimensional culture model is mediated by an autocrine interleukin-1 loop. *Biochemical Journal*, *379*(2), 351–358.

King, K., Davidson, B., Zhou, B. H., Lu, Y., & Solomonow, M. (2009). High magnitude cyclic load triggers inflammatory response in lumbar ligaments. *Clinical Biomechanics*, *24*(10), 792–798.

Klatt, A. R., Paul-Klausch, B., Klinger, G., Kühn, G., Renno, J. H., Banerjee, M., ... Wielckens, K. (2009). A critical role for collagen ii in cartilage matrix degradation: collagen ii induces pro-inflammatory cytokines and mmps in primary human chondrocytes. *Journal of orthopaedic research*, *27*(1), 65–70.

Knight, B. E., Kozlowski, N., Havelin, J., King, T., Crocker, S. J., Young, E. E., & Baumbauer, K. M. (2019). Timp-1 attenuates the development of inflammatory pain through mmp-dependent and receptor-mediated cell signaling mechanisms. *Frontiers in Molecular Neuroscience*, 220.

Knörzer, E., Folkhard, W., Geercken, W., Boschert, C., Koch, M., Hilbert, B., ... Nemetschek, T. (1986). New aspects of the etiology of tendon rupture. *Archives of orthopaedic and traumatic surgery*, *105*(2), 113–120.

Kolch, W., Calder, M., & Gilbert, D. (2005). When kinases meet mathematics: the systems biology of mapk signalling. *FEBS letters*, *579*(8), 1891–1895.

Kolmogorov, A. N., & Fomin, S. V. (1957). *Elements of the theory of functions and functional analysis* (Vol. 1). Courier Corporation.

Korecki, C. L., Costi, J. J., & Iatridis, J. C. (2008). Needle puncture injury affects intervertebral disc mechanics and biology in an organ culture model. *Spine*, *33*(3), 235.

Korecki, C. L., MacLean, J. J., & Iatridis, J. C. (2008). Dynamic compression effects on intervertebral disc mechanics and biology. *Spine*, *33*(13), 1403.

Kreger, S., Bell, B., Bailey, J., Stites, E., Kuske, J., Waisner, B., & Voytik-Harbin, S.

(2010). Polymerization and matrix physical properties as important design considerations for soluble collagen formulations. *Biopolymers: Original Research on Biomolecules*, *93*(8), 690–707.

Krock, E., Currie, J. B., Weber, M. H., Ouellet, J. A., Stone, L. S., Rosenzweig, D. H., & Haglund, L. (2016). Nerve growth factor is regulated by toll-like receptor 2 in human intervertebral discs. *Journal of Biological Chemistry*, *291*(7), 3541–3551.

Kudlow, J., Cheung, C., & Bjorge, J. (1986). Epidermal growth factor stimulates the synthesis of its own receptor in a human breast cancer cell line. *Journal of Biological Chemistry*, *261*(9), 4134–4138.

Kumar, R., Clermont, G., Vodovotz, Y., & Chow, C. C. (2004). The dynamics of acute inflammation. *Journal of theoretical biology*, *230*(2), 145–155.

Kumar, S. (2001). Theories of musculoskeletal injury causation. *Ergonomics*, *44*(1), 17–47. Retrieved from http://www.ncbi.nlm.nih.gov/pubmed/11214897 doi: 10.1080/00140130120716

Kunisch, E., Kinne, R. W., Alsalameh, R. J., & Alsalameh, S. (2016). Pro-inflammatory il-1beta and/or tnf-alpha up-regulate matrix metalloproteases-1 and-3 m rna in chondrocyte subpopulations potentially pathogenic in osteoarthritis: in situ hybridization studies on a single cell level. *International journal of rheumatic diseases*, *19*(6), 557–566.

LaBry, R., Sbriccoli, P., Zhou, B.-H., & Solomonow, M. (2004). Longer static flexion duration elicits a neuromuscular disorder in the lumbar spine. *Journal of Applied Physiology*, *96*(5), 2005–2015.

Ladyzhenskaya, O. A. (2003). Sixth problem of the millennium: Navier-stokes equations, existence and smoothness. *Russian Mathematical Surveys*, *58*(2), 251.

Laidler, K. J. (1984). The development of the arrhenius equation. *Journal of chemical Education*, *61*(6), 494.

Lange, K. L., Little, R. J., & Taylor, J. M. (1989). Robust statistical modeling using the t distribution. *Journal of the American Statistical Association*, *84*(408), 881–896.

Laraia, E. M. S., Silva, I. S., Pereira, D. M., dos Reis, F. A., Albertini, R., de Almeida, P., ... de Tarso Camillo de Carvalho, P. (2012). Effect of low-level laser therapy

(660 nm) on acute inflammation induced by tenotomy of achilles tendon in rats. *Photochemistry and photobiology*, *88*(6), 1546–1550.

Laurent, G. (1987). Dynamic state of collagen: pathways of collagen degradation in vivo and their possible role in regulation of collagen mass. *American Journal of Physiology-Cell Physiology*, *252*(1), C1–C9.

Lautrup, B. (2005). *Physics of Continuous Matter*.

Lavagnino, M., Arnoczky, S. P., Tian, T., & Vaupel, Z. (2003). Effect of amplitude and frequency of cyclic tensile strain on the inhibition of mmp-1 mrna expression in tendon cells: an in vitro study. *Connective tissue research*, *44*(3-4), 181–187.

Lavagnino, M., Gardner, K., & Arnoczky, S. P. (2013). Age-related changes in the cellular, mechanical, and contractile properties of rat tail tendons. *Connective tissue research*, *54*(1), 70–75.

Lee, A. H., & Elliott, D. M. (2017). Freezing does not alter multiscale tendon mechanics and damage mechanisms in tension. *Annals of the New York Academy of Sciences*, *1409*(1), 85.

Lee, B., Zhou, X., Riching, K., Eliceiri, K. W., Keely, P. J., Guelcher, S. A., ... Jiang, Y. (2014). A three-dimensional computational model of collagen network mechanics. *PLoS ONE*, *9*(11), 1–12. doi: 10.1371/journal.pone.0111896

Lee, G. H., Kumar, A., Berkson, E., Verma, N., Bach, B. R., & Hallab, N. (2009). A biomechanical analysis of bone-patellar tendon-bone grafts after repeat freeze-thaw cycles in a cyclic loading model. *The journal of knee surgery*, *22*(02), 111–113.

Lees, S., Pineri, M., & Escoubes, M. (1984). A generalized packing model for type I collagen. *International Journal of Biological Macromolecules*, *6*(3), 133–136. doi: 10.1016/0141-8130(84)90053-9

Le Goff, C., & Cormier-Daire, V. (2011). The adamts (l) family and human genetic disorders. *Human molecular genetics*, *20*(R2), R163–R167.

Le Maitre, C. L., Freemont, A. J., & Hoyland, J. A. (2005). The role of interleukin-1 in the pathogenesis of human intervertebral disc degeneration. *Arthritis research & therapy*, *7*(4), R732.

Le Maitre, C. L., Hoyland, J. A., & Freemont, A. J. (2007). Catabolic cytokine expression

in degenerate and herniated human intervertebral discs: Il-1β and tnfα expression profile. *Arthritis research & therapy*, *9*(4), R77.

LePage, E. C., Stoker, A. M., Kuroki, K., & Cook, J. L. (2021). Effects of cyclic compression on intervertebral disc metabolism using a whole-organ rat tail model. *Journal of Orthopaedic Research®*, *39*(9), 1945–1954.

Leppert, D., Lindberg, R. L., Kappos, L., & Leib, S. L. (2001). Matrix metalloproteinases: Multifunctional effectors of inflammation in multiple sclerosis and bacterial meningitis. *Brain Research Reviews*, *36*(2-3), 249–257. doi: 10.1016/S0165-0173(01)00101-1

Le Visage, C., Yang, S.-H., Kadakia, L., Sieber, A. N., Kostuik, J. P., & Leong, K. W. (2006). Small intestinal submucosa as a potential bioscaffold for intervertebral disc regeneration. *Spine*, *31*(21), 2423–2430.

Liao, H., & Belkoff, S. M. (1999). A failure model for ligaments. *Journal of biomechanics*, *32*(2), 183–188.

Likhitpanichkul, M., Torre, O. M., Gruen, J., Walter, B., Hecht, A. C., & Iatridis, J. C. (2016). Do mechanical strain and tnf-α interact to amplify pro-inflammatory cytokine production in human annulus fibrosus cells? *Journal of biomechanics*, *49*(7), 1214–1220.

Lin, T. W., Cardenas, L., & Soslowsky, L. J. (2004). Biomechanics of tendon injury and repair. *Journal of biomechanics*, *37*(6), 865–877.

Lingham-Soliar, T., & Wesley-Smith, J. (2008). First investigation of the collagen d-band ultrastructure in fossilized vertebrate integument. *Proceedings of the Royal Society B: Biological Sciences*, *275*(1648), 2207–2212.

Liu, Q., Smith, C. W., Zhang, W., Burns, A. R., & Li, Z. (2012). Nk cells modulate the inflammatory response to corneal epithelial abrasion and thereby support wound healing. *The American journal of pathology*, *181*(2), 452–462.

Lu, T., Tian, L., Han, Y., Vogelbaum, M., & Stark, G. R. (2007). Dose-dependent cross-talk between the transforming growth factor-β and interleukin-1 signaling pathways. *Proceedings of the National Academy of Sciences*, *104*(11), 4365–4370.

Lucas, S. R., Bass, C. R., Crandall, J. R., Kent, R. W., Shen, F. H., & Salzar, R. S. (2009). Viscoelastic and failure properties of spine ligament collagen fascicles. *Biomechanics*

and Modeling in Mechanobiology, *8*(6), 487–498. doi: 10.1007/s10237-009-0152-7

Lucas, S. R., Bass, C. R., Salzar, R., Shender, B., & Paskoff, G. (2006). High-rate viscoelastic properties of human cervical spinal intervertebral discs. In *Annual meeting of the american society of biomechanics, american society of biomechanics.*

Lynch, H. A., Johannessen, W., Wu, J. P., Jawa, A., & Elliott, D. M. (2003). Effect of fiber orientation and strain rate on the nonlinear uniaxial tensile material properties of tendon. *Journal of biomechanical engineering*, *125*(5), 726–731.

MacLean, J. J., Lee, C. R., Alini, M., & Iatridis, J. C. (2004). Anabolic and catabolic mrna levels of the intervertebral disc vary with the magnitude and frequency of in vivo dynamic compression. *Journal of Orthopaedic Research*, *22*(6), 1193–1200.

MacLean, J. J., Lee, C. R., Alini, M., & Iatridis, J. C. (2005). The effects of short-term load duration on anabolic and catabolic gene expression in the rat tail intervertebral disc. *Journal of Orthopaedic Research*, *23*(5), 1120–1127.

MacLean, J. J., Lee, C. R., Grad, S., Ito, K., Alini, M., & Iatridis, J. C. (2003). Effects of immobilization and dynamic compression on intervertebral disc cell gene expression in vivo. *Spine*, *28*(10), 973–981.

MacLean, J. J., Roughley, P. J., Monsey, R. D., Alini, M., & Iatridis, J. C. (2008). In vivo intervertebral disc remodeling: kinetics of mrna expression in response to a single loading event. *Journal of Orthopaedic Research*, *26*(5), 579–588.

Maeda, E., Kuroyanagi, K., Ando, Y., & Matsumoto, T. (2019). Effects of substrate stiffness on morphology and mmp-1 gene expression in tenocytes stimulated with interleukin-1β. *Journal of Orthopaedic Research®*.

Maffulli, N., Ewen, S. W., Waterston, S. W., Reaper, J., & Barrass, V. (2000). Tenocytes from ruptured and tendinopathic achilles tendons produce greater quantities of type iii collagen than tenocytes from normal achilles tendons: an in vitro model of human tendon healing. *The American journal of sports medicine*, *28*(4), 499–505.

Maganaris, C. N., Narici, M. V., Almekinders, L. C., & Maffulli, N. (2004). Biomechanics and pathophysiology of overuse tendon injuries. *Sports medicine*, *34*(14), 1005–1017.

Magnusson, S. P., Langberg, H., & Kjaer, M. (2010). The pathogenesis of tendinopathy: balancing the response to loading. *Nature Reviews Rheumatology*, *6*(5), 262–268.

Mahmood, T., & Yang, P.-C. (2012). Western blot: technique, theory, and trouble shooting. *North American journal of medical sciences*, *4*(9), 429.

Maidhof, R., Jacobsen, T., Papatheodorou, A., & Chahine, N. O. (2014). Inflammation induces irreversible biophysical changes in isolated nucleus pulposus cells. *PloS one*, *9*(6), e99621.

Maly, M. R. (2008). Abnormal and cumulative loading in knee osteoarthritis. *Current opinion in rheumatology*, *20*(5), 547–552.

Manesh, K. M., Halámek, J., Pita, M., Zhou, J., Tam, T. K., Santhosh, P., ... others (2009). Enzyme logic gates for the digital analysis of physiological level upon injury. *Biosensors and Bioelectronics*, *24*(12), 3569–3574.

Manning, C. N., Havlioglu, N., Knutsen, E., Sakiyama-Elbert, S. E., Silva, M. J., Thomopoulos, S., & Gelberman, R. H. (2014). The early inflammatory response after flexor tendon healing: a gene expression and histological analysis. *Journal of Orthopaedic Research*, *32*(5), 645–652.

Marchand, F., & Ahmed, A. M. (1990). Investigation of the laminate structure of lumbar disc anulus fibrosus. *Spine*, *15*(5), 402–410.

Marouane, H., Shirazi-Adl, A., & Hashemi, J. (2015). Quantification of the role of tibial posterior slope in knee joint mechanics and acl force in simulated gait. *Journal of biomechanics*, *48*(10), 1899–1905.

Martel-Pelletier, J., McCollum, R., & Pelletier, J.-P. (1993). The synthesis of il-1 receptor antagonist (il-1ra) by synovial fibroblasts is markedly increased by the cytokines tnf-α and il-1. *Biochimica et Biophysica Acta (BBA)-Molecular Cell Research*, *1175*(3), 302–305.

Maruyama, M., Rhee, C., Utsunomiya, T., Zhang, N., Ueno, M., Yao, Z., & Goodman, S. B. (2020). Modulation of the inflammatory response and bone healing. *Frontiers in Endocrinology*, *11*, 386.

Massague, J., & Like, B. (1985). Cellular receptors for type beta transforming growth factor. ligand binding and affinity labeling in human and rodent cell lines. *Journal of Biological Chemistry*, *260*(5), 2636–2645.

Masuda, K., Aota, Y., Muehleman, C., Imai, Y., Okuma, M., Thonar, E. J., ... An, H. S.

(2005). A novel rabbit model of mild, reproducible disc degeneration by an anulus needle puncture: correlation between the degree of disc injury and radiological and histological appearances of disc degeneration. *Spine*, *30*(1), 5–14.

Mattucci, S. F., Moulton, J. A., Chandrashekar, N., & Cronin, D. S. (2012). Strain rate dependent properties of younger human cervical spine ligaments. *Journal of the mechanical behavior of biomedical materials*, *10*, 216–226.

Matuszewski, P. E., Chen, Y.-L., Szczesny, S. E., Lake, S. P., Elliott, D. M., Soslowsky, L. J., & Dodge, G. R. (2012). Regional variation in human supraspinatus tendon proteoglycans: decorin, biglycan, and aggrecan. *Connective tissue research*, *53*(5), 343–348.

Mayne, J., & Robinson, J. J. (1999). Comparative analysis of the kinetic parameters and thermal stability of two matrix metalloproteinases expressed in the developing sea urchin embryo. *The International Journal of Biochemistry & Cell Biology*, *31*(6), 717–724.

McCarthy, D. J., & Smyth, G. K. (2009). Testing significance relative to a fold-change threshold is a treat. *Bioinformatics*, *25*(6), 765–771.

McCawley, L. J., & Matrisian, L. M. (2001). Matrix metalloproteinases: they're not just for matrix anymore! *Current opinion in cell biology*, *13*(5), 534–540.

McElreath, R. (2020). *Statistical rethinking: A bayesian course with examples in r and stan*. Chapman and Hall/CRC.

McGill, S. M. (1997). The biomechanics of low back injury: implications on current practice in industry and the clinic. *Journal of biomechanics*, *30*(5), 465–475.

McGill, S. M., & Brown, S. (1992). Creep response of the lumbar spine to prolonged full flexion. *Clinical Biomechanics*, *7*(1), 43–46.

McGill, S. M., & Norman, R. (1986). Partitioning of the l4-l5 dynamic moment into disc, ligamentous, and muscular components during lifting. *Spine*, *11*(7), 666–678.

McLevey, J. (2021). *Doing computational social science: A practical introduction*. Sage.

Mengoni, M., Luxmoore, B. J., Wijayathunga, V. N., Jones, A. C., Broom, N. D., & Wilcox, R. K. (2015). Derivation of inter-lamellar behaviour of the intervertebral disc annulus. *journal of the mechanical behavior of biomedical materials*, *48*, 164–

172.

Merline, R., Moreth, K., Beckmann, J., Nastase, M. V., Zeng-Brouwers, J., Tralhão, J. G., ... others (2011). Signaling by the matrix proteoglycan decorin controls inflammation and cancer through pdcd4 and microrna-21. *Science signaling*, *4*(199), ra75–ra75.

Michalek, A. J., Funabashi, K. L., & Iatridis, J. C. (2010). Needle puncture injury of the rat intervertebral disc affects torsional and compressive biomechanics differently. *European Spine Journal*, *19*(12), 2110–2116.

Michalek, A. J., & Iatridis, J. C. (2011). Penetrating annulus fibrosus injuries affect dynamic compressive behaviors of the intervertebral disc via altered fluid flow: an analytical interpretation. *Journal of biomechanical engineering*, *133*(8), 084502.

Millar, N. L., Murrell, G. A., & McInnes, I. B. (2017). Inflammatory mechanisms in tendinopathy–towards translation. *Nature Reviews Rheumatology*, *13*(2), 110.

Miller, R. H. (2017). Joint loading in runners does not initiate knee osteoarthritis. *Exercise and sport sciences reviews*, *45*(2), 87–95.

Miyagi, M., Ishikawa, T., Kamoda, H., Suzuki, M., Murakami, K., Shibayama, M., ... others (2012). Issls prize winner: disc dynamic compression in rats produces long-lasting increases in inflammatory mediators in discs and induces long-lasting nerve injury and regeneration of the afferent fibers innervating discs: a pathomechanism for chronic discogenic low back pain. *Spine*, *37*(21), 1810–1818.

Monika Egerbacher, D., Arnoczky, S. P., Caballero, O., & Gardner, K. L. (2008). Loss of homeostatic tension induces apoptosis in tendon cells: An in vitro study. *Clinical Orthopaedics and Related Research*, *466*(7), 1562.

Mullender, M., & Huiskes, R. (1995). Proposal for the regulatory mechanism of wolff's law. *Journal of orthopaedic research*, *13*(4), 503–512.

Murphy, G. (2011). Tissue inhibitors of metalloproteinases. *Genome biology*, *12*(11), 233.

Myers, B. S., McElhaney, J. H., & Doherty, B. J. (1991). The viscoelastic responses of the human cervical spine in torsion: Experimental limitations of quasi-linear theory, and a method for reducing these effects. *Journal of Biomechanics*, *24*(9), 811–817. doi: 10.1016/0021-9290(91)90306-8

Myklebust, J. B., Pintar, F., Yoganandan, N., Cusick, J. F., Maiman, D., Myers, T. J., &

Sances, J. A. (1988). Tensile strength of spinal ligaments. *Spine*, *13*(5), 526–531.

Myles, W. M. (1993). Ophthalmic etymology. *Survey of Ophthalmology*, *37*(4), 306–309. doi: 10.1016/0039-6257(93)90016-Z

Myllyharju, J. (2005). Intracellular post-translational modifications of collagens. In *Collagen* (pp. 115–147). Springer.

Myllylä, R., Wang, C., Heikkinen, J., Juffer, A., Lampela, O., Risteli, M., ... Sipilä, L. (2007). Expanding the lysyl hydroxylase toolbox: new insights into the localization and activities of lysyl hydroxylase 3 (lh3). *Journal of cellular physiology*, *212*(2), 323–329.

Nabeshima, Y., Grood, E., Sakurai, A., & Herman, J. (1996). Uniaxial tension inhibits tendon collagen degradation by collagenase in vitro. *Journal of orthopaedic research*, *14*(1), 123–130.

Nagase, H. (1996). Matrix metalloproteinases. In *Zinc metalloproteases in health and disease* (pp. 173–224). CRC Press.

Nagata, K. (1996). Hsp47: a collagen-specific molecular chaperone. *Trends in biochemical sciences*, *21*(1), 23–26.

Nagata, K. (1998). Expression and function of heat shock protein 47: a collagen-specific molecular chaperone in the endoplasmic reticulum. *Matrix biology*, *16*(7), 379–386.

Nakai, A., Satoh, M., Hirayoshi, K., & Nagata, K. (1992). Involvement of the stress protein hsp47 in procollagen processing in the endoplasmic reticulum. *The Journal of cell biology*, *117*(4), 903–914.

Nakama, L. H., King, K. B., Abrahamsson, S., & Rempel, D. M. (2005). Evidence of tendon microtears due to cyclical loading in an in vivo tendinopathy model. *Journal of Orthopaedic Research*, *23*(5), 1199–1205.

Nelson-Wong, E., Flynn, T., & Callaghan, J. P. (2009). Development of active hip abduction as a screening test for identifying occupational low back pain. *Journal of Orthopaedic & Sports Physical Therapy*, *39*(9), 649-657. Retrieved from https://doi.org/10.2519/jospt.2009.3093 (PMID: 19721214) doi: 10.2519/jospt.2009.3093

Newton, K., & Dixit, V. M. (2012). Signaling in innate immunity and inflammation. *Cold*

Spring Harbor perspectives in biology, *4*(3), a006049.

Ng, B., Chou, S., Lim, B., & Chong, A. (2004). Strain rate effect on the failure properties of tendons. *Proceedings of the Institution of Mechanical Engineers, Part H: Journal of Engineering in Medicine*, *218*(3), 203–206.

Ng, J. K., Kippers, V., Richardson, C. A., & Parnianpour, M. (2001). Range of motion and lordosis of the lumbar spine: reliability of measurement and normative values. *Spine*, *26*(1), 53–60.

Nomura, T., Mochida, J., Okuma, M., Nishimura, K., & Sakabe, K. (2001). Nucleus pulposus allograft retards intervertebral disc degeneration. *Clinical Orthopaedics and Related Research®*, *389*, 94–101.

Norcross, J. P., Lester, G. E., Weinhold, P., & Dahners, L. E. (2003). An in vivo model of degenerative disc disease. *Journal of Orthopaedic Research*, *21*(1), 183–188.

Norman, R., Wells, R., Neumann, P., Frank, J., Shannon, H., Kerr, M., ... others (1998). A comparison of peak vs cumulative physical work exposure risk factors for the reporting of low back pain in the automotive industry. *Clinical biomechanics*, *13*(8), 561–573.

Noyes, F. R., DeLucas, J. L., & Torvik, P. J. (1974). Biomechanics of anterior cruciate ligament failure: An analysis of. *J. Bone Joint Surg. Am*, *56*, 236–253.

Obata, T., Brown, G. E., & Yaffe, M. B. (2000). Map kinase pathways activated by stress: the p38 mapk pathway. *Critical care medicine*, *28*(4), N67–N77.

Oda, J., Tanaka, H., & Tsuzuki, N. (1988). Intervertebral disc changes with aging of human cervical vertebra. from the neonate to the eighties. *Spine*, *13*(11), 1205–1211.

Ogden, R. W. (1997). *Non-linear elastic deformations*. Courier Corporation.

Okuyama, K. (2008). Revisiting the molecular structure of collagen. *Connective tissue research*, *49*(5), 299–310.

Orgel, J. P., Miller, A., Irving, T. C., Fischetti, R. F., Hammersley, A. P., & Wess, T. J. (2001, nov). The In Situ Supermolecular Structure of Type I Collagen. *Structure*, *9*(11), 1061–1069. Retrieved from https://linkinghub.elsevier.com/retrieve/pii/S0969212601006694 doi: 10.1016/S0969-2126(01)00669-4

Osher, S. (1985). Convergence of generalized muscl schemes. *SIAM Journal on Numerical*

Analysis, *22*(5), 947–961.

Osti, O., Vernon-Roberts, B., & Fraser, R. . (1990). 1990 volvo award in experimental studies. anulus tears and intervertebral disc degeneration. an experimental study using an animal model. *Spine*, *15*(8), 762–767.

Oxland, T. R., & Panjabi, M. M. (1992). The onset and progression of spinal injury: a demonstration of neutral zone sensitivity. *Journal of biomechanics*, *25*(10), 1165–1172.

Ozbabacan, S. E. A., Gursoy, A., Nussinov, R., & Keskin, O. (2014). The structural pathway of interleukin 1 (il-1) initiated signaling reveals mechanisms of oncogenic mutations and snps in inflammation and cancer. *PLoS computational biology*, *10*(2), e1003470.

O'Connell, G. D., Sen, S., & Elliott, D. M. (2012). Human annulus fibrosus material properties from biaxial testing and constitutive modeling are altered with degeneration. *Biomechanics and modeling in mechanobiology*, *11*(3-4), 493–503.

Padh, H. (1991). Vitamin c: newer insights into its biochemical functions. *Nutrition Reviews*, *49*(3), 65–70.

Pandit, A., Ashar, R., & Feldman, D. (1999). The effect of tgf-beta delivered through a collagen scaffold on wound healing. *Journal of Investigative Surgery*, *12*(2), 89–100.

Panjabi, M. M., & Courtney, T. W. (2001). High-speed subfailure stretch of rabbit anterior cruciate ligament: changes in elastic, failure and viscoelastic characteristics. *Clinical Biomechanics*, *16*(4), 334–340.

Panjabi, M. M., Moy, P., Oxland, T. R., & Cholewicki, J. (1999). Subfailure injury affects the relaxation behavior of rabbit acl. *Clinical Biomechanics*, *14*(1), 24–31.

Panjabi, M. M., Yoldas, E., Oxland, T. R., & Crisco III, J. J. (1996). Subfailure injury of the rabbit anterior cruciate ligament. *Journal of Orthopaedic Research*, *14*(2), 216–222.

Pardo, A., & Selman, M. (2005). Mmp-1: the elder of the family. *The international journal of biochemistry & cell biology*, *37*(2), 283–288.

Parkinson, R. J., & Callaghan, J. P. (2007). The role of load magnitude as a modifier of the cumulative load tolerance of porcine cervical spinal units: progress towards a

force weighting approach. *Theoretical Issues in Ergonomics Science*, *8*(3), 171–184.

Peng, B., Hao, J., Hou, S., Wu, W., Jiang, D., Fu, X., & Yang, Y. (2006). Possible pathogenesis of painful intervertebral disc degeneration. *Spine*, *31*(5), 560–566.

Perumal, S., Antipova, O., & Orgel, J. P. (2008). Collagen fibril architecture, domain organization, and triple-helical conformation govern its proteolysis. *Proceedings of the National Academy of Sciences*, *105*(8), 2824–2829.

Petruska, J. A., & Hodge, A. J. (1964). A subunit model for the tropocollagen macromolecule. *Proceedings of the National Academy of Sciences of the United States of America*, *51*(5), 871.

Pluijm, S. M., Van Essen, H. W., Bravenboer, N., Uitterlinden, A. G., Smit, J. H., Pols, H. A., & Lips, P. (2004). Collagen type I α1 Sp1 polymorphism, osteoporosis, and intervertebral disc degeneration in older men and women. *Annals of the Rheumatic Diseases*, *63*(1), 71–77. doi: 10.1136/ard.2002.002287

Porter, S., Clark, I. M., Kevorkian, L., & Edwards, D. R. (2005). The adamts metalloproteinases. *Biochemical Journal*, *386*(1), 15–27.

Prasad, P., King, A., & Ewing, C. (1974). The role of articular facets during+ gz acceleration. *Journal of applied mechanics*, *41*(2), 321–326.

Provenzano, P. P., Heisey, D., Hayashi, K., Lakes, R., & Vanderby Jr, R. (2002). Subfailure damage in ligament: a structural and cellular evaluation. *Journal of Applied Physiology*, *92*(1), 362–371.

Przybylski, G. J., Carlin, G. J., Patel, P. R., & Woo, S. L.-Y. (1996). Human anterior and posterior cervical longitudinal ligaments possess similar tensile properties. *Journal of orthopaedic research*, *14*(6), 1005–1008.

Purmessur, D., Walter, B., Roughley, P., Laudier, D., Hecht, A., & Iatridis, J. (2013). A role for tnfα in intervertebral disc degeneration: a non-recoverable catabolic shift. *Biochemical and biophysical research communications*, *433*(1), 151–156.

Puxkandl, R., Zizak, I., Paris, O., Keckes, J., Tesch, W., Bernstorff, S., ... Fratzl, P. (2002). Viscoelastic properties of collagen: synchrotron radiation investigations and structural model. *Philosophical Transactions of the Royal Society of London. Series B: Biological Sciences*, *357*(1418), 191–197.

Quinn, K. P., & Winkelstein, B. A. (2007). Cervical facet capsular ligament yield defines the threshold for injury and persistent joint-mediated neck pain. *Journal of biomechanics*, *40*(10), 2299–2306.

Rennekamp, B., Kutzki, F., Obarska-Kosinska, A., Zapp, C., & Gräter, F. (2019). Hybrid kinetic monte carlo/molecular dynamics simulations of bond scissions in proteins. *Journal of Chemical Theory and Computation*, *16*(1), 553–563.

Retief, E., Parker, M. I., & Retief, A. E. (1985). Regional chromosome mapping of human collagen genes alpha 2(I) and alpha 1(I) (COLIA2 and COLIA1). *Human Genetics*, *69*(4), 304–308. doi: 10.1007/BF00291646

Reynolds, A., Rubin, J., Clermont, G., Day, J., Vodovotz, Y., & Ermentrout, G. B. (2006). A reduced mathematical model of the acute inflammatory response: I. derivation of model and analysis of anti-inflammation. *Journal of theoretical biology*, *242*(1), 220–236.

Ricard-Blum, S. (2011). The collagen family. *Cold Spring Harbor perspectives in biology*, *3*(1), a004978.

Ricard-Blum, S., & Ballut, L. (2011). Matricryptins derived from collagens and proteoglycans. *Frontiers in bioscience (Landmark edition)*, *16*, 674–697.

Richardson, S. M., Freemont, A. J., & Hoyland, J. A. (2014). Pathogenesis of intervertebral disc degeneration. In *The intervertebral disc* (pp. 177–200). Springer.

Riesz, F., & Nagy, B. S. (1955). Functional analysis, frederick ungar pub. *Co., New York*.

Rigby, B. J., Hirai, N., Spikes, J. D., & Eyring, H. (1959). The mechanical properties of rat tail tendon. *The Journal of general physiology*, *43*(2), 265–283.

Riihimäki, H., Tola, S., Videman, T., & Hänninen, K. (1989). Low-back pain and occupation. a cross-sectional questionnaire study of men in machine operating, dynamic physical work, and sedentary work. *Spine*, *14*(2), 204–209.

Riley, G. (2003). The pathogenesis of tendinopathy. a molecular perspective. *Rheumatology*, *43*(2), 131–142.

Risbud, M. V., & Shapiro, I. M. (2014). Role of cytokines in intervertebral disc degeneration: pain and disc content. *Nature Reviews Rheumatology*, *10*(1), 44.

Roberts, S., Menage, J., & Urban, J. (1989). Biochemical and structural properties of the

cartilage end-plate and its relation to the intervertebral disc. *Spine*, *14*(2), 166–174.

Roh, J. S., & Sohn, D. H. (2018). Damage-associated molecular patterns in inflammatory diseases. *Immune network*, *18*(4).

Ruberti, J. W., & Hallab, N. J. (2005). Strain-controlled enzymatic cleavage of collagen in loaded matrix. *Biochemical and biophysical research communications*, *336*(2), 483–489.

Sabio, G., & Davis, R. J. (2014). Tnf and map kinase signalling pathways. In *Seminars in immunology* (Vol. 26, pp. 237–245).

Saini, K., Cho, S., Dooling, L. J., & Discher, D. E. (2020). Tension in fibrils suppresses their enzymatic degradation–a molecular mechanism for 'use it or lose it'. *Matrix Biology*, *85*, 34–46.

Salvatier, J., Wiecki, T. V., & Fonnesbeck, C. (2016). Probabilistic programming in python using pymc3. *PeerJ Computer Science*, *2*, e55.

Sandri, M. (1996). Numerical calculation of lyapunov exponents. *Mathematica Journal*, *6*(3), 78–84.

Sarver, J. J., & Elliott, D. M. (2005). Mechanical differences between lumbar and tail discs in the mouse. *Journal of Orthopaedic Research*, *23*(1), 150–155.

Sasaki, N., & Odajima, S. (1996). Elongation mechanism of collagen fibrils and force-strain relations of tendon at each level of structural hierarchy. *Journal of Biomechanics*, *29*(9), 1131–1136. doi: 10.1016/0021-9290(96)00024-3

Schappacher-Tilp, G., Leonard, T., Desch, G., & Herzog, W. (2015). A novel three-filament model of force generation in eccentric contraction of skeletal muscles. *PloS one*, *10*(3), e0117634.

Schechtman, H., & Bader, D. (1997). In vitro fatigue of human tendons. *Journal of biomechanics*, *30*(8), 829–835.

Schollum, M. L., Robertson, P. A., & Broom, N. D. (2010). How age influences unravelling morphology of annular lamellae–a study of interfibre cohesivity in the lumbar disc. *Journal of anatomy*, *216*(3), 310–319.

Scholma, J., Schivo, S., Camacho, R. A. U., van de Pol, J., Karperien, M., & Post, J. N. (2014). Biological networks 101: Computational modeling for molecular biologists.

Gene, *533*(1), 379–384.

Schroer, A. K., Ryzhova, L. M., & Merryman, W. D. (2014). Network modeling approach to predict myofibroblast differentiation. *Cellular and molecular bioengineering*, *7*(3), 446–459.

Scott, A., Backman, L. J., & Speed, C. (2015). Tendinopathy: update on pathophysiology. *journal of orthopaedic & sports physical therapy*, *45*(11), 833–841.

Séguin, C. A., Pilliar, R. M., Roughley, P. J., & Kandel, R. A. (2005). Tumor necrosis factorα modulates matrix production and catabolism in nucleus pulposus tissue. *Spine*, *30*(17), 1940–1948.

Seifert, A. M., Messing, K., & Dumais, L. (1997). Star wars and strategic defense initiatives: Work activity and health symptoms of unionized bank tellers during work reorganization. *International Journal of Health Services*, *27*(3), 455–477.

Sekton, B. (2010, sep). Matrix metalloproteinases — an overview. *Research and Reports in Biology*, 1. Retrieved from http://www.dovepress.com/matrix-metalloproteinases-ndash-an-overview-peer-reviewed-article-RRB doi: 10.2147/RRB.S12043

Sharma, P., & Maffulli, N. (2006). Biology of tendon injury: healing, modeling and remodeling. *Journal of musculoskeletal and neuronal interactions*, *6*(2), 181.

Shearer, T., Parnell, W. J., Lynch, B., Screen, H. R., & Abrahams, I. D. (2020). A recruitment model of tendon viscoelasticity that incorporates fibril creep and explains strain-dependent relaxation. *Journal of Biomechanical Engineering*, *142*(7), 071003.

Shingleton, W. D. (1996). Collagenase: A key enzyme in collagen turnover. *Biochemistry and Cell Biology*, *74*(6), 759–775. doi: 10.1139/o96-083

Siegmund, T., Allen, M. R., & Burr, D. B. (2008). Failure of mineralized collagen fibrils: modeling the role of collagen cross-linking. *Journal of biomechanics*, *41*(7), 1427–1435.

Sivan, S. S., Hayes, A. J., Wachtel, E., Caterson, B., Merkher, Y., Maroudas, A., ... Roberts, S. (2014). Biochemical composition and turnover of the extracellular matrix of the normal and degenerate intervertebral disc. *European Spine Journal*, *23*(3), 344–353.

Sive, J., Baird, P., Jeziorsk, M., Watkins, A., Hoyland, J., & Freemont, A. (2002). Expression of chondrocyte markers by cells of normal and degenerate intervertebral discs. *Molecular Pathology*, *55*(2), 91.

Smith, L. J., Nerurkar, N. L., Choi, K.-S., Harfe, B. D., & Elliott, D. M. (2011). Degeneration and regeneration of the intervertebral disc: lessons from development. *Disease models & mechanisms*, *4*(1), 31–41.

Snedeker, J. G., & Foolen, J. (2017). Tendon injury and repair – A perspective on the basic mechanisms of tendon disease and future clinical therapy. *Acta Biomaterialia*, *63*, 18–36. Retrieved from https://doi.org/10.1016/j.actbio.2017.08.032 doi: 10.1016/j.actbio.2017.08.032

Sobajima, S., Kompel, J. F., Kim, J. S., Wallach, C. J., Robertson, D. D., Vogt, M. T., ... Gilbertson, L. G. (2005). A slowly progressive and reproducible animal model of intervertebral disc degeneration characterized by mri, x-ray, and histology. *Spine*, *30*(1), 15–24.

Solomonow, M. (2004). Ligaments: a source of work-related musculoskeletal disorders. *Journal of Electromyography and Kinesiology*, *14*(1), 49–60.

Solomonow, M. (2006). Sensory–motor control of ligaments and associated neuromuscular disorders. *Journal of Electromyography and Kinesiology*, *16*(6), 549–567.

Solomonow, M. (2012). Neuromuscular manifestations of viscoelastic tissue degradation following high and low risk repetitive lumbar flexion. *Journal of Electromyography and Kinesiology*, *22*(2), 155–175.

Solomonow, M., Baratta, R., Zhou, B.-H., Burger, E., Zieske, A., & Gedalia, A. (2003). Muscular dysfunction elicited by creep of lumbar viscoelastic tissue. *Journal of Electromyography and Kinesiology*, *13*(4), 381–396.

Solomonow, M., Baratta, R. V., Banks, A., Freudenberger, C., & Zhou, B. H. (2003). Flexion–relaxation response to static lumbar flexion in males and females. *Clinical Biomechanics*, *18*(4), 273–279.

Solomonow, M., Zhou, B.-H., Baratta, R., & Burger, E. (2003). Biomechanics and electromyography of a cumulative lumbar disorder: response to static flexion. *Clinical Biomechanics*, *18*(10), 890–898.

Solomonow, M., Zhou, B. H., Baratta, R. V., Lu, Y., Zhu, M., & Harris, M. (2000). Biexponential recovery model of lumbar viscoelastic laxity and reflexive muscular activity after prolonged cyclic loading. *Clinical Biomechanics*, *15*(3), 167–175.

Solomonow, M., Zhou, B. H., Lu, Y., & King, K. B. (2012). Acute repetitive lumbar syndrome: a multi-component insight into the disorder. *Journal of bodywork and movement therapies*, *16*(2), 134–147.

Standring, S. (2008). *Gray's Anatomy: The Anatomical Basis of Clinical Practice* (40th ed.).

Sternlicht, M. D., & Werb, Z. (2001). How matrix metalloproteinases regulate cell behavior. *Annual review of cell and developmental biology*, *17*(1), 463–516. doi: 10.1146/annurev.cellbio.17.1.463

Stokes, I. A., Aronsson, D. D., Spence, H., & Iatridis, J. C. (1998). Mechanical modulation of intervertebral disc thickness in growing rat tails. *Journal of spinal disorders*, *11*(3), 261–265.

Stokes, I. A., & Iatridis, J. C. (2004). Mechanical conditions that accelerate intervertebral disc degeneration: overload versus immobilization. *Spine*, *29*(23), 2724–2732.

Strogatz, S. H. (2018). *Nonlinear dynamics and chaos: with applications to physics, biology, chemistry, and engineering*. CRC press.

Sun, H. B., Li, Y., Fung, D. T., Majeska, R. J., Schaffler, M. B., & Flatow, E. L. (2008). Coordinate regulation of il-1β and mmp-13 in rat tendons following subrupture fatigue damage. *Clinical orthopaedics and related research*, *466*(7), 1555–1561.

Suto, K., Urabe, K., Naruse, K., Uchida, K., Matsuura, T., Mikuni-Takagaki, Y., ... Itoman, M. (2012). Repeated freeze–thaw cycles reduce the survival rate of osteocytes in bone-tendon constructs without affecting the mechanical properties of tendons. *Cell and tissue banking*, *13*(1), 71–80.

Suzuki, K., Enghild, J. J., Morodomi, T., Salvesen, G., & Nagase, H. (1990). Mechanisms of activation of tissue procollagenase by matrix metalloproteinase 3 (stromelysin). *Biochemistry*, *29*(44), 10261–10270.

Tampier, C., Drake, J. D., Callaghan, J. P., & McGill, S. M. (2007). Progressive disc herniation: an investigation of the mechanism using radiologic, histochemical, and

microscopic dissection techniques on a porcine model. *Spine*, *32*(25), 2869–2874.

Tateuchi, H., Koyama, Y., Akiyama, H., Goto, K., So, K., Kuroda, Y., & Ichihashi, N. (2017). Daily cumulative hip moment is associated with radiographic progression of secondary hip osteoarthritis. *Osteoarthritis and cartilage*, *25*(8), 1291–1298.

Taylor, J. B., Goode, A. P., George, S. Z., & Cook, C. E. (2014). Incidence and risk factors for first-time incident low back pain: a systematic review and meta-analysis. *The Spine Journal*, *14*(10), 2299–2319.

Taylor, S. C., & Posch, A. (2014). The design of a quantitative western blot experiment. *BioMed research international*, *2014*.

Thornton, G. M., Shao, X., Chung, M., Sciore, P., Boorman, R. S., Hart, D. A., & Lo, I. K. (2010). Changes in mechanical loading lead to tendonspecific alterations in mmp and timp expression: influence of stress deprivation and intermittent cyclic hydrostatic compression on rat supraspinatus and achilles tendons. *British journal of sports medicine*, *44*(10), 698–703.

Thorpe, C., Chaudhry, S., Lei, I., Varone, A., Riley, G., Birch, H., ... Screen, H. (2015). Tendon overload results in alterations in cell shape and increased markers of inflammation and matrix degradation. *Scandinavian journal of medicine & science in sports*, *25*(4), e381–e391.

Thorpe, C. T., Streeter, I., Pinchbeck, G. L., Goodship, A. E., Clegg, P. D., & Birch, H. L. (2010). Aspartic acid racemization and collagen degradation markers reveal an accumulation of damage in tendon collagen that is enhanced with aging. *Journal of Biological Chemistry*, *285*(21), 15674–15681.

Tobolsky, A., & Eyring, H. (1943). Mechanical properties of polymeric materials. *The Journal of chemical physics*, *11*(3), 125–134.

Toktaş, Z. O., Ekşi, M. c., Yılmaz, B., Demir, M. K., Özgen, S., Kılıç, T., & Konya, D. (2015). Association of collagen I, IX and vitamin D receptor gene polymorphisms with radiological severity of intervertebral disc degeneration in Southern European Ancestor. *European Spine Journal*, *24*(11), 2432–2441. doi: 10.1007/s00586-015-4206-5

Toosizadeh, N., Nussbaum, M. A., Bazrgari, B., & Madigan, M. L. (2012). Load-relaxation

properties of the human trunk in response to prolonged flexion: measuring and modeling the effect of flexion angle. *PloS one*, *7*(11), e48625.

Torp, S. (1975). Effects of age and of mechanical deformation on the ultrastructure of tendon. *Structure of fibrous biopolymers*, 223–250.

Torricelli, P., Veronesi, F., Pagani, S., Maffulli, N., Masiero, S., Frizziero, A., & Fini, M. (2013). In vitro tenocyte metabolism in aging and oestrogen deficiency. *Age*, *35*(6), 2125–2136.

Troeberg, L., Tanaka, M., Wait, R., Shi, Y. E., Brew, K., & Nagase, H. (2002). E. coli expression of timp-4 and comparative kinetic studies with timp-1 and timp-2: insights into the interactions of timps and matrix metalloproteinase 2 (gelatinase a). *Biochemistry*, *41*(50), 15025–15035.

Troyer, K. L., & Puttlitz, C. M. (2011). Human cervical spine ligaments exhibit fully nonlinear viscoelastic behavior. *Acta biomaterialia*, *7*(2), 700–709. Retrieved from http://www.ncbi.nlm.nih.gov/pubmed/20831909 doi: 10.1016/j.actbio.2010.09.003

Troyer, K. L., Shetye, S. S., & Puttlitz, C. M. (2012). Experimental characterization and finite element implementation of soft tissue nonlinear viscoelasticity. *Journal of biomechanical engineering*, *134*(11), 114501.

Tschesche, H., & Farr, M. (2000). Biomolecular interaction of matrix metalloproteinases and their inhibitors timps. In *Proteome and protein analysis* (pp. 289–300). Springer.

Tsuzaki, M., Guyton, G., Garrett, W., Archambault, J., Herzog, W., Almekinders, L., ... Banes, A. (2003). Il-1β induces cox2, mmp-1,-3 and-13, adamts-4, il-1β and il-6 in human tendon cells. *Journal of Orthopaedic Research*, *21*(2), 256–264.

Tuderman, L., Myllylä, R., & Kivirikko, K. I. (1977). Mechanism of the prolyl hydroxylase reaction: 1. role of co-substrates. *European Journal of Biochemistry*, *80*(2), 341–348.

Tzafriri, A. R., Bercovier, M., & Parnas, H. (2002). Reaction diffusion model of the enzymatic erosion of insoluble fibrillar matrices. *Biophysical journal*, *83*(2), 776–793.

Uchida, H., Tohyama, H., Nagashima, K., Ohba, Y., Matsumoto, H., Toyama, Y., & Yasuda, K. (2005). Stress deprivation simultaneously induces over-expression of

interleukin-1beta, tumor necrosis factor-alpha, and transforming growth factor-beta in fibroblasts and mechanical deterioration of the tissue in the patellar tendon. *Journal of biomechanics*, *38*(4), 791–798.

Ulrich, J. A., Liebenberg, E. C., Thuillier, D. U., & Lotz, J. C. (2007). Issls prize winner: repeated disc injury causes persistent inflammation. *Spine*, *32*(25), 2812–2819.

Urban, J. P., & Roberts, S. (2003). Degeneration of the intervertebral disc. *Arthritis Res Ther*, *5*(3), 120.

Urban, J. P., Smith, S., & Fairbank, J. C. (2004). Nutrition of the intervertebral disc. *Spine*, *29*(23), 2700–2709.

Van Herp, G., Rowe, P., Salter, P., & Paul, J. (2000). Three-dimensional lumbar spinal kinematics: a study of range of movement in 100 healthy subjects aged 20 to 60+ years. *Rheumatology*, *39*(12), 1337–1340.

Veres, S. P., Brennan-Pierce, E. P., & Lee, J. M. (2015). Macrophage-like u937 cells recognize collagen fibrils with strain-induced discrete plasticity damage. *Journal of Biomedical Materials Research Part A*, *103*(1), 397–408.

Veres, S. P., Harrison, J. M., & Lee, J. M. (2013). Repeated subrupture overload causes progression of nanoscaled discrete plasticity damage in tendon collagen fibrils. *Journal of Orthopaedic Research*, *31*(5), 731–737.

Veres, S. P., Harrison, J. M., & Lee, J. M. (2014). Mechanically overloading collagen fibrils uncoils collagen molecules, placing them in a stable, denatured state. *Matrix Biology*, *33*, 54–59.

Viggiani, D., & Callaghan, J. P. (2021). The effects of an acute maximal seated lumbar spine flexion exposure on low back mechanical pain sensitivity. *Journal of Applied Biomechanics*, *38*(1), 12–19.

Viidik, A. (1968). A rheological model for uncalcified parallel-fibred collagenous tissue. *Journal of Biomechanics*, *1*(1), 3–11.

Viidik, A. (1973). Functional properties of collagenous tissues. In *International review of connective tissue research* (Vol. 6, pp. 127–215). Elsevier.

Virtanen, P., Gommers, R., Oliphant, T. E., Haberland, M., Reddy, T., Cournapeau, D., ... others (2020). Scipy 1.0: fundamental algorithms for scientific computing in

python. *Nature methods*, *17*(3), 261–272.

Visse, R., & Nagase, H. (2003). Matrix metalloproteinases and tissue inhibitors of metalloproteinases: structure, function, and biochemistry. *Circulation research*, *92*(8), 827–839.

Vo, N. V., Hartman, R. A., Yurube, T., Jacobs, L. J., Sowa, G. A., & Kang, J. D. (2013). Expression and regulation of metalloproteinases and their inhibitors in intervertebral disc aging and degeneration. *The Spine Journal*, *13*(3), 331–341.

Vodovotz, Y., Chow, C. C., Bartels, J., Lagoa, C., Prince, J. M., Levy, R. M., ... others (2006). In silico models of acute inflammation in animals. *Shock*, *26*(3), 235–244.

Vu, T. T., Marquez, J., Le, L. T., Nguyen, A. T. T., Kim, H. K., & Han, J. (2018). The role of decorin in cardiovascular diseases: more than just a decoration. *Free Radical Research*, *52*(11-12), 1210–1219.

Vuust, J., & Piez, K. A. (1972). A kinetic study of collagen biosynthesis. *Journal of Biological Chemistry*, *247*(3), 856–862.

Walker, B. F. (2000). The prevalence of low back pain: a systematic review of the literature from 1966 to 1998. *Clinical Spine Surgery*, *13*(3), 205–217.

Walker, B. F., & Williamson, O. D. (2009). Mechanical or inflammatory low back pain. what are the potential signs and symptoms? *Manual therapy*, *14*(3), 314–320.

Walker, J. M. (2009). The bicinchoninic acid (bca) assay for protein quantitation. *The protein protocols handbook*, 11–15.

Walter, B., Likhitpanichkul, M., Illien-Junger, S., Roughley, P. J., Hecht, A. C., & Iatridis, J. C. (2015). Tnfα transport induced by dynamic loading alters biomechanics of intact intervertebral discs. *PloS one*, *10*(3), e0118358.

Wang, T., Chen, P., Zheng, M., Wang, A., Lloyd, D., Leys, T., ... Zheng, M. H. (2018). In vitro loading models for tendon mechanobiology. *Journal of Orthopaedic Research®*, *36*(2), 566–575.

Wang, X. T., & Ker, R. F. (1995). Creep rupture of wallaby tail tendons. *The Journal of experimental biology*, *198*(3), 831–845.

Wang, X. T., Ker, R. F., & Alexander, R. M. (1995). Fatigue rupture of wallaby tail tendons. *Journal of experimental biology*, *198*(3), 847–852.

Weathington, N. M., van Houwelingen, A. H., Noerager, B. D., Jackson, P. L., Kraneveld, A. D., Galin, F. S., ... Blalock, J. E. (2006). A novel peptide cxcr ligand derived from extracellular matrix degradation during airway inflammation. *Nature medicine*, *12*(3), 317.

Weber, A., Wasiliew, P., & Kracht, M. (2010). Interleukin-1 (il-1) pathway. *Sci. Signal.*, *3*(105), cm1–cm1.

Weiler, C., Nerlich, A., Zipperer, J., Bachmeier, B., & Boos, N. (2002). 2002 sse award competition in basic science: expression of major matrix metalloproteinases is associated with intervertebral disc degradation and resorption. *European Spine Journal*, *11*(4), 308–320.

Weiler, C., Nerlich, A. G., Bachmeier, B. E., & Boos, N. (2005). Expression and distribution of tumor necrosis factor alpha in human lumbar intervertebral discs: a study in surgical specimen and autopsy controls. *Spine*, *30*(1), 44–53.

Welgus, H., Jeffrey, J., Stricklin, G., Roswit, W., & Eisen, A. (1980). Characteristics of the action of human skin fibroblast collagenase on fibrillar collagen. *The Journal of biological chemistry*, *255*(14), 6806–6813.

Welgus, H. G., Jeffrey, J. J., & Eisen, A. Z. (1981). The collagen substrate specificity of human skin fibroblast collagenase. *Journal of Biological Chemistry*, *256*(18), 9511–9515. Retrieved from http://dx.doi.org/10.1016/S0021-9258(19)68792-2 doi: 10.1016/s0021-9258(19)68792-2

Wen, N., Lavaste, F., Santin, J. J., & Lassau, J. P. (1993, jun). Three-dimensional biomechanical properties of the human cervical spine in vitro. *European Spine Journal*, *2*(1), 2–11. Retrieved from http://link.springer.com/10.1007/BF00301048 doi: 10.1007/BF00301048

West-Mays, J. A., Strissel, K. J., Sadow, P. M., & Fini, M. E. (1995). Competence for collagenase gene expression by tissue fibroblasts requires activation of an interleukin 1 alpha autocrine loop. *Proceedings of the National Academy of Sciences*, *92*(15), 6768–6772.

White, a. a., & Panjabi, M. M. (1990). *Clinical Biomechanics of the Spine Volume 2.* Philadelphia: Lippincott Company.

Wiet, M. G., Piscioneri, A., Khan, S. N., Ballinger, M. N., Hoyland, J. A., & Purmessur, D. (2017). Mast cell-intervertebral disc cell interactions regulate inflammation, catabolism and angiogenesis in discogenic back pain. *Scientific reports*, *7*(1), 12492.

Wilke, H.-J., Neef, P., Caimi, M., Hoogland, T., & Claes, L. E. (1999). New in vivo measurements of pressures in the intervertebral disc in daily life. *Spine*, *24*(8), 755–762.

Willett, T. L., Labow, R. S., Avery, N. C., & Lee, J. M. (2007). Increased proteolysis of collagen in an in vitro tensile overload tendon model. *Annals of biomedical engineering*, *35*(11), 1961–1972.

Wong, V. W., Akaishi, S., Longaker, M. T., & Gurtner, G. C. (2011). Pushing back: wound mechanotransduction in repair and regeneration. *Journal of Investigative Dermatology*, *131*(11), 2186–2196.

Woo, S. L.-Y., Peterson, R. H., Ohland, K. J., Sites, T. J., & Danto, M. I. (1990). The effects of strain rate on the properties of the medial collateral ligament in skeletally immature and mature rabbits: a biomechanical and histological study. *Journal of Orthopaedic Research*, *8*(5), 712–721.

Woolf, C. J., & Salter, M. W. (2000). Neuronal plasticity: increasing the gain in pain. *science*, *288*(5472), 1765–1768.

Wren, T. A., Lindsey, D. P., Beaupré, G. S., & Carter, D. R. (2003). Effects of creep and cyclic loading on the mechanical properties and failure of human achilles tendons. *Annals of biomedical engineering*, *31*(6), 710–717.

Wuertz, K., Godburn, K., MacLean, J. J., Barbir, A., Stinnett Donnelly, J., Roughley, P. J., ... Iatridis, J. C. (2009). In vivo remodeling of intervertebral discs in response to short-and long-term dynamic compression. *Journal of Orthopaedic Research*, *27*(9), 1235–1242.

Wünsch, E., & Heidrich, H.-G. (1963, jan). Zur quantitativen Bestimmung der Kollagenase. *Hoppe-Seyler´s Zeitschrift für physiologische Chemie*, *333*(Jahresband), 149–151. Retrieved from https://www.degruyter.com/document/doi/10.1515/bchm2.1963.333.1.149/html doi: 10.1515/bchm2.1963.333.1.149

Yang, G., Marras, W. S., & Best, T. M. (2011). The biochemical response to biomechanical

tissue loading on the low back during physical work exposure. *Clinical Biomechanics*, *26*(5), 431–437.

Yasuda, T. (2014). Type ii collagen peptide stimulates akt leading to nuclear factor-κb activation: Its inhibition by hyaluronan. *Biomedical Research*, *35*(3), 193–199.

Yingling, V. R., Callaghan, J. P., & McGill, S. M. (1997). Dynamic loading affects the mechanical properties and failure site of porcine spines. *Clinical Biomechanics*, *12*, 301–305. doi: 10.1016/S0268-0033(97)00009-0

Yoganandan, N., Kumaresan, S., & Pintar, F. A. (2000). Geometric and mechanical properties of human cervical spine ligaments. *Journal of biomechanical engineering*, *122*(6), 623–629.

Yoganandan, N., Pintar, F., Butler, J., Reinartz, J., Sances, J. A., & Larson, S. J. (1989). Dynamic response of human cervical spine ligaments. *Spine*, *14*(10), 1102–1110.

Yu, J., Fairbank, J. C., Roberts, S., & Urban, J. P. (2005). The elastic fiber network of the anulus fibrosus of the normal and scoliotic human intervertebral disc. *Spine*, *30*(16), 1815–1820.

Yurube, T., Takada, T., Suzuki, T., Kakutani, K., Maeno, K., Doita, M., ... Nishida, K. (2012). Rat tail static compression model mimics extracellular matrix metabolic imbalances of matrix metalloproteinases, aggrecanases, and tissue inhibitors of metalloproteinases in intervertebral disc degeneration. *Arthritis research & therapy*, *14*(2), 1–14.

Zahalak, G. I. (1981). A distribution-moment approximation for kinetic theories of muscular contraction. *Mathematical biosciences*, *55*(1-2), 89–114.

Zahalak, G. I., & Ma, S.-P. (1990). Muscle activation and contraction: constitutive relations based directly on cross-bridge kinetics. *Journal of biomechanical engineering*, *112*(1), 52–62.

Zapp, C., Obarska-Kosinska, A., Rennekamp, B., Kurth, M., Hudson, D. M., Mercadante, D., ... others (2020). Mechanoradicals in tensed tendon collagen as a source of oxidative stress. *Nature communications*, *11*(1), 1–8.

Zehr, J. D., Buchman-Pearle, J. M., & Callaghan, J. P. (2020). Joint fatigue-failure: a demonstration of viscoelastic responses to rate and frequency loading parameters

using the porcine cervical spine. *Journal of Biomechanics*, *113*, 110081.

Zeigler, A., Richardson, W., Holmes, J., & Saucerman, J. (2016). A computational model of cardiac fibroblast signaling predicts context-dependent drivers of myofibroblast differentiation. *Journal of molecular and cellular cardiology*, *94*, 72–81.

Zhang, C., Gullbrand, S. E., Schaer, T. P., Lau, Y. K., Jiang, Z., Dodge, G. R., ... Smith, L. J. (2020). Inflammatory cytokine and catabolic enzyme expression in a goat model of intervertebral disc degeneration. *Journal of Orthopaedic Research®*, *38*(11), 2521–2531.

Zhang, J.-M., & An, J. (2007). Cytokines, inflammation and pain. *International anesthesiology clinics*, *45*(2), 27.

Zhang, Z., Garron, T. M., Li, X.-J., Liu, Y., Zhang, X., Li, Y.-Y., & Xu, W.-S. (2009). Recombinant human decorin inhibits tgf-β1-induced contraction of collagen lattice by hypertrophic scar fibroblasts. *Burns*, *35*(4), 527–537.

Zi, Z. (2011). Sensitivity analysis approaches applied to systems biology models. *IET systems biology*, *5*(6), 336–346.

Zioupos, P., Currey, J. D., & Casinos, A. (2001). Tensile fatigue in bone: are cycles-, or time to failure, or both, important? *Journal of theoretical biology*, *210*(3), 389–399.

Zitnay, J. L., Jung, G. S., Lin, A. H., Qin, Z., Li, Y., Yu, S. M., ... Weiss, J. A. (2020). Accumulation of collagen molecular unfolding is the mechanism of cyclic fatigue damage and failure in collagenous tissues. *Science advances*, *6*(35), eaba2795.

Zitnay, J. L., Lin, A. H., & Weiss, J. A. (2021). Tendons exhibit greater resistance to tissue and molecular-level damage with increasing strain rate during cyclic fatigue. *Acta Biomaterialia*, *134*, 435–442.

Zwambag, D. P., Molladavoodi, S., Guerreiro, M. J., DeWitte-Orr, S. J., & Gregory, D. E. (2020). Immuno-stimulatory capacity of decorin in the rat tail intervertebral disc and the mechanical consequence of resultant inflammation. *European Spine Journal*, *29*(7), 1641–1648.

APPENDICES

Appendix A

Statistical Models

This Appendix simply includes details of the statistical model fitting for each of the experiments, mainly the trace-plots and diagnostic measures like the Monte Carlo Standard Errors, effective sample sizes, and the $\hat{r}$-values.

The most important diagnostic is the trace-plot, which ideally shows that the model has converged to a steady-state distribution with very few divergences. The typical analogy is that the traceplots should look like a "fuzzy caterpillar."

A.1 Study I

Presented here are the resulting trace plots for **Study I**.

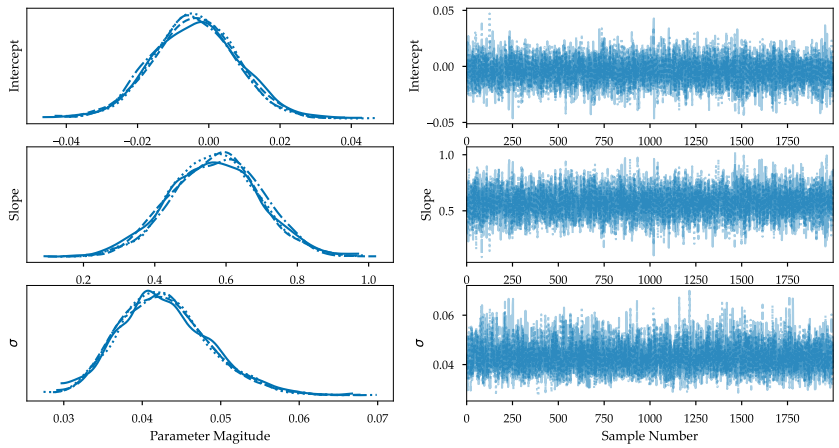

Figure A.1: Posterior distributions (left) and trace plots (right) for the statistical model for the parameter α.

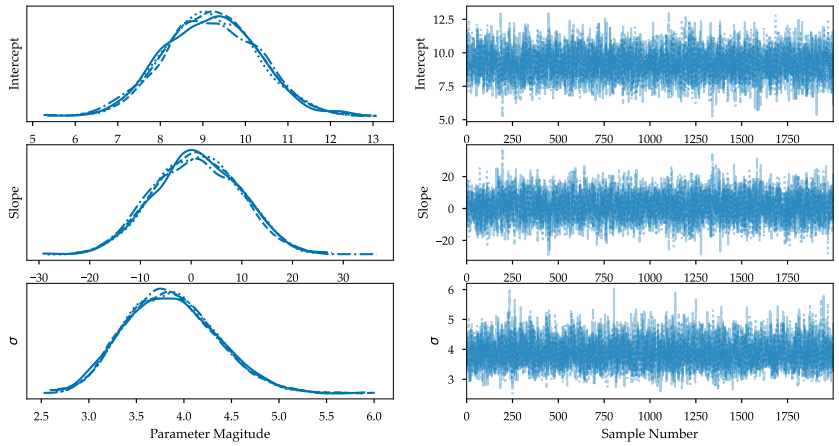

Figure A.2: Posterior distributions (left) and trace plots (right) for the statistical model for the parameter β.

A.2 Study II

Presented here are the resulting trace plots for **Study II**.

Table A.1: Summary of the statistical models for both α and β.

	mean	sd	hdi_1.5%	hdi_98.5%	mcse_mean	mcse_sd	ess_bulk	ess_tail	r_hat
α **Model**									
b	-0.0	0.0	-0.0	0.0	0.0	0.0	3720.9	3525.6	1.0
m	0.6	0.1	0.3	0.8	0.0	0.0	3809.1	3591.3	1.0
sigma	0.0	0.0	0.0	0.1	0.0	0.0	4389.1	3609.2	1.0
β **Model**									
b	9.2	1.1	6.8	11.4	0.0	0.0	3590.2	4319.5	1.0
m	1.2	8.5	-16.1	19.8	0.1	0.1	3660.7	4108.6	1.0
sigma	3.9	0.5	2.9	4.9	0.0	0.0	3660.4	2873.1	1.0

A.3 Study III

Presented here are the resulting trace plots and raw blot images for **Study III**.

A.3.1 Raw Blot Images

It is customary to include the accompanying raw Western Blots when presenting blot data.

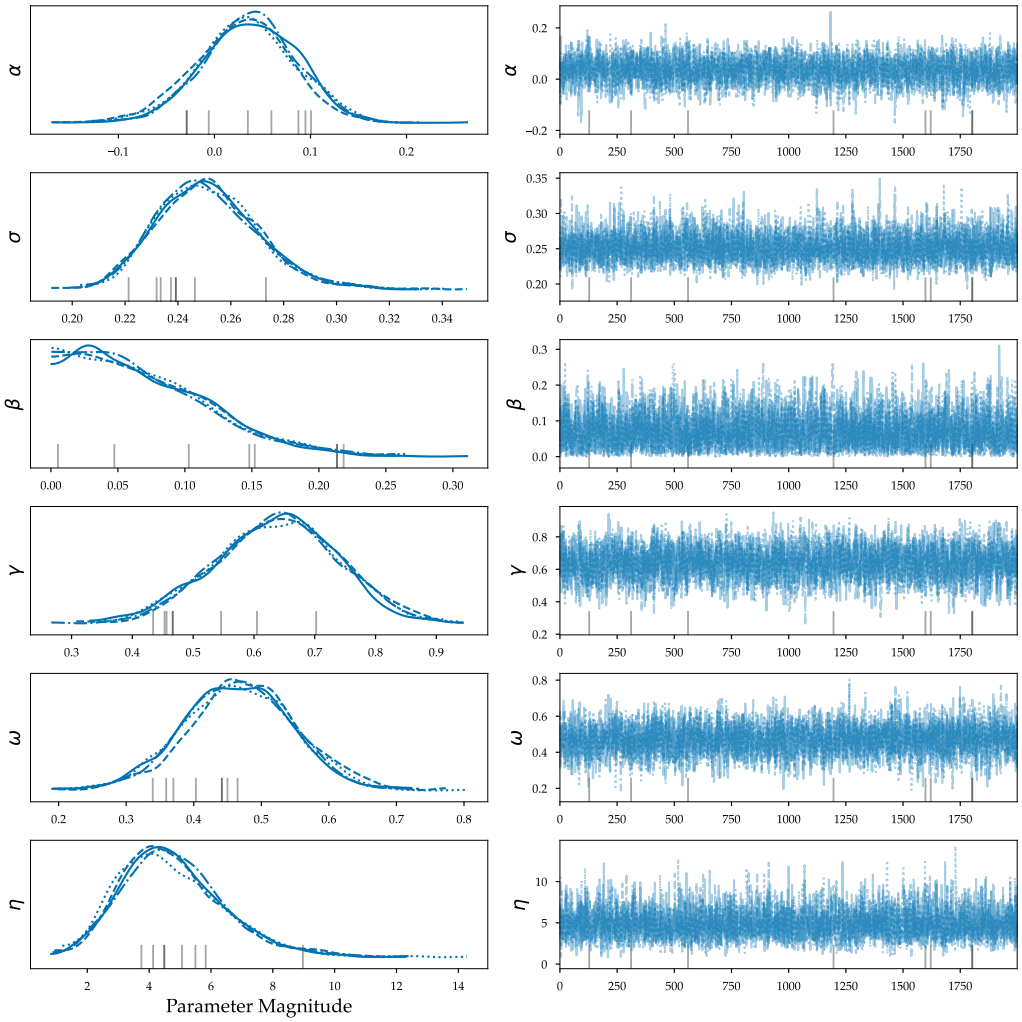

Figure A.3: Trace plot for the model parameters in Study II.

A.3.2 Statistical Models

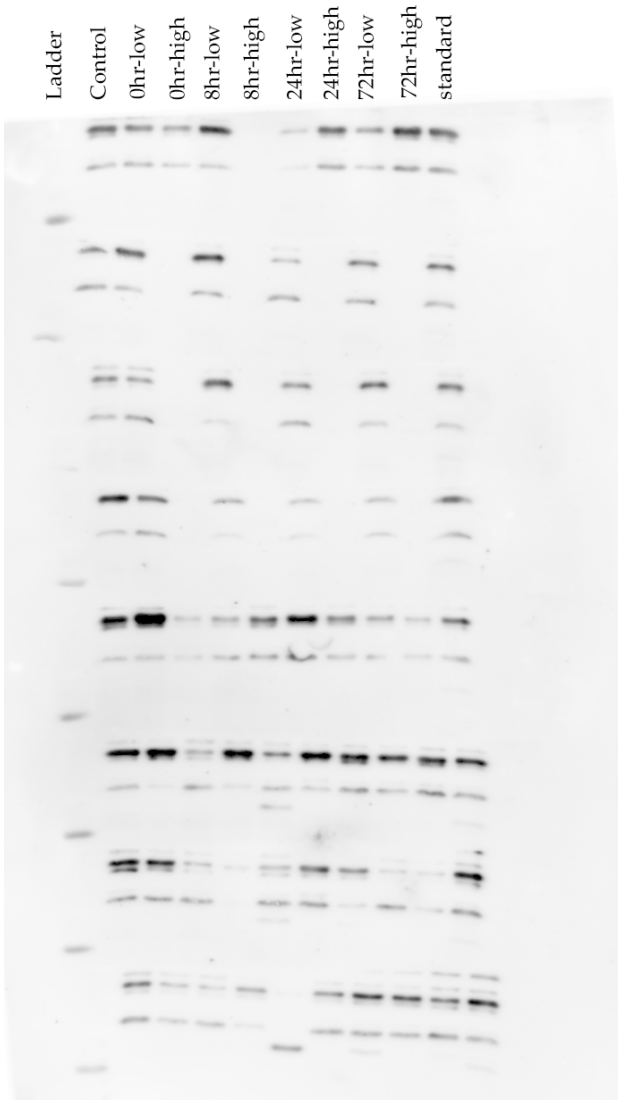

Figure A.4: Raw Western Blot Image for IL-1β.

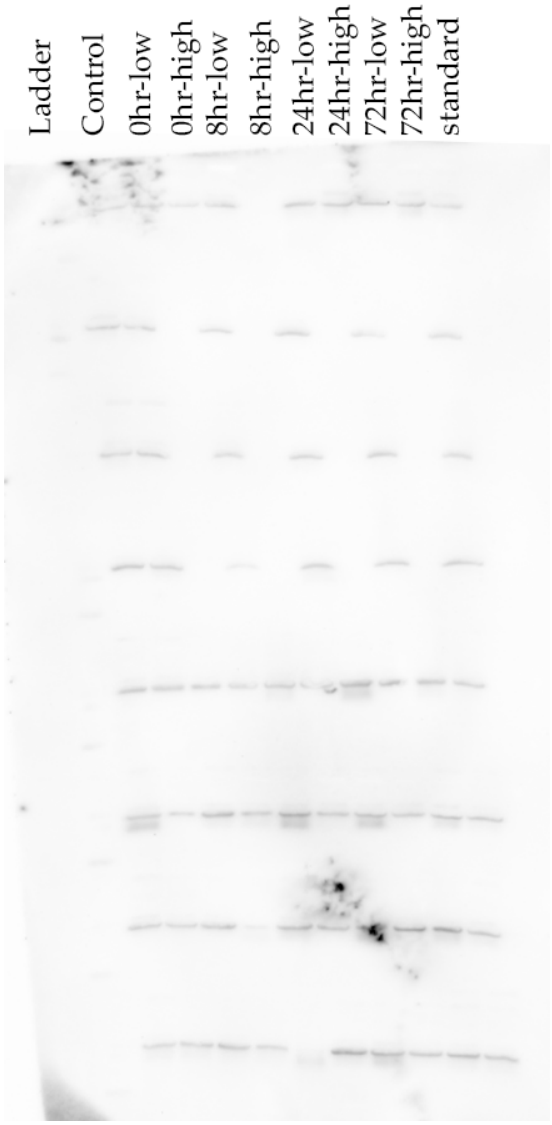

Figure A.5: Raw Western Blot Image for TIMP-1.

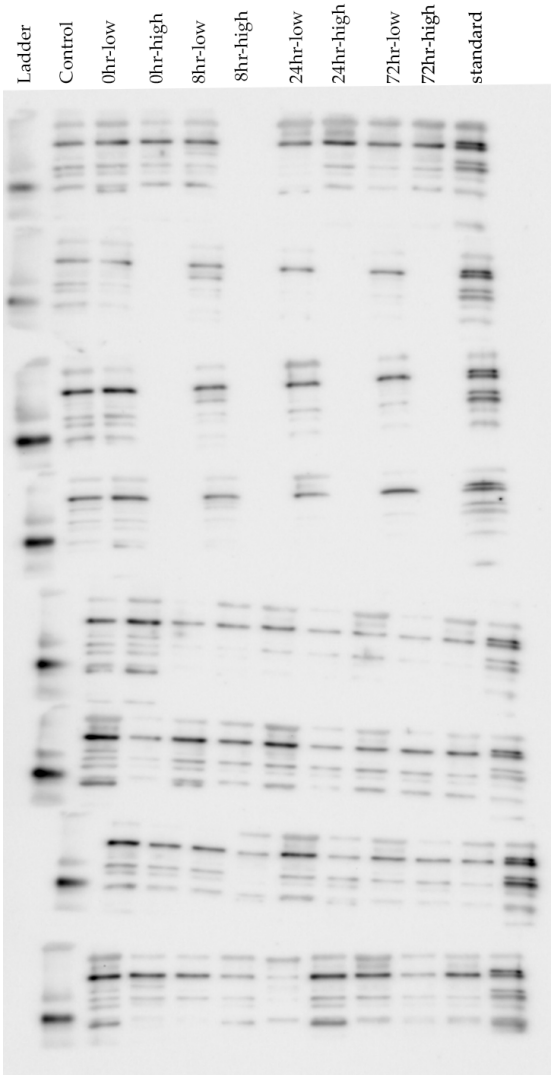

Figure A.6: Raw Western Blot Image for MMP-1.

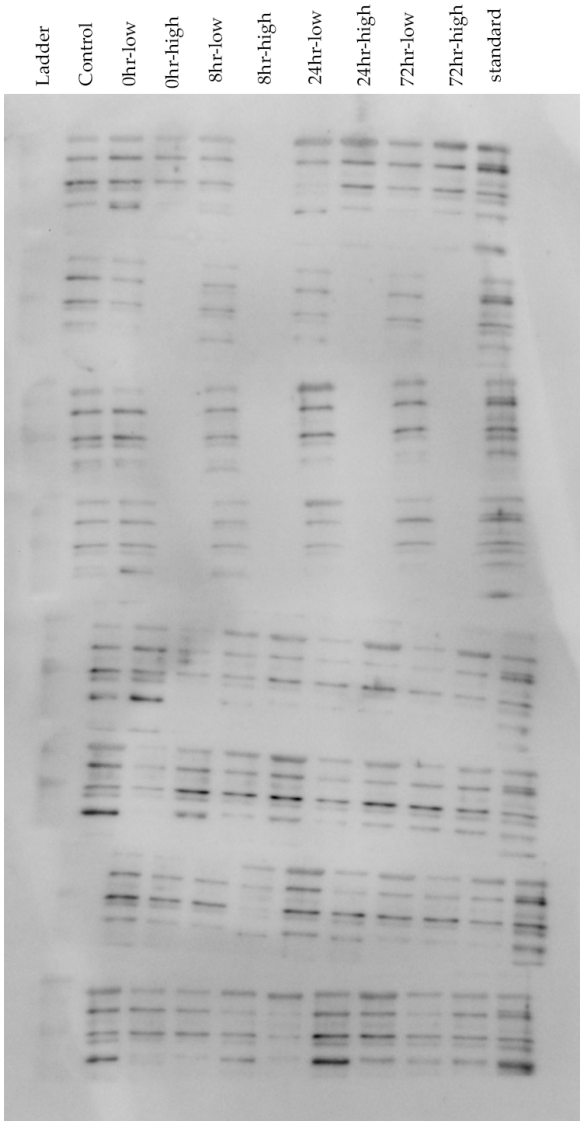

Figure A.7: Raw Western Blot Image for MMP-8.

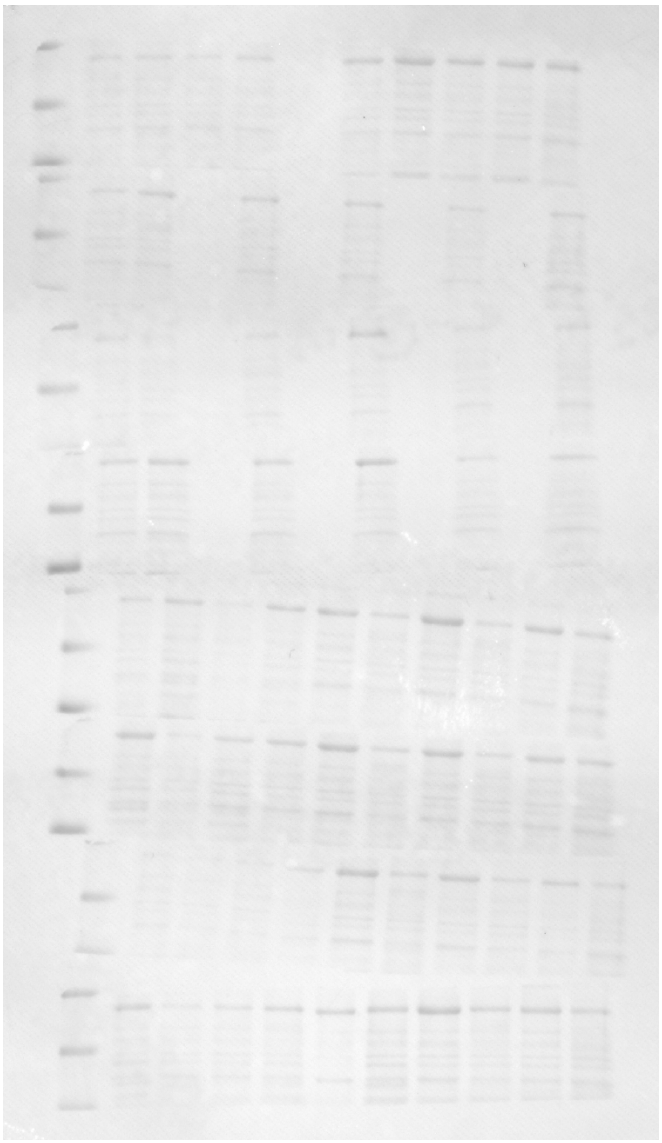

Figure A.8: Raw Western Blot Image for Ponceau Staining on the heavier proteins (50 - 75 kDa).

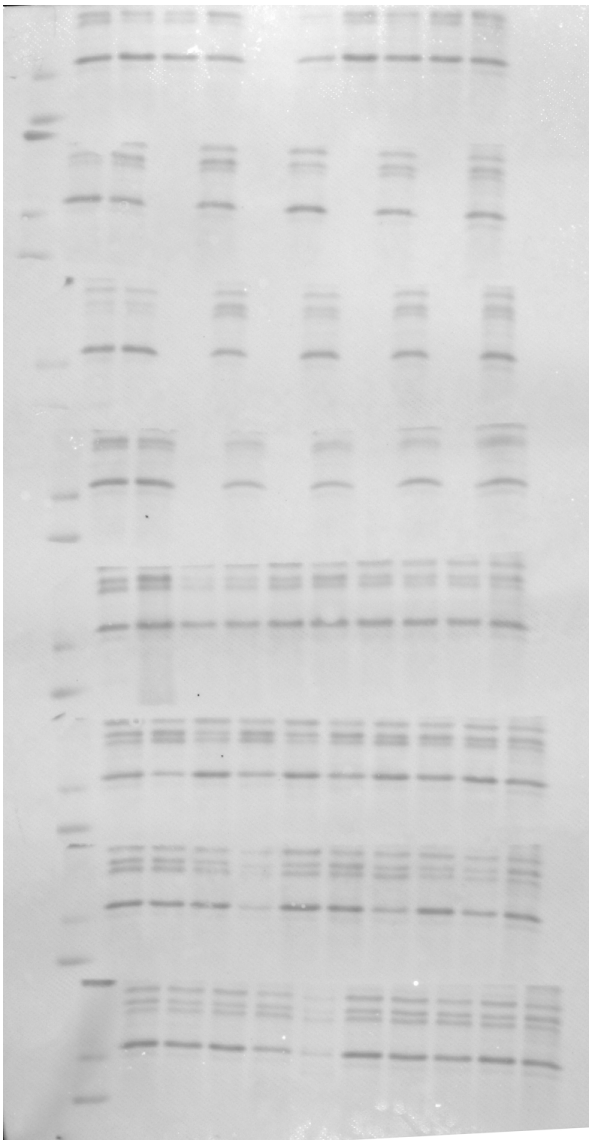

Figure A.9: Raw Western Blot Image for Ponceau Staining for light proteins (20-37 kDa).

(a) IL-1β

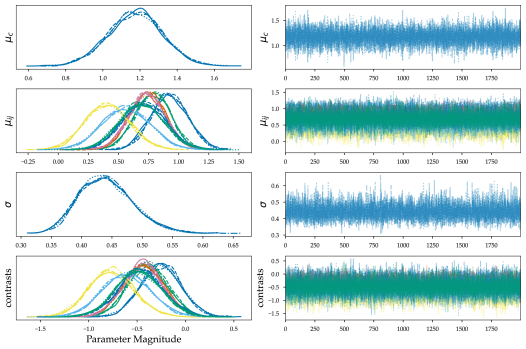

(b) TIMP-1

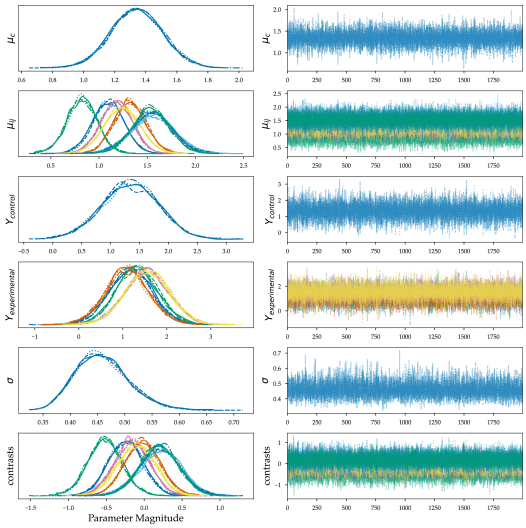

Figure A.10: Traceplots for the IL-1β and TIMP-1 statistical models. As can be seen from the Western Blot Images, some data were unavailable for TIMP-1 quantification, the statistical model tries to impute missing data, or at least calculate likely values for what the missing data could have been given the other data. Thus Y_{control} and $Y_{\text{experimental}}$ are the imputed distributions.

(a) MMP-1

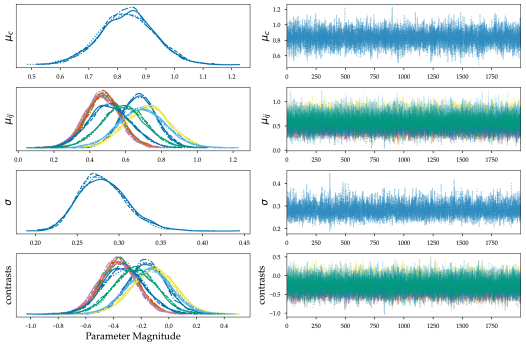

(b) MMP-8

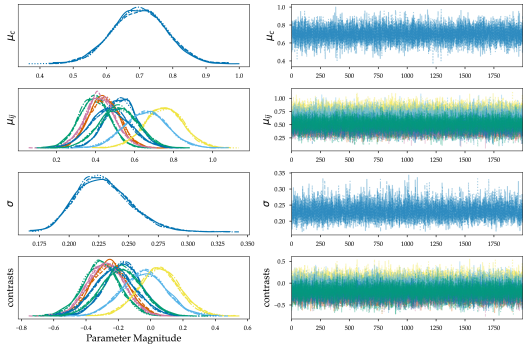

Figure A.11: Traceplots for the IL-1β and TIMP-1 statistical models.

(a) Neutral Zone Length

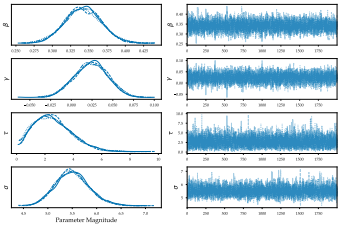

(b) Flexion Stiffness

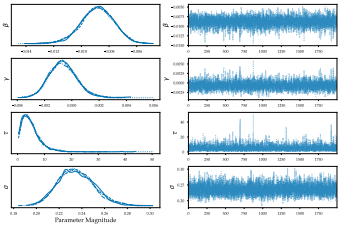

(c) Extension Stiffness

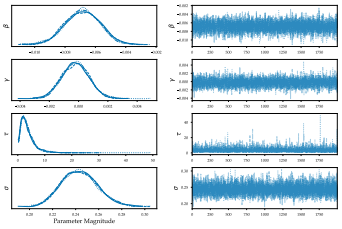

Figure A.12: Traceplots for the mechancial outcome variables.

Appendix B

A Fermi Estimate of the Collagen Concentration in Rat Tail Tendons

B.1 Motivation

This section details two estimates of the number of collagen molecules in a small volume of a rat tail tendon fascicle. This is important since the rate of chemical reactions are typically described in terms of the concentrations of reactants. The first is a Fermi-estimate based on the packing structure of collagen and the estimated volume of the RTT specimens. Fermi estimates are named after the Italian physicist Enrico Fermi, who was renowned for his ability to attain highly accurate estimates of physical parameters based on few assumptions and dimensional analysis.

B.2 Methods

B.2.1 Geometry

The assumed geometry of the RTT is cylindrical with a length of 3500 μm and a radius of 500 μm. These are based on optical measurements from Study II which also represents the experimental configuration for Study III.

B.2.2 A Fermi-Estimate

A single volume unit is a rhomboid of length $5D$ ($D = 67$ nm) whose lengths are given by the Hulmes quasi-hexagonal packing scheme. In the wet rat tail, the total volume of the rhomboid is then:

$$V_T = (1.37)\,(1.47)\,(335)\,\mathrm{nm}^3 = 675\mathrm{nm}^3 \tag{B.1}$$

This unit of volume contains one, roughly cylindrical, collagen molecule, whose length is $4.4D$, and radius is 0.602 nm, for a total volume of 335.6 nm^3. This gives a packing density of approximately:

$$\varrho = \frac{V_{col}}{V_T} = \frac{\pi\,(0.602)^2\,(294.8)\ \mathrm{nm}^3}{675\ \mathrm{nm}^3} \tag{B.2}$$

$$= 0.497 \tag{B.3}$$

So the molecules pack into the microfibril with 45% packing efficiency. These microfibrils pack into the fibres with a roughly hexagonal packing efficiency of 91%. Likewise, the fibres pack into the fascicle roughly hexagonally, with a packing efficiency of 91%, which then pack into the tendon with yet another factor of 91%. Stacking all of these together, we end up with a volumetric packing efficiency of 37% ($0.91 \times 0.91 \times 0.91 \times 0.497$). The

estimated total volume of our 3500 μm long rat tail tendon samples is:

$$V_{tendon} = \pi\,(500)^2\,(3500)\ \ \mu\text{m}^3 \tag{B.4}$$

$$= 2.749\ \mu\text{L} \tag{B.5}$$

So then, the estimated volume of collagen molecules is then:

$$V_{collagen} = 0.37 \times 2.749\ \mu\text{L} = 1.02\ \mu\text{L} \tag{B.6}$$

Which given the volume of each collagen molecule, gives:

$$n_{col} = \frac{1.02\ \mu\text{L}}{335.6 N_A\ \text{nm}^3/\text{mol}} \approx 5.0\ \text{nmol} \tag{B.7}$$

For a total concentration of:

$$[\text{col}] = \frac{n_{col}}{V_T} = \frac{5.0\ \text{nmol}}{2.749\ \mu\text{L}} = 1.83\text{mM} \tag{B.8}$$

B.2.3 Checking this Concentration

According to this calculation, approximately 63% of the wet-volume of tendon is water. Each collagen trimer has an approximate molar mass of 285 kDa. Thus, the estimated mass-density of the tendon can be approximated as:

$$\rho_{\text{tendon}} = \frac{m_w + m_{col}}{V_T} \tag{B.9}$$

$$= \frac{\rho_w 0.63 V_T + V_T\,(1.83\ \text{mM}) \times (285\ \text{kDa})}{V_T} \tag{B.10}$$

$$= 1.15\ \text{g/cm}^3 \tag{B.11}$$

We thus approximate that the wet density of tendons is approximately 1.15 g/cm^3, which is remarkably close to what is measured (between 0.8 and 2.7 g/cm^3).